



HAL
open science

Diarylethenes used as molecular switches for the connection of gold nanoparticles

Angeline Dileseigres

► **To cite this version:**

Angeline Dileseigres. Diarylethenes used as molecular switches for the connection of gold nanoparticles. Micro and nanotechnologies/Microelectronics. Sorbonne Université, 2023. English. NNT : 2023SORUS014 . tel-04051785

HAL Id: tel-04051785

<https://theses.hal.science/tel-04051785>

Submitted on 30 Mar 2023

HAL is a multi-disciplinary open access archive for the deposit and dissemination of scientific research documents, whether they are published or not. The documents may come from teaching and research institutions in France or abroad, or from public or private research centers.

L'archive ouverte pluridisciplinaire **HAL**, est destinée au dépôt et à la diffusion de documents scientifiques de niveau recherche, publiés ou non, émanant des établissements d'enseignement et de recherche français ou étrangers, des laboratoires publics ou privés.

Sorbonne Université

Ecole doctorale 397 Physique et chimie des matériaux

Institut des NanoSciences de Paris (INSP) / Equipe Physico-chimie et dynamique des surfaces

Diarylethenes used as molecular switches for the connection of gold nanoparticles

Par Angeline DILESEIGRES

Thèse de doctorat de physique et chimie des matériaux

Dirigée par Olivier PLUCHERY

Présentée et soutenue publiquement le 8 février 2023

Devant un jury composé de :

FELIDJ Nordin, Professeur et rapporteur

ISHOW Eléna, Professeure et rapportrice

CONSTANTIN Doru, Directeur de recherche et examinateur

MAISONHAUTE Emmanuel, Professeur et examinateur - président du jury

SCHEER Elke, Professeure et examinatrice

PLUCHERY Olivier, Professeur et directeur de thèse

A toutes celles et ceux qui m'ont donné envie de faire de la science

Acknowledgements

J'aimerais tout d'abord remercier le directeur de l'INSP Massimiliano Marangolo ainsi que la directrice de l'école doctorale 397 (Physique et chimie des matériaux) Nadine Witkowski.

J'aimerais ensuite remercier mon directeur de thèse Olivier Pluchery pour m'avoir confié ce projet de thèse fort intéressant et ambitieux. Je le remercie en particulier pour la liberté qu'il m'a laissée dans mon travail et qui m'a permis de développer ma capacité à faire de la recherche en autonomie.

Un immense merci aux physiciens et chimistes de l'université de Constance qui ont travaillé sur le projet ANR-DFG Plasmochrom dans le cadre duquel s'est déroulée ma thèse. Merci à Elke Scheer, Johannes Boneberg, Sergei Snegir et Leon Ruf du département de physique de l'université de Constance pour toute l'aide qu'ils m'ont fournie et tout ce qu'ils m'ont appris, en particulier concernant les mesures spectroscopiques sur les diaryléthènes. Merci à Thomas Huhn et Lukas Holz pour m'avoir fourni toutes les molécules de diaryléthène dont j'ai eu besoin pour mon projet de thèse, pour m'avoir appris à les utiliser, et enfin pour avoir répondu à toutes mes questions à propos de ces molécules fascinantes. Je tiens à souligner à quel point j'ai apprécié travailler avec eux tous durant mes missions à Constance.

Merci à Maxime Maurice, doctorant au laboratoire PROMES de l'université de Perpignan, pour ses simulations de dimères de nanoparticules d'or qui m'ont permis de mieux comprendre mon travail expérimental et sont venues l'enrichir.

Je remercie tous les membres de mon jury de thèse d'avoir accepté d'évaluer mon travail, les rapporteurs, Eléna Ishow et Nordin Felidj, les examinateurs, Elke Scheer et Doru Constantin, et enfin, le président de ce jury et examinateur, Emmanuel Maisonhaute.

Je remercie également les membres de mon comité de suivi de thèse, Laurent Delannoy, Emmanuel Maisonhaute, et Franck Vidal qui fut aussi un parrain de thèse attentif et disponible, pour avoir suivi avec intérêt le déroulement de mon travail de thèse.

Merci à Geoffroy Prévot, responsable de l'équipe Physicochimie et dynamique des surfaces ainsi qu'à tous les autres membres de l'équipe. Je remercie en particulier Emmanuelle Lacaze

qui a également travaillé sur le projet PlasmoChrom et qui m'a beaucoup aidée pour la préparation de ma soutenance, et Hervé Cruguel qui m'a formée à l'utilisation de l'AFM.

Un grand merci à Yoann Prado dont l'aide a été précieuse dans pratiquement tous mes travaux expérimentaux en salle de chimie. Je le remercie également de m'avoir fourni une quantité non négligeable de nanoparticules d'or et de bons conseils.

Je tiens à remercier les doctorants et post-doctorants de l'INSP avec qui j'ai passé de bons moments et que j'ai vraiment apprécié côtoyer au quotidien : Helen Ibrahim, Haïfa Jeridi, Tomás Rego, Pedro Lourenço, Thibaut Lacroix, Mathis Cameau, Thibault Deletang, Thomas Tran, Sarah Vincent, ainsi que tous les autres, avec une mention spéciale pour les représentants des doctorants Marine Bossert, Benoit Reynier et Niccolò Avallone. Merci également à ceux avec qui j'ai partagé mon bureau, Guillaume Diot, Fredrik Johansson, et Pedro Silva.

Je terminerai par remercier ma famille pour son soutien, non seulement pendant ces trois années de thèse mais également pendant mes huit années d'études à Sorbonne Université.

Merci à tous.

Contents

ACKNOWLEDGEMENTS	4
CONTENTS	1
INTRODUCTION	4
CHAPTER 1: STATE OF THE ART	10
I - PHOTOCROMIC MOLECULES USED AS MOLECULAR SWITCHES: THE MAIN FAMILIES	10
1 - <i>Diarylethenes</i>	11
2 - <i>Two other important families: azobenzenes and spiropyrans</i>	14
3 - <i>Molecular machines</i>	16
II - FOCUS ON DIARYLETHENES	17
1 - <i>Switching mechanism</i>	17
2 - <i>Quantum yield and fatigue</i>	20
a - Quantum yield	20
b - Fatigue.....	27
3 - <i>Applications</i>	29
III - GOLD NANOPARTICLES: LOCALIZED SURFACE PLASMON RESONANCE (LSPR), PLASMONIC ANTENNAS, AND APPLICATIONS	37
1 - <i>Description of the localized surface plasmon resonance (LSPR)</i>	37
2 - <i>Gold nanoparticles acting like plasmonic nanoantenna</i>	44
a - Near field radiated by a spherical nanoparticle.....	44
b - The concept of plasmonic nanoantenna.....	46
3 - <i>Applications of gold nanoparticles</i>	48
4 - <i>Using the plasmonic nanoantenna effect of the gold nanoparticles to solve the issue of the asymmetric switching of diarylethenes</i>	50
IV - GOLD NANOPARTICLES DIMERS	55
1 - <i>Hybridization model of the plasmonic modes of nanoparticles forming a dimer</i>	55
2 - <i>Spectral signature of gold nanoparticles dimers</i>	57
3 - <i>Tunability of the gap of a dimer</i>	57
4 - <i>Measurement of a dimer's gap distance: plasmon ruler equation (PRE)</i>	61
CHAPTER 2: EXPERIMENTAL METHODS	65
I - SYNTHESIS, DEPOSITION, AND GRAFTING PROCEDURES	65
1 - <i>Diarylene molecules of the present study: C5HT-di-PSAc and Cl-C5HT-PSAc</i>	65
a - Requirements and main characteristics.....	65
b - Synthesis	66
c - Deprotection	68
d - Storage	69
2 - <i>Gold nanoparticles: synthesis and deposition</i>	69
a - Synthesis of 19 nm Turkevich gold nanoparticles	69
b - Synthesis of 28 and/to 51 nm Bastús gold nanoparticles.....	70
c - An important parameter: the surfactant	72
d - Deposition of gold nanoparticles on an indium-tin oxide (ITO) substrate	72
3 - <i>Grafting of the DAE molecules on AuNPs deposited on an ITO substrate</i>	75
a - DAE grafting protocol 1 (samples of chapter 5.I and 6).....	75
b - DAE grafting protocol 2 (samples of chapter 5.II).....	77
II - INSTRUMENTATION AND SETUPS.....	80
1 - <i>UV-visible spectroscopy</i>	80
a - Principle of the technique and instrumental basics	80
b - Technical performances of the Jasco V-750.....	83
c - Spectroscopy of molecules in solution	87
d - Spectroscopy of species on a substrate.....	89
2 - <i>Irradiation LEDs setups</i>	90
a - The LEDs	90
b - At the INSP	91
c - At Konstanz university	93
3 - <i>Dark field optical microscopy</i>	95

4 - DF-microscopy coupled to UV-visible spectroscopy: recording the spectrum of a single gold nanoparticle.....	98
5 - Atomic Force Microscopy (AFM)	100
CHAPTER 3: MONITORING THE ADSORPTION OF THIOL MOLECULES ON GOLD NANOPARTICLES USING THE LSPR.....	104
I - DETERMINATION OF THE AMOUNT OF THIOL REQUIRED TO REACH SURFACE SATURATION	105
1 - Saturation experiments.....	105
a - MUDA.....	106
b - MHDA	108
c - Colloidal stability	109
2 - Gold nanoparticle surface saturation (full coverage) - experimental determination and geometrical calculation.....	110
a - Experimental determination	110
b - Geometrical calculation.....	111
c - Experimental versus calculated value: comparison	112
II - PREDICTIVE ANALYTICAL MODEL FOR THE LSPR PEAK WAVELENGTH SHIFT	113
1 - Derivation of the model.....	113
a - Sensitivity factor of 22 nm spherical AuNPs and dependence of the LSPR on the solvent refractive index	113
b - Calculation of the LSPR shift generated by the adsorption of a full monolayer of molecules	114
c - Evaluation of the coverage of the nanoparticle surface using the Maxwell-Garnett model.....	117
d - Application to the case of spherical plasmonic nanoparticles	118
2 - LSPR wavelength shift at full coverage: calculated versus measured	119
III - FUNCTIONALIZATION KINETICS	120
1 - Adsorption reaction kinetics measurements	120
2 - Functionalization time and adsorption reaction kinetics	122
CHAPTER 4: SWITCHING KINETICS OF DIARYLETHENES C5HT-DI-PSAC AND CL-C5HT-PSAC IN SOLUTION	124
I - STRUCTURE AND RELATED PROPERTIES OF THE MOLECULAR SWITCHES	124
1 - Impact of each component of the molecules on its properties.....	125
a - The photochromic unit	125
b - The hetaryl moieties (thiophene rings).....	127
c - The bridging unit (perhydrocyclopentene ring).....	127
d - The methyl groups (on the photochromic unit)	128
e - The phenylene linkers.....	129
f - The thiol functions protected by acetyl groups	129
2 - UV-Visible spectral characteristics of the opened and closed form of the molecules.....	129
II - KINETICS OF THE RING CLOSING REACTION: IRRADIATION OF THE SWITCHES WITH UV LIGHT	132
1 - Steady-state UV-visible spectroscopy measurements.....	132
a - Spectral features corresponding to the closed form	132
b - Photostationary state (PSS)	133
2 - Assessment of the fatigue resistance of the molecules.....	136
a - Evolution of the absorbance at a specific wavelength and at the isosbestic point	136
b - Potential origins of the degradation in Cl-C5HT-PSAc and nature of its by-product (BP)	138
c - Strategies to prevent degradation: introducing specific substituents	140
d - Prediction of fatigue resistance	141
III - SWITCHING IN BOTH DIRECTIONS: REVERSIBILITY, SYMMETRY, AND STABILITY	142
1 - Reversibility: back-switching (ring-closing reaction).....	142
2 - Symmetry of the switching.....	144
3 - Stability of the molecular switches under consecutive UV/visible exposure (cycles).....	145
IV - QUANTUM YIELD AND SWITCHING RATIO CALCULATIONS.....	149
1 - Quantum yields (QYs) calculations.....	149
2 - Switching ratio (SRs) calculations	154
CHAPTER 5: INFLUENCE OF THE PLASMONIC ANTENNA EFFECT ON THE SWITCHING KINETICS OF THE DIARYLETHENES GRAFTED ON SUPPORTED GOLD NANOPARTICLES .	158
I - ADSORPTION AND SWITCHING OF CL-C5HT-PSH AND C5HT-DI-PSH ON 28 NM AUNPS DEPOSITED ON ITO	159
1 - Cl-C5HT-PSH	159
a - Stepwise UV-visible spectroscopy monitoring and subsequent switching measurements.....	159
b - Influence of the gold nanoparticles size: 28 nm and 35 nm.....	163
c - Influence of the deprotection method and suppression of the desilanization step	169

2 - C5HT-di-PSH.....	171
II - ADSORPTION AND SWITCHING OF A MONOLAYER OF C5HT-DI-PSH ON 28 NM AuNPs DEPOSITED ON ITO	175
1 - Adsorption of C5HT-di-PSH on 28 nm gold nanoparticles deposited on ITO: in situ UV-visible spectroscopy monitoring.....	175
a - Control experiments: Evolution of λ_{LSPR} upon injection of solvent.....	176
b - Influence of the solvent degassing	179
c - Influence of the deprotection of the molecules on the grafting.....	180
d - Evolution of λ_{LSPR} upon injection of C5HT-di-PSH solution: grafting	183
2 - Switching of C5HT-di-PSH grafted on 28 nm gold nanoparticles deposited on ITO	186
III - DETERMINATION OF THE INFLUENCE OF THE PLASMONIC NANOANTENNA EFFECT ON THE REVERSIBLE SWITCHING KINETICS: COMPARISON WITH THE KINETICS IN SOLUTION.....	191
1 - Calculation of the switching ratio for C5HT-di-PSH grafted on 28 nm AuNPs deposited on ITO.....	191
2 - Comparison of the SR values obtained for molecules in solution and molecules grafted on 28 nm AuNPs deposited on ITO	193
3 - Quenching due to the connection to the AuNPs versus LSPR enhancement provided by the nanoantenna effect of the AuNPs	197
CHAPTER 6: WORKING AT THE SINGLE NANOPARTICLE SCALE: COUPLED MEASUREMENTS OF THE OPTICAL RESPONSE OF NEIGHBOR AND DAE-FUNCTIONALIZED GOLD NANOPARTICLES	200
I - PLASMONIC SPECTRA OF SINGLE 51 NM GOLD NANOPARTICLES.....	200
1 - The zone of interest: dark field microscopy	200
2 - Confirmation of the isolation: AFM characterization.....	202
3 - Dark field microscopy coupled to UV-visible spectroscopy: UV-visible spectrum of a single 51 nm AuNP	204
II - ELABORATION OF ASYMMETRIC DIMERS OF GOLD NANOPARTICLES	206
1 - Assessment of the satellite nanoparticles presence and plasmonic dimers formation	206
2 - Dark field microscopy coupled to UV-visible spectroscopy measurements: effect of the 28 nm satellite nanoparticles on the initial 51 nm nanoparticles	212
a - Single 51 nm AuNPs	212
b - Neighbor AuNPs/asymmetric plasmonic dimers.....	214
c - The neighbor nanoparticles method to form plasmonic dimers	217
III - ASSESSMENT OF THE INTERPARTICLE DISTANCE IN THE ASYMMETRIC DIMERS	218
1 - Hybridization of the plasmonic modes: case of an asymmetric dimer	218
2 - Calculation of the gap distance: application of the "plasmon ruler equation" to our results.....	219
3 - Simulation of the optical response of the asymmetric plasmonic dimers by BEM method (collaboration)	220
IV - MEASUREMENT OF THE SWITCHING OF 51 NM AuNPs FUNCTIONALIZED BY C5HT-DI-PSH	224
1 - Adsorption of C5HT-di-PSH on single 51 nm AuNPs.....	224
2 - Switching of C5HT-di-PSH molecules grafted on single 51 nm AuNPs.....	229
CONCLUSION	234
PERSPECTIVES: TOWARDS THE FABRICATION OF DIMERS WITH GOLD NANOPARTICLES CONNECTED BY A DIARYLETHENE MOLECULE	236
REFERENCES.....	238
APPENDIX.....	252
LIST OF FIGURES	279
LIST OF TABLES	290

Introduction

For decades, the industry of microelectronic devices followed the rhythm dictated by Moore's law which states that "the number of transistors in a dense integrated circuit doubles about every two years". However, in 2016, the Semiconductor Industries of America declared that the pursuit of Moore's law would be abandoned and even earlier than that in their 2011 International Technology Roadmap they predicted that CMOS technology would be replaced by "completely new" technologies that they regrouped under the name "beyond CMOS". One of these technologies is carbon-based molecular electronics which consists in fabricating electronic components with functionalities provided by molecules presenting specific properties, synthesized in an optimized manner. Some of these molecules can be used as molecular switches. The ones used for this PhD work are diarylethenes which are bistable and photochromic. It means that they exist under two stable forms and that they isomerize from one to the other in response to light exposure. UV light is used to go from the open, non-conductive OFF state (with a restricted π -system) to the closed, conductive ON state (with an extended π -system). Visible light is used to do the opposite. These molecules are based on the "ring opening/ring-closure principle" since everything happens in the central ring, with a reactive carbon-carbon bond opening and closing it in response to light. The ability of diarylethene molecules to control the conductivity, to isomerize with very low geometrical modifications, their high responsivity and fatigue resistance make them promising candidates to be implemented in molecular switches based molecular electronics devices. However, an issue with these molecules is that **their switching is asymmetric**: their ring-closing reaction possess a much higher quantum yield than their ring-opening reaction. We precisely characterized for the molecules of our study the ratio of visible photons over UV-photons necessary to open or close the central ring of the photochromic unit respectively. We anticipated a switching ratio (SR) greater than 1 (this is the asymmetry).

The aim of this PhD work was to solve this asymmetric switching issue by connecting the diarylethene molecules to gold nanoparticles. The latter were chosen for several reasons, first, gold nanoparticles are small enough to be used as electrodes to connect the diarylethenes, used here as molecular switches. One first issue here, was to investigate if the binding of diarylethenes to **the metallic nanoparticle was going to deactivate the photoswitching or not**. There are always some risks that placing a metal in the vicinity of the photoactive core acts as a quenching channel. Our experiments addressed this question. A crucial second advantage

of the gold nanoparticles is their plasmonic properties. Gold nanoparticles generate a LSPR: localized surface plasmon resonance which designates the oscillation of the electrons from the conduction band in reaction to incident light. This property is particularly useful for the monitoring of the adsorption of a chemical species at the surface of the AuNPs, in the present case diarylethenes with thiol termination, taking advantage of their high affinity with gold. Gold nanoparticles electrodes were also used as plasmonic nanoantennas to focus and amplify the electromagnetic field around them creating the so-called “hot spots” in their close vicinity where the molecular switches are grafted. The goal was to use these hot spots to increase the efficiency (quantum yield) of the diarylethenes’ photoconversion reactions, especially that of the reaction with the much lower quantum yield i.e., the photocycloreversion. Our interrogation here was to characterize if the nano-antenna effect could rebalance the switching ratio, bringing it closer to 1. Note that both phenomena taking place around the gold nanoparticles, the LSPR and the creation of hot spots, occur when the dimension of the illuminated object is inferior to the wavelength of the incident light.

This PhD work was mainly conducted at the Institut des NanoSciences de Paris (INSP) in the physico-chemistry and dynamics of surfaces (Physurf) team. This team is built around eight research axes: self-assembly at the nanometric scale, interfaces dynamics, surface functionalization, interfaces and organic films, 2D materials, nanoparticles, optoelectronics, and plasmonics and sensors. They aim at a better understanding of the structural, optical, and electronic properties of low-dimensions systems that are the surfaces, interfaces, and nano-objects. In doing so, the team uses its expertise in the growth and synthesis of nanomaterials and the study of their properties through a large array of experimental and theoretical techniques.

This PhD project has been funded by the ANR (Agence Nationale de la Recherche) in the frame of the franco-german ANR-DFG project PlasmoChrom “Investigation of the electronic transport through photochromic molecules under plasmonic excitation”. This project was dedicated to the study of electronic transport properties of photoswitchable molecules in metal-molecule-metal junctions under light irradiation. In my case, the photochromic properties of diarylethene molecules connected to gold nanoparticles were investigated to bring an answer to the following issue: Is it possible to enhance the switching efficiency of photochromic molecules using the optical antenna effects of the electrodes to which they are connected. This project involved the mastering of the tailored synthesis of molecular switches, the

understanding of electrical transport through metal-molecule-metal junctions, and the ability to use plasmonics to generate photo-assisted transport.

Three groups were involved in this project, a first group from the physics department of Konstanz University, which is part of the research team led by Pr. Dr. Elke Scheer (AG Scheer). Her research team is specialized in mesoscopic physics and conduct research about nanoelectronics (transport phenomena occurring at very small scales), mesoscopic superconductivity, spin transport phenomena and nanomagnetism in nanostructure, molecular electronics (electric and thermoelectric properties and transport mechanisms of single-molecule junctions), nanooptoelectronics (optical and nanoplasmonic control of the transport through nanoconductors). The Scheer group is expert in the study of single-molecule junctions (SMJs) using mechanically controllable break junctions (MCBJs). They explained the relatively low conductance ratio between open and closed state of diarylethenes (DAEs) after discovering a change of the level alignment of DAEs to Au electrodes by analyzing the current-voltage characteristics of DAE SMJs at low temperature^{1,2}. They also demonstrated the reversible switching in situ of the conductance of DAEs grafted on a graphene-based film used as an electrode in a micron-sized electronic device^{3,4}. The group also masters the study of plasmonic effects occurring in metallic point contacts using surface propagating plasmons and antenna effects⁵⁻⁷ which represented a crucial expertise to tackle the enhancement of the quantum yields of DAE molecules in SMJs using SPPs. They confirmed the possibility to optically control the transport in metallic nanostructures (metallic contact points) using SPPs⁵. They managed to show that the SPPs enhance the switching probability for the ring-opening reaction and that the switching is maintained at low temperature (30 K) although its probability is reduced.

In the frame of the Plasmochrom project, this group formed by Pr. Dr. E. Scheer, Apl. Pr. Dr. J. Boneberg, Dr. S. Snegir (post-doc), T. Möller (post-doc), and L. Ruf (PhD student) investigated tunable single-molecule junctions with leads patterned with gratings optimized for exciting propagating surface plasmon polaritons (SPPs) using MCBJs.

A second group of organic chemistry experts from the chemistry department of Konstanz University led by Dr. Thomas Huhn, who is a specialist in the (tailored) synthesis of diarylethenes, was involved. His group made regular collaborations with that of Pr. Dr. E. Scheer and thus provided all the molecules for their electronic transport studies^{1,3,4,8-11}. The Huhn group developed DAEs with sulfur-free photochromic units to avoid un-desired bonding of the thiophenes' sulfur atoms to Au electrodes. Conjugated heteroatom-rich side chains were

attached to these molecules that exhibited picosecond¹² and even sub-picosecond ring-closing kinetics¹³. They demonstrated the reversible switching of this type of DAE molecules organized in SAMs, they studied their properties by STM^{3,4,9,14,15}, and they also used them to connect metal contacts^{9,11,16}. Upon replacement of the hexafluorocyclopentene bridging unit by a tetrafluorocyclobutene, the ring-opening QY of this type of DAEs was increased. It was also the case when adding longer side chains of the rigid oligo(phenylene ethynylene) OPE-type^{16,17}. The group also implemented these DAEs in molecular devices with flexible graphene-oxide electrodes⁴.

In the frame of the Plasmochrom project, this group formed by Dr. T. Huhn and his PhD student L. Holz, synthesized all the diarylethene molecules.

The third group involved in the Plasmochrom project was formed by O. Pluchery, E. Lacaze, and myself from the Physurf team of INSP, previously described. O. Pluchery is expert in the study of electrical properties (via STM, KPFM, and conductive AFM) and plasmonic properties¹⁸ (via optical microscopy and spectroscopy properties of supported gold nanoparticles functionalized with organic molecules. His group studied the Coulomb blockade generated by a double tunnel junction made of AuNPs connected by organic ligands using low temperature STM in vacuum. They measured the current resulting from single electron tunneling, the transparency of the tunnel junction in function of the length of the molecules by STS^{19,20}, the conduction regimes through the molecules by conducting AFM [Plu16]. They also studied the effect of a molecular layer on which AuNPs were deposited on the apparent work function of these AuNPs using KPFM²¹. E. Lacaze is a specialist of the study of DAEs organized in SAMs on gold surface Au (111) by STM²². Her group studied the self-organization of the DAEs on the Au(111) surface in function of their molecular structure, the influence of the environment of the DAEs on the Au(111) surface on their photochromic properties, and the effect the intermolecular interactions of DAEs have on both their photo- and electrically induced switching²³.

This PhD manuscript is divided in six chapters followed by a general conclusion and an overview of the perspectives opened by the PhD work it reports.

The first chapter consists in a bibliographical work conducted to present the basics and the state of the art of the two main aspects of this PhD work i.e., the molecular switches

(particularly the photoactive ones) and the gold nanoparticles with a focus on their plasmonic properties.

The second chapter introduces all the experimental procedures involved in the preparation of the samples (synthesis, deposition, and functionalization of the gold nanoparticles) as well as all the experimental techniques used to perform measurement on the samples: UV-visible spectroscopy, dark field microscopy, dark field microscopy coupled to UV-visible spectroscopy, atomic force microscopy, and LEDs setups.

The third chapter reports a study of the progressive functionalization of spherical 22 nm gold nanoparticles by thiol molecules (MUDA and MHDA) and its kinetics using UV-visible spectroscopy. This study relies on one of the main plasmonic property of the AuNPs which is their localized surface plasmon resonance that appear as an intense peak on the spectra. Through the evolution of this peak (LSPR peak wavelength shift), it is possible to monitor the evolution of functionalization. An analytical model to predict the value of this LSPR peak wavelength shift is also presented.

The fourth chapter is dedicated to a photokinetic study of the two diarylethene molecules used in this PhD work in solution. UV-visible spectroscopy measurements of the molecules solutions upon irradiation give us information about the degree of reversibility and symmetry of the switching of the molecules (calculations of switching ratios), their photoconversion reaction kinetics, and their fatigue resistance.

The fifth chapter concerns the monitoring of the adsorption of both diarylethene molecules on 28 nm AuNPs deposited on ITO substrates with two different procedures, and more importantly, the subsequent switching measurements performed on the samples. The value of the LSPR peak wavelength shift induced by the adsorption of the DAEs on the AuNPs was calculated and compared to the experimentally obtained value. Values of the switching ratios of the DAEs when grafted on AuNPs are calculated from the switching measurements (evolution of the absorbance of the molecules in function of the irradiation time) and compared to the value calculated for DAEs in solution. The aim being to assess the presence or not of a LSPR enhancement effect from the AuNPs on the switching of the diarylethene molecules.

The sixth chapter deals with the results obtained while working at the single nanoparticle scale. On the one hand, the fabrication and characterization by dark field microscopy coupled

to UV-visible spectroscopy and AFM of asymmetric plasmonic gold nanoparticles dimers is presented. On the other hand, the functionalization of 51 nm AuNPs deposited on ITO by diarylethene molecules is studied at the single nanoparticle scale and subsequent switching measurements are performed at the same scale but the same way it had been done in the previous chapter for a large number of AuNPs. These results obtained at the single AuNP scale reinforce those obtained at the global scale (large ensemble of AuNPs) since the measured switching are analogous (comparable values of switching ratio).

Chapter 1: State of the art

In this first chapter, the molecules used here as molecular switches for this PhD work, diarylethenes (molecules whose electrical conductance can be switched), are presented. Other photochromic compounds which can also be used as molecular switches are also introduced. The plasmonic properties of gold nanoparticles to which the diarylethenes will be connected are described. As mentioned in the introduction, gold nanoparticles are both used as electrodes and plasmonic nanoantenna to attempt to compensate the low quantum yield in one of the switching directions by locally amplifying the visible light received by the molecules. Strategies previously implemented to solve that issues are reviewed and put in perspective with ours. Finally, the case of gold nanoparticles dimers is considered, their plasmonic and spectral properties are described, and the tuning and measurement of the dimer gap is addressed.

I - Photochromic molecules used as molecular switches: the main families

According to the IUPAC, photochromism is defined as the “reversible transformation of a molecular entity between two forms, A and B, having different absorption spectra, induced in one or both directions by absorption of electromagnetic radiation. The spectral change produced is typically, but not necessarily, of visible colour and is accompanied by differences in other physical properties. The thermodynamically stable form A is transformed by irradiation into form B. The back reaction can occur thermally (photochromism of type T) or photochemically (photochromism of type P)”²⁴. Upon photoisomerization, the absorption properties are not the only ones to be modified, the physicochemical properties of the molecule, including its refractive index, electrochemical behavior, and in the case of diarylethenes conductance. A molecular switch is a molecular system that exhibit reversible conversion between two or more stable states in response to an external stimulus leading to a conformational and environmental modification of the switch²⁵. The first condition in order for a molecule to be used as a switch is to be bistable i.e., to possess two different stable isomeric forms, and to be reversibly convertible between these two forms upon excitation by an external stimulus. Then, further requirements appear as essential especially in the perspective to implement applications based on these molecular switches. In the case of a photochromic molecular switch, they are the following: the photoconversion must be easily and selectively triggered (by light of a specific wavelength), the thermal interconversion must be prevented on a large enough temperature range (particularly important for data storage applications), both

isomers should be highly resistant to fatigue (i.e., able to undergo a large number of switching cycles without, or extremely weak, molecular degradation and sub-product production), both isomers should have a fast response time (switching cycles should be able to alternate quickly), the switching must be highly efficient (the quantum yield of both isomerization reactions and the absorption of both isomers must be high) in solution and in the solid state, both isomers should be readily detectable and characterizable, and finally, if the molecular switch is included in a macromolecular structure, the properties of the aforementioned structure must be preserved upon the switching^{25,26}. The main families of photoresponsive molecular switches, presented hereafter, are the azobenzenes, the spiropyrans, and the diarylethenes. However, other families of photoresponsive molecular switches exist, amongst them are the fulgimides, hemithioindigos, chalcones/flavyliums, dihydroindolizines, and dihydropyrenes²⁷.

It can be underlined that light is a particularly advantageous stimulus, it is readily available and can be remotely and precisely (high spatiotemporal resolution) applied for a chosen duration. It is also versatile: a large range of wavelengths is available, the intensity of illumination can be easily controlled, the light can be polarized when needed, and it generates fewer by products than other types of stimuli. All these elements contribute to explain the attractiveness of photo-responsive compounds^{27,28}.

1 - Diarylethenes

Photochromic diarylethenes were discovered by M. Irie while he was studying photoresponsive polymers, the monomer unit made of 2,3-di(2,5-dimethyl-3-thienyl)butene was then isolated and its photochemistry (and that of its derivatives) was studied by Irie et al. leading to the first diarylethene-related publication in 1988. Diarylethenes (DAEs) are stilbene derivatives, the most common, and primarily developed type of DAEs are the 1,2-diarylperfluorocyclopentenes, then followed 1,2-diarylmaleic anhydrides and 1,2-diarylmaleimides, and finally 1,2-diarylperhydrocyclopentenes were developed. All these DAEs are usually synthesized with heterocyclic aryl groups in order to obtain thermally irreversible P-type photochromes, crucial property for the applications of DAEs as memories, switches, and molecular machines. It should be noted that the perfluorocyclopentene, maleic anhydride, maleimide cycloalkene, and perhydrocyclopentene groups are used here as bridging unit which prevent the Z/E isomerization of the molecule so that it does not compete with the photoisomerization. The role of each part of a diarylethene molecule is detailed in Chapter 4.I.1 based on the diarylethenes molecules used for this PhD work. However, all the previously

mentioned types of DAE exhibit quite similar photochromic properties, thermal stability, and resistance to fatigue, the only affected characteristic is the position of their spectral features, going to higher wavelength when going from perhydrocyclopentene to perfluorocyclopentene, and finally to maleic anhydride or maleimide cycloalkene groups^{26,29,30}.

DAEs reversibly isomerize between a closed and an open form upon irradiation with light of a certain wavelength, generally UV light for the ring-closing reaction and visible light for ring-opening reaction. Both reactions generally occur in the ps time range, as measured in many time-resolved spectroscopy studies. As can be seen in Figure 1.1, the photoconversion and the electronic and geometric change it triggers can be illustrated using the example of 1,2-bis(2,5-dimethyl-3-thienyl)perfluorocyclopentene, a typical DAE molecule. In the open-ring isomer, the π -conjugation is localized, restricted to each thiophene ring, and its spectrum is similar to that of a substituted thiophene. In the closed-ring isomer, the HOMO-LUMO gap of the molecule is decreased, the π -conjugation is delocalized on the whole molecule that turns from colorless to red. Note that the color depends on the size of the π -system. In inverse dithienylethenes (DTEs), dithienylethenes with the thiophene rings linked to the ethene moiety at the 2-positions, the π -system of the closed form is short because restricted to its central part explaining their yellow color. In normal DTEs, diarylethenes with the thiophene rings linked to the ethene moiety at the 3-positions, the π -system is large because delocalized on the whole molecule, its absorption band is therefore shifted to longer wavelength explaining their purple or blue color. Upon irradiation with visible light, the π -system is interrupted by the opening of the reactive C-C bond, explaining the disappearing of the coloration. The molecule also undergoes a small geometric change upon ring-closing, it stretches of 0.7 nm vertically, shrinks of 0.11 nm horizontally, and its thickness slightly decreases^{26,31}.

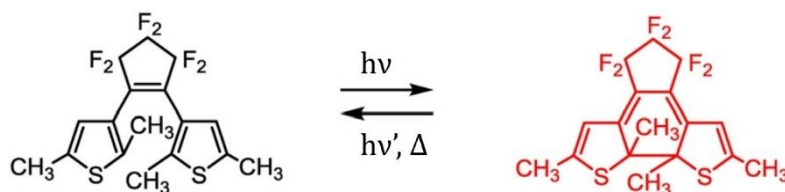


Figure 1.1: Example of a typical and widely studied diarylethene: 1,2-bis(2,5-dimethyl-3-thienyl)perfluorocyclopentene. Adapted from²⁶.

Typically, the open-ring isomer of diarylethenes have a large absorption band at short wavelengths in the UV range or very close to it. Upon irradiation with UV light and subsequent conversion to the closed ring isomer, the intensity of the aforementioned peak corresponding

to the open form decreases and a broad absorption band corresponding to the closed form appears in the visible range (see Figure 1.2), explaining the coloration of the molecule. This large spectral shift of the absorption is due to the delocalization of the electrons from the π -system which is extended to the whole molecule when it is its closed form. The position of the band depends on the type of ring and their substituents but also on the type of bridging unit. It is therefore tunable in function of the application envisioned for the synthesized DAE. The intensity of the bands and their corresponding molar absorption coefficient is also crucial since the sensitivity of the molecule towards light depends on it. For example, adding phenyl rings at the 5- and 5'-positions of a dithienylethene (type of DAEs used in the present PhD work) makes its absorbance band redshift and its molar absorption coefficient increase from 5.0×10^3 to $1.1 \times 10^4 \text{ M}^{-1}\text{cm}^{-1}$, the band can even be further redshifted and its molar absorption coefficient further increased by adding electron-withdrawing substituents to the phenyl rings in para position. In general, enlarging the π -system by introducing electron-rich substituents makes the molar absorption coefficient increase²⁶.

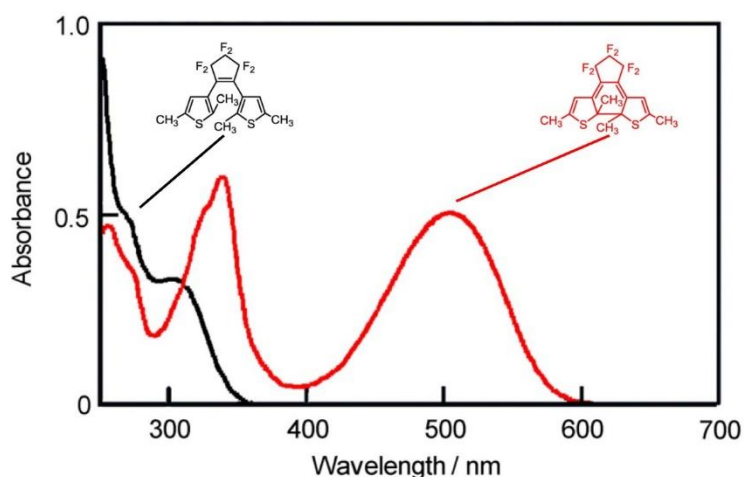


Figure 1.2: Example of the absorption spectrum of a typical diarylethene (1,2-bis(2,5-dimethyl-3-thienyl)perfluorocyclopentene). Adapted from²⁶.

It can be noted that inverse DTEs have spectral features that have the opposite behavior than that of normal DTEs. For the closed isomer, because the π -conjugation is limited to the photochromic unit in this type of DAE molecules, the absorbance band is completely blueshifted while for the opened form it is the other way around: the peaks is largely redshifted. The position of the absorbance maxima is therefore completely different according to the type (normal or inverse) of the DAEs rendering them suitable for completely different types of applications: optical memories for the former and full color displays for the latter²⁶.

The best synthesized DAEs exhibit incredible thermal stability with a half-life at room temperature superior to 400 000 years, a maximum number of repeatable cycles superior to 10 000, the QY of their ring-closing reaction is close to 1 meaning that the probability to convert all the molecules from the ring-open for to the ring-closed one upon UV irradiation is almost 100 %, both their reaction occur in the ps time range, and they are able to switch reversibly in the single crystalline phase²⁶.

2 - Two other important families: azobenzenes and spiropyrans

Azobenzene molecules consist in two aromatic rings linked by an azo group (double nitrogen bond, N=N). They are photochromic and can also be thermochromic but are mainly used for their photochromism, indeed, upon irradiation the molecules are reversibly interconvertible from their trans (Z) isomer to their cis (E) isomer; this interconversion is accompanied by a large geometrical change and a molecular movement (see Figure 1.3), the dipole moment and absorption spectrum of the molecules are also modified. Azobenzenes were discovered in 1834 and their photochromism was reported for the first time by G.S Hartley in 1937^{25,32,33}.

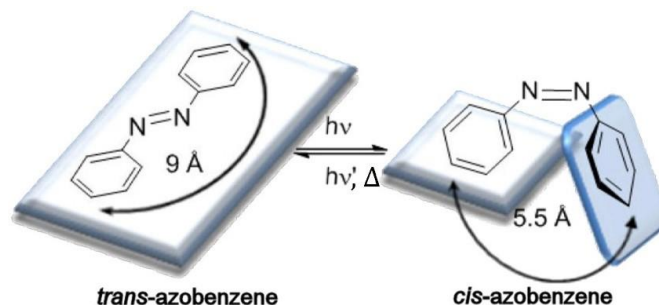


Figure 1.3: Structure and photoisomerization of an azobenzene. The distance between the carbon atoms in position 4 goes from 9 Å to 5.5 Å upon isomerization from the flat E form with no dipolar moment to the Z form with an angular geometry and a 3.0 D dipolar moment. Adapted from²⁵.

The predominant more stable E isomer is photoconverted to the 12 kcal.mol⁻¹ less stable Z isomer by light of a wavelength in the 320 - 380 nm range, while the opposite reaction takes place upon irradiation with a light of a wavelength in the 400 - 450 nm range. Both photoreactions are ultra-fast (ps range) but the thermal relaxation from the cis to the trans isomer can take from ms to days. Geometrically speaking, the molecule folds itself and one of the rings rotates to minimize steric repulsion with the one it was facing²⁵. The spectroscopic features and the main classes of azobenzenes are presented in the Appendix (see A.1) as well

as the photochromic reaction undergone by this type of molecules: the transitions involved and its mechanism.

Spiroprans, with their many interconnected properties, constitute the most versatile class of molecular switches. In spite of their “multichromism”, spiroprans were mostly studied and used for their photochromism. Structurally, a spiroprans consists of two pyran rings separated by a chiral “spiro” center. The first spiropran, dibenzo-spiropran, originally designated as a by-product of coumarin derivatives synthesis, was discovered and named by Decker in 1908, it is acidochromic but not photochromic. Derivatives such as α - and β -naphthospiroprans, which are thermochromic, then emerged but it is the photochromic indolinobenzospirans (which are also thermochromic), obtained by condensation of Fischer indole with salicylaldehyde, that triggered massive interest in this family of compounds and defined its base structure (see Figure 1.4). Actually, spiropran (SP) designates the closed form of the molecules which can be converted to its open form called merocyanine (MC) differing in planarity, acidity, reactivity, polarity and dipole moment, polarizability, and electronic structure^{34–36}.

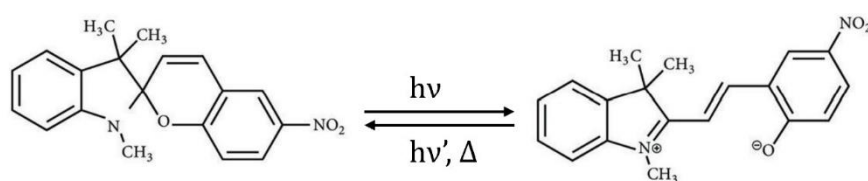


Figure 1.4: Typical photochromic indolinobenzospiran in its spiro (SP) form on the left and its merocyanine (MC) form on the right.

The thermochromism and photochromism, including the photoswitching mechanism, of spiroprans are described in the Appendix (see A.2).

It would be less relevant to use azobenzenes or spiroprans for this project due to the important geometrical change they undergo upon their photochromic switching. In the case of spiroprans, the two parts located on each side of the asymmetric carbon are situated in two different planes for the SP isomer, and then in the same plane for the MC isomer. Although the two isomers exhibit different degree of conjugation, this geometrical change upon photoswitching is not desirable for applications of the molecules in molecular electronics devices. Besides, the location of the anchoring site on the five-membered ring, usually used to graft this type of molecules to surfaces, is not adapted to the connection to two electrodes.

Additional synthetic steps would be required to create at least another anchoring site. Regarding the azocompounds, although these molecules possess an anchoring site at each of their extremity, rendering possible their connection to two electrodes, they also undergo an undesired geometrical change upon photoswitching. The two parts located on each side of the N=N bond are located in the same plane for trans-azobenzene but then in two different planes for cis-azobenzene, which is not compatible with applications as a switch in molecular electronics.

3 - Molecular machines

The importance of molecular switches was highlighted in 2016 when J.-P. Sauvage, J.F. Stoddart, and B.L. Feringa were awarded the Nobel Prize “for the design and synthesis of molecular machines”³⁷. In 1983, J.-P. Sauvage developed novel synthetic routes based on the use of copper complexes for the synthesis of catenanes³⁸ (see Figure 1.5). The latter are constituting elements of a molecular machine which is “a multicomponent molecular system with defined energy input that is capable of performing a measurable and useful secondary function reversibly either at the nanoscale or, if amplified through collective action, at larger scales”³⁹. Catenanes consist in interlocked molecular rings forming chains in which the two entities are linked by a mechanical bond that allow them to move relative to each other, an important characteristic for their integration in machines^{37,38}. In 1991, J.F. Stoddart synthesized a new type of rotaxanes, the donor-acceptor rotaxanes, including the so-called “molecular shuttle” which is a molecular axle inserted in a molecular ring able to move anywhere along that axle but blocked at the extremities⁴⁰ (see Figure 1.5). By introducing molecular switches units in the axle, the movement of the ring on the axle became controllable by an external stimulus⁴⁰. Stoddart and co-workers considered the molecular shuttle as a prototype for the construction of molecular switches and machines based on molecules containing mechanical bonds⁴⁰. He and his team then developed some of the first molecular machines such as molecular lifts and molecular muscles⁴¹. Finally, Ben L. Feringa fabricated the first molecular motor (photoactive unidirectional rotary motor) in 1999 which led to the development of new molecular machines^{39,42,43}. After demonstrating single-molecule motion and achieving the transition between rotational and translational motion, they built a nano-car based on third-generation symmetrical molecular motors corresponding to the meso- (R,S-R,S) isomer of the nano-car. It operates at low temperature on a Cu(111) surface and moves along a globally linear trajectory upon excitation with a STM tip triggering propulsion⁴² (see Figure 1.5).

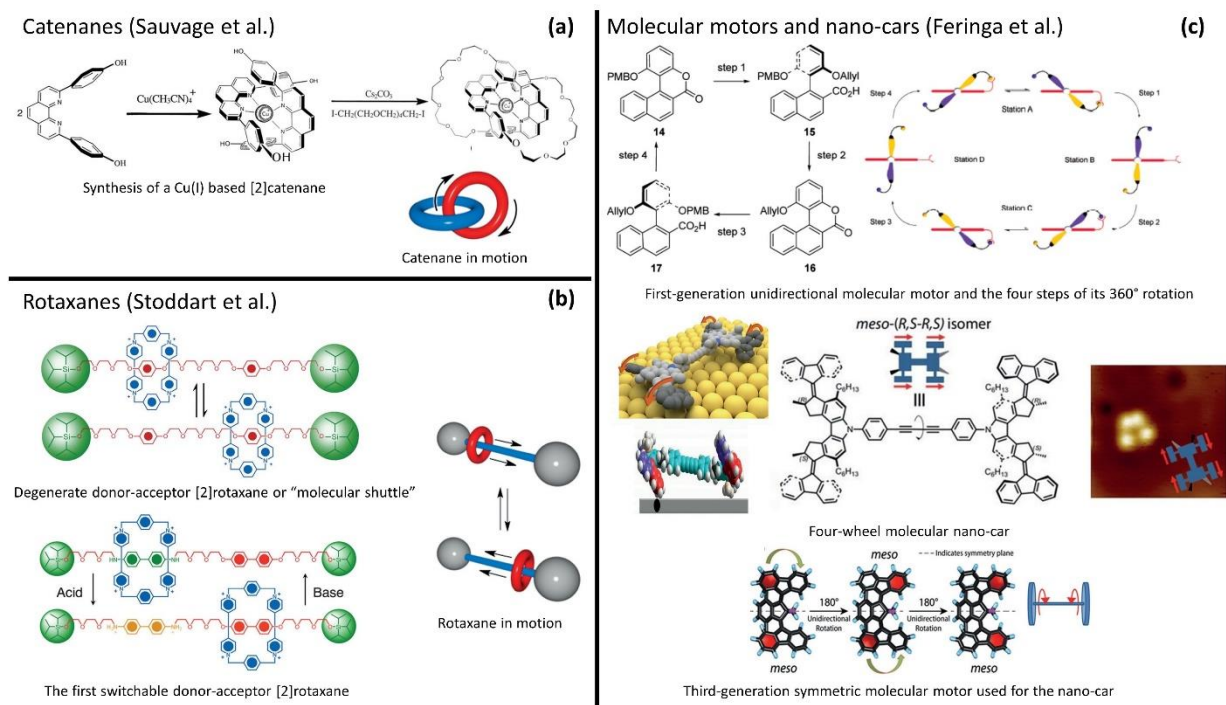


Figure 1.5: (a) Synthesis of a [2]catenane obtained by a double cyclization following Grubbs ring-closing methodology of an entwined compound with a copper(I) center formed from a 1,10-phenanthroline derivative. (b) A degenerate donor-acceptor [2]rotaxane or "molecular shuttle". The CBPQT⁴⁺ ring moves back and forth (1000 times a second in acetone at room temperature) along the axle in between its two terminal hydroquinone recognition sites. (Top) The first switchable donor-acceptor [2]rotaxane whose switching is triggered by drop of acid that protonates the benzidine recognition unit where the presence of the CBPQT⁴⁺ ring is favored. Upon the protonation, the presence of the ring becomes more favored on the biphenol unit to which it migrates. Back-switching is triggered by an addition of base (Bottom). (c) Chemical structure and steps occurring during the rotation of a first-generation biaryl-based 4-step unidirectional molecular rotary motor (Top left). Schematic representation of the four steps composing its 360° rotation (Top right). Molecular models and structure and STM image of a four-wheel molecular nano-car based on rotary motors (Middle). Chemical structure of the third-generation symmetric molecular motor used for the nano-car. Adapted from^{38,40,42,43}.

II - Focus on diarylethenes

1 - Switching mechanism

The mechanism of both the ring-opening and ring-closing reactions has been unraveled by theoretical calculations. More specifically, Boggio-Pasqua et al.⁴⁴ made a complete active space self-consistent field (CASSCF) study of the potential energy surface (PES) topology and a molecular mechanics-valence bond (MMVB) computation of the dynamics on a model

diarylethene (1,2-di(3-thienyl)ethene). Perrier et al.³¹ used complete active space second-order perturbation theory (CASPT2) to perform energy evaluations on CASSCF optimized geometries on a slightly different model DAE (1,2-di(3-thienyl)ethene with a perhydrocyclopentene bridging unit). Mendive-Tapia et al.⁴⁵ described the mechanism of the two photochromic reactions based on the synthesis of these two approaches and others. They also proposed a mechanism for the formation of the by-products that always accompanies the ring-opening reaction⁴⁵.

For the cyclohexadiene (CHD) and hexatriene (HT) isomers, the former corresponding to the closed form and the latter to the open form (see Figure 1.6), under C_2 symmetry the excited states $S_1(1B)$ and $S_2(2A)$ are the two lowest in the Franck-Condon (FC) region. Time dependent density functional theory (TD-DFT) calculations showed that $S_1(1B)$ is an optically active ionic state, whereas $S_2(2A)$ is a dark covalent state^{26,45}.

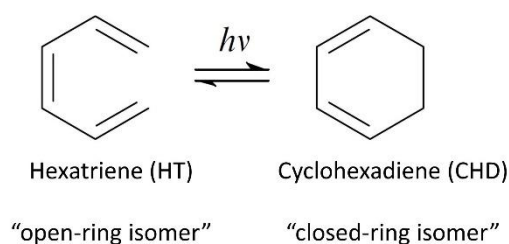


Figure 1.6: Chemical structure of the two isomers hexatriene (HT) and cyclohexadiene (CHD). Adapted from⁴⁶.

As can be seen in Figure 1.7, all the studies showed that the photochromic reactions take place on the PES corresponding to the covalent $S_1(2A)$ state. $S_1(1B)$ and $S_1(2A)$ states of CHD^* minima are very close in energy and according to minimum energy paths at the CASSCF level, rapid radiationless decay in the FC region from 1B to 2A and equilibration towards the $S_1(2A)$ CHD^* minimum occur soon after initial vertical excitation. The analysis of minimum energy paths from the FC and conical intersection geometries in dihydrobenzobisthiophene at the CASSCF level suggests that the system relaxes from the FC structure to the CHD^* minimum on the 1B PES. It uses the energy provided by the initial excitation of the ground state to undergo a geometrical change until it reaches a point on the conical intersection of CHD 1B/2A where an efficient decay to the HT^* minimum on the 2A PES is possible^{26,45}.

The origin of the photochromic properties in diarylethenes is the presence and accessibility of the conical intersection labelled ConInt1 on the left scheme of Figure 1.7 (see

the tip of the triangular orange shape, labelled as ContInt1 in white) or CI(o) on the right scheme of Figure 1.7 and the orthogonal orientation of its branching space in regard to the opening/closing reaction coordinate⁴⁵.

The steps of the mechanism of the ring closing reaction are represented by arrows on both schemes of Figure 1.7. In the description of the steps of this mechanism given hereafter, it will be indicated to which arrow of the schemes of Figure 1.7 the explained step corresponds to. For the ring-closing reaction, non-adiabatic molecular dynamics simulations show that upon UV irradiation, the molecule in its open form is excited to the lowest energy FC state 1B (first arrow on both schemes) and undergoes fast internal conversion to the PES 2A which is close in energy (second arrow on both schemes). As shown in Figure 1.7, the system (excited state wave packet) progresses along the 2A PES (second arrow on the left scheme or third arrow on the right scheme) until it reaches the conical intersection 2A/1A (ConInt1 on the left scheme or CI(o) on the right scheme) the system then decays efficiently to $S_0(1A)$ at the conical intersection. The system then keeps decaying to the ground state PES (third arrow on the left scheme or fourth arrow on the right scheme) until the minimum corresponding to the closed ring form. This mechanism which does not involve to overcome any energy barrier explains why the ring-closure reaction is so fast and effective as shown by the high value of its quantum yield^{26,45-47}.

For the ring-opening reaction, as can be seen in Figure 1.7, the system has to overcome an energy barrier (formed by the transition state labelled TS_5 on the left scheme or 2ATS on the right scheme) on the $S_1(2A)$ PES (at CHD* minimum on the left scheme or 2Ac minimum on the right scheme) to reach the conical intersection and then undergoing fast deactivation to the ground state, through the same relaxation seam involved in the ring-closing (represented by the wavy white arrow between HT* and ContInt₁ on the left scheme, or the two red arrows going from 2Ao on the right scheme), where the open isomer is formed. The presence of this barrier explains why this reaction is temperature dependent and has a low and photoirradiation wavelength dependent quantum yield (QY). The value of the ring-opening reaction QY (determined experimentally) depends on the height of the barrier i.e., the energy difference on the $S_1(2A)$ PES between the open and the closed form isomers. The height can be adjusted by modifying the substituents on the photochromic unit. It also controls the production of eventual by-products whose formation would be favored if it implied to overcome a lower energy barrier than for the ring-opening^{26,45-47}.

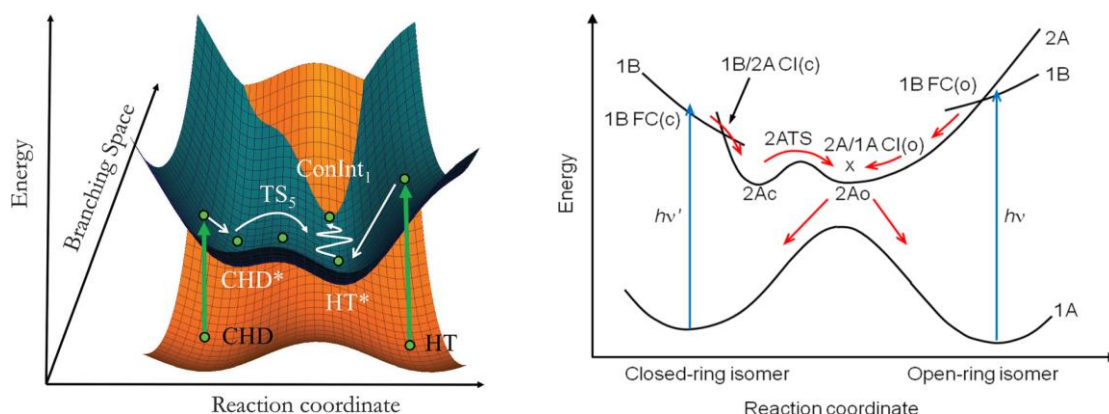


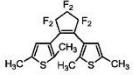
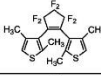
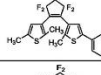
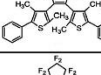
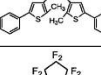
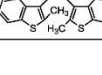
Figure 1.7: On the left, scheme of the known switching mechanism of diarylethene. The energies for the $S_0(1A)$ (orange, bottom) and $S_1(2A)$ (green, top) electronic states are represented in the space of two nuclear coordinates: (1) reaction coordinate: the internuclear C-C distance connecting CHD and HT isomers and (2) branching space coordinate: a linear combination of the gradient difference vector (GDV) and the derivative coupling vector (DCV) at the conical intersection ($ConInt_1$). On the right, two-dimensional simplification of the PESs describing the reaction paths for the ring-closing and ring-opening reactions of the diarylethene. The letters “c” and “o” in parenthesis respectively stand for “closed” form and “open” form. Adapted from^{26,45}.

2 - Quantum yield and fatigue

a - Quantum yield

The quantum yield corresponds to the probability for the molecule to react upon absorption of a photon⁴⁸ or the ratio of number of absorbed photons and photogenerated molecules⁴⁹. A high quantum yield (QY) is required both for efficiency and sensitivity (also linked to the molar absorption coefficient). The respective quantum yield of the ring-closing and ring-opening reaction of a few common 1,2-diarylperfluorocyclopentenes are given in Table 1.1.

Table 1.1: Values of the ring-closing and ring-opening quantum yields of a few common diarylethenes. Adapted from²⁶.

Dithienylethene molecule	$\Phi_{O \rightarrow C}$	$\Phi_{C \rightarrow O}$
	0.40	0.12
	0.21	0.13
	0.53	0.119
	0.45	0.018
	0.59	0.013
	0.31	0.29

The determination of the quantum yields of a photochemical reaction is rarely easy nor straightforward. Although the QYs are generally determined by the change of concentration of photoreactive species along with the photoisomerization reactions using absorption spectroscopy⁴⁸⁻⁵² and/or chromatography^{49,53,54}, there are almost as many quantum yield determination methods as research groups. Note that absorption spectroscopy allows to monitor the evolution of the concentration but also the amount of light absorbed. Chemical actinometry is generally used for photon flux determination, but new methods that do not require to use it have been developed^{48,49}. Less conventional methods based on various techniques (NMR, laser flash photolysis, and peak-height analysis of size exclusion chromatography) have also been developed⁴⁸. Furthermore, the diversity of quantum yield determination methods, often with home-made setups, can render the comparison of the values obtained difficult⁴⁸. Most methods are based on the rate equations used to describe the photoisomerization process.

Ichikawa et al.⁵³ monitored the concentration of the open-ring form and that of the two diastereoisomers of the closed-ring form throughout the photocyclization reaction by High Precision Liquid Chromatography (HPLC). They expressed the evolution of the population of the three species with time using differential equations. They performed numerical simulations based on these equations and managed to obtain the values of the quantum yield for each isomer. Uno et al.⁵⁴ used HPLC to determine the conversion (commonly used to calculate the QYs) and the values of the QYs. The QYs were determined using conversion curves fitted with

monoexponential functions. Conversion curves are curves representing the evolution of the absorbance of a solution at a given wavelength under irradiation with UV light until reaching the photostationary state (PSS) and then visible light until full bleaching (conversion as close as possible from the starting state). Let us remind that according to the IUPAC, the photostationary state is “a steady state reached by a reacting chemical system when light has been absorbed by at least one of the components. At this state, the rates of formation and disappearance are equal for each of the transient molecular entities formed”²⁴. Uno et al. injected the solutions at the PSS in the HPLC and separated it in two solutions, one containing the open isomer and the other the closed isomer. The conversion could be obtained by integrating the chromatogram at the wavelength of the isosbestic point. They also used another method for which they extracted the spectrum of each isomer and normalized it at the isosbestic point wavelength. The combination of these two spectra that matches best the spectrum at the PSS gives the proportion of each isomer at the PSS.

Stranius et Börjesson⁵² proposed methods based on UV-visible spectroscopy measurements to calculate the QY in solution, and in the solid state, with a specific attention to taking into account thermal effects. They used a kinetic model of the isomerization process that they implemented in an easy-to-use program that can fit experimental data to the kinetic model and then numerically solve an ordinary differential equation for each step of their fitting procedure. They claim the advantage of their method is the possibility to fit data to theory with no requirement for analytical solutions or mathematical simplifications. They distinguished two regimes: total absorption and low absorption regime (regarding the absorption of the closed-ring isomer). In the former, a linear dependence between the concentration of open-ring isomer and the irradiation time can be obtained, and thus the quantum yield can be extracted from a linear fit of the absorbance at a specific wavelength versus the irradiation time. In the latter, the rate equation describing the full reaction can be simplified in the equation describing the conversion of the open-ring isomer.

Micheau et al.⁵⁰ studied 18 thermally irreversible photochromic diarylethene derivatives with various bridging rings, and lateral aryl moieties. They (simultaneously) determined the QYs using numerical kinetic modeling, they also developed their own software, on curves representing the absorption in function of time (kinetic curves at two different wavelength), recorded by UV-visible spectroscopy under continuous irradiation, and associated to chemical

actinometry measurements. Ferrioxalate was used as an actinometer to measure the intensity of the light used for the photokinetic measurements on the DAEs.

An accurate, straightforward (provided one possesses a photoreaction quantum yield measurement system), and actinometer-free method is that of Higashigushi et al.⁴⁹ who proposed a quantum yield determination method “by the global fitting of prolonged change of concentration against absorbed photon numbers”. They used it to determine the QYs of three common DAEs. They fitted (least square fitting) the curves describing the evolution of the number of molecules by equation 1a and 1b respectively (see below). Their method is based on the measurement of the absorbed number of photons in an absolute (direct measurement of light intensity) manner. They expressed the evolution of the number of open-ring molecules n_a and closed-ring molecules n_b with the time in differential equations (1.1a and 1.1b):

$$\frac{dn_a}{dt} = -\Phi_{a \rightarrow b} F_a + \Phi_{b \rightarrow a} F_b \quad (1.1a)$$

$$\frac{dn_b}{dt} = \Phi_{a \rightarrow b} F_a - \Phi_{b \rightarrow a} F_b \quad (1.1b)$$

These number of molecules are connected to the number of absorbed photons per unit of time by equations 1.2a and 1.2b:

$$F_a = n_p \left(\frac{\varepsilon_a n_a}{\varepsilon_a n_a + \varepsilon_b n_b} \right) \quad (1.2a)$$

$$F_b = n_p \left(\frac{\varepsilon_b n_b}{\varepsilon_a n_a + \varepsilon_b n_b} \right) \quad (1.2b)$$

With Φ and ε the quantum yield and the molar absorption coefficient at the irradiation wavelength, respectively.

They used a photoreaction quantum yield measurement system (Shimadzu, QYM-01) to measure the number of absorbed photons for excitation per unit time (n_p) and to calculate the irradiated number of photons n_{irr} using $n_p, n_p = (1 - 10^{-A})n_{irr}$. Note that the QYM-01 carries the illumination and the recording of the evolution of the absorbance. They started by measuring the number of closed ring molecules (n_b) and calculated the number of open ring molecules (n_a) at the PSS:

$$n_a = n_{a,ini} - n_b \quad (1.3a)$$

$$n_b = \frac{A_{det}}{\varepsilon_b} \frac{\nu N_A}{1000} \quad (1.3b)$$

With $n_{a,ini}$ the total number of molecules present in solution, ν the volume of solution, N_A Avogadro's number, and A_{det} the absorbance determined at λ_{max} in the visible region where the open-ring isomers do not absorb.

They injected these values (n_a and n_b) into the equations linking them to the number of absorbed photons by unit of time (respectively 1.2a and 1.2b). By plotting the evolution of the number of molecules with the time (reaction duration) and fitting it with the appropriate equation (1.1a for the photocyclization or 1.1b for the photocycloreversion) using a least square fit, they obtained the values of the QYs.

Finally, Stadler et al.⁴⁸ established a method for the determination of quantum yields of various photo-induced reactions (including "switching" reactions such as the E-Z isomerization of azobenzenes it was tested on). Note that the validity of their method was confirmed by a test made with an actinometer (ortho-nitrobenzaldehyde). They chose to use a fiber coupled UV-Vis spectrometer, LED irradiation sources (cheap, flexible, and with an easily adjustable photon flux by varying the forward current), and a calibrated spectrophotometer coupled to an integrating sphere for precise measurements of the LED photon flux (optical power output) instead of using actinometers. They modified the spectrometer's sample holder to illuminate the sample through an aperture ($d = 0.9$ cm) perpendicularly to the spectrometer beam. They measured the absorbance spectra in regular sampling intervals while simultaneously irradiating and stirring the sample.

They gave a demonstration based on rate equations to make a connection between the absorbed light and the spectral changes caused by the depletion of reactants. They also distinguished two cases, weakly and strongly absorbing solutions. In the first case (low absorbance, $A' < 0.1$), both reactions approximatively followed first order kinetics, the associated data could thus be fitted by a mono-exponential function. In the second case (high absorbance, $A' > 2$), the reaction is apparent zero order and they recommend to use a linear function to fit the data. In the end, they used the following expression to obtain the quantum yield:

$$\Phi = \frac{k_{fit}c_0}{I_0(1-10^{-A'_i})} \quad (1.4)$$

With k_{fit} the time constant extracted from the fit, c_0 the concentration of the analyzed solution, I_0 the intensity of the light source (LED), and A'_i the initial absorbance at the irradiation wavelength.

Note that in Chapter 4, another method has been used, it was considered the most adapted to the data we wanted to use to calculate quantum yield values. This other method is explained in detail in Chapter 4.IV.1.

The quantum yield of the ring-closing reaction is usually larger than that of the ring-opening reaction. It is explained by the energy barrier present for the ring-opening reaction and absent for the ring-closing one. The height of this barrier is directly correlated with the value of the quantum yield, since the higher it is, the lower is the probability to overcome it and thus the lower is the quantum yield^{26,51}. The QY of the ring-opening reaction depends on the size of the π -system of the molecule, the larger it is, the more the QY decreases. This is due to the decrease of the antibonding character of the C-C bond that closes when it is in the excited singlet state²⁶. This difference between the QYs of the two reactions creates an asymmetry of the diarylethene's switching. Managing to increase the QYs of both reactions and especially that of the ring-opening reaction to correct the asymmetry of the switching are two goals of the research in the area of DAEs.

The open form of a dithienylethene molecule exist in two conformations: parallel (P), with the thiophene rings in mirror symmetry; and antiparallel (AP), with the thiophene rings in C_2 symmetry and thus coplanar, enabling the overlap involved in the cyclization reaction. Therefore, the ring-closing reaction can only occur in the antiparallel conformation in conformity with the Woodward-Hoffman rules. For unsubstituted DTEs the populations of molecules in the P and in the AP conformation are the same, introducing a maximum threshold of 0.5 regarding the photocyclization quantum yield. The P population undergoes emission (luminescence) while the AP population undergoes the ring-closing reaction. There are ways to favorize the AP conformation to increase the photocyclization QY, attaching bulky substituents to the thiophene rings at the reactive carbon atoms^{29,46,55} or inserting the DAEs in a crystalline or polymeric matrix which constrain the molecules to adopt the AP conformation. It also works following the same principle, when the DAEs are inserted in molecular cavities such as

cyclodextrins. The quantum yields can reach 1 if a population of AP conformers exclusively is achieved^{55,56}.

Recently, new strategies were developed to increase the QYs of the photoconversion reactions such as the use of triplet state sensitizers (described below) and the use of plasmonic nanoantennas on which the molecules are attached (described further, see Chapter 1.III.5).

Triplet states can be involved through intersystem crossing from the excited singlet states (S_1) or by photosensitization. The use of photosensitizing groups is explored as a mean to increase quantum yield of photocyclization and cyclophotoreversion reactions. The first example of successful triplet state sensitization was reported by Jukes et al.⁵⁵ in 2004 proving that sensitized photocyclization from a triplet state by irradiation of the attached metal center is possible. The authors used Ru(II) complexes ($\text{Ru}(\text{bpy})_3$) as sensitizers to obtain efficient photocyclization from a “low-lying triplet state”. Upon photoexcitation into the lowest Ru-to-bpy $^1\text{MLCT}$ state followed by intersystem crossing to emitting $^3\text{MLCT}$ states, photoreactive ^3IL states are populated by an efficient energy transfer process. The involvement of these ^3IL states explains the higher quantum yield of the photocyclization (> 0.5). Strong steric repulsion between the bulky substituents on the dithienylperfluorocyclopentene bridge bearing the chelating bipyridine sites or the $\text{Ru}(\text{bpy})_3$ moieties forces the system to adopt nearly exclusively the reactive antiparallel conformation. The photocyclization reaction occurs both upon excitation to the ^1IL state, localized on the photochromic part, and upon excitation to the $^1\text{MLCT}$ state at lower energy, localized on the $\text{Ru}(\text{bpy})_3$ part, with almost identical quantum yields. In contrast to the photocyclization reaction from a singlet state, which is known to occur in a few picoseconds, here the reaction occurs on the nanosecond time scale. Equilibrium exists between the $^3\text{MLCT}$ and ^3IL states, which are close in energy, resulting in a competition between the emissive and reactive processes.

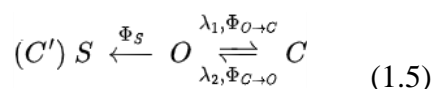
In 2015, Murata et al⁵⁷. showed that it was possible to increase the quantum yield of the cyclization reaction of 1,2-bis(2-hexyl-3-benzothienyl)-perfluorocyclopentene (BTHex), and 1,2-bis(2-isopropyl-3-benzothienyl)perfluorocyclopentene (BTiPr) by using various triplet state sensitizers such as xanthone, 4-methoxybenzophenone, phenanthrene, coronene, pyrene, benz[a]anthracene, and acridine (only for BTiPr).

More recently, Friedrich et al.⁵⁸ compared the performances of two 1,2-diarylperfluorocyclopentenes, one bearing a biacetyl triplet-state sensitizer at each extremities

(in para position of its phenylene units), the other one bearing a single biacetyl sensitizer at the 2-position of its thiophene unit. They determined the quantum yields of their photocyclization and photocycloreversion and conducted transient state spectroscopy in order to unravel the switching mechanism through the triplet pathway. On the one hand, the disubstituted DAE mainly switches from the triplet state, it possesses lower QYs but a higher fatigue resistance. On the other hand, the monosubstituted diarylethene mainly switches from the singlet state and exhibits higher QYs.

b - Fatigue

Photochromic reactions involve chemical bonds rearrangement during which unwanted and non-reversible side reactions take place. They occur during the ring-closing reaction and lead to the formation of undesired by-products thus limiting the number of cycles of the photochromic reaction due to the decrease in the non-damaged molecules still able to reversibly switch^{29,51,59}. Fatigue is described in the following equation:



No matter how small the quantum yield of the by-product reaction is, the effect on the maximum switching cycles is huge. As shown by the numbers given by Irie et al.²⁶, for $\Phi_S = 0.001$, and even if $\Phi_{O \rightarrow C} = 1$, 63% of the population of A will have been degraded after 1000 switching cycles; therefore, to reach 10 000 switching cycles, we need to have $\Phi_S < 0.0001$. Fatigue resistance can readily be determined by UV-visible spectroscopy measurements, a diluted DAE solution is irradiated with UV light (λ_1) until the photostationary state is reached (or at least 90% of it) and then irradiated with visible light (λ_2) until as many molecules as possible are switched back to the open state (all of them ideally): a switching cycle is performed. At the end of each cycle, the absorbance of one of the isomers is measured (in function of where the by-product absorbs), cycles are repeated until the absorbance change of the monitored isomer decreases to 80% of the first cycle: the maximum repeatable cycle number has been reached.

The main strategies to reduce fatigue is to use particular groups and specific substitutions, for example a diarylethene with benzothiophene rings (with lower reactivity towards singlet oxygen) instead of thiophene rings with methyl groups at the 4- and 4'-positions

of the ring which limits the production of the six-membered condensed ring by-product responsible for the fatigue of most DAEs; or to work with the molecules in the crystalline phase or in polymeric matrixes where rearrangement into side products and oxygen diffusion are hindered.

Fatigue thus designates the degradation of the molecules upon irradiation leading to the formation of unwanted byproduct (BP) whose structure is shown in Figure 1.8. It is one of the most important elements to consider while designing a DAE since fatigue limits the maximum number of repeatable switching cycles the molecule can undergo and therefore that of an eventual device based on this molecule.

According to Mendive-Tapia et al.⁴⁵, the starting point of the BP formation is the dissociation of one of the two C-CH₂ bonds or the C-S bond of the closed-ring (CHD) isomer. Two intermediates are formed upon the breaking of this bond which then combine to form the by-product. The formation of the by-product is due to the existence of a transition state on the S₁(2A) PES creating access to a S₁(2A)/S₀(1A) conical intersection seam from which the molecule decays to the ground state where the side product is formed. As shown in Figure 1.8, following excitation to the FC region, an internal conversion between 1B and 2A takes place (first green arrow on the schemes), corresponding to the modification of the conjugation in the π -system which is distributed differently on its eight carbons. After the completion of the nonadiabatic decay from 1B to 2A the system travels along the S₁(2A) PES to the S₁(2A) CHD* minimum where the system equilibrates (dotted green arrow ① on the right scheme). The adiabatic reactivity on this PES (TS barriers between CHD* and HT* isomers - TS₅ and between CHD* and the side product - TS₄) is what controls the efficiency of the ring-opening reaction and thus the generation of the side-product. The system then either overcomes the TS₅ barrier (corresponding to the adiabatic excited state photochromic reaction) to reach the flat HT plateau (white arrow going from CHD* to HT* on the left scheme), meaning that the molecule will be photoconverted into the open-ring isomer or it overcomes the TS₄ barrier (white arrow going from CHD* to SeamGeom on the left scheme or green arrow ② on the right scheme) resulting in the C-CH₂ or C-S bond breaking of one of the five-member rings (and formation of the BP). Note that an elongation of the bond to be broken occurs while the system evolves towards TS₄, the efficiency of that step depends on the adiabatic reactivity governed by the substituents born by the molecule. After is has overcome the TS₄ barrier, the molecule decays non adiabatically to the ground state (where the by-product is formed) through the conical

intersection seam directly connected to that transition state. The amount of kinetic energy available for the system (depending on the amount of energy gained by the relaxation from the FC and the temperature) dictate which barrier it will overcome: the one corresponding to TS_4 that leads to the generation of by-product or the barrier corresponding to TS_5 that leads to the conversion to the open isomer^{26,45}.

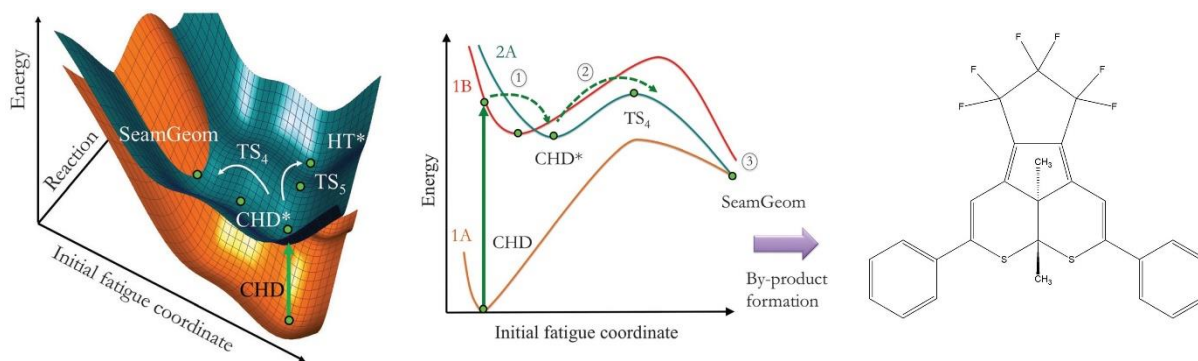


Figure 1.8: On the left, scheme of the fatigue mechanism leading to the formation of the by-product of diarylethenes. The energies for the $S_0(1A)$ (orange, bottom) and $S_1(2A)$ (green, top) electronic states are represented in the space of two nuclear coordinates: (1) reaction coordinate: the internuclear C-C distance connecting CHD and HT isomers and (2) initial fatigue coordinate: the internuclear C-CH₂ distance. In the middle, scheme of the fatigue mechanism after the vertical excitation of the system in the FC region. On the right, structure of the by-product. Adapted from⁴⁵.

3 - Applications

Diarylethenes can be used for a large number of applications in very different fields. As shown in the review of Irie et al.²⁶, they can be used to fabricate many types of optical memories (three-dimensional optical memories, near field optical memories, holographic memories, and single-molecule memories) especially since they are particularly adapted to nondestructive readout (using IR absorption or Raman spectral changes).

Cheng et al.⁶⁰ reviewed the applications of photochromic dyes for photocontrol in biomedicine, they give several examples of the use of diarylethenes as fluorescence probes or biomarkers for fluorescence super-resolution biosensing and (bio)imaging due to their unique abilities to modulate fluorescence signals in a remote, photocontrolled manner. Examples of diarylethene photoactivatable chemotherapeutic agents for photopharmacology are also reported, including that of a potential trigger in smart drugs that undergo photoswitchable

conformational changes that promote biological activity used for oxygen independent photodynamic therapy (PDT) for cancer.

Some applications rely on the use of diarylethene based photodeformable materials involving the use of DAEs in their crystalline phase. Let us remind that photodeformable materials are a type of materials based on molecules able to convert light (photonic energy) to mechanical work (mechanical energy) and thus possess photoinduced deformable properties^{26,28}. The deformation is a macroscopic manifestation of the sum of all the individual conformational changes (isomerizations) or results from changes in the packing modes of the molecules²⁸. In the review of Huang et al.²⁸ devoted to photodeformable crystals, fifteen different photodeformable diarylethene single crystals are presented, they possess various shapes (square plate shape, rectangular plate shape, diamond-like shape, rod shape, ribbon shape, and lamellar shape) and exhibit various photodeformable behaviors such as bending, twisting, bursting, curling, rolling, shrinkage, and expansion. Note that molecular deformation depends on different factors such as the irradiation direction, the light intensity, the reconstruction of the irradiated surface, the temperature. These crystals have possible applications in molecular machines, actuators, micro- and nano-mechanical devices²⁸.

For example, a photodeformable cocrystal diarylethene-perfluoronaphthalene exhibiting a reversible bending motion repeatable more than 250 times was implemented as a molecular crystal cantilever. This cantilever could lift a metal ball whose weight varied from 200 to 600 times heavier than itself (see Figure 1.9). The cantilever underwent a maximum stress more than two orders of magnitude larger than that taking place in a muscle and comparable to that present in piezoelectric crystals²⁸. Another rodlike cocrystal made of two diarylethenes could be used as an actuator to make some gears rotate upon its bending (see Figure 1.9). This cocrystal also had mechanical properties similar to that of a piezoelectric crystal²⁸. Interesting examples of hybrid actuators are also given, one made of a diarylethene silesquioxane hybrid and another one made of diarylethenes and nanowire crystals of aluminum oxide²⁸.

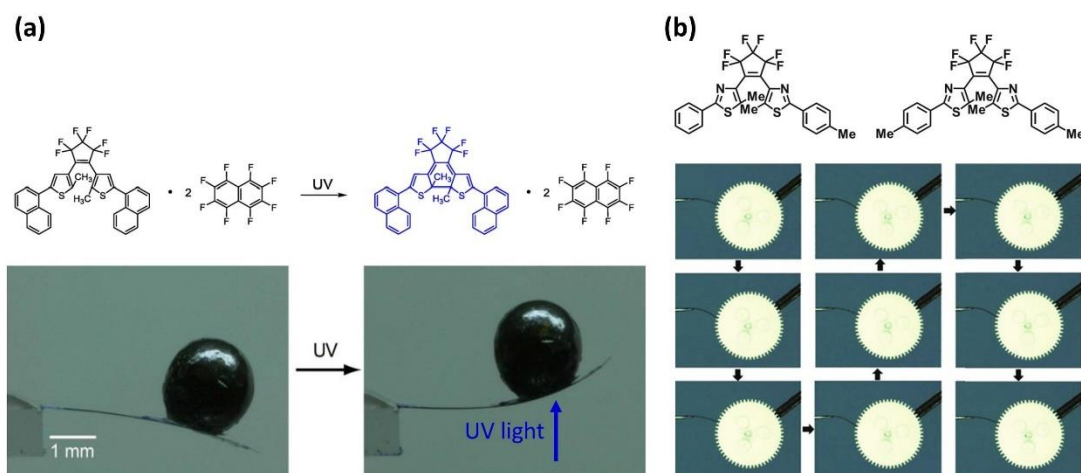


Figure 1.9: (a) Structure of the diarylethene and of perfluoronaphthalene used to make the cocrystal implemented as a molecular crystal cantilever (top). Bending (photomechanical work) of the 0.17 mg molecular crystal cantilever (made of the cocrystal represented above) lifting a 46.77 mg lead ball. The direction of the UV light irradiation is indicated by the blue arrow (bottom). (b) Structures of the diarylethene molecules used to make the rod-shaped cocrystal implement as an actuator (top). Bending (photomechanical deformation) of the actuator triggering the rotation of the gears of a wheel (bottom). Adapted from^{26,28}.

Examples of photo-responsive molecular and supramolecular systems with applications in information processing and binary logic containing DAEs used as molecular photoswitches able to mimic conventional electronic components are presented in the review of Andréasson et Pischel²⁷. They underline the fact that with the adequate molecular design the excited state processes energy- and electron transfer can be adapted to the logic operation or function that the photoswitch must execute²⁷.

Some molecular systems able to function with the same characteristics than that of conventional electronic circuits made of physically wired multiple logic gates, can be implemented in reconfigurable devices with high logic complexity. These molecular systems are eligible to highly complex functional integration (see the example of S-R latch below) meaning that the devices in which they are implemented has a functioning that can be described with a truth table of a multi-gate circuit with gates corresponding to the whole system (and not one gate, one molecular unit). These devices also present reconfigurable molecular logic operations meaning that it is possible to execute different logic operations by applying different input or selecting different reading of the output(s)²⁷.

This requirement of the reconfigurability of the devices renders the fabrication of all-photonics devices more attractive than any other kind. Indeed, for devices using chemical inputs,

it is necessary to add reagents (and so to transport and introduce them) and then to evacuate or neutralize them to reset the device. Neutralization that often require to add more chemicals, increasing the amount of chemical waste. Unlike chemical reagents, light is a traceless input that can be applied remotely with extreme spatiotemporal precision (the switching is thus perfectly controlled) that allows the resetting and cycling with high fatigue resistance without the formation of waste products. The inputs can be readily modified by selecting light sources with various wavelength and applied to the same solutions of photoswitches. Regarding the output, they are simply set based on the spectral properties of the photoswitches by having a look at their absorption- and emission spectra. These devices therefore present input-output homogeneity which allow their large-scale integration²⁷.

Latches or flip-flops form a class of sequential logic devices (two-states memory circuits) comprising set-reset latches (S-R latches) which are circuits made of two NOR or NAND gates cross-coupled by feedback loops. The current output state thus controls the next output state generated upon input application meaning that the circuit keep tracks of its input history creating a “memory effect”. S-R latches are commonly used in conventional electronics building blocks of random-access memories (RAMs). S-R latches possess two inputs: set (S) and reset (R) and an output corresponding to the state Q of the system. Q is linked to a current value Q_{current} corresponding to the memorized state from the input history of the latch, itself connected to a value Q_{next} resulting from the actual input application, that corresponds the output given by the device. The possible entries of an S-R latch are presented further in the truth table given in Figure 1.10. For $S = 1$, the system switches from $Q_{\text{current}} = 0$ to $Q_{\text{next}} = 1$ whereas for $R = 1$ it switches from $Q_{\text{current}} = 1$ to $Q_{\text{next}} = 0$. Note that applying the inputs S or R to the system respectively in the state $Q_{\text{current}} = 1$ and $Q_{\text{current}} = 0$ has not effect. Applying both inputs at the same time ($S = R = 1$) leads to an indeterminate state with no physical meaning. The system also possesses a “do nothing” response corresponding to $Q_{\text{current}} = Q_{\text{next}}$, triggered by $S = R = 0$. According to the memory state Q, the response given after applications of S and R input will be different (see truth table of Figure 1.10)⁶¹.

The conditions to use a molecule as a S-R latch are the following: the molecule must be bistable, its state Q must be readable through well differentiated signal levels (optical signals such as absorbance or fluorescence for example), its $Q = 0$ and $Q = 1$ state must exclusively be addressed by their specific input (S for $Q = 0$ and R for $Q = 1$), its switching must be reversible to guarantee a large number of switching cycles between the Q states, its thermal stability must

be high enough to ensure the existence of a “do nothing” situation ($S = R = 0$) for each of the Q states. Finally, input accumulation should be avoided upon the application of the S or R input for $Q = 1$ or $Q = 0$, respectively (limitation regarding the use of chemical input signals)⁶¹.

Pischel et Andréasson⁶¹ used a P-type dithienylethene (shown in Figure 1.10) whose isomerization quantum yields in methanol have been reported to be 0.57 for the ring-closing reaction and 0.014 for the ring-opening reaction. Implemented in a S-R latch that fulfill all six possible entries given in the truth table of Figure 1.10, the dithienylethene goes from its initial state DTEo (non-absorbent at 595 nm) corresponding to $Q = 0$ to its closed form DTEc (absorbent at 595 nm) corresponding to $Q = 1$ upon UV light irradiation (40 s of UV light at $\lambda = 302$ nm with an intensity $I = 1.5 \text{ mW.cm}^{-2}$) corresponding to the set input $S = 1$. The system goes back to $Q = 0$ upon visible light irradiation (10 min of broadband visible light at $\lambda > 450$ nm with an intensity of 100 mW.cm^{-2}) corresponding to the reset input $R = 1$. Applying the set input S to DTEc ($Q = 1$) beyond the photostationary state or the reset input R to DTEo ($Q = 0$) after it is fully back-isomerized has no effect. Considering the thermal stability of both the open and closed form (no absorption changes detected over 88 h), not doing anything which corresponds to $S = R = 0$ leaves the DTE in its current state whether it is DTEo or DTEc⁶¹.

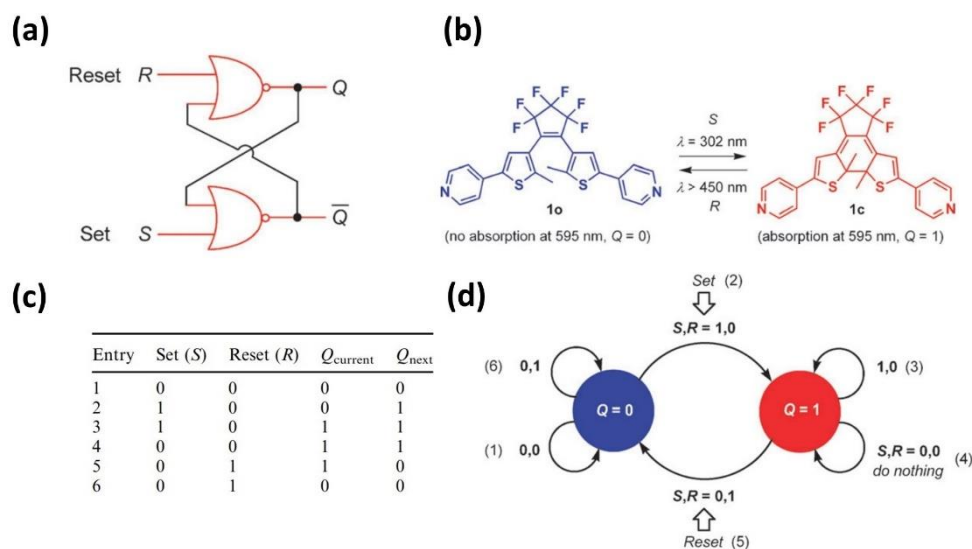


Figure 1.10: (a) Scheme of the working principle of a S-R latch made of two cross-coupled NOR gates circuit, with \bar{Q} the complement of Q . (b) Structure of both isomers of a diarylethene compound usable as a S-R latch and how to switch between them. (c) Truth table of the schematized S-R latch, with Q the current memorized (Q_{current}) state and the following state (Q_{next}), which is the actual response triggered by the input. (d) Scheme of the logic function of a S-R latch, the number between parenthesis corresponds to the entry of the truth table. Adapted from⁶¹.

Andréasson et Pischel²⁷ presented an extremely versatile all-photonicallly operated logic multitasker which is a multiphotochromic molecular system, whose structure is shown in Figure 1.11, that their group synthesized. It is made of two fulgimide units (FG) and a dithienylethene unit (DTE), which are both thermally stable photoswitchable compounds, linked by a non-conjugated central unit so that each of the photoswitches can be addressed independently. Considering that the FG units are in the same isomerization state, the molecular system has four constitutional isomers FGo-DTEo, FGo-DTEc, FGc-DTEo, and FGc-DTEc (o - open, c - closed). The population of such and such isomers in the molecular system can be adjusted by applying the right irradiation (see Figure 1.11): 302 nm light triggers the isomerization of DTEo to DTEc while 397 nm light triggers the isomerization of FGo to FGc. Both types of photoswitches can also be addressed at the same time using 366 nm light to make the whole molecular system isomerize to its close form (FGo-DTEo to FGc-DTEc). From there, red light ($\lambda > 615$ nm) can be used to selectively make DTEc isomerize to DTEo, or green light ($460 < \lambda < 590$ nm) can be used to make the whole molecular system isomerize back to its open form (FGc-DTEc to FGo-DTEo). The specificity of the absorption spectrum of each isomer offers a large variety of outputs read at different wavelengths²⁷.

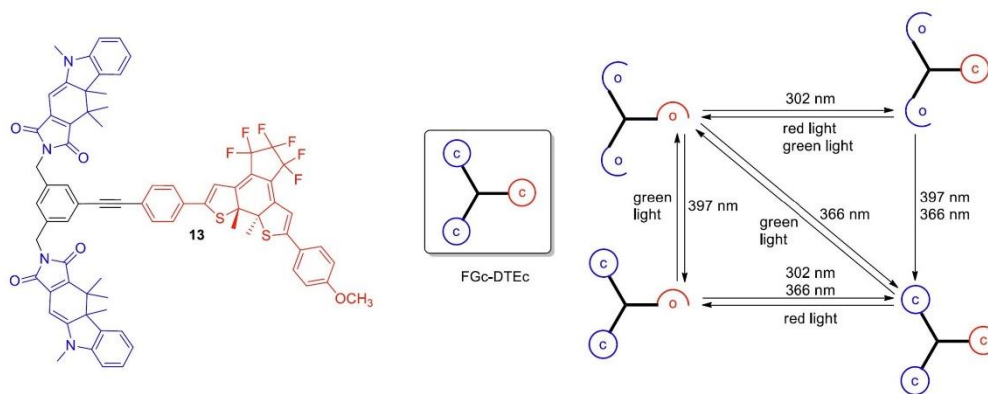


Figure 1.11: Structure of the all-closed isomer FGc-DTEc of their multifunctional photochromic logic molecular system (left) Network formed by all the isomers and the stimuli allowing to switch between them (bottom). The diarylethene unit is represented in red while the fulgimide units are represented in blue. Adapted from²⁷.

The authors fabricated many experimental devices based on that molecular system: AND, XOR, INH, half-adder, halfsubtractor, 4:2 encoder, 2:4 decoder, 2:1 multiplexer, 1:2 demultiplexer, keypad lock, logically reversible transfer gate devices, a parity generator/checker (for error detection in data transmission), and a one-time password generator. All these devices possess the same initial state FGo-DTEo to which they can be reset at any moment via a green light irradiation. Note that FGc is a fluorescence emitter, with an emission maximum at 624 nm used as an additional output for the logic operations²⁷.

Finally, diarylethenes can be used as molecular photoswitches to modulate the optical, magnetic, and electronic (electric conductance) properties in light-driven nanodevices^{26,62}.

Combining gold nanoparticles used as electrodes with diarylethenes to fabricate photocontrolled molecular devices for conductance switching is a clever strategy. Matsuda et al.⁶³ prepared a network of interdigitated gold nanoparticles connected by dithiolated diarylethenes in between two lateral gold electrodes (see Figure 1.12). The DAEs are used as molecular switches to photocontrol the conductance between these two lateral gold electrodes. They achieved the reversible switching of the DAE's conductance upon alternate irradiation with UV and visible light. Note that for bis(2-thienyl)ethene dithiol (third DTE on the right in Figure 1.12) which is an inverse DAE, the switching direction is inverted: the closed-ring isomer corresponds to the "OFF" state.

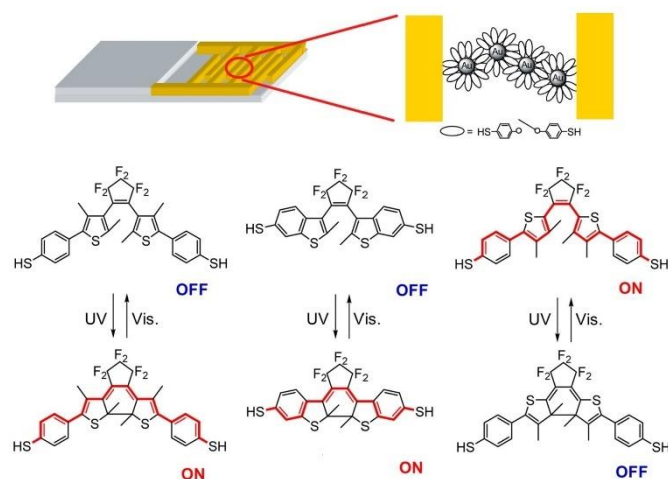


Figure 1.12: Scheme of a gold nanoparticles-diarylethene network. The gold nanoparticles are bridged by the dithiolated diarylethenes: a photocontrolled network of interdigitated gold nanoparticles used as electrodes is obtained, it commands the conductance between the two large gold electrodes. Adapted from^{26,63}.

B.L. Feringa's team measured the change of conductance occurring upon the reversible photoisomerization of single asymmetric diarylethene molecules placed in a matrix of insulating dodecanthiol molecules organized in a SAM on Au (111) through their change of apparent height measured by STM⁶⁴ (see Figure 1.13). They were the first ones to perform this type of measurements on DAEs. The preservation of the reversibility of the switching once the molecule was connected to the gold surface was attributed to the asymmetric structure of the molecule (Figure 1.13). The closed-ring conducting isomer appeared as a bright protrusion on the STM image: the apparent height of the molecule increased upon its photocyclization triggered by UV light. This protrusion disappeared upon irradiation with visible light: the apparent height of the molecule decreased. The same observations were made upon alternate UV and visible light irradiations (see Figure 1.13).

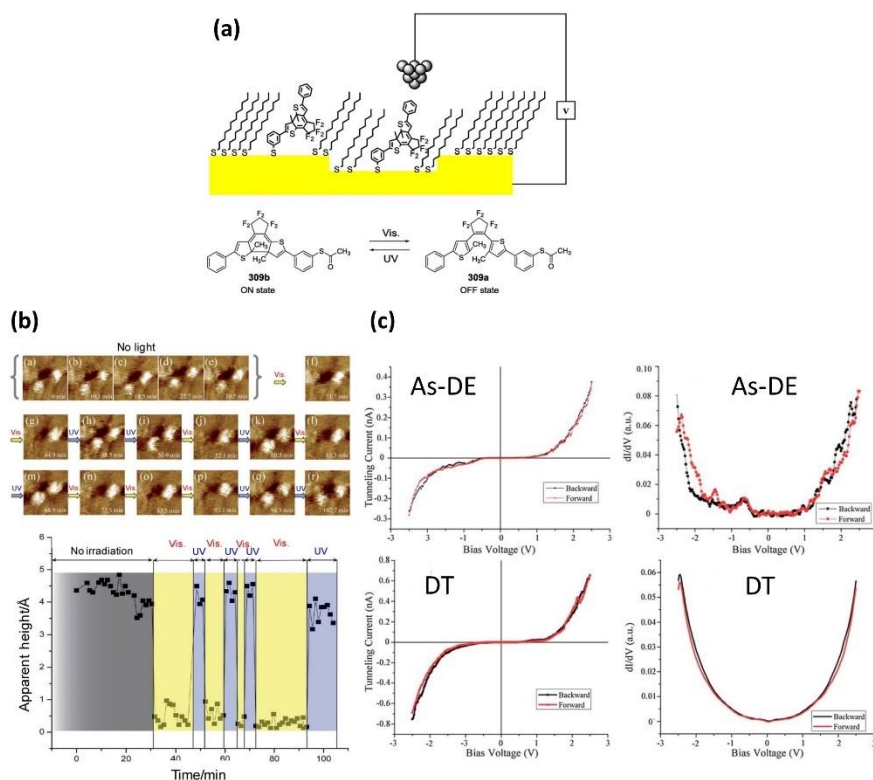


Figure 1.13: (a) Scheme of a SAM containing a dodecanthiol matrix with individual diarylethene integrations scanned by STM in constant current mode (top). Chemical structure of the closed isomer of the asymmetric diarylethene corresponding to its conductive “on” state (left) and of its open isomer corresponding to its insulating “off” state (bottom). (b) Sequence of cropped STM images (of a 100 nm^2 zone) showing the photoinduced switching between the more conductive “on” state of the DAE appearing as bright protrusion with a higher apparent height and the insulating “off” state of the diarylethene for which the protrusion disappears after 13 minutes of visible light irradiation (top). Evolution of the apparent height as a function of the irradiation time (bottom). (c) I-V characteristics and dI/dV curves recorded simultaneously at 77K using the lock in technique (the bias voltage V is applied to the tip and the sample is grounded). Top left: I-V curves of As-DE (average of 160 traces obtained at four different locations). Top right: dI/dV curves of As-DE. Bottom left: I-V curves of DT (average of 1500 traces obtained at five different points and averaged to give the resulting curve. Bottom right: dI/dV curves of DT. Adapted from^{26,64}.

III - Gold nanoparticles: localized surface plasmon resonance (LSPR), plasmonic antennas, and applications

1 - Description of the localized surface plasmon resonance (LSPR)

The interaction between metallic nanoparticles (the electrons from their conduction band) with an electromagnetic field (such as light) possessing a wavelength much larger than their dimensions, results in localized surface plasmons i.e., coherent oscillations of the metal

electrons in resonance with light of the LSPR frequency. The LSPR, schematized in Figure 1.14, results in a strongly enhanced electric near-field localized at the particle surface^{65–68}.

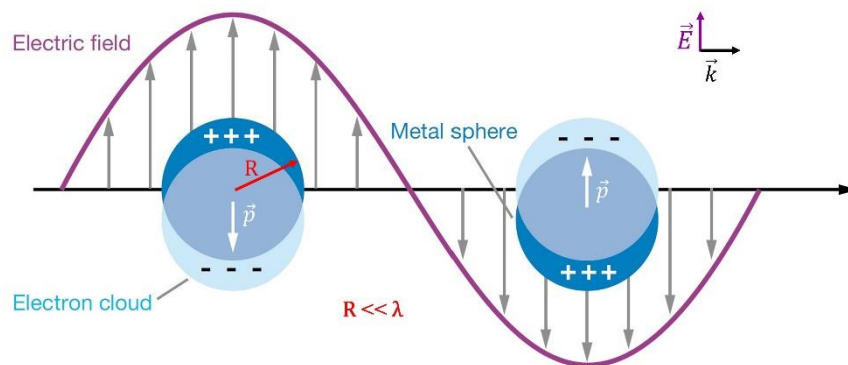


Figure 1.14: Schematic illustration of the localized surface plasmon resonance (LSPR) in metallic nanospheres. The induced (by the incident electric field) polarization \vec{p} is indicated by the white arrows. In response to the incident electric field, the electrons from the metal collectively oscillate, hence the description of the NPs as oscillating dipoles. Adapted from⁶⁵.

The LSPR stems from the confinement of the incident electric field around a spherical metallic nanoparticle with a radius much smaller than the wavelength of the incident electromagnetic wave it receives. G. Mie demonstrated in 1908 that the LSPR is described by the exact solution of the Maxwell equations at the boundary conditions (on the electromagnetic field in the nanospheres) for electromagnetic plane waves (incident light) in interaction with metallic nanospheres exhibiting smaller dimension than the wavelength of the incident light. Mie expressed the extinction (ext), scattering (sca), and related absorption (abs) cross sections deriving from the multipole oscillations. However, when $2R < \lambda/10$ (or $R < 30$ nm), the dipolar oscillations largely predominate, the LSPR can be described using the dipolar or quasi-static approximation (the quadrupolar contributions to the electromagnetic field, and de facto those of higher order are neglected)^{69–71}.

Small NPs with radii far smaller than the wavelength of the incident light but also smaller than the penetration depth of the field are fully polarized by the field, the surface charge density alternatively accumulates at each extremity of the NP, i.e., polarization oscillations occur generating an electric field opposed to the excitation field resulting in a restoring force⁷⁰. As illustrated in Figure 1.15, the plasmon oscillations are partially damped, they decay radiatively (strongly enhanced scattering in the far field) or non-radiatively (absorption at the LSPR frequency). In the radiative channel, the metallic NP becomes a nanoantenna, comparable to a nanometric Hertzian dipole, emitting radiation. Elastic scattering occurs since the frequency

of the emitted photons is equal to that of the incident photons. This scattering can be measured at the single nanoparticle scale, with dark field microscopy for example. In the nonradiative channel, the metallic NP becomes an absorbing medium in which both charge separation and hot carriers (electrons and holes) generation take place. After ultra-fast (fs) electron-electron scattering, energy dissipation from the electronic system to the lattice occurs via electron-phonon coupling processes⁷².

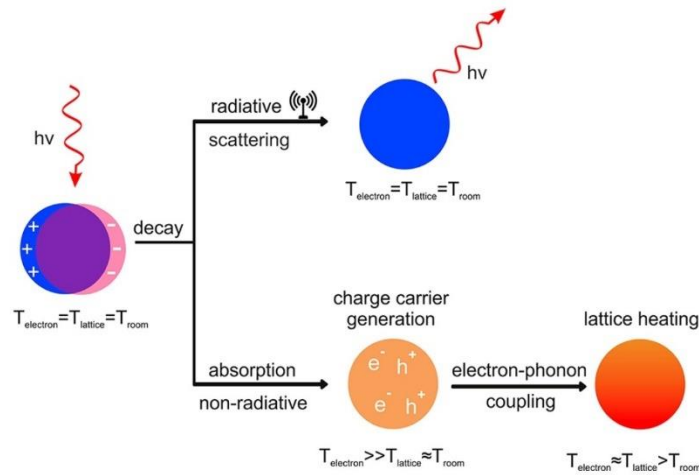


Figure 1.15: Scheme of the two decay channels of a photoexcited plasmonic gold nanoparticle. Subsequently to its excitation by the incident electric field, the LSPR decays both radiatively by re-emitting photons (top) and non-radiatively by generating hot carrier which triggers lattice heating via electron-phonon coupling (bottom). T_{electron} , T_{lattice} , and T_{room} are the temperature of the electron system, the lattice, and the environment, respectively. Reprinted from⁷².

The system is similar to a dipolar oscillator, as drawn in Figure 1.16 the charges oscillates as a whole, with a resonance frequency ω_{plasmon} ⁷⁰. The plasmon resonance frequency or plasmon wavelength for which LSPR occurs depends on parameters such as the metal (gold, silver, etc.), the size (when the dipolar approximation is no longer valid, which is the case for “real”, non-ideal NPs), the shape (spherical, cubic, ellipsoidal, triangular, isocahedral, etc.), and the surrounding medium (solvent, substrate, etc.)⁷². About this last parameter, one must keep in mind that a medium with a higher optical index, directly linked to the dielectric permittivity by $\epsilon_{\text{diel}} = n^2$, means a higher intensity of the plasmon resonance and a larger value of the NPs’ absorption cross-section (see Equations 1.6, 1.7, and 1.8 further). An intense absorbance peak on the UV-visible spectrum of a homogeneous group of noble metal NPs which absorb the incident light beam at ω_{plasmon} constitutes the spectral signature of the NPs, although the NPs also largely scatter the light beam⁷⁰.

In the dipolar approximation, the charge distribution is considered static, from this consideration, the electric field outside of the nanoparticle (see Figure 1.16), which is a sum of the incident field and the field produced by the particle, is derived (see Chapter 3 from the book of Pluchery et Louis⁷⁰ for the full demonstration) and expressed as⁷⁰:

$$\vec{E}_{ext} = \vec{E}_0 - \alpha E_0 \left[-2 \frac{\cos \theta}{r^3} \vec{u}_r - \frac{\sin \theta}{r^3} \vec{u}_\theta \right] \quad (1.6)$$

With alpha the polarizability of the NP which contains its electromagnetic response, given by:

$$\alpha = 4\pi\epsilon_0 R^3 \frac{\epsilon - \epsilon_{diel}}{\epsilon + 2\epsilon_{diel}} \quad (1.7)$$

The external field is maximal when the polarizability is also maximal. The dielectric permittivity being frequency dependent, $|\alpha|$ is thus maximal when $|\epsilon + 2\epsilon_{diel}|$ is minimal. The dielectric permittivity of the surrounding medium, ϵ_{diel} is considered constant and real so that the condition to maximize $|\alpha|$ becomes $Re(\epsilon) + 2\epsilon_{diel} = 0$. For an aqueous solution of gold nanoparticles, $\epsilon_{diel} = 1.77$, the condition is $Re(\epsilon) = 2 \times 1.77 = -3.54$, leading to an intense plasmon resonance at 520 nm, thus explaining the ruby red color of AuNPs solutions.

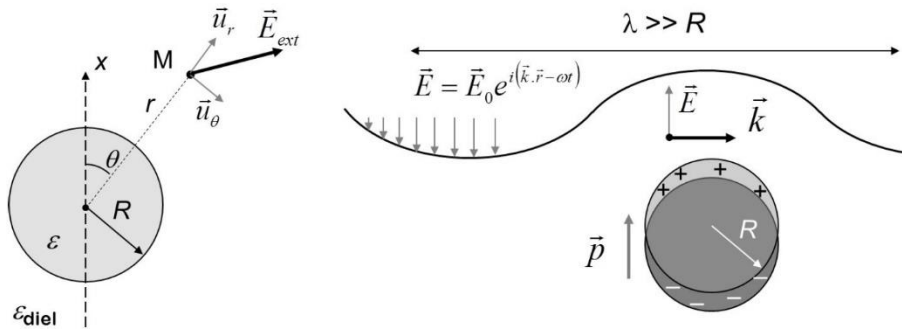


Figure 1.16: Schematics of a metallic nanoparticle with the coordinates required to express the external electric field using the electrostatic model (left). Plasmonic nanoparticle described as an oscillating dipole (the electrons of its LSPR oscillate as a whole) because the wavelength of the excitation wave is much larger than its radius ($\lambda \gg R$) (right). Adapted from⁷⁰.

The extinction (σ_{ext}), scattering (σ_{scatt}), and absorption (σ_{abs}) cross-sections resulting from the interaction of the NP with incident light can be calculated provided the inclusion of a complement to the electrostatic model since light is a propagating wave and not a static electromagnetic field. The light beam undergoes an extinction after the NP absorbed and scattered a part of it, the respective cross section corresponding to each of these frequencies and

thus time dependent phenomena can be calculated using the model of the radiative dipole. Note that the relationship between these cross sections and the previously expressed polarizability is clear, and we have⁷⁰:

$$\sigma_{abs} = \sigma_{ext} - \sigma_{scatt} \quad (1.8)$$

$$\sigma_{ext} = 3 \frac{2\pi}{\lambda} \sqrt{\varepsilon_{diel}} \text{Im}(\alpha) = 9 \frac{2\pi}{\lambda} \varepsilon_{diel}^{\frac{3}{2}} V \frac{\text{Im}(\varepsilon)}{|\varepsilon + 2\varepsilon_{diel}|^2} \quad (1.9)$$

The resonance condition is fulfilled when $\text{Re}(\varepsilon(\omega)) = -2\varepsilon_{diel}$ for $\text{Im}(\varepsilon(\omega))$ small enough, and a negative $\text{Re}(\varepsilon(\omega))$ is mandatory to have a surface plasmon resonance⁷¹. The intensity of the LSPR in resonance is conditioned by the magnitude of $\text{Im}(\varepsilon(\omega))$ which corresponds to loss in the material⁶⁸.

$$\sigma_{scatt} = 3 \frac{(2\pi)^3}{\lambda^4} \varepsilon_{diel}^2 |\alpha|^2 = 3 \frac{(2\pi)^3}{\lambda^4} \varepsilon_{diel}^2 V^2 \left| \frac{\varepsilon - \varepsilon_{diel}}{\varepsilon + 2\varepsilon_{diel}} \right|^2 \quad (1.10)$$

These three cross-sections are useful to describe homogenous metallic nanospheres with a diameter comprised between 10 and 60 nm (see Figure 1.17). Note that all the AuNPs that were used for the present PhD work had sizes included in this interval. Up to 20 nm, absorption dominates, and scattering is neglectable, from 60 to 80 nm absorption and scattering are comparable, and for more than 80 nm, scattering dominates. It was demonstrated by the discrete dipole approximation (DDA) calculations of El-Sayed et al.⁷³. As previously mentioned, the LSPR is independent from the NP size if the dipolar approximation used to describe the NP is valid. Large NPs ($R > 60$ nm) exhibit larger bands corresponding to multipolar plasmonic contributions. The electron cloud of these large NPs no longer homogeneously oscillates over the whole NP, the oscillating dipole description (oscillating opposite charges at each extremity) does not apply to this system. The multipolar plasmonic contributions always appear at shorter wavelengths than the dipolar ones which are redshifted. All the contributions can be analytically described by the Mie model for spherical NPs with terms of orders higher than 2 (1 is for the dipolar contributions) in the multipolar development of the electromagnetic field. Small spherical AuNPs ($R < 5$ nm) have sizes inferior to the mean free path of the conduction band electron of the metal which thus undergo many collisions with the AuNP's surface. It shows on their spectra that present broadened plasmon bands (already visible for $R < 10$ nm). Extremely small AuNPs ($R < 2.5$ nm) have blue-shifted plasmon resonances or exhibit no plasmon bands at all. This is due to a quantum phenomenon called "electronic spill-out" occurring at the surface

of the AuNPs since the radius of the electrons cloud is slightly larger (about 0.5 Å) than the radius of the positively charged sphere made of nuclei^{70,71}.

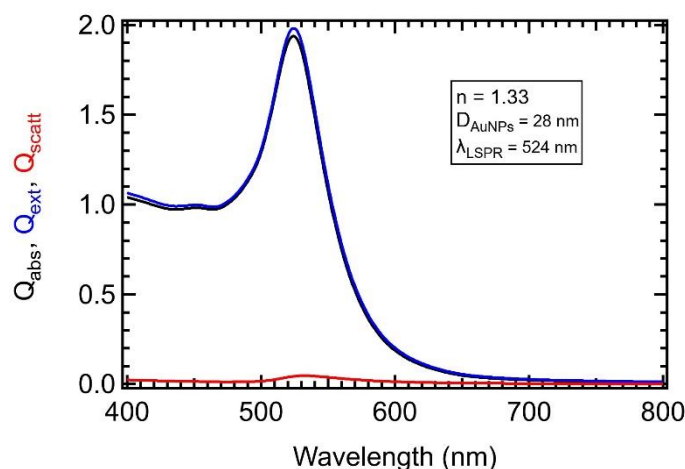


Figure 1.17: Calculated spectra of 28 nm AuNPs showing respectively their absorption, extinction, and scattering efficiencies. $Q = \sigma/\pi R^2$. Calculated with⁷⁴.

Note that the absorbance of non-interacting NPs in sufficiently diluted solutions is directly linked to the extinction cross section by the relation⁷⁰:

$$A = -\frac{1}{\ln(10)} nb\sigma_{ext} \quad (1.11)$$

With n the number of NPs per unit of volume, b the length of the optical path (size of the cuvette in the case of usual spectrophotometry), and σ_{ext} as defined above in Equation 1.9. The position of the plasmon resonance for aqueous solutions of AuNPs can be evaluated using this relation based on the electrostatic model. This position was indeed extensively measured at 519 nm for AuNPs with diameters ranging from 4 to 35 nm, very close to the theoretical value of 520 nm previously mentioned. The extinctions coefficients were precisely measured so that they could be used for calculations with Beer-Lamber law (described in Chapter 2.II.1.a)⁷⁰.

There are several types of interactions influencing the plasmonic properties that cannot be neglected if they are present^{70,75}. The first type is the far-field interaction between NPs when they are close enough from each other which has consequences on the LSPR; its position is modified as well as the absorption cross-section of the NPs. It is however possible to describe assemblies of interacting particles by using an effective medium approximation. Strong near-field interactions between metallic NPs leading to the coupling of their plasmon oscillations

can also occur. The plasmonic coupling between two spherical AuNPs is described further (see Chapter 1.IV.1). The last important interaction to consider is the one between the NPs and the substrate (in the case of supported NPs) which are electromagnetically coupled. On the one hand, the LSPR is modified according to the distance from the substrate especially if the incident electric field is polarized perpendicularly to the interface (see Figure 1.18). When the distance becomes small enough, spectral features corresponding to quadrupolar contributions appear and become comparable to the dipolar one that redshifts. On the other hand, the LSPR is modified according to the metallic, semi-conductor, or dielectric character of the substrate. The oscillating electronic cloud of the AuNP interacts (in a dipole-dipole resembling manner) with the image charges of the substrate. As can be seen in Figure 1.18, when the incident electric field is polarized perpendicularly to the substrate, a charge distribution of opposite sign rises which is exactly the symmetrical image of that of the oscillating dipole (the surface of the substrate can be viewed as the plane of symmetry). The excitation dipole and the induced one are therefore aligned. Conversely, when the incident field is polarized parallelly to the substrate the two dipoles are anti-parallel. A detailed description of the interactions between metallic NPs and their plasmonic coupling in particular as well as their interactions with all types of substrates can be found in the review of Halas et al⁷⁵.

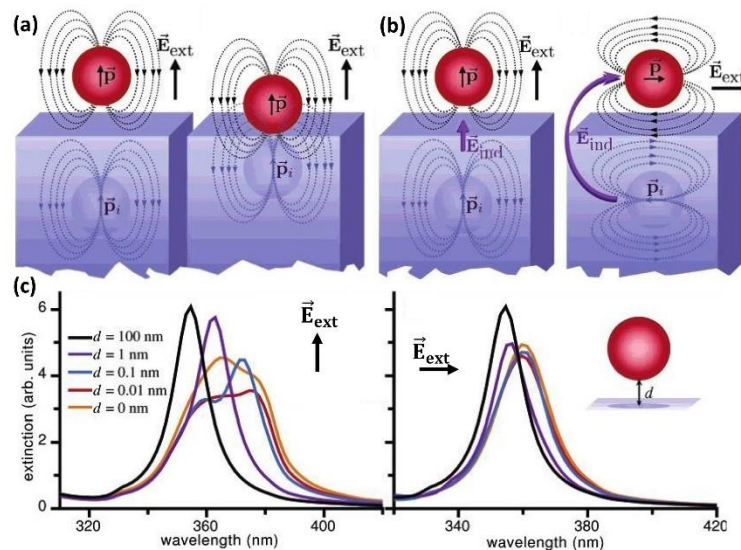


Figure 1.18: (a) Illustration of the electromagnetic coupling between a 10 nm silver NP and an Al_2O_3 substrate in which charge images are induced, in function of the distance between them. (b) Induced local field for an applied field normal (left) and parallel (right) to the interface. (c) Extinction efficiency of the AgNP according to the distance from the substrate d for an external field normal (left) and parallel (right) to the substrate. The influence of the distance on the extinction efficiency is much stronger when the field is normal than when the field is parallel. Adapted from⁷⁶.

2 - Gold nanoparticles acting like plasmonic nanoantenna

Upon excitation at the plasmon resonance frequency, the NP acts like a plasmonic antenna, it radiates a near field electromagnetic wave with an enhanced (up to 10 times) amplitude. The expression of the local field radiated by a nanoparticle, which at $\lambda = 530$ nm is five times larger than the incident field E_0 , is derived from Equation 1.6 and writes⁷⁰:

$$E_{antenna} = E_0 \frac{3\varepsilon}{\varepsilon + 2\varepsilon_{diel}} \quad (1.12)$$

a - Near field radiated by a spherical nanoparticle

The optical near field radiated by a spherical nanoparticle can be described using the oscillating electric dipole model⁷⁷. Let us remind that we mentioned previously that an analogy can be made between an oscillating dipole and a metallic nanoparticle under the effect of an incident electromagnetic field. Here, the dipole can be seen as an elementary source of radiation. Let there be two charges $+q$ and $-q$, separated by a distance d , forming a dipole along the y axis. The dipole, considered much smaller than the wavelength, oscillates at a frequency ω related to the wave vector $k = 2\pi/\lambda$.

The field $\mathbf{E}(\mathbf{r})$ radiated in the direction \mathbf{u} at the point M separated from the center of the dipole by a distance r (see Figure 1.19) is ($e^{-i\omega t}$ factor is implicit)⁷⁷:

$$\mathbf{E}(\mathbf{r}) = \frac{k^2}{4\pi\varepsilon_0} \frac{e^{ikr}}{r} \left\{ [\mathbf{p} - (\mathbf{p} \cdot \mathbf{u})\mathbf{u}] - \frac{1}{ikr} [\mathbf{p} - 3(\mathbf{p} \cdot \mathbf{u})\mathbf{u}] - \frac{1}{k^2 r^2} [\mathbf{p} - 3(\mathbf{p} \cdot \mathbf{u})\mathbf{u}] \right\} \quad (1.13)$$

$\mathbf{E}(\mathbf{r})$ is the sum of three contributions (in square brackets of Equation 1.13), the first term corresponds to the far-field dipolar radiation and is responsible for the radiated energy flux, it decays as $1/r$. The second term corresponds to the induction field, it decays as $1/r^2$. The third term corresponds to the near field, it decays as $1/r^3$ and thus dominates at short distances. It is the most important term in the context of this work. The frontier between the near and the far field is clearly visible on the plot of $\mathbf{E}(\mathbf{r})$ along x in function of kr (see Figure 1.19). It is materialized by a slope break located at $kr = 1$ with $r = \lambda/2\pi$ and $\mathbf{E}(\mathbf{r})$ along x ⁷⁷:

$$\mathbf{E}(\mathbf{r}) = \frac{k^3}{4\pi\varepsilon_0} e^{ikr} \mathbf{p} \left\{ \frac{1}{kr} + \frac{i}{(kr)^2} - \frac{1}{(kr)^3} \right\} \quad (1.14)$$

Consequently, at distance from the dipole shorter than $\lambda/2\pi$, corresponding to about 50 nm for a 20 nm diameter spherical nanoparticle in the visible range, the near field dominates, at longer distances, the far field does. The consequences on the far field of a modification occurring in the near field is visible in the case of an aggregating aqueous solution of gold nanoparticles. When the AuNPs in solution are well dispersed (no aggregation), the solution is red. Upon aggregation of the AuNPs, their local near-field waves interact, and the solution turns blue⁷⁰.

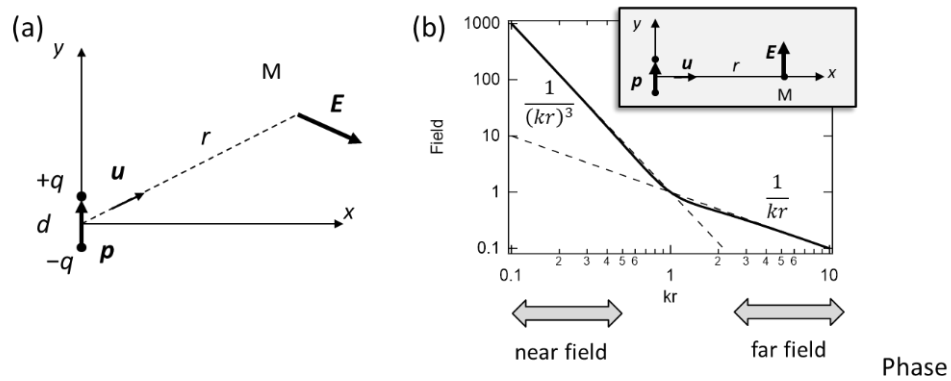


Figure 1.19: (a) Oscillating dipole (at the origin) and its radiated electric field at point M located at a distance r from the center of the dipole. Logarithmic plot of the amplitude of the electric field as a function of the distance from the center, along the x axis showing the two radiation zones of the dipole: the near field with a decay in $1/kr^3$ and the far field with a decay in $1/kr$. Reprinted from⁷⁷.

When $r \ll \lambda$ ($kr \rightarrow 0$), the electric field writes with the expression obtained in the electrostatic limit (retardation effects are neglected in the near field limit)⁷⁷:

$$\mathbf{E}(r) = \frac{1}{4\pi\epsilon_0 r^3} [3(\mathbf{p} \cdot \mathbf{u})\mathbf{u} - \mathbf{p}] \quad (1.15)$$

In the end, the electromagnetic field radiated by a metallic nanosphere can be calculated using the dipolar approximation with Equation 1.12 or 1.6 with the expression of the polarizability α (see Equation 1.7). Rodríguez-Fernández et al.⁷⁸ made the calculation at $\lambda_{\text{LSPR}} = 520$ nm for a 12 nm gold nanoparticle in water illuminated by a plane wave with field an amplitude \mathbf{E}_0 and a wavevector \mathbf{k} . As can be seen in Figure 1.20, the electric field is strongly enhanced along the direction of \mathbf{E}_0 in the close vicinity of nanosphere (4-5 nm around it maximum). The near-field enhancement factor, which can go up to 20, is defined as $|E/E_0|^2$.

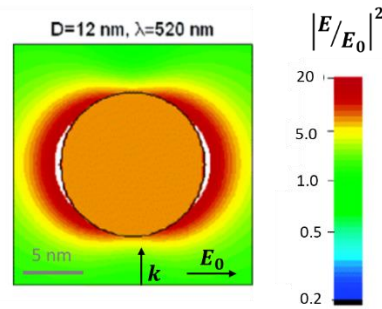


Figure 1.20: Electromagnetic field radiated by a gold nanoparticle illuminated at its plasmon resonance $\lambda_{\text{LSPR}} = 520 \text{ nm}$ in water corresponding to a near-field enhancement of a factor 20 in the vicinity of the AuNP. Reprinted from⁷⁷.

b - The concept of plasmonic nanoantenna

The enhancement provided by the local field is limited to the close surroundings of the nanoparticles which is designated as a plasmonic nanoantenna (PNA). A parallel is made with conventional microwave and radiofrequency antennas (RFAs). An antenna is an intermediate/transducer between far-field radiations and local fields (local currents in conductive elements). PNAs can convert energy from local electromagnetic near fields to far field optical radiation extremely efficiently^{71,79}. PNAs, with their dimensions corresponding to that of the electromagnetic radiations wavelength, can be viewed as nanoscale equivalents of RFAs although the two types of antennas have working principles based on different physical phenomena. Electrical antennas (radiowave and microwave antennas) are powered by high-frequency voltage sources. These antennas induce current oscillations (oscillating polarization) which in turn produce radiowave and microwave radiations. Plasmonic nanoantennas are supplied by high-frequency optical sources that induce optical current in them, producing plasmonic oscillation in the UV to IR range⁷⁹.

All plasmonic structures exhibiting a local field enhancement are nanoantennas with a certain efficiency⁷⁷. PNAs of many different types exist, metallic nanoparticles of various shapes (spherical, rod-like, triangular, star-like), core-shell systems, classical yet miniaturized Yagi-Uda antennas, and V-shaped antennas⁷⁹. The plasmonic nanoantenna effect stems from the strong coupling of LSPRs in metals (coherent free electron oscillations) to the continuum (free space radiation), analogously to what RFAs do. At λ_{LSPR} (optical resonance), optically resonant PNAs channel electromagnetic energy from the continuum to nanometer-scale volumes through the excitation of LSPRs, and then radiate it back to the continuum with high efficiencies⁷⁹.

An efficient plasmonic nanoantenna must possess a large and tunable cross-section i.e., the ability to efficiently collect electromagnetic energy from the incident radiation (light) and provide a strong near-field enhancement i.e., the ability to transfer the most of that energy in the PNA surroundings (nano-scale volumes)⁸⁰. The directionality of the antenna, which designates the emission or reception efficiency of the antenna according to the direction of the incident light, must also be considered. It affects the efficiency of both the excitation and the collection. A relevant design, including directions for which light reception and/or emission is very efficient, allows to obtain high quantum efficiency super-bright single-photon sources with strong directionality⁷¹.

Considering their strong interaction with light, the potential of metallic NPs for an utilization as optical antenna has been largely explored⁷¹. Metallic NPs can be used as PNAs; at resonance (λ_{LSPR}), NPs reach their maximal light absorption and scattering capacity. Their optical response is tunable and spectrally narrow. Their extinction cross section is then several times larger than their physical cross-section (size at resonance). It explains the presence of hot spots (zones with massively amplified fields) and the efficiency of the light focusing. These hot-spots can be used to strongly enhance (by several orders of magnitude) light-matter interactions^{79,80}. Metallic NPs are efficient optical receivers meaning that they efficiently collect far the field of incident radiation (plane wave) and focus it, in specific directions, into local near-fields confined in their close vicinity (nano-scale volumes, so far below the size of the wavelength). Metallic NPs are also efficient emitters since they can enhance the decay rates of a local source provided the resonance of the metallic NP or NP array is tuned accordingly⁷¹. However, one can note that due to their high level of symmetry, the directionality of spherical nanoparticles, like the ones used in this work, is poor⁷⁷.

An example of metallic nanoparticle PNA is shown in Figure 1.21, it is a silver nanorod for which the local electromagnetic field was calculated for three of its plasmonic modes. The extension of the near field (a few nm) is of the order of magnitude of the NP size (400 x 100 x 50 nm³). The first mode ($n = 1$) is an oscillating dipole with a LSPR located at 1375 nm, the second ($n = 2$, $\lambda_{LSPR} = 770$ nm), and third ($n = 3$, $\lambda_{LSPR} = 630$ nm) plasmonic modes are higher energy modes. Each mode exhibits local electromagnetic field enhancements represented in different colors in function of their intensity. The hot spots (zones with the highest enhancement factor, $EF = 100$) are represented in red^{70,80}.

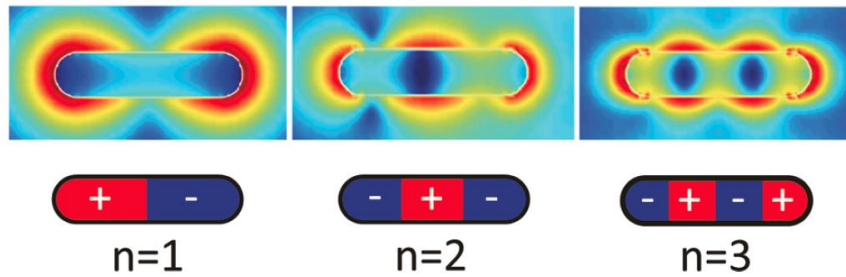


Figure 1.21: Illustration of the concept of plasmonic nanoantenna through the example of a $400 \times 100 \times 50 \text{ nm}^3$ silver nanorod. Mapping of the calculated near-field for three plasmonic modes ($n = 1$, $\lambda_{\text{LSPR}} = 1375 \text{ nm}$; $n = 2$, $\lambda_{\text{LSPR}} = 770 \text{ nm}$; $n = 3$, $\lambda_{\text{LSPR}} = 630 \text{ nm}$), blue and red correspond to an enhancement factor of respectively 0.1 and 100. The nanorod is on a glass substrate and illuminated from the top by a plane wave tilted 20° with respect to the vertical direction and polarized along its long axis. Reprinted from⁷⁰.

To summarize, PNAs enable light guiding and localization below the diffraction limit (and thus at dimensions smaller than light wavelength) thanks to the incident electromagnetic energy confinement at the surface of the PNA by the coherent plasmonic excitations. They provide light-matter interactions (electron-photon coupling) enhancement, strong and tunable coupling between localized electric/electrochemical/mechanical phenomena and far-field radiation of a system PNA/active material. A coupled system emitter/PNA exhibit a more efficient emission at specific frequency for which the antenna is resonant, it appears in the spectral response of the emitter⁷⁹.

3 - Applications of gold nanoparticles

Gold nanoparticles and more broadly noble metal nanoparticles are used in many different fields for applications rendered possible by their plasmonic properties. One of these fields is biomedicine with applications in biomedical imaging, cancer therapy, drug delivery, pharmacokinetics, biodistribution, and tumor targeting. A related field is that of plasmonic biosensing with applications in the detection of viruses, pollutants, allergens, and of a specific chemical or biomolecule in general, and the development of lab-on-a-chip and point-of-care diagnosis devices via the combination with microfluidics. One can note that the few examples found of the measurement at the single nanoparticle scale of the modifications induced by the functionalization of AuNPs regarded biological sensing studies. In their review, Zamora et al.⁸¹ reported the following, their study of the spectral changes undergone by 100 nm AuNPs introduced in the intracellular matrix. In solution, the AuNPs appeared orange on the dark-field microscopy images and their LSPR peak was located at 645 nm. For AuNPs introduced inside

cells, the LSPR peak was located at different wavelengths (633, 603 and 582 nm) according to the component of the cell it was in contact with. These differences were of course observable on the images on which the AuNPs appeared of different colors. They also gave the example from a study of Shannahan et al.⁸², of the interaction of 20 nm and 110 nm citrated silver nanoparticles (AgNPs) with cholesterol molecules which resulted in a redshift of 38 nm (from 572 to 610 nm) for the 20 nm AgNPs and of 99 nm (from 512 to 611 nm) for the 110 nm AgNPs indicating the grafting of the cholesterol molecules at the surface of the AgNPs.

A totally different field in which applications of AuNPs can be found is that of photocatalysis^{83,84}, including hot-electrons assisted chemistry (see Figure 1.22), for applications in energy such as better harvesting of solar power through solar water splitting⁸³, the design of more efficient solar cells comprising plasmonic NPs⁸⁴, and photoreduction of CO₂ to fuels⁸⁵. Another main application is the catalysis of various organic reactions including photochemical ones for which H₂ and/or O₂ dissociations are key steps. Mukherjee et al.⁸⁶ reported the dissociation of H₂ molecules adsorbed on AuNPs at room temperature. The dissociation of O₂ was also reported⁸³ and is particularly important for oxidation reactions. Zheng et al.⁸⁷ showed the photocatalysis of the dehydrogenation of formic acid on anisotropic Pd-Au nanorods. Biochemical reactions can also be photocatalyzed, Cortés et al.⁸⁸ reported the photocatalysis of the reduction of 4-NTP to 4-ATP by the hot electrons of the Ag nanoantennas the molecules are grafted on.

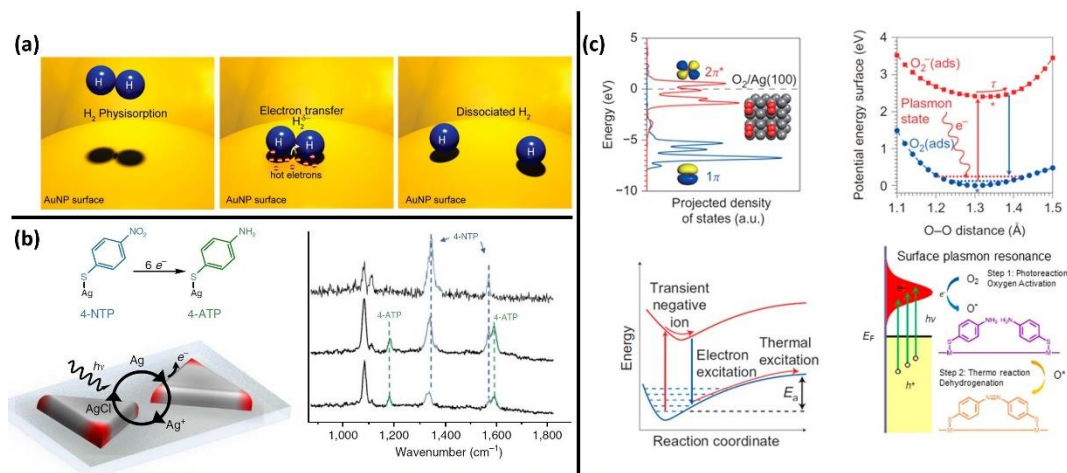


Figure 1.22: (a) Scheme illustrating the SERS detection of the reduction of 4-NTP to 4-ATP by hot-electrons generated at the tip of the Ag antenna, in the presence of 0.1M HCl, and under illumination at $\lambda = 633$ nm and 1mW (left). Time-dependent Raman spectra showing the conversion of 4-NTP (blue peak) to 4-ATP (green peaks) (right). (b) Illustration representing the mechanism of H₂ dissociation by plasmon-induced hot electrons generated at the surface of the AuNPs. (c) O₂ dissociation by plasmon-induced hot electrons. Top left: density of states of O₂ adsorbed on an Ag (100) surface calculated by DFT, the dashed line materializing the Fermi level of Ag, the blue curve the bonding orbitals of O₂, and the red line the antibonding orbitals of O₂. Top right: PES of O₂ and O₂ on Ag(100). An energy transfer occurs from the hot electrons to the O₂ (activating the molecules) vibrational mode after they get transferred back to Ag. Bottom left: scheme of O₂ dissociation triggered by vibrationally excited states. Bottom right: aerobic oxidation of p-ATP mediated by hot-electrons acting on the antibonding orbital of the O₂ molecule, producing the long-lived O₂ that oxidizes p-ATP. Adapted from^{83,86,88}.

Finally, noble metal NPs also found applications in the now very commonly used analytical techniques that are surface-enhanced Raman spectroscopy⁸⁹ (SERS) and tip-enhanced Raman spectroscopy⁹⁰ (TERS). The large signal enhancement provided by the NPs allowed the development of these techniques and their application in the detection of species present in extremely low quantities⁹¹, in single molecule chemistry⁹², in surface characterization of various materials⁹³, in spectroelectrochemistry which allows the in-situ monitoring of diverse chemical reactions leading to the identification of reactional intermediates and unravelment of mechanisms, and sensing (of pH, hydrocarbons, glucose, DNA/NRA, proteins, etc.)⁸⁹.

4 - Using the plasmonic nanoantenna effect of the gold nanoparticles to solve the issue of the asymmetric switching of diarylethenes

Before looking into the case of gold nanoparticles, it is interesting to start with that of flat gold surfaces. Katsonis et al.⁹⁴ monitored the switching of meta-phenyl-linked diarylethenes grafted on a flat Au(111) surface by STM and UV-visible spectroscopy. They showed that the

time required to make meta-phenyl-linked DAEs on gold switch was an order of magnitude higher than the time it takes to make the molecules switch in solution. This difference was attributed to the “shortening of the lifetime of the excited state of the molecule by interaction with the metallic surface” i.e., to quenching.

Regarding the case of metallic nanoparticles in solution, Yamaguchi et al.⁹⁵ showed that reversible switching occurred for DAEs used as ligands on gold and silver nanoparticles (from 2.2 to 6.7 nm) dispersed in ethyl acetate, but also that quenching was present for both reactions although they tried to increase the distance between the DAE and the NP with a five-units methylene chain. They monitored the reactions with thin-layer chromatography and found lower conversion (ratio of the QYs) for the DAEs grafted on NPs in solution than for DAE molecules alone in solution. They showed that the cyclization was more affected by quenching than the cycloreversion. They attributed the partial preservation of the photochromic properties to the speed of the cyclization reactions (< ps).

Finally, regarding the case of DAEs grafted on supported AuNPs, Ikeda et al.⁹⁶ showed that DAEs with a phenyl linker (similar to C5HT-di-PSH, one of the molecule used in this PhD work, but with one more methyl on the position 3 of the thiophen ring and with a perfluorocyclopentene ring as bridging unit) embedded in a 3.6 nm AuNPs network underwent reversible photochromism but that both reactions were very slow. The photocycloreversion was the slowest, this slowdown was attributed to severe quenching by energy transfer. As summarized in Figure 1.23, Van der Molen et al.³³ used DAEs as bridges between 10 nm AuNPs organized in a 2D array. These molecules are equivalent to ours except for the cross-conjugated meta-phenyl linker (or spacer), in the case of C5HT-di-SH (our molecule, presented in the next chapter), the linker is a para-phenyl linker. They showed that the ring-closure QY decreased from 0.4 to 0.07 upon connection of the DAEs to AuNPs in solution. The switching was also monitored by optical spectroscopy following the evolution of LSPR peak position. Since according to them, their molecules were sufficiently decoupled from the electrode, this decrease was not attributed to strong electronic coupling causing charge transfer (electron and/or holes) from the excited state of the molecule to the metal. It was the problem observed in devices switching in only one direction (case of Dulić et al.⁹⁷). Instead, they attributed it to quenching via energy transfer due to the interaction with the mirror dipoles in the metallic gold electrodes.

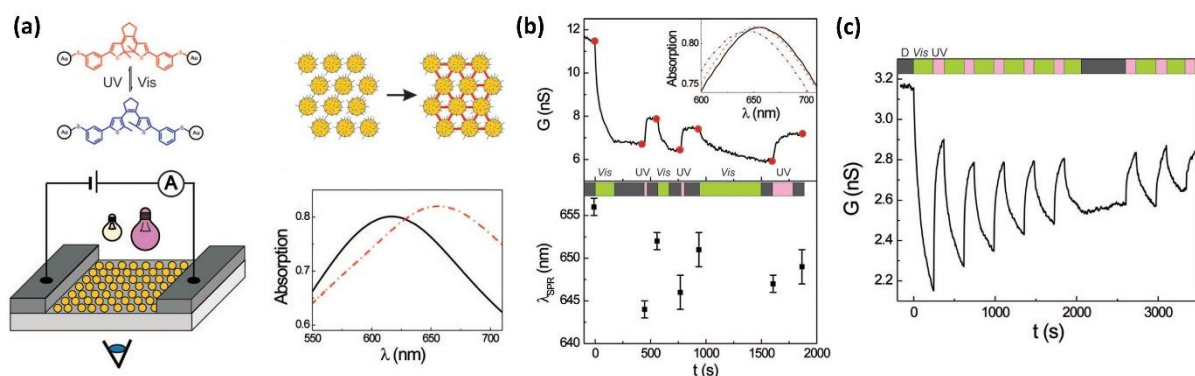


Figure 1.23: (a) Diarylethene molecules in their “on” state (red) and open, “off” state (blue). Schemes of 2D networks: of gold nanoparticles protected by octanethiols (left side of the arrow) and connected by diarylethene molecules in their “on” state (right side of the arrow). Scheme of the setup used to measure light-induced (Hg lamp) conductance switching or optical switching (low-intensity white light source). Absorption spectra of the 2D AuNPs network before (solid, black line) and after (red, dash-dotted line) insertion of the diarylethene molecules to bridge the AuNPs, which made the LSPR peak shift, and the conductance increase of a factor of 18. (b) Conductance and molecular switching. They kept the sample in the dark until $t = 0$. They made the experiment in an argon flow cell at room temperature. The sample undergoes an alternance of illumination with either visible (green) or UV (pink) light and period in the dark, after which an optical spectrum is recorded and the conductance at that time t is indicated by a red dot. The evolution of G versus the time is plotted in the upper graph, while that of λ_{LSPR} versus the time is plotted in the lower graph. Visible light illumination makes G and λ_{LSPR} increase, while UV light illumination makes them decrease. Inset: First three optical spectra: black, solid line, spectrum at $t = 0$; blue, dash-dotted line, after first visible illumination, λ_{LSPR} decreased; red, dashed line, after first UV illumination, λ_{LSPR} increased, closer to its initial value. The optical spectra demonstrate the molecular switching, DAEs in their “off” state having a lower permittivity than DAEs in their “on” state. Conductance switching cycles. The conductance G is plotted versus illumination time t for a sample with all its DAE bridges in the ON state. In the dark, before the beginning of the measurements (at $t < 0$) the sample conductance is constant. At $t = 0$, visible light illumination starts, G immediately decreases, upon UV irradiation (at $t = 245$ s), G increases again. Eight switching cycles consisting in 245 s of visible light irradiation followed by 125 s of UV light irradiation were performed. For $2095 < t < 2650$ s the sample was left in the dark. The experiment was done in an argon flow cell at room temperature. To determine G , they recorded I-V curves, with $-10 < V < 10$ V, so that for each molecular junction the bias was at most ~ 10 mV (linear regime). Note that in real time, this experiment lasted over 5 h. Adapted from³³.

On another note, Kobatake’s group was the first one that studied the effect of the distance from the AuNP on the photochromic properties of DAEs but without directly connecting them to gold. Nishi and Kobatake^{98,99} studied the switching of gold nanoparticles bearing polymeric chains (polystyrene) of various lengths containing diarylethene units. They started with the reference, i.e., free DAE in toluene with a chain length of 11 nm, a 97 % conversion was obtained. Then, they measured a first Au-polyDAE sample in toluene with a chain length of 20 nm and AuNPs with a 7.4 nm diameter, a 96 % conversion was obtained. It

was compared to that of a second Au-polyDAE sample in toluene with a chain length of 11 nm and AuNPs with a 5.9 nm diameter for which an 80 % conversion was obtained. The reduction of the chain length of Au-polyDAE induced a decrease of the photochromic conversion (and therefore of the QY of the photocyclization reaction). This lower conversion was attributed to the quenching of more DAEs of the shorter chain which are closer from the AuNP. Both Au-polyDAE displayed a lower conversion (72 and 70% respectively) when they were deposited on quartz substrates. It was attributed to the fact that unlike in solution, the chains are not extended but some of them are twisted, bent etc. which gets a part of the chromophores closer to the AuNPs and therefore quenched. The interparticle distance was also shorter than in solution introducing interactions (and thus quenching) of the polymeric chains not only with the AuNP they are attached to but also with the AuNPs around them. Finally, they studied a block copolymer constituted of a 6.1 diameter AuNP with a 12 nm styrene chain and a 63 nm DAE chain attached to the styrene chain, exhibiting a 94% conversion in toluene: no quenching thanks to the styrene chain that keeps the chromophore chain far enough from the AuNP. On the quartz substrate, the conversion dropped to 68 % for the same reasons than previously explained for the Au-polyDE.

Nishi et al.^{100,101} studied various Au-polyDAE systems (see Figure 1.24) and measured the plasmonic enhancement factor obtained for different AuNP diameter, distances between the gold surface and the chromophore, and DAE structures. The enhancement was not affected by the structure of the DAE. A larger enhancement factor was measured for larger AuNPs (from 0.47 for a 4 nm diameter to 2.9 for a 41 nm diameter)¹⁰¹. No enhancement was measured for short polymeric chain due to quenching or for too long polymeric chains no longer affected by the LSPR.

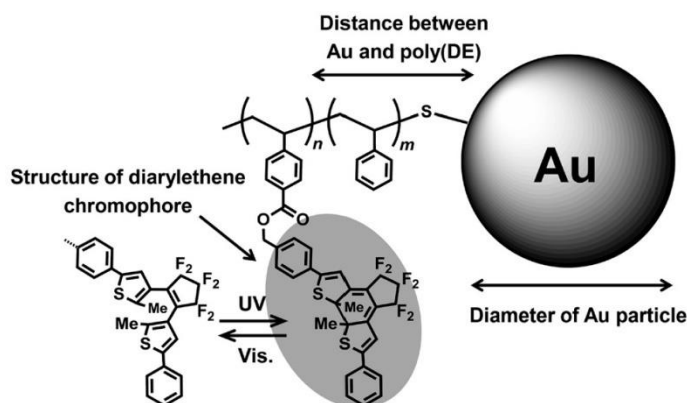


Figure 1.24: Scheme of the structure of their Au-poly(DE) systems. Reprinted from¹⁰¹.

Tsuboi et al.¹⁰² reported the acceleration via a LSPR enhancement effect of the one photon photocycloreversion reaction (ring-opening) of two different diarylethenes embedded in a polymer (PMMA) film coated on 30 nm AuNPs deposited on a glass substrate (either randomly or organized in dimers with a gap distance of 140 nm). Both studied DAEs had a perfluorocyclopentene ring as a bridging unit, one had benzothiophene linkers and the other one has phenylene linkers with the usual additional methyl group on the third position of the thiophene ring of the photochromic unit. The main and crucial difference these DAEs have with the ones we studied is that they do not possess a thiol anchor group. They were not meant to be directly connected to the AuNPs and indeed they were not.

The authors develop the following model. In resonant irradiation conditions i.e., by irradiating the sample with light of the same wavelength than that of the LSPR, the electric field E_p near the gold surface is $E_p = gE_0$ with E_0 the electric field of the incident light and g the enhancement factor. The interaction between the molecule and the enhanced electric field depends on a term $-\mu E_p$ in a matrix element of interaction energy, where μ is the dynamic molecular dipole. Applied to the case of a one-photon permitted molecular transition (optical absorption), the probability of optical absorption of the molecule is proportional to the square of this term ($-\mu E_p$) based on Fermi's golden rule, explaining the molecular absorption enhancement. Based on this model, the quantum yield of the photochemical reactions triggered by light absorption should be increased by the LSPR.

However, the plasmon enhancement factor (proportional to g^2) predicted by the model is $10^2 - 10^5$ far superior to that measured, 1.5 for the DAE with the benzothiophene groups and 2.5 for the DAE with the phenylene groups. The explanation proposed by the authors is the following, the DAE molecules are either too far from the AuNPs to be affected by the enhancement, too close from the AuNPs which make the usual quenching (energy transfer from DAEs to gold) appear or at the right distance from the AuNPs to have their photoconversion reaction enhanced by the LSPR. An averaged enhancement factor was then measured, its value was reduced by the molecules in the first two described situations.

Nishi et al.¹⁰¹ studied the enhancement of the photocycloreversion (one photon reaction) of a diarylethene polymeric shell made of 17 nm chains attached to 18 nm gold nanoparticles in solution (50/50 THF/water mixture). The photochromic unit bears two phenylene groups, one as a terminal group, the other which act as a linker to an ethyl group connected to the polymeric chain via a C-O bond. Consequently, the DAEs are not directly connected to the gold

which contributes to reduce quenching issues. They reported enhancement factors of 2 to 5 according to the irradiation wavelength used, in agreement with the values of Tsuboi et al¹⁰².

IV - Gold nanoparticles dimers

In order to obtain dimers, one can either go for a bottom-up approach^{72,103–106} by using synthesized gold AuNPs (with high monodispersity), usually bound by a molecular linker (but not in our case) and eventually deposited on substrates, preferably patterned to have control on the dimer positioning; or a top-down approach^{67,107,108} by using techniques based on e-beam lithography and subsequent pulsed laser etching.

It is important to make the distinction between a plasmonic dimer and a dimer according to the chemistry definition (see Figure 1.25). A plasmonic dimer is made of two constitutive entities whose plasmon resonances are coupled. In some cases, there is a chemical linker binding the two entities, in some cases, as it will be the case in Chapter 6, there is no chemical linker binding the two entities. Conversely, a dimer according to chemistry is made of two chemical species which are chemically bonded to each other or assembled via van der Waals interactions, again, it will not be the case in Chapter 6. Consequently, from the point of view of plasmonics, we will be in presence of dimers whereas from the point of chemistry, we will simply be in presence of neighbor gold nanoparticles.

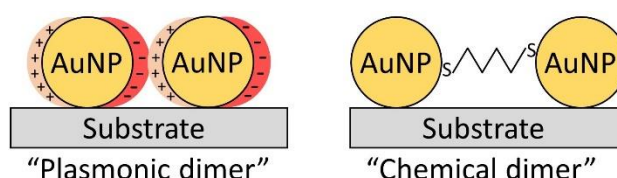


Figure 1.25: Scheme underlining the difference between a plasmonic dimer and a chemical dimer.

1 - Hybridization model of the plasmonic modes of nanoparticles forming a dimer

The model of the hybridization of plasmon modes has been developed by Nordlander et al.^{75,109}, it is analogous to the linear combinations of atomic orbitals (LCAO) model used in chemistry. Indeed, an AuNP can be viewed as an atom and an AuNPs dimer as a diatomic molecule in which two atoms are paired since they share electrons via bonding molecular orbitals. When two AuNPs form a dimer, they are close enough from each other to couple through Coulomb interactions. As shown in Figure 1.26, their intrinsic plasmonic modes

become coupled and they hybridize making four new plasmon modes with different properties appear^{72,108}. Two of these modes are bonding ones, located at lower energy than that required to excite the LSPR of the single AuNP, and the two other modes are antibonding ones, located at higher energy than that required to excite the LSPR of the single AuNP¹¹⁰. The coupling modes resulting from the coupling in the direction parallel to the dimer axis of the dipoles excited on the two AuNPs are equivalent to σ -type orbitals, whereas the coupling modes resulting from the coupling in the direction perpendicular to the dimer axis of the dipoles excited on the two AuNPs are equivalent to π -type orbitals.

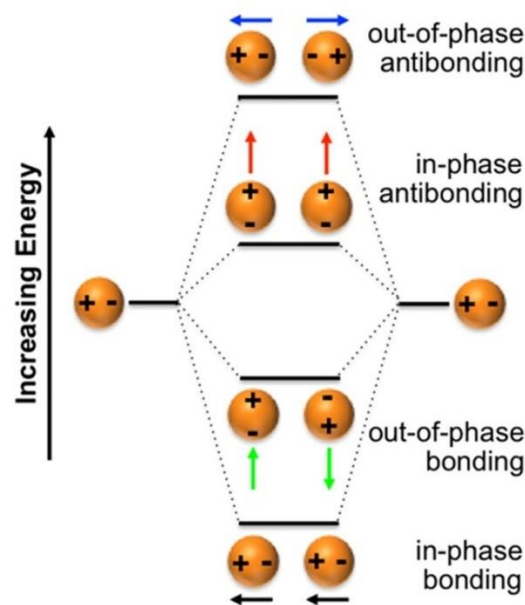


Figure 1.26: Typical plasmonic modes hybridization diagram for a dimer of spherical nanoparticles. Adapted from¹¹¹.

The observability of the plasmonic modes by spectroscopy is defined by their effective dipole moments. For a symmetric dimer, two of the modes possess a nonzero dipole moment and the two others possess a dipolar moment equal to zero. The former, well coupled to the far field and thus radiative, are the bright modes, in this case the longitudinal bonding dipolar plasmon (LBDP) and the transversal antibonding dipolar plasmon (TADP). The latter, unable to couple to the far field and thus non-radiative, are the dark modes, impossible to observe by spectroscopy^{72,75,110,112}. For the LBDP, the dipoles of the AuNPs are aligned and therefore, its induced dipole is large and strongly coupled to the far field. It is the largest induced dipole of all the modes resulting from the coupling, it is consequently the mode that dominates the optical response of the plasmonic dimer⁷⁵.

2 - Spectral signature of gold nanoparticles dimers

Yim et al.¹⁰⁵ measured in air and with unpolarized light, the scattering spectra of individual 60 nm AuNPs and 60 nm AuNPs dimers linked by ethylenediamine (imposing a gap distance of about 2 nm) deposited on ITO. The spectrum from a single 60 nm AuNP presents one LSPR peak located at 540 nm whereas the spectrum of a 60 nm AuNPs dimer presents two plasmon peaks respectively located at 540 (peak corresponding to the TADP) and 680 nm (peak corresponding to the LBDP). They observed slight spectral differences due to the AuNPs morphology differences and, in the case of the dimer, they also observed differences in the gap size, which is surprising since the gap size is supposed to be fixed because of the use of EDA molecules as linker: the gap distance should always be equal to the length of the molecular linker. The peaks on their simulated spectra were redshifted compared to the experimental ones. Regarding their intensity, the peaks corresponding to the dimers were always more intense than the peak of the monomer (similar to what was experimentally observed). However, the peak corresponding to the LBDP mode was more intense than the peak corresponding to the TADP mode whereas on the experimental spectra both peaks were of comparable intensity¹⁰⁵.

Esashika et al.¹⁰⁶ measured the scattering spectra in solution of their dimers of 50 nm and 60 nm AuNPs with gaps of 1.5 nm. In their case, the intensity of the LBDP (located around 540 nm) was always inferior to that of the TADP (located around 640 nm) on their experimental spectra, whereas the intensity of the LBDP was always superior to that of the TADP on their calculated spectra.

3 - Tunability of the gap of a dimer

By adjusting the gap distance between the NPs, one can tune the strength of the coupling and therefore the resonance frequency of the obtained hybridized plasmonic modes as well as the strength of the electromagnetic field generated between the two NPs (hot spot)^{105,106,108,110}. Esashika et al.¹⁰⁶ demonstrated the tunability of the interparticle gap, they prepared AuNPs dimers (coupled via the van der Waals interactions between the -COOH terminated alkyl chains they bear) with well-defined and uniform gaps (measured by cryo-TEM) in bulk suspension and measured the scattering spectra of single dimers in very low concentration suspensions by micro-Raman spectroscopy. They fabricated dimers of various sizes (by using AuNPs with a diameter ranging from 20 nm to 80 nm) and with various gap distances by changing the alkyl chain length from 5 to 15 carbons (the smaller the alkyl chain, the smaller the gap). On the one

hand, they demonstrated that the magnitude of the redshift of the peak corresponding to the longitudinal mode increases with decreasing gap distance in the expected order: C_{15} ($d_{\text{gap}} = 3.9$ nm, $\lambda_{\text{LBDP}} = 574$ nm) $<$ C_{10} ($d_{\text{gap}} = 2.2$ nm, $\lambda_{\text{LBDP}} = 596$ nm) $<$ C_7 ($d_{\text{gap}} = 1.5$ nm, $\lambda_{\text{LBDP}} = 608$ nm) $<$ C_5 ($d_{\text{gap}} = 1$ nm, $\lambda_{\text{LBDP}} = 627$ nm). On the other hand, they showed that the degree of the redshift of the longitudinal mode is less significant with a decrease in AuNP size. It is explained by the dependence of the magnitude of the redshift on the relative distance of the AuNPs (the ratio interparticle gap/AuNP diameter) as well as its absolute distance. Both trends were confirmed by their FDTD (Finite Difference Time Domain) simulations in water.

Both experimental and theoretical studies conducted on dimers of nanoparticles of various shapes and sizes unanimously demonstrated that, as illustrated in Figure 1.27, the peak corresponding to the collective mode (LBDP) redshifts upon reduction of the gap distance for the incident light polarized in the direction parallel to the dimer axis whereas it slightly blueshifts for incident light polarized in the direction perpendicular to the dimer axis^{67,68,75,103–106,108,112,113}. A reduced gap distance means a stronger coupling and a larger charge accumulation in the gap zone¹¹³. The polarization dependence of the coupling can be explained by a simple dipole-dipole coupling model^{67,68}. On the one hand, the dipole-dipole interaction is attractive for parallel polarization, decreasing the plasmon frequency (this decrease corresponds to the redshift of the plasmon band). On the other hand, the dipole-dipole interaction is repulsive for perpendicular polarization, increasing the plasmon frequency (this increase corresponds to the blueshift of the plasmon band). The interparticle interactions and thus the plasmonic coupling are much stronger for parallel polarization since the redshift in parallel polarization is much larger than the blueshift in perpendicular polarization⁶⁷.

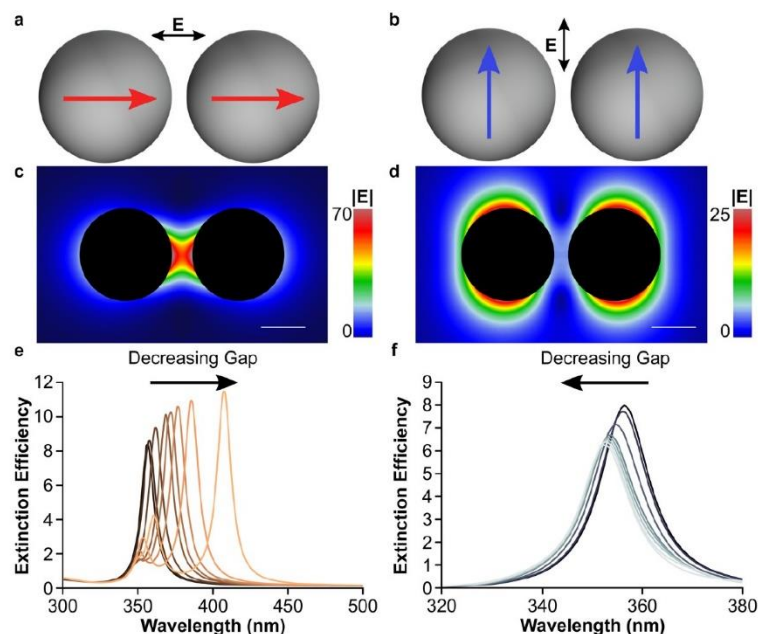


Figure 1.27 : Plasmon coupling in dimers of spherical nanoparticles separated with small gaps. (a) Constructive dipolar coupling in spherical AgNPs with light polarized along the dimer axis. (b) Destructive interference between the dipoles of spherical AgNPs with light polarized perpendicularly to the dimer axis. (c) Electric field intensity of 10 nm spherical AgNPs separated by a 5 nm gap interfering constructively. The scale bar is 10 nm. (d) Electric field intensity of 10 nm spherical AgNPs separated by a 5 nm gap interfering destructively. The scale bar is 10 nm. (e) Extinction efficiency of a dimer of 10 nm spherical AgNPs with gaps of 50 (darkest trace), 40, 30, 20, 10, 5, 4, 3, 2, and 1 (lightest trace) nm, and with light polarized along the dimer axis. (f) Same as (e) but for light polarized perpendicularly to the dimer axis. Reprinted from⁶⁸.

Yoon et al.¹⁰⁴ claim that gap morphology is the most decisive factor regarding the position of the LBDP peak. They made an experimental and theoretical study of individual ideal spherical and non-ideal faceted 50 nm AuNPs dimers. Both have the same gap distance of 1.3 nm fixed by a SAM of 1,8-octanedithiol linker but the ideal dimers exhibit spectral uniformity i.e., same position of the longitudinal bonding dipolar plasmon (LBDP) coupling peak while the non-ideal dimers exhibit high spectral nonuniformity.

This difference is due to the many possibilities regarding the gap morphology of the nonideal dimers. To limit all the possible configurations, they studied hybrid dimers made of an ideal spherical AuNS and a non-ideal faceted AuNP (icosahedron with rounded corners and edges, found experimentally for citrate reduction-based synthesis), to investigate the influence of crystal facet orientation in the gap. They considered three theoretical configurations for the hybrid dimers: face, edge, or point contact (see Figure 1.28). For the ideal dimer model, only one configuration is possible and was therefore considered: a 0D point contact. The position of

the peak corresponding to the LBDP was calculated to be 732 nm for an ideal dimer with a 1 nm gap and 695 nm with a 1.25 nm gap. As shown in Figure 1.28, FDTD calculations predict a blue shift of the longitudinal bonding dipolar plasmon coupling mode for hybrid dimers with point and edge contacts due to the lower plasmonic coupling whereas a redshift is predicted for face contact due to the stronger coupling.

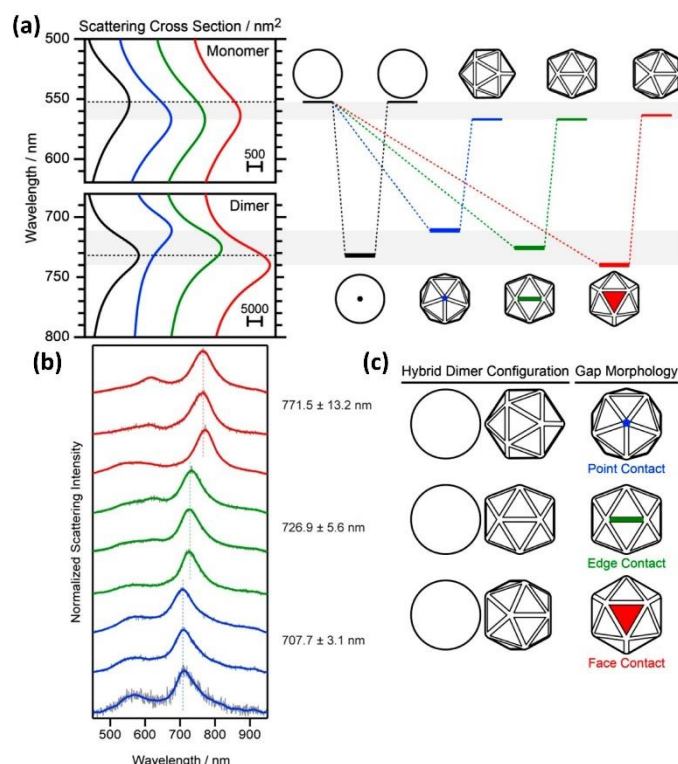


Figure 1.28: (a) Experimental representative dark field scattering spectra of individual hybrid dimers (50 nm AuNS - 50 nm AuNP) of each class. The three classes were defined according to the position of the LBDP mode on the scattering spectra. The point-contact class, in blue, comprising the dimers for which the LBDP is located at 707.7 ± 3.1 nm; the edge-contact class, in green, comprising the dimers for which the LBDP is located at 726.9 ± 5.6 nm; the face-contact class, in red, comprising the dimers for which the LBDP is located 771.5 ± 13.2 nm. (b) Simulated spectra by the FDTD method of ideal and hybrid dimers and their corresponding plasmon hybridization diagram. The results for the ideal dimers are in black, those for the hybrid dimers are respectively in blue (point contact), green (edge contact), and red (face contact). (c) Scheme of the three hybrid dimers configurations: point contact (blue), edge contact (green), face contact (red). Adapted from¹⁰⁴.

All 62 experimentally measured (by DF microscopy) scattering spectra of hybrid dimers could be associated to a gap morphology based on the position of the peak corresponding to the LBDP coupling mode (see Figure 1.28). For the face contact case, which is the one involving

the strongest plasmonic coupling and thus for which a redshift was expected, all the dimers with a LBDP band at 771.5 ± 13.2 nm were assigned to it. For the edge contact case, which is a case involving a weaker coupling than the ideal case and thus for which a small blueshift was expected, all the dimers with a LBDP band at 726.9 ± 5.6 nm were assigned to it. Finally, for the point contact case, which is the case with the weakest coupling compared to the ideal case and thus for which a large blueshift was expected, all the dimers with a LBDP band at 707.7 ± 3.1 nm were assigned to it. They verified that the blue-shift trends were not caused by monodispersity variations with respect to both the size and the sphericity of the dimer's AuNPs or by the choice of the stabilizing agent on the surface of the AuNPs.

It was also stressed out by Schumacher et al.⁷² that the position of the peak corresponding to the LBDP for nonideal dimers (comprising the same gap distance because bound by the same linker molecule but made of faceted AuNPs) varies in the order of magnitude of tens of nanometers due to the many possible configurations of the crystal facets in the gap (different gap morphologies).

4 - Measurement of a dimer's gap distance: plasmon ruler equation (PRE)

The redshift of the longitudinal mode (LBDP) provides a true measure of the distance between the nanoparticles (gap distances) and of the resultant field enhancement factor since the magnitude of the plasmon shift induced by the dimerization depends on the strength of the interparticle coupling, which itself depends on the interparticular distance^{67,106}. Jain et al.⁶⁷ studied the localized surface plasmon resonances (scattering spectra) in lithographically fabricated gold nanodisc pairs (with a diameter of 88 nm and a thickness of 25 nm) on quartz substrates with different interparticle distances (212, 27, 17, 12, 7, and 2 nm) using microabsorption spectroscopy and electrodynamic simulations. They evidenced the polarization dependence of the plasmon coupling as well as the quasi-exponential decay of the plasmonic shift with interparticle gap for polarization along the interparticle axis. More importantly, they demonstrated the universal scaling of the distance decay of plasmon coupling. Indeed, the authors showed, with both DDA simulations and experimental results (theirs and that of other groups) that the fractional plasmon wavelength shift (the ratio of shift and the wavelength of the LSPR peak of a single AuND) for polarization along the interparticle axis decays nearly exponentially with the interparticle gap with a decay length that is roughly about 0.2 in units of the particle size. Indeed, by plotting the fractional plasmon shift obtained for all the systems with different particle size for different nanoparticle size (see Figure 1.29), shape,

metal type, or medium dielectric constant (these parameters only influencing the amplitude of the fractional shift) versus the scaled gap distance (the ratio of the gap distance and the AuND diameter), they always found the same value of the decay length⁶⁷.

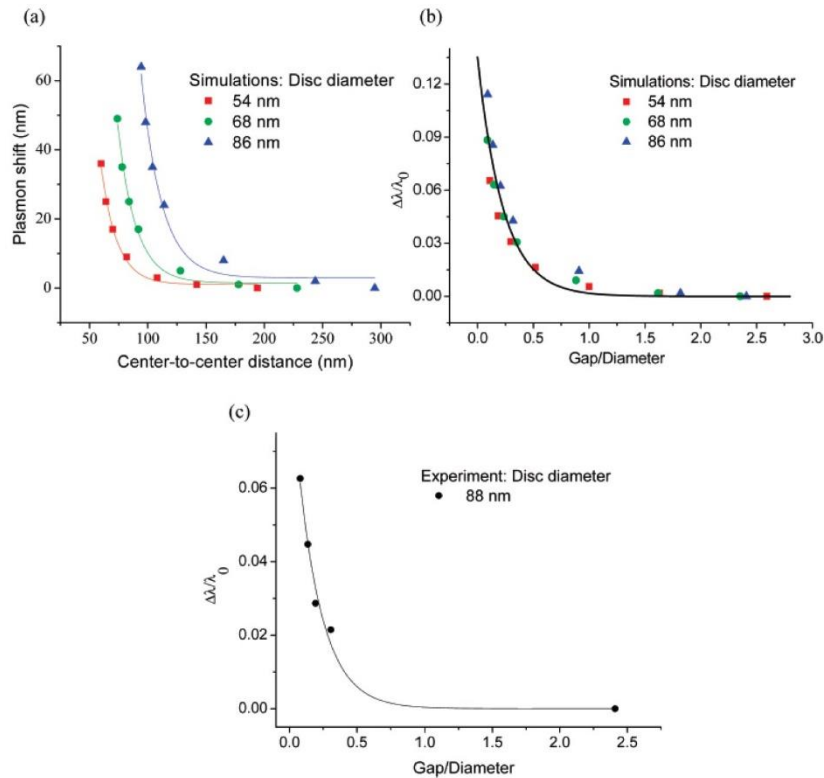


Figure 1.29: (a) Simulated plasmon shift vs the center-to-center distance in an Au disc dimer for different disc diameters and their least-squares fits to single-exponential decay function $y = y_0 + a \cdot e^{-x/l}$. The decay lengths l extracted from the fit are respectively 13.7, 15.5, and 17.7 nm for nanodisc of respective diameter $D = 54, 68,$ and 86 nm. b) Simulated fractional plasmon shift vs the ratio of interparticle gap to nanodisc diameter for discs with various diameters which all follow the same trend and were all fitted by a single-exponential decays (solid curves) of equation $y = a \cdot e^{-x/\tau}$ with $a = 0.14 \pm 0.01$ and $\tau = 0.23 \pm 0.03$. (c) Experimental fractional plasmon shift measured for an 88 nm diameter disc in function of the ratio of gap to diameter and its exponential fit (solid curve) with $a = 0.10 \pm 0.01$ and $\tau = 0.18 \pm 0.02$. Adapted from⁶⁷.

They qualitatively explained the quasi-exponential distance decay, the polarization dependence, and the universal scaling behavior (indicated by the decay constant τ) of interparticle plasmon coupling with a dipolar-coupling model. It results of a combination of two factors: the dependence of the single-particle polarizability on the cubic power of the particle dimension ($\alpha \propto D^3$) and the decay of the plasmonic near-field as the cubic power of the inverse distance between the NPs ($I_d \propto 1/d^3$).

Kreibig and Vollmer's dipolar coupling model explains interparticle plasmon coupling effects. The dipolar near field of a plasmonic particle decays in $1/d^3$, the plasmon coupling strength therefore becomes a function of d^{-3} , exhibiting a quasi-exponential decay. The polarization dependence is explained by the orientation dependence of the near field. The size-scaling law comes from the fact that the fractional plasmon shift ($\Delta\lambda/\lambda_0$) corresponds to the strength of the interparticle electromagnetic coupling relative to the intraparticle plasmonic restoring potential. The interparticle dipolar coupling potential decays with center-to-center distance as d^{-3} whilst the intraparticle restoring potential, corresponding to the inverse of the dipole polarizability, is inversely proportional to the volume (D^3). Consequently, $\Delta\lambda/\lambda_0$ depends on $(d/D)^{-3}$ or $(s/(D + 1))^{-3}$ and since the plasmonic coupling strength depends on both the separation s and diameter D to the power -3 , the function can be dimensionally scaled explaining its validity for dimers made of NPs of different sizes but also metal type and in different media since the fractional shift only depends on $(s/D+1)^{-3}$.

From this universal scaling behavior, they derived an empirical plasmon ruler equation (PRE) which allows to calculate an estimation of the gap distance between the nanoparticles of a dimer using the experimentally measured value of the spectral plasmon shift (redshift of the peak corresponding to the LBDP mode):

$$\frac{\Delta\lambda}{\lambda_0} \approx 0.18 \exp\left(\frac{\left(\frac{-s}{D}\right)}{0.23}\right) \quad (1.16)$$

Which is more convenient to rewrite as:

$$\Delta\lambda \approx 0.18 \exp\left(\frac{\left(\frac{-s}{D}\right)}{0.23}\right) \cdot \lambda_0 \quad (1.17)$$

With $\Delta\lambda$ the plasmon shift, λ_0 the single particle plasmon wavelength maximum, s the inter particle separation, and D the diameter of the nanoparticle.

This scaling law has been verified many times through various experimental^{108,112} and theoretical studies¹⁰³. For examples, Dickreuter et al.¹⁰⁸ recently confirmed that the redshift of the LBDP mode increases with the decrease of the gap distance (and thus the increase of the plasmonic coupling) and evolves following the trend predicted by the universal scaling law. They fabricated dimers of spherical 90 nm AuNPs with different gap distances from 35 to 4.3 nm (measured by SEM) by e-beam lithography and characterized them individually by dark

field spectroscopy. All the spectra were recorded with the incident light polarized along the dimer axis. The experimental spectra corresponded well to the spectra they calculated using the MNPBEM Matlab package (BEM simulations). The LBDP becomes increasingly prominent and shifts from 615 nm to 680 nm while the gap width decreases from 35 nm to 4 nm. The resonant wavelengths of the LBDP were plotted versus the relative gap widths $d = s/D$ (s the gap distance and D the diameter, in their case 90 nm), and this plot could be fitted by the plasmon ruler equation.

Conclusion

In this PhD work, we thus attempted to confirm the potential of AuNPs to be used as electrodes to connect diarylethenes and, unlike in the work of Matsuda et al. or Van der Molen et al., without using larger gold electrodes connected to the AuNPs electrodes. We also aimed at further evaluating the potential of AuNPs to be used as a plasmonic antenna to correct the usual switching asymmetry issue of DAEs. It was decided to graft the molecules directly on the AuNPs, unlike what was done in the work of Kobatake's or Murakoshi's group who used DAE-based polymers, to preserve the conductivity of the system keeping in mind that it must be adapted to molecular electronics applications. Furthermore, the assembly of gold nanoparticles dimers was also explored as well as their individual characterization by dark field microscopy coupled to UV-visible spectroscopy. Working at the scale of one or a couple of AuNPs brought us to monitor the functionalization of AuNPs by diarylethene molecules at the single AuNP scale and then, to measure the switching of the DAE molecules at the same which had not been reported before.

Chapter 2: Experimental methods

I - Synthesis, deposition, and grafting procedures

1 - Diarylethene molecules of the present study: C5HT-di-PSAc and Cl-C5HT-PSAc

a - Requirements and main characteristics

Diarylethene molecules that will be designated as C5HT-di-PSAc ($C_{31}H_{28}O_2S_4$, $M_w = 560.8 \text{ g.mol}^{-1}$) and Cl-C5HT-PSAc ($C_{23}H_{21}ClOS_3$, $M_w = 445.1 \text{ g.mol}^{-1}$) were chosen. The structure of their open (colorless) and closed (purple) form is shown in Figure 2.1. Cl-C5HT-PSAc is the asymmetric version of C5HT-PSAc. A photo of a solution of C5HT-di-PSAc in its open and closed form is shown in Figure 2.2 in the Appendix.

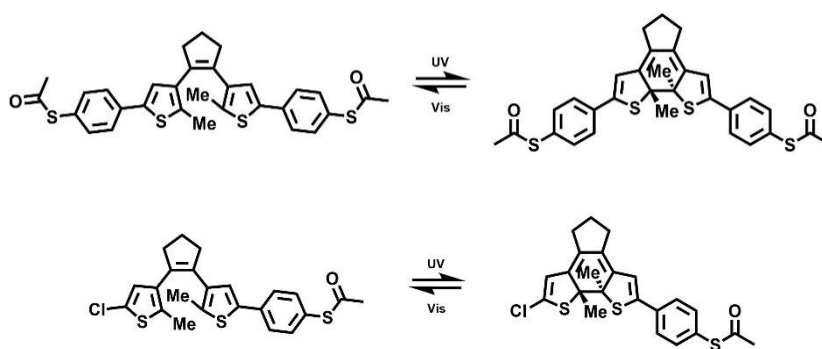


Figure 2.1: Structure of the opened and closed forms of the molecules C5HT-di-PSAc (above) and Cl-C5HT-PSAc (below).



Figure 2.2: Solution of C5HT-di-PSAc at $1.25 \times 10^{-5} \text{ M}$ in DMF before any irradiation so with most of the molecules are in the open state (colorless solution on the left) and after UV irradiation with most of the molecules in the closed state (purple solution on the right).

The choice of the diarylethene molecules for this study was based on three criteria. The first one is the location of the absorbance maximum of the DAEs in the visible (related to the back-switching) which had to correspond to the LSPR absorption maximum of the gold nanoparticles (from 520 to 540 nm according to their size). The absorbance maximum (in solution in DMF) in the visible of C5HT-di-PSAc is at 546 nm while that of Cl-C5HT-PSAc is at 492 nm, so close enough from the plasmon resonance to expect an influence from the antenna effect of the AuNPs. The second criterion regarded the length of the molecular extremities (on both sides of the photochromic unit) which had to be sufficient to ensure electronic decoupling with the metallic nanoparticles. The length of C5HT-di-PSAc is 17.50 Å in its closed form and 17.91 Å in its open form (distance S-S), that of Cl-C5HT-PSAc is 13.48 Å in its closed form and 13.86 Å in its open form (distance S-Cl), both distances were calculated using Arguslab.

Finally, the last criterion was to have thiol functions as terminal substituent on the molecular extremities (on both sides of the photochromic unit) to be able to graft the molecules on AuNPs. The DAE molecules are acetyl terminated, it corresponds to their protected form, thiol functions which are sensitive to oxidation and prone to formation of disulfides had to be protected. However, following the deprotection procedure described in (Chapter 2.I.1.d) thiols functions are retrieved and available for grafting on gold.

b - Synthesis

The diarylethene molecules were synthesized by L. Holz (PhD student under the supervision of T. Huhn at the chemistry department of Konstanz university). The purity and structure of the final product was verified by ¹H NMR at Konstanz university.

Both molecules are derived from a parent diarylethene, the bis(chloro)thienylcyclopentene whose synthesis, presented in Figure 2.3, was described by Lucas et al.¹¹⁴. 2-chloro-5-methylthiophene (commercially available molecule) undergoes a Friedel-Crafts acetylation with a 1,5-dicarboxylic dichloride (glutaryl dichloride, with AlCl₃ in CS₂ at 0 °C), the resulting molecule is a 1,5-diaryl-1,5-diketone (98% yield). This diketone undergoes a (ring closing) McMurry reaction with TiCl₃(THF)₃ or TiCl₄(THF)₃ and Zn in THF at 40 °C which is responsible for the formation of the central cyclopentene ring. This McMurry reaction is carried out in two consecutive steps in a “one-pot” procedure. The parent dithienylethene i.e., the bis(chloro)thienylcyclopentene is obtained with a 50% yield.

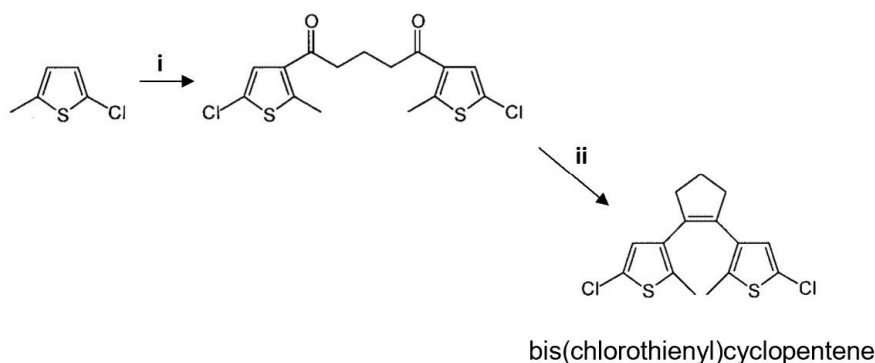


Figure 2.3: Synthesis of bis(chlorothieryl)cyclopentene (parent DAE). i) glutaryl dichloride, AlCl_3 , CS_2 , 98%; ii) Zn , $\text{TiCl}_3(\text{THF})_3$, THF, 50%. Adapted from ¹¹⁴.

The chloro terminal substituents it possesses at the 5-position of the thiophene rings make it easy to functionalize symmetrically or unsymmetrically. The synthesis of our two molecules from this parent DAE, presented in Figure 2.4, are described in the publication of Lucas et al. (group of B. Feringa)¹¹⁴ for the exchange reaction and the treatment with tributylborate and in the publication of Browne et al.¹¹⁵ for the Suzuki coupling and the acetylation.

The parent DAE underwent a chlorine/lithium exchange, it was lithiated with $n\text{BuLi}$ in THF at room temperature and treated with $\text{B}(\text{O}i\text{Bu})_3$ yielding the bis(boronic ester) **A**. The compound **C** (45% yield) was obtained by Suzuki coupling of **A** with 1-bromo-4-*tert*-butylthiobenzene (**B**). The last step to obtain the final compound with a 29 % yield is the substitution of the *t*Bu groups by acetyl groups (acetylation). This symmetric DAE molecule is *S,S'*-((cyclopent-1-ene-1,2-diylbis(5-methylthiophene-4,2-diyl))-bis(4,1-phenylene)) diethanethioate, in all the manuscript it will be designated as C5HT-di-PSAc.

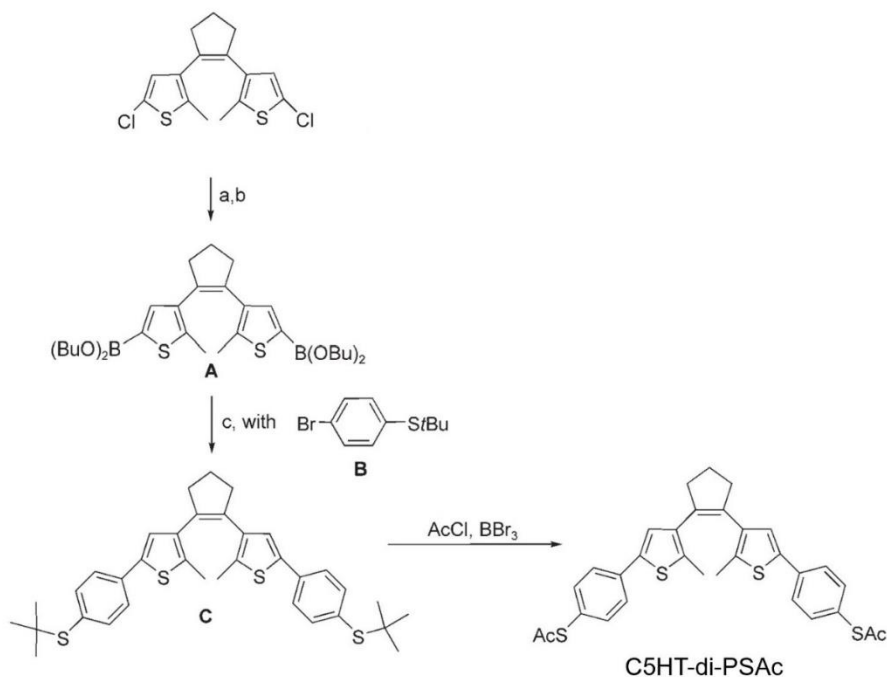


Figure 2.4: Synthesis of C5HT-di-PSAc. a) $n\text{BuLi}$, THF, 298 K; b) $\text{B}(\text{OBu})_3$, THF, 298 K; c) ArBr , $[\text{Pd}(\text{PPh}_3)_4]$, 2M aqueous Na_2CO_3 , ethylene glycol, THF, reflux. Adapted from ¹¹⁵.

The asymmetric version of this molecule (on which a chlorine atom at the 5-position of the thiophene ring remains) is obtained (with an unspecified yield) by introducing a modification during the chlorine/lithium exchange, the dose of $n\text{BuLi}$ was reduced, 1 equivalent is used (for the symmetric molecule, the dose of $n\text{BuLi}$ was 2.1 times superior to that of bis(chloro)thienylcyclopentene). The following reactions are the same than for the symmetric compound (C5HT-di-PSAc). This asymmetric molecule (obtained with an unspecified yield) is *S*-(4-(4-(2-(5-chloro-2-methylthiophen-3-yl)cyclopent-1-en-1-yl)-5-methylthiophen-2-yl)phenyl) ethanethioate, it will be designated as Cl-C5HT-PSAc in all the manuscript.

c - Deprotection

A diluted solution of acetyl-protected DAE in ethanol or dimethylformamide (DMF) was put in a 2-necks round-bottom flask. Note that before dilution, highly concentrated solutions of DAE have the usual yellow/orange color¹¹⁶. After dilution the solution is colorless and upon deprotection it turns light yellow (see Figure A.2.1 in the Appendix).

10 mL of ammonia were poured in a round-bottom flask sealed with a rubber septum with a narrow plastic tube inserted in it. At the other end of this plastic tube a 1 mL syringe (plunger removed) filled with a small piece of cotton and approximately 0.8 mL of anhydrous

sodium sulfate (this Na_2SO_4 helps to dry the stream of wet ammonia) is connected via a needle to the round-bottom flask containing the DAE solution (the needle must be immersed in the solution). A photo of the setup is shown in the Appendix (see Figure A.2.2).

A syringe from which the handles were cut off is inserted in a flexible plastic tube which is connected to a Schlenk line itself connected to a N_2 tank. This tube is connected to the round-bottom flask containing the ammonia via the syringe bearing a needle.

A gentle stream of ammonia and nitrogen was passed through the solution for 15 minutes. A solution of deprotected molecule is obtained.

d - Storage

The solids of C5HT-di-PSAc and Cl-C5HT-PSAc (protected molecules) as received from L. Holz were stored in the dark (fridge), so were the solutions prepared from these solids.

However, solutions of C5HT-di-PSH and Cl-C5HT-PSH (deprotected molecules) which are prone to oxidation and disulfide formation are not stored, they are prepared just before use and preserved from air exposure (handled in round-bottom flask connected to a balloon filled with nitrogen).

2 - Gold nanoparticles: synthesis and deposition

a - Synthesis of 19 nm Turkevich gold nanoparticles

A modified (by Y. Prado, chemical engineer at INSP) Turkevich-Frens protocol^{117–120} was used.

All glassware has been washed with aqua regia (HNO_3/HCl), then strongly washed with demineralized water (18 M Ω) and let in water bath overnight.

In a 100 mL three neck flask, equipped with a condenser and a temperature controller, 492 μl of a 25 mM HAuCl_4 ($\text{HAuCl}_4 \cdot \text{H}_2\text{O}$, Sigma-Aldrich, St. Louis, MO, USA, 50% Au basis) aqueous solution (0.0123 mmol) diluted with 56 mL of milliQ water was heated with a heating plate.

Once boiling appeared, under vigorous stirring, 200 μ l of a 0.34 M (0.068 mmol) citrate solution (SC, Fluka, >99.0%) was injected. We thus have citrate/Au = 5.5.

At t = 1 min after the injection, the solution turns light purple; then, at t = 5 min, the color turns red. At t = 10 min, the heating was stopped, and the solution slowly cooled down at room temperature for up to 20 minutes.

b - Synthesis of 28 and/to 51 nm Bastús gold nanoparticles

A modified (by Y. Prado, chemical engineer at INSP) protocol from N. G. Bastús et al.¹²¹ was used.

All glassware has been washed with aqua regia (HNO_3/HCl) then strongly washed with demineralized water and let in water bath overnight.

Mother solutions

Sodium citrate solution at 0.34 M : 50 mg SC in 0.5 ml milliQ water

Sodium citrate solution at 3 mM : 70 mg SC in 80 ml milliQ water

Seed particles

A/ In a 100 mL three neck flask, equipped with a condenser and a temperature controller, 492 μ l of a 25 mM HAuCl_4 aqueous solution (0.0123 mmol) diluted with 56 mL of milliQ water was heated with a heating plate.

Once boiling appeared, under vigorous stirring, 200 μ l of the 0.34 M SC (0.068 mmol, citrate/Au = 5.5) was injected.

After the color of the solution turned red, the heating was stopped, and the solution slowly cooled down at room temperature.

Seeded growth: from 19 to 28 (B), 35 (C), 43 (D), 51 (E) nm

B/ In a 100 mL three neck flask, equipped with a condenser and a temperature controller containing 28 mL of the seed solution, at 90°C, 0.25 mL of a 25 mM HAuCl_4 solution (0.00625

mmol) was injected, followed by another addition of 0.25 mL of a 25 mM HAuCl₄ solution (0.00625 mmol) 30 min later.

After 30 min, 10 mL of the dispersion were extracted, and the remainder solution was diluted by adding 10 mL of a 3 mM solution of sodium citrate.

C/ In the same vessel containing diluted B solution, at 90°C, 0.25 mL of a 25 mM HAuCl₄ solution (0.00625 mmol) was injected, followed by another addition of 0.25 mL of a 25 mM HAuCl₄ solution (0.00625 mmol) 30 min later.

After 30 min, 10 mL of the dispersion were extracted, and the remainder solution was diluted by adding 10 mL of a 3 mM solution of sodium citrate.

D/Same as C/.

E/ In the same vessel containing diluted B solution, at 90°C, 0.25 mL of a 25 mM HAuCl₄ solution (0.00625 mmol) was injected. The sample was not diluted. The heating was stopped, and the solution slowly cooled down at room temperature.

The size of the AuNPs from each batch was determined from its UV-visible spectrum according to the method of Haiss et al.¹²² (based on the characteristics of the LSPR peak), and from TEM images via an analysis with image J (see Table 2.1). In the tables, the size given will be the aimed one in order to not create confusion about the type of AuNPs used. The size measured with any of the techniques is larger than the expected one indicating that the AuNPs grew more than they should have during the synthesis. Furthermore, several elements could explain the different result obtained with the two techniques. First, although TEM measurements are the ones commonly used and trusted, this technique does not take into account the layer of surfactant molecules present around the AuNPs, the method of Haiss et al. does. Second, measuring the size of AuNPs in the size range that we are using on TEM image is delicate since the AuNPs are not perfectly spherical. Finally, the method of Haiss et al. is very sensitive to the aggregation of the AuNPs that makes the LSPR peak redshift to higher wavelengths explaining the larger sizes sometimes obtained with this method. All these reasons indicate that the size cannot be determined with more precision than 3 nm, confirming the choice to use the aimed size.

An illustration showing spectra of 28 and 50 nm AuNPs, their TEM image and the typical red solution is given in Figure 2.5.

Table 2.1: Batches of AuNPs synthesized and used for the studies, sizes calculated using TEM images and the method of Haiss et al.¹²².

AuNPs	Aimed size (nm) (Bastús)	Size (nm) (Haiss method)	Size (nm) (TEM)
YPOP45B	28	30	25
YPOP45C	35	47.5	33
AD05B	28	24	29
YPOP46B	28	30	/
YPOP49B	28	35	27.5
YPOP57B	28	28	29
YPOP57E	51	50	60

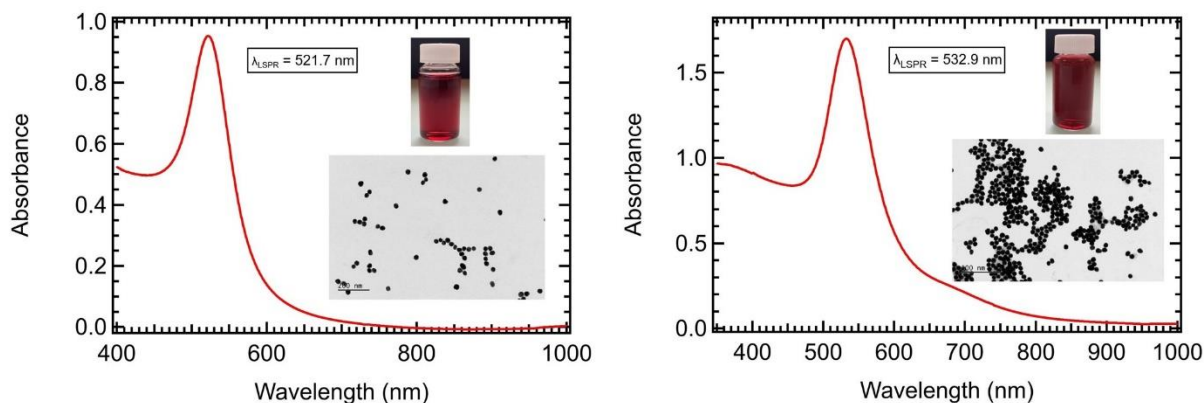


Figure 2.5: UV-visible spectrum, TEM image and photo of the red solution obtained for 28 nm AuNPs (YPOP49B) and 50 nm AuNPs (YPOP57E).

c - An important parameter: the surfactant

The surfactant present at the surface of the gold nanoparticles we are using is citrate. Since it is very labile, it is adapted to our use of the AuNPs i.e. covalently graft molecules on them. Citrates are easily replaced by thiol-terminated molecules that will form Au-S bonds with the gold nanoparticle¹²³. The formation of this type of bond is highly favored due to the strong affinity between gold and thiol functions.

d - Deposition of gold nanoparticles on an indium-tin oxide (ITO) substrate

The deposition was made differently according to the type of samples prepared. The deposition protocol was inspired by that of Cha et al.¹²⁴ for the deposition of AuNPs on glass.

30 Ohms ITO substrates (YSUB/ITOSOL30/1, 20 x 10 mm, 30 Ohms from SOLEM) were used. They are a piece of glass (thickness = 1.1 mm in our case) with an ITO coating on it (thickness = 80 nm in our case). It is a transparent and conductive substrate with a sheet resistance $R_s = 25 - 35$ ohms and a total light transmission of 82-86 % in the visible range. It was chosen for both its conductivity and optical transparency. Regarding the size of the AuNPs, the use of AuNPs with a larger size than 20 nm allows to limit the number of AuNPs aggregates present on the ITO substrate after the deposition.

AuNPs deposition protocol 1

For part of the samples presented in Table 2.3 and Table 2.4 corresponding to the results of Chapter 5.I (Adsorption of Cl-C5HT-PSH and C5HT-di-PSH on 28 nm gold AuNPs deposited on ITO: stepwise UV-visible microscopy monitoring):

ITO substrates are cleaned: they are washed a first time with acetone (VWR, Normapur) (the substrates are put in a beaker with acetone which is placed in the sonicator for 3 minutes). The substrates are then rinsed with ethanol (VWR, Normapur) and put in a beaker with ethanol which is placed in the sonicator for 3 minutes. This last step is repeated a second time.

The substrates are dried with the nitrogen gun and then immersed in an ethanolic 1% APTES (3-Mercaptopropyl)trimethoxysilane, 95%, Sigma-Aldrich) solution: 0.1 mL of APTES in 10 mL of absolute ethanol (VWR, Normapur) for 30 minutes.

The substrates are then rinsed with ethanol and put in a beaker with ethanol which is placed in the sonicator for 3 minutes. This step is repeated 2 times (3 washes total).

The substrates are dried with the nitrogen gun and then put on a Petri dish which is placed in a laboratory oven (air oven) at a fixed temperature for a given time (see column 2 of Table 2.3 and Table 2.4). The gold nanoparticles solution must be taken out of the refrigerator at least 10 minutes before the end of the 3 hours so it warms up to room temperature. Once the substrates are taken out of the laboratory oven, the Petri dish is left a few minutes on the laboratory bench, so the substrates cool down to room temperature.

The sample is immersed in a beaker containing either 25 nm or 35 nm (see Table 2.3 and Table 2.4) gold nanoparticles solution for 1 hour (except for one sample, see Table 2.3) and

then rinsed with deionized water and dried with a nitrogen gun. After AuNPs deposition, the samples have a typical reddish color (see Figure A2.3 in the Appendix).

AuNPs deposition protocol 2

For a part of the samples presented in Table 2.5 corresponding to the results of Chapter 5.II (Adsorption of C5HT-di-PSH on 25 nm AuNPs deposited on ITO: in situ UV-visible spectroscopy monitoring):

ITO substrates are cut so that they can fit in the custom sample holder built in Konstanz University (shown in Figure A.2.3 in the Appendix). This sample holder fits in the spectrophotometer cuvette used for this experiment (QS high-precision cell 100-10-40 from Hellma). It is a hollow rectangle in stainless steel with two pads in Teflon, one with a notch to fit in the lower extremity of the sample, one held by a screw that can be loosened and rotated the time to insert the sample and then tightened again once it is in place. Its length is 8 mm shorter than that of the cuvette (45 mm) so that a stirring bar can be used.

Then the steps are the same as those described above in AuNPs deposition protocol 1, it is however important to note that for the fabrication of these sample, only 28 nm gold nanoparticles were used. After AuNPs deposition, the samples have a typical reddish color (see Figure A2.3 in the Appendix).

AuNPs deposition protocol 3

For part of the samples presented in Table 2.2 (ADITOR and ADITO 80) Table 2.3 (ADITO81) and Table 2.4 (ADITO82) corresponding to the results of Chapter 6.

The steps are the same as for AuNPs deposition protocol 1 except for the second to last step. Indeed, to get a lower density and to ensure that only one face of the substrate is covered with nanoparticles, a drop-casting of the gold nanoparticles is made on the substrate. A few drops are deposited on the substrates and left for a few minutes according to the desired density (see column 4 of Table 2.2). The sample is then rinsed with deionized water and dried with a nitrogen gun.

The samples ITO/AuNPs that did not undergo subsequent treatment are presented in Table 2.2.

Table 2.2: Samples ITO/AuNPs prepared following the different AuNPs deposition protocols.

Sample	Baking	AuNPs	AuNPs deposition
ADITO55	120 °C - 1 h	YPOP45B 28 nm	Immersion 1 h
ADITO56	120 °C - 1 h	YPOP45C 35 nm	Immersion 1 h
ADITO62	120 °C - 1h 30	YPOP46B 28 nm	Immersion 1 h
ADITOC	120 °C - 3 h	YPOP57B 28 nm	Immersion 30 min
ADITOR	120 °C - 3 h 20	YPOP57E 51 nm	Dropcasting 1 min
ADITO80	120 °C - 1 h 30	YPOP57E 51 nm YPOP57B 28 nm	Dropcasting 3min Dropcasting 15 min

3 - Grafting of the DAE molecules on AuNPs deposited on an ITO substrate

a - DAE grafting protocol 1 (samples of chapter 5.I and 6)

Some sample went through a masked desilanization step (see Table 2.3 and Table 2.4). All amine functional groups were removed from the ITO surface except for those binding the AuNPs. The AuNP-adsorbed ITO substrate was immersed in a NaOH solution (concentration indicated in Table 2.3 and Table 2.4) for 1 to 4 hours (see Table 2.3 and Table 2.4). The desilanization step was inspired by the dimer fabrication protocol of Cha et al.¹²⁴. This step is supposed to prevent AuNPs from a second deposition to place themselves on the surface around the AuNPs already present. Instead, the attachment of the AuNPs from the second deposition to thiol-terminated molecules grafted on the AuNPs from the first deposition is favored.

The DAE solution is deprotected according to the procedure described in Chapter 2.I.1.c. The ITO substrate coated with AuNPs is inserted in the 2-necks round-bottom flask containing the deprotected DAE solution (-SH) under a strong nitrogen flow to prevent air to enter the flask (we remind that the deprotected solution is extremely sensitive to air).

A balloon filled with nitrogen is finally placed on one of the flask's necks to ensure a nitrogen overpressure throughout the experiment. The concentration of the DAE solution and

the immersion time of the ITO/AuNPs substrate in this deprotected solution were not always the same. They are reported in Table 2.3 and Table 2.4 for each sample.

After the functionalization of the AuNPs took place, the samples are no longer sensitive to air (the -SH is now a -S-Au), they are taken out of the flask, rinsed with ethanol and dried with the nitrogen gun. The setup used for this grafting protocol is shown in Figure A.2.2 in the Appendix.

Table 2.3: Samples ITO/AuNPs/Cl-C5HT-PSH prepared following DAE grafting protocol 1.

Sample	Baking	Desilanization	AuNPs	AuNPs deposition	DAE (Cl-C5HT-PSH) in EtOH
ADITO46	120 °C - 1 h	NaOH 0.8 mM - 1 h	YPOP45B 28 nm	Immersion 1 h	6.36×10^{-4} M 15 h
ADITO47	120 °C - 1 h	NaOH 0.8 mM - 1 h	YPOP45C 35 nm	Immersion 1 h	6.36×10^{-4} M 15 h
ADITO48	120 °C - 1 h	NaOH 0.8 mM - 1 h	YPOP45C 35 nm	Immersion 1 h	6.36×10^{-4} M 15 h
ADITO49	120 °C - 1 h	NaOH 0.8 mM - 1 h	YPOP45B 28 nm	Immersion 1 h	3.21×10^{-4} M 3 h
ADITO60	120 °C - 1 h	None	YPOP45B 28 nm	Immersion 1 h	6.38×10^{-4} M 4 h
ADITO61	120 °C - 1 h	None	YPOP45B 28 nm	Immersion 1 h	6.38×10^{-4} M 8 h
ADITO69	140 °C - 1h 30	NaOH 1.8 mM - 4 h	AD05B 28 nm	Immersion 20 min	4.0×10^{-4} M 15 h 20
ADITO81	120 °C - 1 h 30	None	YPOP57E 51 nm	Dropcasting 3 min	1.0×10^{-3} M 17 h

Some of the samples require additional comments, for ADITO46, the septum popped out during the night, leading to the evaporation of the solution in the round-bottom flask and probable crystallization of the molecules on the surface.

Regarding ADITO60 and ADITO61, the deprotection of the DAE solution was done differently, by adding a few drops of ammonia^{11,125} directly in the solution (see Figure A.2.1 in the Appendix).

Table 2.4: Samples ITO/AuNPs/C5HT-di-PSH prepared following DAE grafting protocol 1.

Sample	Baking	Desilanization	AuNPs	AuNPs deposition	DAE (C5HT-di-PSH) in EtOH
ADITO64	120 °C - 3 h	NaOH 1.8 mM - 3 h 30	YPOP46B 28 nm	Immersion 1 h	5.78×10^{-4} M 14 h 55
ADITОВI	120 °C - 3 h	NaOH 1.8 mM - 4 h	YPOP46B 28 nm	Immersion 1 h	5.78×10^{-4} M 15 h 10
ADITO82	120 °C - 1 h 30	None	YPOP57E 51 nm	Dropcasting 3 min	1.0×10^{-3} M 17 h

For ADITO64 and ADITОВI, the solution was murky at the end so either some air entered the round-bottom flask or formation disulfide spontaneously occurred.

b - DAE grafting protocol 2 (samples of chapter 5.II)

A pristine ITO substrate (that will be used as a reference) cut to fit in the custom sample holder and the aforementioned sample holder are cleaned with acetone and extensively rinsed with DMF. The pristine ITO substrate is put in the sample holder with the conductive face facing the exterior. The assemblage of both is re rinsed with DMF and then inserted inside the cuvette containing 2 mL of DMF and a stirring bar. DMF was chosen to avoid evaporation issues. The baseline is recorded without stirring on the Jasco V-750 spectrophotometer.

Stabilization phase

The ITO substrate coated with 25 nm AuNPs is rinsed with DMF and put in the sample holder, the assemblage is rinsed with DMF and inserted in the cuvette containing 2 mL of DMF and the stirring bar. The cuvette is placed in the spectrophotometer and the stirring is switched on (500 rpm). The acquisition of UV-visible spectra is launched in automatic mode for 4 to 6h (one try was made over a full night, see Table 2.5). A series of spectra is obtained for which, at the end of the measurements, the LSPR peak wavelength has stabilized around a value.

Adsorption phase

About an hour before the end of the stabilization phase, the DAE solution is prepared and deprotected (following the procedure described in Chapter 2.I.1.c), control experiments were made without deprotecting the solution though. 0.5 mL of the solution are collected in a syringe. The sample holder is removed from the cuvette, the solution is injected in the cuvette,

after 10 s during which the solution is homogenized (we are still under 500 rpm stirring), the sample holder is put back in the cuvette and a timer is started. The acquisition of UV-visible spectra in automatic mode is launched as fast as possible for at least 15 hours.

Data treatment

A unique .csv file containing all the spectra and the times of the experiment at which they were recorded is obtained. On the one hand, this file is treated with a python program that cuts it in smaller files containing each 200 spectra with the data organized differently so that the format of our spectra obtained from a Jasco spectrophotometer correspond to the output format of a Cary 60 spectrophotometer. This Cary 60 was used by a colleague in Konstanz University who wrote the Matlab procedure used in the next step of the data treatment to fit the LSPR peak on each spectrum. On the other hand, the values of recording time of the spectra are extracted by groups of 200 values (corresponding to the 200 spectra of each smaller files) and put in time files, these time files are required to run the Matlab script for the fitting of the LSPR peaks.

Each shorter file containing 200 spectra (the Matlab procedure crashes when used a file containing too many spectra) is treated by a Matlab script written by L. Ruf (PhD student at Konstanz University). This script is based on the nonlinear least-squares curvefitting tool (lsq-curvefit) of Matlab 2020b. It allows to fit the LSPR peak (in my case in the 500 – 575 nm static fitting range) of each spectrum, the uncertainty on the fit of λ_{LSPR} is around 0.1 nm. Files (.txt) are created (still with Matlab) containing the values of λ_{LSPR} and of the absorbance at λ_{LSPR} . These files are concatenated as well as the time files and the absorbance isotherm describing the evolution of λ_{LSPR} vs the time (or absorbance at λ_{LSPR} vs the time) are obtained¹²⁶.

Table 2.5: Samples ITO/AuNPs/DAE prepared following DAE grafting protocol 2.

Sample	AuNPs	DAE molecule*	Concentration of the DAE solution inside the cuvette (μM)	Acquisition time of a spectrum (s)	Time after DAE solution injection (s)
ADITO8	YPOP57B	Control ND	/	23	30
ADITOB	YPOP57B	Control ^D	/	24	30
ADITO1	YPOP57B	C5HT-di-PSAc ND	2.5	33	10
ADITO5	YPOP57B	Cl-C5HT-PSAc ND	2.5	23	20
ADITOC	YPOP57B	C5HT-di-PSH ^D	4	24	30
ADITOD	YPOP49B	C5HT-di-PSH ND	5	24	20
ADITOG	YPOP49B	C5HT-di-PSH ND	5	24	10
ADITOH	YPOP49B	C5HT-di-PSH ND	5	24	13
ADITOI	YPOP49B	C5HT-di-PSH ND	5	24	12

* : ND means the molecules was in solution in non-degassed solvent whereas D means the molecule was in solution in degassed solvent.

Comments (specific to each sample):

ADITOC: A solution of DAE-di-Ac was prepared from a stock solution in dichloromethane with DMF degassed 3 times (according to the pump and thaw procedure described below), it was deprotected before being diluted. During the deprotection, some DAE solution to deprotect went into the syringe linked to the round-bottom flask containing ammonia. The solution went from colorless to yellow, to blue and then green. After dilution, the solution to inject was blue. Some solution was put aside in a vial for analysis, it was left at air for 5 minutes, it turned purple as usually observed after the switching of the molecules. A gas bubble was formed during collection of the solution: 4 mL instead of 5 were in the syringe (the concentration of solution in the cuvette was recalculated). In the end, no condensation inside the cuvette was observed.

After ADITOC, DMF is no longer degassed. A 100 mL stock solution at 3.57×10^{-5} M in DMF of DAE-di-Ac is prepared from a stock solution in dichloromethane. Every dilution is now made from 3.5 mL of this stock solution + 1.5 mL of DMF = 5 mL of DAE-di-Ac solution at 2.5×10^{-5} M that are deprotected. 0.5 mL of the deprotected solution are then collected and injected in the cuvette.

ADITOD: The stabilization phase had to be relaunched, sample was left in the cuvette in the solution (without stirring) for 36h.

ADITOG: A change of color from colorless to yellow and then to blue during the deprotection step was observed. At the moment of injecting, the solution had turned purple. After the end of the experiment, the sample was taken out, rinsed with DMF and dried with the N₂ gun.

ADITOH: The stabilization phase was performed over a whole night. A change of color from colorless to blue during the deprotection step was observed. There was a bug during the recording of the first spectrum, so this spectrum has been discarded from the results. At the end of the experiment, the sample was taken out, rinsed with DMF and dried with the N₂ gun.

ADITOI: A change of color from colorless to yellow then blue during the deprotection step was observed. At the end of the experiment the sample was taken out, rinsed with DMF and dried with the N₂ gun.

Degassing of the solvent

Degassed DMF was obtained by first evacuating 50 mL of DMF (N,N-dimethylformamide RPE – for analysis, ref 444926 from Carlo Erba) under strong stirring (\approx 1000 rpm) at \approx 0.5 mbar for 15 minutes and back-filling the Schlenk Flask with nitrogen. Afterwards a total of 3 freeze-pump-thaw cycles were performed. Freezing at -196° C for 8 min, pumping at \approx 0.5 mbar for 15 min, thawing at air (ambient temperature) for 10 minutes then in a 50° C water bath for 10 min.

II - Instrumentation and setups

1 - UV-visible spectroscopy

a - Principle of the technique and instrumental basics

UV-visible spectroscopy is based on the interaction of light (electromagnetic wave) and electrons from the material to characterize on which the light arrives. This technique can be used to identify, characterize, and quantify (spectrophotometric dosage) chemical species in a non-destructive manner. It can also be used to monitor a chemical transformation. Upon the

interaction of the incident light and the sample transmission, absorption, reflection, and scattering can occur. For absorption to occur, the energy of the photon received must be equal to the energy difference between a molecule's ground and excited state, it triggers an electronic transition. In agreement with Planck equation, the absorption band corresponding to that transition will appear at the wavelength corresponding to the energy difference between the levels ($E = hc/\lambda$)¹²⁷.

An absorption band has 3 main characteristics which are its position (wavelength), its intensity (absorbance) and its width. The position is related to the quantification of the energy levels as described by Bohr's relationship ($h\nu = |E_f - E_i|$), the intensity varies according to how permitted the transition is (according to the selection rules) and the width depends on the energy of the excited level involved in the transition ($E = E_{\text{electronic}} + E_{\text{vibrational}} + E_{\text{rotational}}$). The electronic levels are the main contribution to the absorbance bands, but the latter are broadened by vibrational (up to a few tenth of nm contribution) and rotational sub-levels (up to a few nm contribution). The absorption bands are indicative of the molecular structure of the sample and will shift in wavelength and intensity depending on the molecular interaction and environmental conditions.

An absorption band in the visible represents electronic transitions between atomic orbitals within the same electronic shell whereas an absorption band in the UV range corresponds to electronic transitions between molecular orbitals from two different electronic shells. Transitions between molecular orbitals are depicted by absorption bands in the UV range, however highly π -conjugated molecules (like the closed-ring DAEs) present transitions between their molecular orbitals occurring in the visible, explaining why these molecules are colored.

A UV-Visible spectrophotometer measures the transmittance (T) i.e., the amount of light transmitted through a sample by dividing the intensity of the transmitted light ($I_{(\lambda)}$) by the intensity of the incident light ($I_{0(\lambda)}$).

$$T = I_0 / I_{0(\lambda)} \quad (2.1)$$

The transmittance is linked to the absorbance (A) by the relationship:

$$A = -\log \frac{I_{(\lambda)}}{I_{0(\lambda)}} = -\log T \quad (2.2)$$

Absorbance measurements allow to access the molar absorption coefficient (ϵ_s) of the measured species (s), and to its concentration $[s]$ using Beer-Lambert law:

$$A = \epsilon_s l [s] \quad (2.3)$$

The absorbance (A) and thus the transmittance (T) is simply proportional to the sample's molar absorption coefficient, concentration (ϵ_s), and to the dimension of the cuvette l (defining the pathlength of the light). It is important to note that the molar absorption coefficient is wavelength dependent.

The main parts of the spectrophotometer, schematized in Figure 2.6, are the light source (a deuterium lamp for the UV region from 190 to 350 nm and a halogen lamp for the near UV to the near IR region from 330 and 900 nm), the monochromator, and the detector (a silicon photodiode for the V-730, a photomultiplier tube for the V-750 from Jasco)¹²⁸.

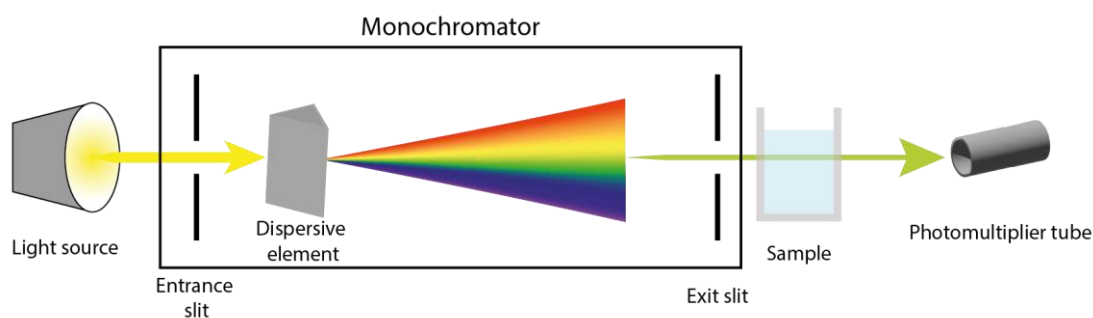


Figure 2.6: Scheme of the main components of a single-beam UV-visible spectrophotometer similar to the Jasco V-750.

The monochromator is composed of an entrance slit, a first mirror, a diffraction grating, a second mirror and an exit slit. Multichromatic light from one of the light sources enters the monochromator by the entrance slit, it is collimated onto the diffraction grating by the first mirror. The diffraction grating, which is rotating, selects discrete wavelengths one after another. The light is then refocused onto the exit slit by the second mirror (adjustments can be made to modify the spectral band width). The light is focused one last time by another series of mirrors and oriented on the sample¹²⁸.

The spectrophotometers that we used can be operated in two types of optical configurations: single and double beam. However, since it was only used in single beam mode, it is the only one that will be explained here. In the single-beam arrangement, the light source,

the monochromator, the sample, and the detector are in series, the transmittance is obtained directly upon detection of the monochromatic light that just passed through the sample. It was used in baseline correction mode so the value of I_0 is determined at the beginning of the measurement by recording a baseline with either the solvent (if working with solutions) or a pristine substrate (if working with substrates).

b - Technical performances of the Jasco V-750

All the tests were performed using the parameters reported in Table 2.6. Pristine ITO samples that will be called T1, T2 and T3 were used as well as sample ADITOC prepared as described in Table 2.2, and before any grafting of DAE took place so in all this part it is a sample ITO/AuNPs(28 nm). T1, T2, T3 and ADITOC are cut substrates since all the tests were performed using the custom sample holder made in Konstanz university in a quartz cuvette (QS high-precision cell 100-10-40 from Hellma).

Table 2.6: Parameters used for all the UV-visible measurements (tests and experiments) performed with the Jasco V-750 spectrophotometer.

Photometric	Abs
Bandwidth	L5.0 nm
Response (time)	0.24 s
Data interval	1.0 nm
Scan speed	1000 nm/min
Number of accumulations	1
Correction	Baseline

A first test was performed without putting anything in the spectrophotometer, it aimed at evaluating the value of the noise and its stability over time. The baseline was recorded immediately after switching on the spectrophotometer, then four spectra were recorded between 400 and 900 nm, an initial one right after the baseline and then one every one hour up to 3 hours. These spectra are shown in Figure 2.7. Since the spectra are superimposable, the average value of the noise can be calculated with the absorbance data of any of them. The initial spectrum was chosen and a value of 1.55×10^{-5} was obtained.

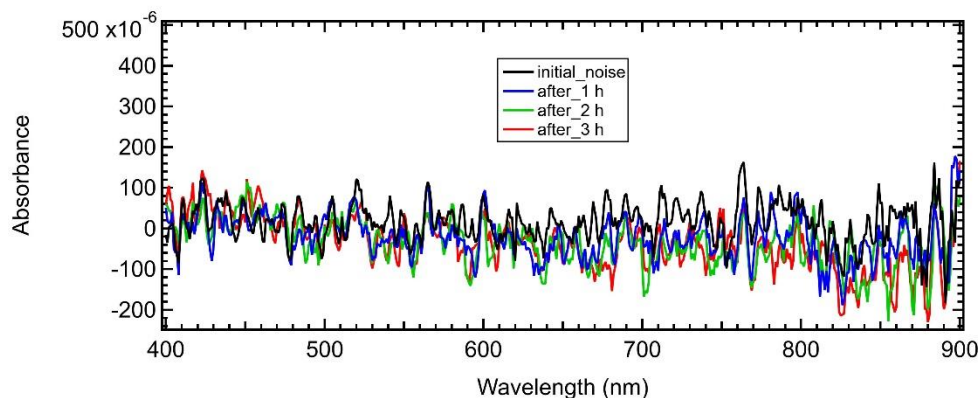


Figure 2.7: Noise and stability over time test (test n°1), UV-visible spectra recorded every hour without putting anything inside the spectrophotometer.

A second test was made to evaluate the signal to noise ratio. Three spectra of an ITO substrate with 28 nm gold nanoparticles deposited on it were recorded in a row (between 400 and 800 nm) after the baseline was recorded with a pristine ITO substrate that will be called T2. These spectra are shown in Figure 2.8, note that the absorption band between 600 nm and 800 nm present on all the spectra comes from aggregates of AuNPs. The fluctuations of the absorbance were calculated by subtracting the second spectrum to the first one (any subtraction between the 3 spectra could be made since they are superimposable). A value of 1.20×10^{-5} was found, it is almost similar to that of the noise calculated above. This test was performed with the baseline recorded with two other pristine ITO substrates respectively T1 and T3 yielding the same result.

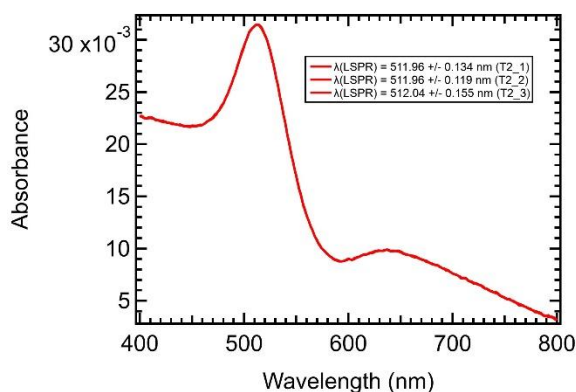


Figure 2.8: Signal to noise ratio test (test n°2) 3 spectra of an ITO substrate with 28 nm gold nanoparticles deposited on it recorded in a row.

A third test, that could be made by plotting the results obtained for the second test differently, consisted in plotting each first spectrum of the three spectra recorded in a row for

the second test on the same graph. The same thing is also done with each second spectra and each third spectra. The difference between the three spectra plotted on each graph is the pristine ITO substrate that was used for the recording of the baseline (either T1, T2 or T3). By looking at these graphs, we can have an idea of the influence on the values of the wavelength and the absorbance of the LSPR peak that recording the baseline with different pristine ITO substrates has. It is important since it has been done for the UV-visible spectra of the samples (they were not all recorded with the same pristine ITO substrate). The results for all the first spectra recorded with the baseline recorded with T1, T2, and T3 respectively are shown in Figure 2.9. This graph was chosen because it is the showing the largest difference regarding the position of the plasmon peak: 0.8 nm (0.39 nm for all the second spectra and 0.5 for all the second spectra). Regarding the largest difference for the absorbance value, it appears for all the third spectra (4.42×10^{-3}), it was of 4.29×10^{-3} for all the first spectra and of 4.34×10^{-3} .

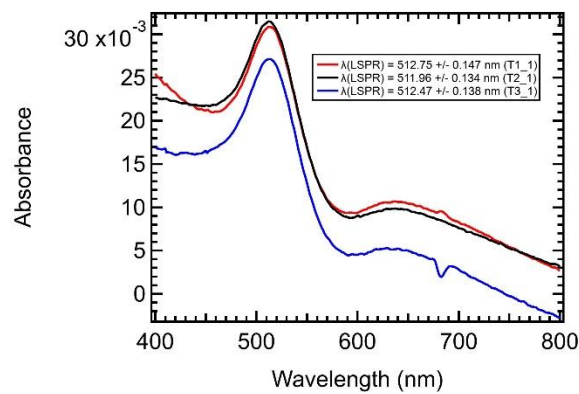


Figure 2.9: Influence of recording the baseline with different pristine ITO substrate test (test n°3). First spectra recorded during test n°2 with the baseline recorded with T1, T2, and T3 respectively.

A fourth test was carried out to evaluate the stability in time of the wavelength and absorbance values of the plasmon peak. Nine spectra of an ITO substrate with 28 nm AuNPs deposited on it were recorded every 15 minutes (between 400 and 800 nm). All the spectra were fitted with a Lorentzian between 500 and 525 nm, the values of λ_{LSPR} and absorbance at λ_{LSPR} were extracted from these fits. Both series of values were plotted versus the time as can be seen in Figure 2.10. The difference between the maximum and minimum values of the wavelength and absorbance respectively of the LSPR peak was calculated. It is of 0.5 nm for λ_{LSPR} and of 4.02×10^{-4} for the absorbance at λ_{LSPR} . These two values are of tremendous importance for the interpretation of the results presented in Chapter 5.

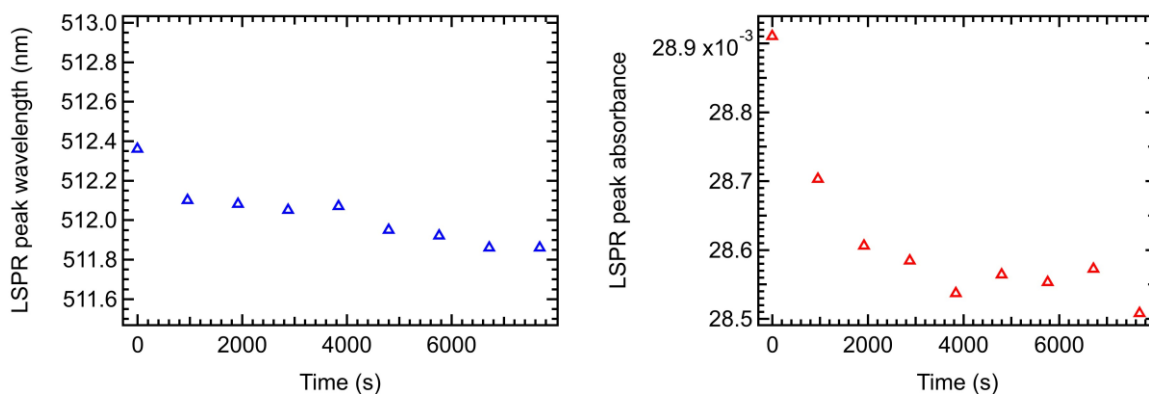


Figure 2.10: Stability in time of the wavelength and absorbance values of the plasmon peak test (test n°4). LSPR peak wavelength and absorbance values of 9 UV-visible spectra of an ITO substrate with 28 nm gold nanoparticles deposited on it recorded every 15 minutes.

A fifth and last test was made, it is related to the in-situ monitoring of the adsorption of the DAE molecules on 28 nm AuNPs deposited on ITO experiments (see Chapter 2.I.3.b for the experimental procedures and Chapter 5.II for the results). A step of the experiment is to lift the sample holder (with the ITO/AuNPs substrate in it) originally plunged in the cuvette containing solvent, and to put it back in after injecting a volume of the DAE solution inside the cuvette. We need to know what influence the repositioning of the sample holder has on the value of λ_{LSPR} that we are monitoring during the whole experiment. The test consisted in recording a spectrum, lifting, and putting back the cuvette and recording a second spectrum. The reproducibility was ensured by repeating the test 3 times and with different baselines recorded either with T1, T2 or T3. The example of the results obtained for the third repetition with the baseline recorded with T3 is shown in Figure 2.11, note that the absorption band between 600 nm and 800 nm present on all the spectra comes from aggregates of AuNPs. It was shown because it is the one showing the largest difference regarding the value of λ_{LSPR} , repositioning induced a shift of 0.24 nm. For the assays with the baseline recorded with T1 it was 0.15 nm, and for those with the baseline recorded with T2 it was 0.12 nm. Regarding the absorbance (it is less important since it is not the monitored parameter but still). For the tries with the baselines recorded with T1 and T2 the spectra before and after repositioning were superimposable (perfectly for T1, quite for T2). For T3, a tangible difference (1.226×10^{-3}) in the absorbance was observed (also visible on Figure 2.11).

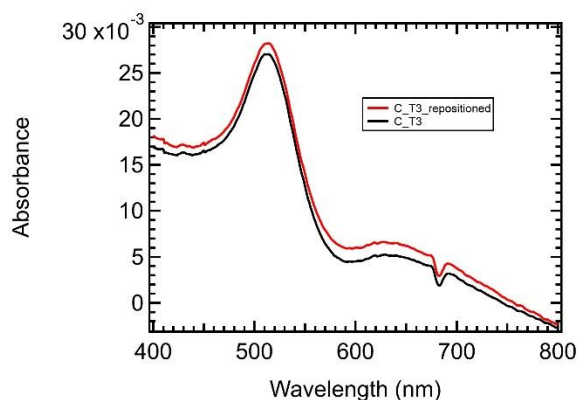


Figure 2.11: Influence of the repositioning of the sample holder test (test n°5). Spectra recorded before and after lifting and putting back the sample holder (with the ITO/AuNPs substrate in it) in the cuvette.

According to Jasco¹²⁹, the accuracy for the measurement of the wavelength is 0.2 nm. Regarding the absorbance it is of 5×10^{-4} . The position and height of the LSPR peak i.e., the values of λ_{LSPR} and absorbance at λ_{LSPR} were extracted by fitting the LSPR peaks with a Lorentzian in Igor Pro. The incertitude on the fit value of λ_{LSPR} was given by Igor Pro whereas the incertitude on the fit value of the absorbance at λ_{LSPR} was calculated with a formula expressing the propagation of uncertainty applied to the uncertainty on the parameters of the fit given by Igor Pro. For ADITOC (the sample used for all the tests), the incertitude on the fit of the LSPR peak was in the interval 0.13 to 0.15 nm for λ_{LSPR} and in the interval 3.9×10^{-3} to 5.1×10^{-3} for the absorbance at λ_{LSPR} .

c - Spectroscopy of molecules in solution

Related to the results presented in Chapter 3

The UV-visible spectra were recorded with a Jasco V-730. A quartz cuvette (QS high-precision cell 100-10-40 from Hellma) was used for all the measurements. The baselines were systematically recorded with the cuvette filled with deionized water before each series of measurements. The LSPR position was evaluated by fitting the peaks with a gaussian function restricted to a wavelength range of 30 nm centered on the maximum. Both the LSPR wavelength and absorbance maximum were extracted. With this approach, the measurement accuracy for the peak wavelength was 0.05 nm.

Saturation experiments consisted in adding a fixed volume of thiol solution (50 μL) of a specific concentration to a fixed volume of AuNPs solution (2 mL) with a fixed

concentration (0.66×10^{-9} mol/L) several times (a new aliquot of the AuNPs solution is used every time the experiment is repeated) by progressively increasing the concentration of the thiol solution until saturation of the AuNPs, materialized by a plateau on the plot of the LSPR peak wavelength versus the thiol quantity in solution, was reached. A spectrum is recorded 15 minutes after the mixing (to make sure the functionalization was fully completed before the acquisition of the spectrum) between 350 and 1000 nm with an acquisition time of 39 s. The stirring was always stopped before the acquisition of a spectrum. In other words, each spectrum corresponds to a fresh mixture of AuNPs and thiol solution of a specific concentration. The thiol concentration of each solution was calculated so that the final concentration in the cuvette after the mix (AuNPs + thiols) reached the following values: 0.13, 0.86, 2.07, 3.66, 4.91, 6.34, 17.68, and 39.01 μ M. Thiol mother solutions were prepared with 2.5 mM of thiol (MUDA or MHDA) and 0.1 M of NaOH in water (the dissolution of thiols in water was facilitated by a slight increase in temperature). The thiol solutions (for each mix) were obtained by dilution of their corresponding mother solution in water.

Kinetics experiments consisted in monitoring the functionalization kinetics of AuNPs in solution after the addition of a thiol solution of a given concentration. The reaction took place and was monitored in situ in the spectrophotometer cuvette after adding 50 μ L of a MUDA solution to 2 mL of AuNPs at 0.66×10^{-9} mol/L. The concentration of MUDA was 0.86 μ M in the final solution (inside the cuvette). UV-visible spectra were recorded successively for 20 min between 490 and 550 nm with an acquisition time of 18 s. No stirring at all was used for this experiment.

Related to the results presented in Chapter 4

The UV-visible spectra were recorded with a Cary 60 set on “medium speed” (600 nm/min), the recording range of the spectra was 230 - 900 nm, the recording duration of a spectrum was 75 s. The resolution in absorbance of the spectrophotometer is 1×10^{-3} . A quartz cuvette (QS high-precision cell 100-10-40 from Hellma) was used, it allows to measure in a very wide wavelength range 200 - 2500 nm. It is important for us since our molecules absorb in the UV. All the measurements were made with approximately 2 mL of a 1.25×10^{-5} M solution in degassed dimethylformamide (DMF) under 600 rpm stirring. DMF is one of the least volatile organic solvents so working with it should prevent evaporation issues, even more since we use it degassed. A stock solution was prepared for each molecule so that all the

experiments were made with the exact same solution. Working with different solutions would involve concentration differences (even small) and therefore absorbance variations.

Photokinetics measurements of the DAE in solution were carried out following the procedure described hereafter. The cuvette and the stirring bar were cleaned with acetone and dried. The stirring bar was placed inside the cuvette and approximately 2 mL of DAE solution were introduced with a glass pipette. The PTFE lid of the cuvette is placed on top of it and wrapped with parafilm to further reduce the possibility of solvent evaporation. The stirring is started. The aliquot of solution to be used was illuminated with visible light (505 nm) for 10 minutes to start with all the molecules in the opened state. The first recorded spectrum (“zero spectrum”, see below) must be checked for the presence of the characteristic absorption band in the visible of the molecules in the opened state. If no band of this kind is present, the visible illumination was efficient, and the measurements can be continued. The experiment parameters (forward current for the LEDs, duration of the irradiation, number of irradiations and eventually number of irradiation cycles for specific cycles measurements) are entered in the python script (written by S. Snegir, post-doc at Konstanz university) controlling the setup (see Chapter 2.II.2.c) and saved. The “zero spectrum” is recorded manually, the shutters (which had been opened manually for the pre-experiment visible irradiation and the recording of the “zero spectrum”) are closed manually before the experiment is launched in automatized mode.

In the end, a .csv file is obtained containing all spectra recorded during an experiment. This file is treated with a Matlab script (written by S. Snegir, post-doc at Konstanz university). The same experiment parameters that were entered in the python script controlling the setup are entered in the Matlab script. The script is then able to retrieve the absorbance value at a specific wavelength (the “monitoring wavelength”) for all the spectra and to plot these absorbance value versus the irradiation time.

d - Spectroscopy of species on a substrate

Related to the results presented in Chapter 5

All the spectra were recorded with the Jasco V-750 using the parameters previously reported in Table 2.6. The wavelength range was the only parameter that varied, it only slightly influences the recording duration of one spectrum, which is not a crucial parameter for the switching measurements.

For the samples of Chapter 5.I, which were made with ITO substrates as received and therefore with dimensions that allowed to put them in the substrate sample holder from Jasco: a substrate of ITO was placed in the sample holder, the conductive face towards the direction from which the beam arrives. It was used to record the baseline. Then, the sample (ITO/AuNPs/DAE) was placed in the sample holder and a first spectrum before any irradiation was recorded (reference spectrum). Irradiations could then be performed using the setup described in Chapter 2.II.2.b. The duration of each irradiation was timed manually with a chronometer. A spectrum was recorded in between every irradiation. The spectra were fitted in Igor with a lorentzian function, the same wavelength interval was used for the series of spectra recorded for the same sample but was not the same for every sample. The interval used for every sample can be found in Table A2.1 in the Appendix. The incertitude on the fit of the LSPR peak was in the interval 0.036 to 0.465 nm for λ_{LSPR} and in the interval 4.02×10^{-4} to 3.6×10^{-2} for the absorbance at λ_{LSPR} .

For the samples of Chapter 5.II, which were made with cut ITO substrates so that they can fit in the custom sample holder made in Konstanz (but then no longer in the substrate holder of the Jasco spectrophotometer). The sample (ITO/AuNPs/DAE) was placed in the custom sample holder (conductive face facing the direction from which the beam arrives) the custom sample holder was simply put in the empty quartz cuvette (QS high-precision cell 100-10-40 from Hellma). The cuvette was then placed in the Jasco spectrophotometer. In that case, the “cuvette version” of the setup described in Chapter 2.II.2.b was used to perform the illuminations. The duration of each irradiation was timed manually with a chronometer. A spectrum was recorded in between every irradiation. The spectra were fitted in Igor with a lorentzian function between 500 and 540 nm. The incertitude on the fit of the LSPR peak was in always around 0.1 nm for λ_{LSPR} and in the interval 5.7×10^{-3} to 9.5×10^{-3} for the absorbance at λ_{LSPR} .

2 - Irradiation LEDs setups

a - The LEDs

Two LEDs pre-mounted on wired metal core board were used, the UV LED which is a Nikkiso VPS1A1 emitting at 300 nm and an Osram OSCONIQ P3030 emitting at 505 nm. The main characteristics of the LEDs are summarized in Table 2.7 (the wavelength bandwidth was extracted from the emission spectra of Figure 2.12) and their emission spectrum, recorded in

Konstanz university, are shown in Figure 2.12. The light power of each LED was always adjusted by changing the current while the bias remained fixed at corresponding V_f . The LEDs were always used with appropriate heatsinks to regulate their temperature.

Table 2.7: Main characteristics of the LEDs

LED	I_f (mA)	V_f (V)	P_0 (mW)	Viewing angle (°)	Wavelength bandwidth (nm)
Nikkisio VPS1A1 UV (300 nm)	350	6	30	130	25
Osram OSCONIQ P3030 Visible (505 nm)	350	2.7-3	1000	130	32.5

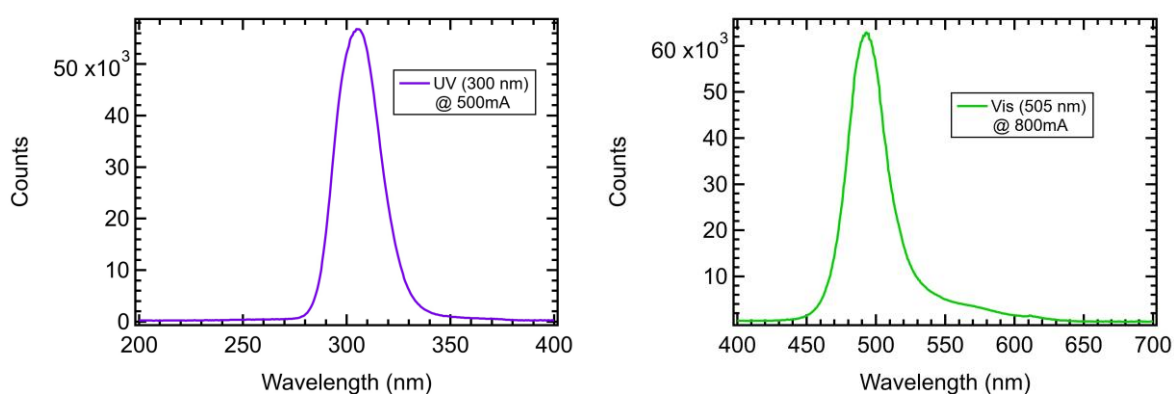


Figure 2.12: Emission spectra of the LEDs.

b - At the INSP

It was chosen to have the illumination setup inside of the analysis chamber of the Jasco V-750 spectrophotometer. A custom stand corresponding to the dimension of the chamber was built. Two versions of this setup were used, the first one called the “substrate version”, shown in Figure 2.13, is for the samples made with “full” ITO substrates (samples from Chapter 5.I) while the second version, shown in Figure 2.14, called the “cuvette version” is for the samples made with “cut” ITO substrates (samples from Chapter 5.II). Unlike the irradiation LEDs setup in Konstanz (presented in the next part), this one does not have shutters. Shutters allow to switch on the LEDs before irradiating the sample to let the light flux from the LEDs stabilize, then the

shutters are opened, and the irradiation starts. The stabilization time of the light flux was tested (see Figure A.2.5 in the Appendix) and we considered it was short enough to omit the use of shutters.

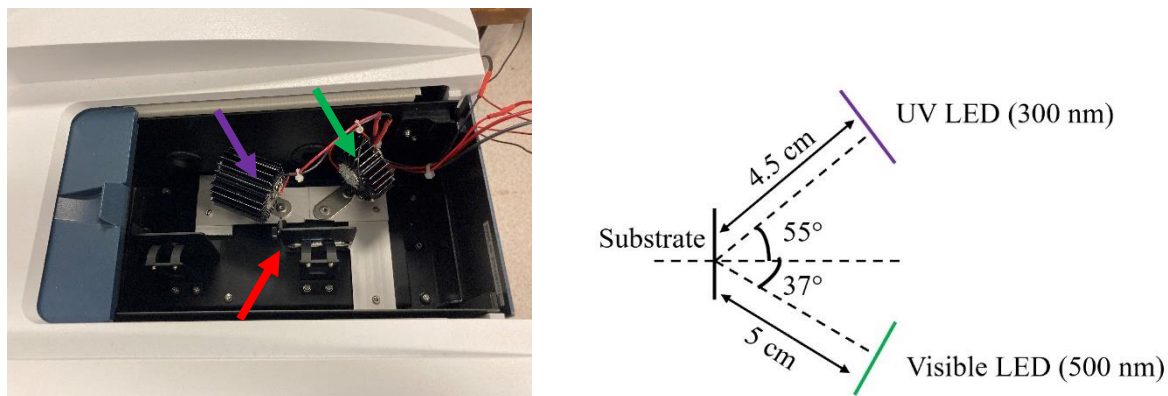


Figure 2.13: Setup for a sample directly put inside the sample holder for substrates from Jasco (“substrate version”). The sample holder, UV LED and visible LED are respectively indicated by a red arrow, a purple arrow, and a green arrow.

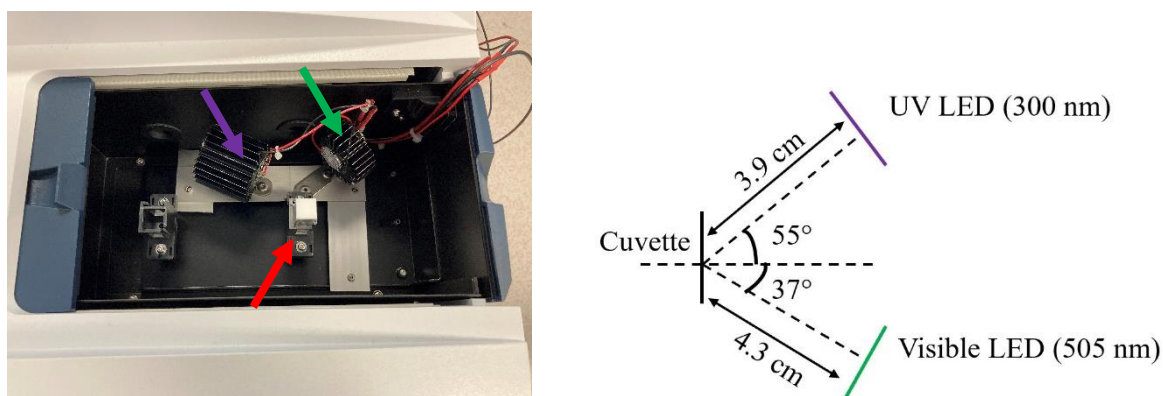


Figure 2.14: Setup for a sample inside the quartz cuvette (“cuvette version”). The cuvette, UV LED and visible LED are respectively indicated by a red arrow, a purple arrow, and a green arrow.

The LEDs were connected to a power supply (IPS 4303, RS Pro), the switching on and off of the LEDs was operated manually after setting the V_f and adjusting the I_f value corresponding to the desired light power.

The luminous power received by the sample was measured for both version of the setup with a power meter PM120VA from Thorlabs equipped with a Si sensor (measurement range 200 - 1100 nm for the light and 50 nW - 50 mW for the power) from the same brand. The power

received by the sample was measured by recreating the setup outside the chamber and placing the sensor in the same geometry as it would be placed in if it was in the chamber (see Figure A.2.6 in the Appendix). The flux in W/cm² was calculated for the current values used during the experiments (see Table 2.8) by dividing the value of the power in W by the surface of the active area of the sensor (0.709 cm²).

Table 2.8: LEDs parameters for the switching measurements presented in Chapter 5 given for both versions of the setup.

“Substrate version” of the set-up – Chapter 5.I samples				
LED	I (A)	P (mW)	Φ (mW/cm ²)	Φ_{photons} (photons/s/cm ²)
UV	0.24	0.178	0.251	3.79×10^{14}
Vis	0.7	2.26	3.19	8.10×10^{15}
“Cuvette version” of the set-up – Chapter 5.II samples				
LED	I (A)	P (mW)	Φ (mW/cm ²)	Φ_{photons} (photons/s/cm ²)
UV	0.07	5.5×10^{-2}	0.194	2.93×10^{14}
Vis	0.67	1.30	2.65	6.74×10^{15}

c - At Konstanz university

The following description corresponds to the LEDs setup used in Konstanz university to carry out all the measurements presented in Chapter 4. The numeration of the elements of the setup corresponds to the one given in the caption of Figure 2.15 (photo of the setup).

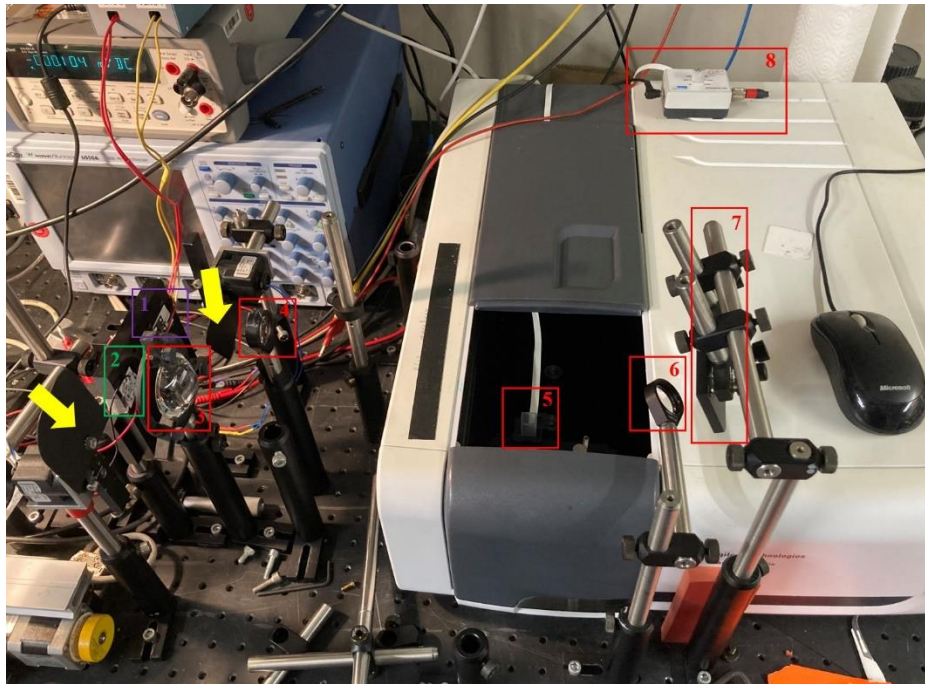


Figure 2.15: Setup used in Konstanz university for the irradiation (LEDs, on the left) and recording of the spectra (Cary 60 spectrophotometer, on the right). The following additional elements were also used: 1 - UV LED (300 nm); 2 - Visible LED (505 nm); 3, 4, 6 - Lenses; 5 - Quartz cuvette; 7 - Mirrors; 8 - Stirrer; yellow arrows – Shutters.

The LEDs (1,2) were placed beside the Cary 60 spectrophotometer (Agilent) on an optics table, an arrangement of optical elements was used to direct and focus the light beams on the quartz cuvette (5) inside the spectrophotometer. The lenses (3,4) placed in front of the LEDs collect the UV and visible light respectively and change the divergent beam path to a parallel one. The two mirrors (7) placed on the right side of spectrophotometer change the direction of the UV/vis light so that it arrives on the cuvette. A lens (6) placed after one of the mirrors further focuses the light from the visible LED. A magnet platform, connected to the control of the stirrer (8) which drives a stirring bar (at 600 rpm) inside the cuvette was placed below the cuvette. The two LEDs remained switched on throughout the whole experiment, they were switched on 10 s before the beginning of each experiment. This time was found suitable to heat up the LEDs and to get stable light flux. Two shutters (yellow arrows) were placed in front of the LEDs to be able to irradiate with one of them at the time for a defined amount of time, or to block both irradiations. The shutters and their control unit were designed and fabricated by the mechanics workshop of Konstanz university. The LEDs were connected to a power source (B2962A, Keysight) connected to the computer on which the software of the spectrophotometer is run. The switching on and off of the LEDs as well as the opening and

closing of the shutters were controlled by a python-script (written by S. Snegir, post-doc at Konstanz university) running on the computer.

The power of the light received by the sample was measured after replacing the cuvette by a suitable sensor connected to a power meter (see Figure A.2.6 in the Appendix). A LM-2 UV (250-400 nm) from coherent for the UV light and a LM-2 (400-1200 nm) from Coherent for the visible light. The results of the power measurements are shown for both LEDs in Figure 2.16.

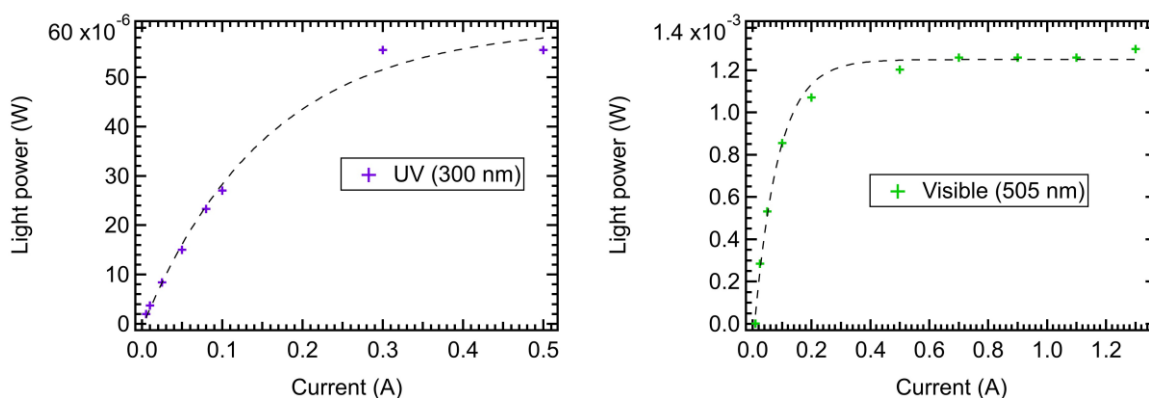


Figure 2.16: Power measurements for both LEDs.

The flux in W/cm^2 was calculated (see Table 2.9) for the current values used during the experiments (0.5 A for the UV LED and 1.3 A for the visible LED) by dividing the value of the power in W by the surface of the active area of the sensor (0.283 cm^2 for the LM-2 UV and 0.490 cm^2 for LM-2).

Table 2.9: LEDs parameters for the switching measurements presented in Chapter 4.

LED	I (A)	P (mW)	Φ (mW/cm^2)	Φ_{photons} ($\text{photons}/\text{s}/\text{cm}^2$)
UV	0.5	5.5×10^{-2}	0.194	2.93×10^{14}
Vis	1.3	1.30	2.65	6.74×10^{15}

3 - Dark field optical microscopy

Dark field (DF) microscopy is based on the light scattering of the analytes in the focal plane of oblique illumination which is transferred into the objective lens, or the charge coupled

device (CCD) camera¹³⁰. The samples requiring dark-field observation are those possessing refractive indices very close to that of their surroundings and are therefore impossible to image properly with conventional bright field microscopy. They are also those that require to work under the diffraction limit (it is the case with AuNPs)¹³⁰.

The working principle of dark-field microscopy is illustrated by the scheme in Figure 2.17. When there is a sample on the stage, the light follows the path described hereafter. A circular ring of oblique light rays is produced upon blocking the central light rays along the optical axis of the microscope by the DF obturator. This ring enters the condenser top lens which collects the light from the outer part of the ring and focuses it on the sample. Since the condenser (Abbe-style) top lens is spherically concave, it makes the light rays form a hollow cone with the tip of this cone hitting the sample's plane. After hitting the sample, the light is either absorbed, transmitted, or scattered. The scattered light enters the objective lens and is therefore the only light measured, the transmitted light does not^{131,132}.

When there is no sample on the stage, since the numerical aperture of the condenser is greater than that of the objective, the oblique rays cross before reaching the objective front lens, hence the “dark field”^{131,132}.

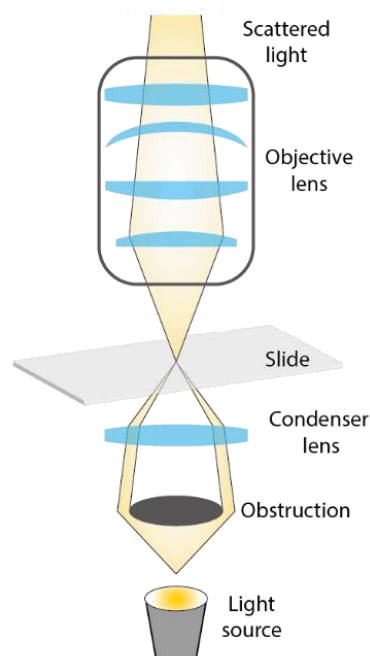


Figure 2.17: Scheme of the elements of a microscope in dark-field configuration and of the path that light takes in such configuration.

This technique presents various advantages including low imaging background (unlike bright field microscopy) which greatly improves the sensibility of the sensing, high sensitivity (and signal-to-noise ratio), high spatial and temporal resolution, single particle analysis accuracy, and cost-effectiveness¹³⁰.

In our case, this microscopy technique was used to image single gold nanoparticles (of 28 and 51 nm) deposited on ITO substrates provided their density was low enough to distinguish them (or rather their Airy disk) and they were not too aggregated (which they were not after an efficient deposition method was found). We used a Nikon Eclipse LV 100 equipped with two objectives: a TU Plan Fluor 10x/0.30 and a TU Plan Fluor 100x/0.90. The microscope was always used with the same settings, the luminosity set at 75 %, the white balance made in bright field mode on a pristine substrate of ITO and a gain value of 6.2. Two images of each zone of interest with both magnifications (10x and 100 x) were taken, the first one with an exposure time of 500 ms, the second one with an exposure time of 700 ms.

An example of the images that were obtained is given in Figure 2.18, showing single 51 nm AuNPs (the green dots) on ITO, the dots of other colors are aggregates of different sizes.



Figure 2.18: Dark field microscopy images with 10x magnification and 100x magnification of single 51 nm AuNPs (the green dots) on ITO (zone B of sample ADITO81). Luminosity 75 %, gain 6.2 x, exposure time 700 ms.

4 - DF-microscopy coupled to UV-visible spectroscopy: recording the spectrum of a single gold nanoparticle

Dark field microscopy was coupled to UV-visible spectroscopy via an adequate optical fiber. The microscope is still the LV 100 from Nikon, connected to a spectrophotometer QE Pro from Ocean Optics via a SMA-SMA optical fiber with a 50 μm diameter and a numerical aperture of 0.22 (a M14L02 from Thor Labs).

This technique was used to measure the UV-visible spectrum of single 51 nm gold nanoparticles deposited on ITO substrates. More precisely, it was used to study asymmetric AuNPs dimers and the functionalization of AuNPs by DAE molecules at the single gold nanoparticle scale.

The first advantage of this technique is that, unlike the UV-visible spectra recorded with the Jasco V-750 which corresponds to the average response of a population of AuNPs, the spectra recorded with the UV-visible spectrophotometer coupled to the optical microscope correspond to the response of a single AuNP. Two other advantages are the fact that it is a rather fast (the recording of a spectrum takes about 10 s) and non-invasive technique (no contact between the probe and the nano-object). Its limitations are related to the density of AuNPs present on the ITO substrate (it must not exceed 2 AuNP/ μm^2) and their size which must be superior to 28 nm.

The experimental procedure to record the spectrum of a single gold nanoparticle is the following. In the operating software of the microscope, a reticule was displayed: it is used to aim at the AuNP to analyze. The center of this reticule must correspond to the zone “seen” by the optical fiber. In order to make both correspond, the optical fiber was plugged in a halogen lamp (HL-2000-FHSA from Ocean Optics). The reticule was centered on the light spot coming out of the optical fiber and the latter was then connected to the spectrophotometer. The operating software of the spectrophotometer was started in Reflectance mode, and the parameters of the measurement entered. The same parameters, reported in Table 2.10, were used for the recording of all the individual AuNP spectra shown in this manuscript.

Table 2.10: Parameters used for the recording of all the UV-visible spectra of individual gold nanoparticles with the QE Pro spectrophotometer.

Integration time (ms)	1000
Scans to average	10
Boxcar width	30
Electric dark	On
Nonlinearity correction	On
Trigger mode	Continuous
Strobe/lamp enable	Off

Once the parameters were entered, the baseline was recorded. The reticule must aim at a zone without AuNPs on the sample if the baseline is recorded directly on it. It is also possible to record the baseline on a pristine ITO substrate. Both manners are giving a similar baseline. First, the “white” which corresponds to the maximal measurable signal was recorded with the microscope switched back to bright field. Second, the “dark” which corresponds to the lowest measured signal (the noise) was recorded with the microscope in DF mode again. Single AuNP spectra were recorded by aiming at chosen AuNPs. It has to be noted that the reticule, once it has been aligned is never moved until the end of the measurement session. Any displacement on the sample is made thanks to the automated stage the optical microscope is equipped with. Aiming at the center of an AuNP requires extremely small displacements (0.2 μm typically) that the precision of the stage allows to make.

The stage is the key element that allows to measure a specific set of AuNPs located in a zone of interest. After a sample destined to be analyzed by dark field microscopy coupled to UV-visible spectroscopy has been prepared, one must look for zones of interest i.e., a zone with a set of well separated AuNPs to measure. The sample is explored by controlling the stage manually. Once a zone is found, its horizontal and vertical distance from the top (or the tip of one of the branches) an asymmetrical V shaped mark is written down and will be used to come back to this zone any time it needs to be measured.

An example of a zone of interest with a set of 20 AuNPs (of 51 nm) and the spectrum of a single AuNP spectrum is given in Figure 2.19.

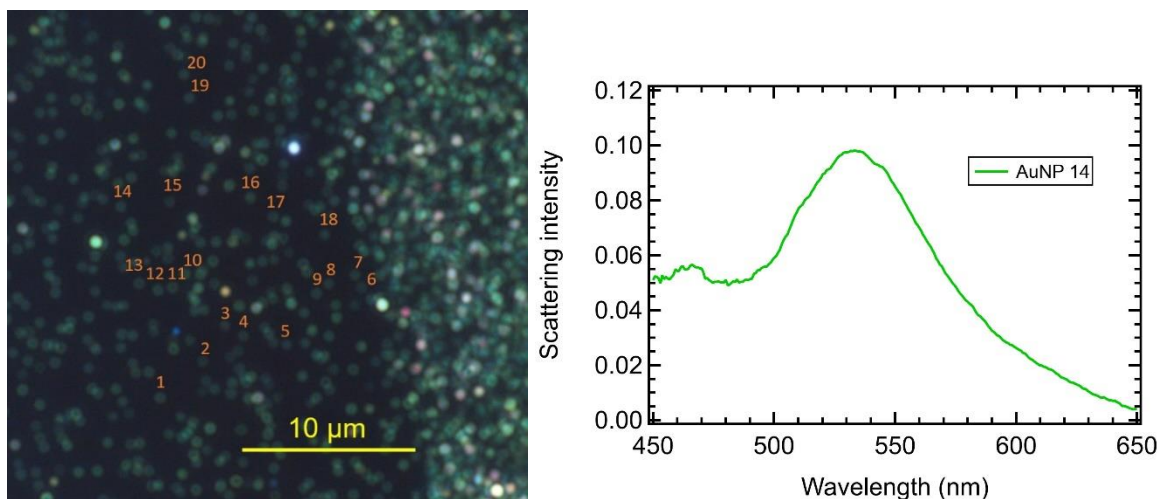


Figure 2.19: DF image (magnification 100x, 75 % luminosity, 6.2 x gain, and 700 ms exposure time) of a zone of interest with a set of 20 AuNPs (zone C from sample ADITOR) and spectrum of AuNP 14 from this set.

A test was made to evaluate the precision and reproducibility of the measurements. We need to check if we obtain the same values of the LSPR peak wavelength and absorbance. The spectrum of 20 AuNPs were recorded during two different measurement sessions (so all the settings were done twice, especially the recording of the “Dark” and “White”). These AuNPs are those from the zone of interest C of ADITOR shown in Figure 2.19. The LSPR peak from each spectrum (except those of AuNPs 3 and 4 that presented a dent) was fitted with a Gaussian between 511.7 and 573.1 nm (with Igor Pro). The results of the fits are shown in Table A2.2 and the uncertainty values Δu on the fit values are shown in Table A2.3 (the uncertainty value on the fit of λ_{LSPR} was given directly by Igor Pro, the incertitude on the fit value of the absorbance at λ_{LSPR} was calculated with the law of propagation of uncertainty applied to the uncertainty on the parameters of the fit given by Igor Pro). The average difference between the value of λ_{LSPR} measured the first and second time is 4.5 nm with an average uncertainty on the fit of 1.7 nm which is also the uncertainty on the measurement. For the absorbance at λ_{LSPR} the average difference is 7.1883×10^{-3} with an average uncertainty on the fit of 2.0×10^{-2} .

5 - Atomic Force Microscopy (AFM)

The atomic force microscope (AFM) was used to characterize all the samples based on ITO substrates. This characterization allows to check the quality and uniformity of the gold nanoparticles deposition on the ITO substrate and to verify the aspect of the gold nanoparticles after the DAE molecules were grafted on them. Since the AFM that we used is equipped with a precision (up to the tenth of μm) automatized stage, it was also possible to characterize a

specific set of AuNPs located in a specific zone (see Chapter 2.II.4 and Chapter 6) with this technique. The horizontal and vertical distances of the zone of interest from the mark made on the ITO substrate is entered in the AFM software and the zone can be accessed to. The AFM that we used is a NX 20 from Park, the tips were either RTESPA 300 from Bruker or NCHR pre-mounted tips from Park.

The AFM is a high-resolution (0.1 to 1 nm in height) scanning probe microscopy technique of which we remind the general principle and setup. It is based on the interaction between a probe and a surface to obtain a 3D image of the surface. As schematized in Figure 2.20, an AFM is composed of a tip, a soft cantilever, a laser beam, and a photodiode (quadrant photodetector). The laser beam is aligned on the tip which interact with the surface. These interactions make the tip moves or induces a modification of the oscillation frequency of the tip, controlled by the piezo it is connected to. The movements of the tip induce a variation of the position of the laser beam on the photodetector. These lateral and vertical variations are recorded and translated in electric signal by a piezo connected to the tip and used to reconstitute an image of the sample.

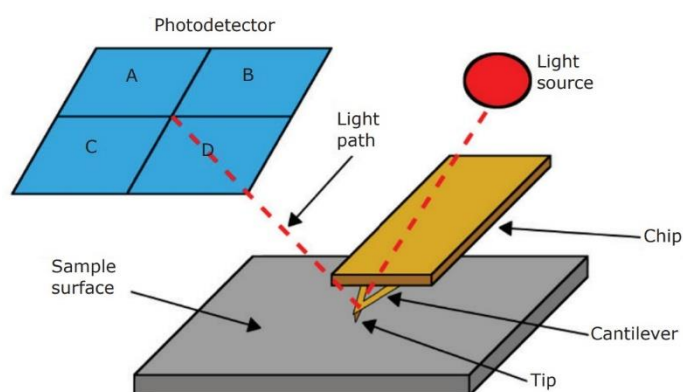


Figure 2.20: Scheme illustrating the main elements of an AFM. Reprinted from¹³³.

This technique allows the study of the geometry, topography and three-dimensional arrangement of the surface. Its advantages are the possibility to work with a nanometric resolution on all kind of materials, to get a lot of information (2D, 3D, potential/force curves, roughness, etc.), the possibility to work in different environments (in air, under vacuum, in a N₂ atmosphere, in solution). Its few drawbacks are the friction forces it may apply on the sample, the tip-surface convolution that induces a lowering of the resolution and the fragility of the tip.

There are three main manners to perform topography measurements: contact mode, non-contact mode and tapping mode; I mostly used the latter. Contact mode (repulsive) involves soft physical contact with the surface (tip-surface friction forces). It is based on the exploitation of coulombic repulsive interactions (10^{-9} N). This mode can only be used on hard materials (metals, ceramics etc.) but not to follow steep roughness (high risk of breaking the tip). In non-contact mode (attractive) the tip has no contact with the surface, the tip-cantilever vibrations are measured, the cantilever oscillates near the surface. This mode is based on the exploitation of the very weak van der Waals forces (therefore, very weak interactions between the tip and the surface). It is mainly used on soft and/or elastic materials and biological samples.

Tapping mode (or intermittent contact mode) represents a compromise between contact and non-contact mode, the tip softly touches the surface but by intermittence. Near the surface, the interaction between the tip and the surface induces a variation of the oscillation frequency of the tip (of the cantilever actually which oscillates at its nominal value f_0 , typically 300-400 kHz). The nature of the surface triggers its own variation of frequency linked to its chemical nature, or the adsorbate present on top of it. This mode appears as the most polyvalent one since it can be used on most surfaces.

To perform topography measurement in Tapping mode with the AFM, the laser was aligned on top of the tip. The SUM value which represents the intensity of the light coming from the laser projected on the tip was checked. If it is null, either the tip is broken or completely misaligned, if the value is weak, the tip is either damaged or misaligned. The alignment of the tip has to be done every time that the tip is changed. It is achieved by turning the two appropriate screws that control the position of the laser beam. Then, two other values were checked: “VER” and “HOR” which have to be as close as possible from 0, and are related to the position of the laser in the photodiode that receives the signal. They can be respectively modified with the appropriate screws.

The sample was put in the center of the sample holder, the zone to analyze was located using the optical microscope and the tip was placed above it. The “tuning” of the oscillation frequency of the cantilever was made (automatically). The approach (of the tip to the surface of the sample) was made (also automatically). The measurement was then started after carefully choosing a set of parameters (depending on the sample to image) that will allow to get the best quality image. The parameters used to obtain the images of the samples presented in Table 2.3, Table 2.4 and Table 2.5 are reported in Table 2.11.

Table 2.11: Parameters used to measure in Tapping mode.

Image size (μm)	5
Resolution (samples/line)	512
Scan rate (Hz)	0.5
Z servo gain	1
Set point (nm)	38
Amplitude (nm)	80
Frequency of the tip (kHz)	287
Drive (%)	2.5

The “images” obtained with the AFM cannot directly be used, they must be treated (treatment of the signal, color of the image, scale, height profile, etc.) with a software. In our case, Gwyddion was used, an example of images is given in Figure 2.21.

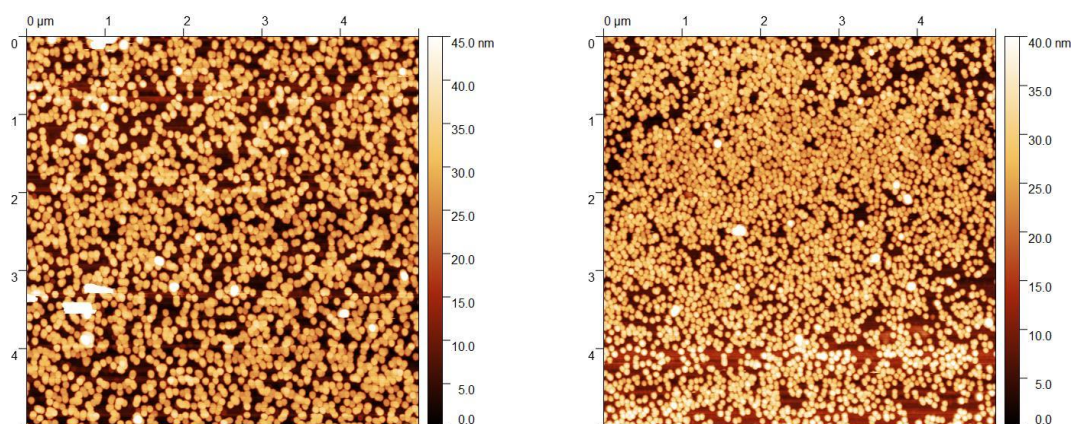


Figure 2.21: AFM images obtained in Taping mode of samples ADITOI (left) and ADITOC (right), they are both made of an ITO substrate covered with a layer of 28 nm gold nanoparticles functionalized with C5HT-di-PSH.

Chapter 3: Monitoring the adsorption of thiol molecules on gold nanoparticles using the LSPR

In this chapter, a method to monitor and confirm the functionalization of gold nanoparticles will be presented. We know that the functionalization processes on curved spherical nanoparticles surface are different than those of flat gold surfaces. The radius of curvature as well as the existence of binding sites with very different reactivity are determinant¹³⁴. We used spherical 22 nm AuNPs stabilized by a layer of citrates^{135,136} as synthesized according to the famous (slightly modified) Turkevich synthesis^{117–119,137}. These citrates, weakly bound to the AuNPs surface, are readily replaced by the linear thiol molecules^{138–140} we chose to use, presented in Figure 3.1: 11-mercaptoundecanoic-acid (MUDA) and 16-mercaptohexadecanoic-acid (MHDA). The only difference between these two molecules is the length of their carbon chain which can influence the stability of the nanoparticles functionalized with either one of them. These molecules have been chosen because they allow to preserve the colloidal stability of the AuNPs upon replacement of the citrates. Indeed, they both possess a carboxylic acid as terminal group which under its deprotonated form is negatively charged, exactly like the citrates they replace which are also negatively charged and therefore ensure colloidal stability via electrostatic repulsion. The content of this chapter was published in Dileseigres, A. S.; Prado, Y.; Pluchery, O., How to Use Localized Surface Plasmon for Monitoring the Adsorption of Thiol Molecules on Gold Nanoparticles? *Nanomaterials* **2022**, *12* (2), 292.

The surface coverage obtained for different amount of thiol and the typical completion time of the functionalization reaction will be investigated. For example, Wang et al.¹⁴⁰ demonstrated that a complete ligand exchange (11-mercaptoundecanoate) was achieved on 14 nm AuNPs using a sequence of cryo-TEM images to visualize the progressive replacement of diagnostic protecting polyoxometalate anions. They have shown that 2800 alkanethiolates were necessary to saturate the nanoparticle surface.

The evolution of the spectra induced by the increasing thiol concentration is shown in Figure 3.2 for MUDA and Figure 3.4 for MHDA. All the spectra were fitted and the values of the LSPR wavelength were extracted from the fits. These λ_{LSPR} values are reported in Table 3.1. The main feature that clearly appear on the spectra is the characteristic LSPR peak located at 520 nm that is usually measured for spherical gold nanoparticles in water^{18,143}.

a - MUDA

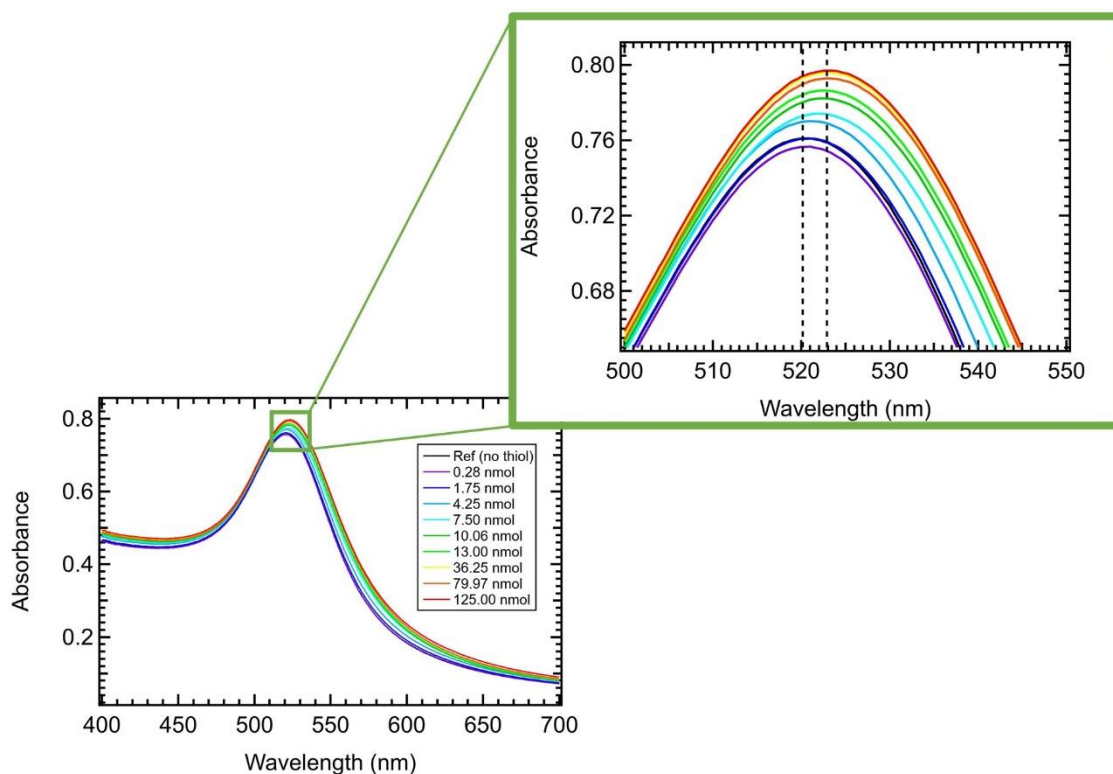


Figure 3.2: UV-visible spectra of 22 nm spherical gold nanoparticles in solution on which MUDA is progressively adsorbed. The resulting LSPR wavelength shift is 2.7 nm. Zoom on the LSPR peak maximum (in the green frame).

The AuNPs spectrum undergoes a redshift upon the adsorption of the MUDA molecules. It is clearly visible by looking at the spectra from Figure 3.2: the LSPR peak wavelength increases from 520.18 nm to 522.91 nm with the quantity of thiol (0 to 125 nmol) added to the reacting solution in the cuvette, yielding a LSPR peak wavelength shift $\Delta\lambda_{LSPR}$ of 2.7 nm. This spectral shift is due to the modification (increase) of the refractive index of the AuNPs' environment induced by the presence of MUDA molecules at the surface of the AuNPs^{65,141,144,145}.

In the case of MUDA, a FTIR spectroscopy analysis was also performed to confirm the adsorption of the MUDA molecules in similar conditions than those used for the saturation experiments. The experiments were conducted with two solutions, a pristine 18 nm citrate decorated AuNPs solution and a volume of this solution that was functionalized by mixing with a 2 μ M MUDA solution. Both solutions were drop-casted on silicon substrates and the spectra were recorded. More details about the preparation of the samples and the recording of the spectra are given in the Appendix. The two recorded FTIR spectra are shown in Figure 3.3.

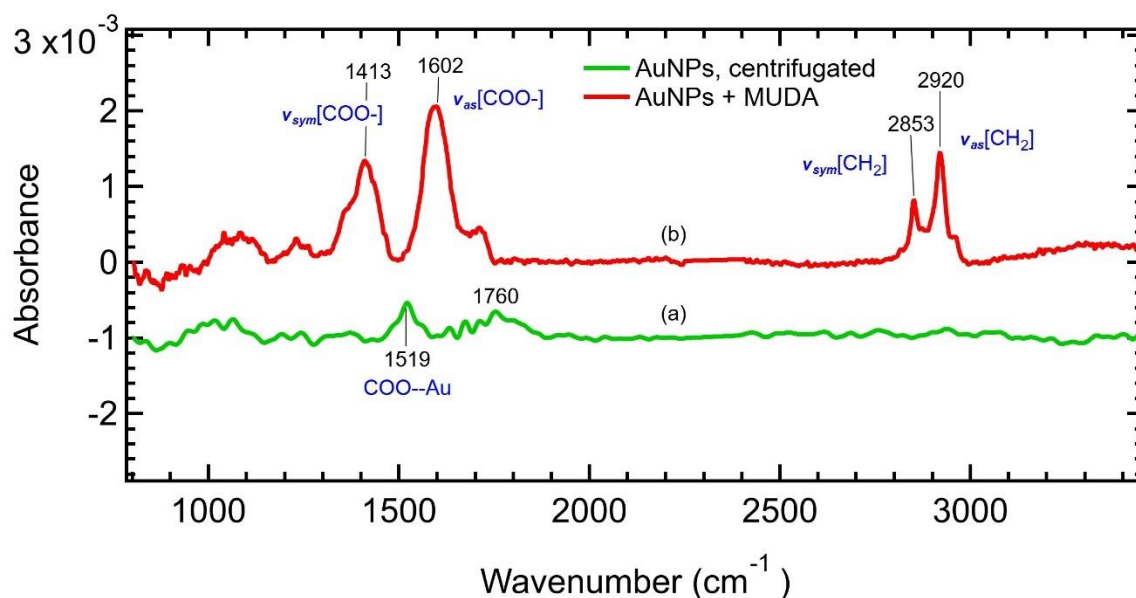


Figure 3.3: FTIR (Fourier-Transform Infra-Red) adsorption spectra of the two AuNPs solutions (citrate decorated - spectrum (a) and MUDA-functionalized - spectrum (b)) drop-casted on silicon substrates, recorded in Transmission with 70° incidence.

The spectrum (a) of the citrate decorated AuNPs only displays two small features emerging from the background noise. The first feature consists of vibrations located at 1760 cm^{-1} which corresponds to the stretching modes of water vapor that could not be fully suppressed by the data treatment procedures. The second feature, located at 1519 cm^{-1} , is attributed to the -COO moieties of the citrates in interaction with gold. Indeed, since the amount of citrate on the AuNPs surface is very low, the signal is quite noisy and impairs the clear identification of the peaks. The attribution to the citrates was nevertheless made, based on what is observed for free citrate molecules for which the asymmetric and symmetric modes are detected at 1385 cm^{-1} and 1575 cm^{-1} respectively^{123,136}. The spectrum (b) of the MUDA-functionalized AuNPs displays clearly defined and identifiable peaks corresponding to molecular vibrations we expected to find. The bands at 2853 and 2920 cm^{-1} were assigned to

the C-H bonds' stretching modes of all the methyl groups of MUDA's aliphatic chain. Regarding the two strong modes at 1413 and 1602 cm^{-1} , they were attributed to the carbonyl of the carboxylate moieties of MUDA. Finally, the bump present on both spectra at 1100 cm^{-1} is due to the slight oxidation of the substrates. The FTIR spectra analysis confirmed the functionalization of the AuNPs by MUDA and therefore the relevance of the quantitative analysis we are conducting with the saturation experiments.

b - MHDA

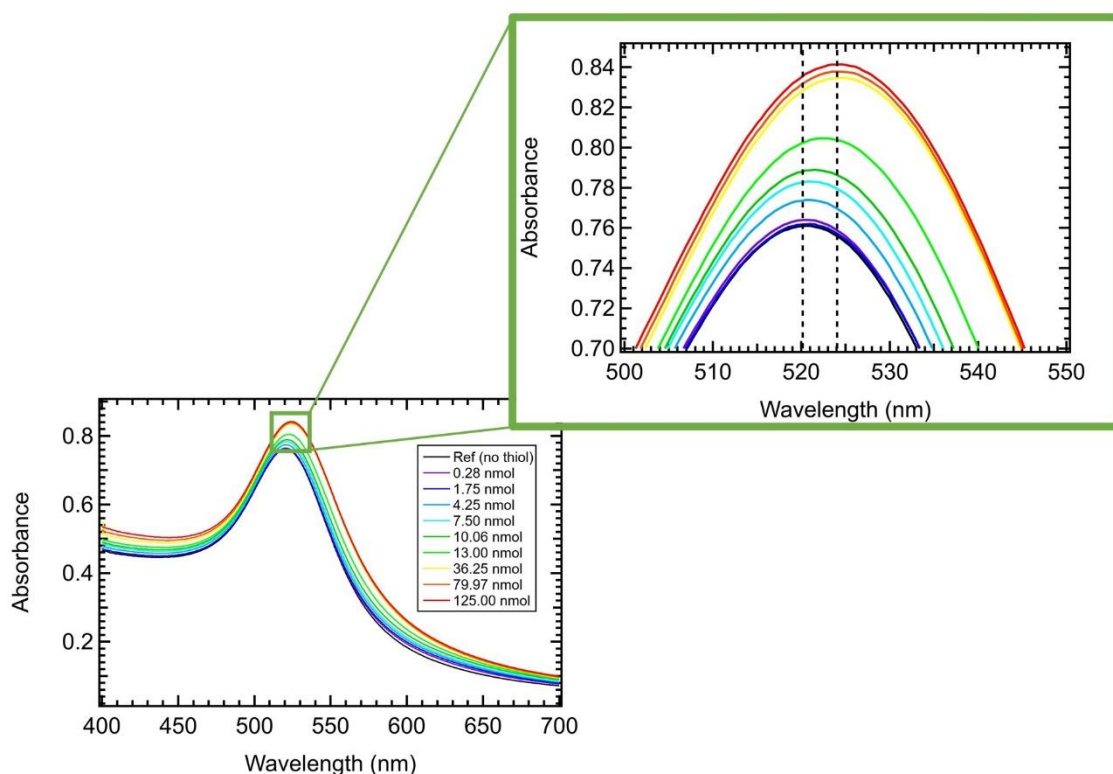


Figure 3.4: UV-visible spectra of 22 nm spherical gold nanoparticles in solution on which MHDA is progressively adsorbed. The resulting LSPR wavelength shift is 3.9 nm. Zoom on the LSPR peak maximum (in the green frame).

First, let us remind that the only difference between MUDA and MHDA is that the latter possess a longer aliphatic chain (11 alkyl groups for MUDA versus 16 alkyl groups for MHDA). The same trend than for MUDA is observed for MHDA, the AuNPs spectrum undergoes a redshift upon the adsorption of the MHDA molecules. It is observed on the spectra from Figure 3.4: the LSPR peak wavelength increases from 520.18 nm to 524.07 nm with the quantity of thiol (0 to 125 nmol) added to the reacting solution in the cuvette, yielding a LSPR peak wavelength shift $\Delta\lambda_{LSPR}$ of 3.89 nm. This spectral shift is due to the modification (increase) of

the refractive index of the AuNPs' environment induced by the presence of MUDA molecules at the surface of the AuNPs^{65,141,144,145}.

Table 3.1: Saturation experiments parameters (concentration of the added aliquot, amount of thiol added to the reacting solution, and concentration of the reacting solution) and measured LSPR peak wavelengths for MUDA and MHDA.

#	[Thiol] (μM) in the added aliquot	n_{thiol} (nmol) added	[Thiol] (μM) in the solution	λ_{LSPR} (nm) measured for MUDA	λ_{LSPR} (nm) measured for MHDA
0	0	0	0	520.18	520.18
1	6	0.28	0.13	520.19	520.19
2	35	1.75	0.86	520.42	520.30
3	85	4.25	2.07	520.88	520.49
4	150	7.50	3.66	521.81	520.79
5	201	10.06	4.91	522.33	521.25
6	260	13.00	6.34	522.42	522.40
7	725	36.25	17.68	522.91	524.26
8	1599	79.97	39.01	522.95	524.16
9	2500	125.00	60.98	522.91	524.07

c - Colloidal stability

The colloidal stability of the AuNPs in aqueous solution is electrostatically ensured by the negatively charged citrate ligands present at the surface of the AuNPs. The citrate decorated AuNPs are directly obtained from the Turkevich synthesis and used as is. Since we work in aqueous solution to perform the saturation experiments, the pH of the solution is 7. Both MUDA and MHDA molecules possess a carboxylic acid of $\text{pK}_a = 5$ as a terminal group. We thus have $\text{pK}_a (-\text{COOH}) < \text{pH}$, meaning that the carboxylic functions are under their deprotonated negatively charged form (COO^-) in aqueous solution. These negative charges continue to ensure the colloidal stability of the AuNPs when the MUDA or MHDA molecules progressively replace the citrate ions¹⁴⁶. The use of charged molecules is crucial, indeed, when trying to monitor the functionalization of the AuNPs with electrically neutral thiol molecules (of equivalent size to that of MUDA) such as dodecanethiols (DDT), the colloidal stability could not be preserved leading to the aggregation of the AuNPs. The aggregation has immediate consequence on the UV-visible spectra: the peaks are broadened and the resulting LSPR peak wavelength is much larger than it should be (in the case of DDT, $\Delta\lambda_{\text{LSPR}} = 15.6 \text{ nm}$)¹⁴⁷⁻¹⁴⁹. The results of a saturation experiment conducted with DDT are shown in Figure A.3.1 in the Appendix.

2 - Gold nanoparticle surface saturation (full coverage) - experimental determination and geometrical calculation

a - Experimental determination

We are now going to focus on the evolution of the LSPR peak wavelength with the amount of thiol added to the AuNPs solution as plotted in Figure 3.5. The choice to plot the evolution of the LSPR peak wavelength and not that of the LSPR peak absorbance is not innocent. Haes et al.¹⁵⁰ made the choice to follow the evolution of the LSPR peak absorbance to monitor the functionalization of silver nanotriangles, Dahlin et al.¹⁵¹ did the same for several noble metal nanostructures but the data treatment required to attain a sensibility high enough to yield exploitable results was really heavy. Besides, unlike the LSPR peak wavelength the LSPR peak absorbance is affected by certain experimental processes such as dilution which makes the absorbance decrease, or by the presence of aggregation that renders the interpretation of the data more difficult.

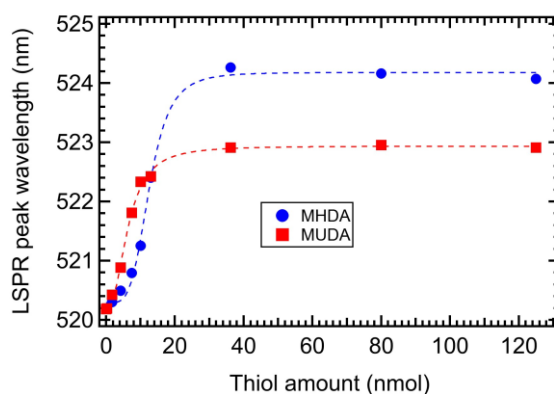


Figure 3.5: Evolution of the LSPR peak wavelength as a function of the added amount of thiol, MUDA (red square) and MHDA (blue dots). The dotted curves are guides for the eye.

As can be seen in Figure 3.5, for both MUDA and MHDA a plateau is reached for an added amount of thiol of about 20 nmol. The appearance of that plateau suggests that full coverage of the AuNPs surface was reached. The value of the amount of thiol required to fully cover the AuNPs surface can be readily calculated using basic geometrical considerations.

b - Geometrical calculation

First, we can start by calculating the AuNP concentration in solution C_{NP} assuming that all the HAuCl_4 complexes were reduced to metallic gold, $C_{NP} = [\text{HAuCl}_4]/N_{at}$ with $[\text{HAuCl}_4]$ the concentration of chloroauric acid in the final volume of AuNPs solution (after addition of citrate). Considering that we have spherical nanoparticles of diameter D that have crystallized in a fcc lattice, they contain a number of gold atoms $N_{at} = \frac{\pi}{6} \cdot \frac{\rho D^3}{M} \cdot N_{Av}$ with $\rho = 19.3 \text{ g/cm}^3$ the density of gold, $M = 197 \text{ g/mol}$ the molar weight of gold, and N_{Av} the Avogadro number¹⁵². In the case of gold, this formula can be simplified as $N_{at} = 30.9 \cdot D^3$ with D the diameter of the AuNPs expressed in nm. By injecting the expression of N_{at} into that of C_{NP} we arrive to:

$$C_{NP} = \frac{[\text{HAuCl}_4]}{30.9 \times D^3} \quad (3.1)$$

For our 22 nm AuNPs, $C_{NP} = 0.66 \times 10^{-9} \text{ mol.L}^{-1}$.

Second, we need to calculate the number of thiol molecules N_{thiol} that are grafted on the surface of the AuNPs in the case of the formation of a full monolayer. N_{thiol} is proportional to the surface of the gold nanoparticles $S_{NP} = \pi D^2$ and depends on the average thiol surface density p (expressed as a number of molecules/nm²) within a SAM, so that $N_{thiol} = \pi D^2 p$. According to Vericat et al.¹⁵³, $p = 1/(0.2165 \text{ nm}^2) = 4.619 \text{ molec/nm}^2$ for a flat Au (111) surface. For spherical nanoparticles, values ranging from 5.26 to 5.88 molec/nm² were determined^{154–156}. Consequently, a value of $p = 5.5 \text{ molec/nm}^2$ will be used, leading to a value of $N_{thiol} = 8440$ thiols molecules (number of molecules required to saturate the surface of a 22 nm gold nanoparticle).

Finally, the thiol concentration necessary to saturate the surface can be calculated, it can be written as $C_{thiol}^{sat} = C_{NP} \times N_{thiol}$. In the case of gold and by taking into account the previously derived formulas, C_{thiol}^{sat} can be expressed by two equivalent equations:

$$C_{thiol}^{sat} = 17.4 \times C_{NP} \times D^2 \quad (3.2)$$

$$C_{thiol}^{sat} = 0.56 \times \frac{[\text{HAuCl}_4]}{D} \quad (3.3)$$

In our case, the amount of thiol necessary to fully functionalize the surface of the AuNPs contained in the 2 mL volume that we use for the saturation experiments can readily be calculated as follows: $C_{NP} \times V_2 \times N_{thiol} = 11.1 \text{ nmol}$.

c - Experimental versus calculated value: comparison

The value of 11.1 nmol calculated above is now compared to the previously determined experimental value of 20 nmol. The experimentally determined value is larger than the calculated value. This larger experimental value corresponds to $N_{thiol} = 15\,160$ molecules packed with a density of 10 molec/nm². Using the values reported in Table 3.1, it is possible to convert this number of molecules value into a saturation concentration value. After 20 ± 2 nmol were introduced in the cuvette already containing the 2 mL of AuNPs solution, the total volume was 2.05 mL. Consequently, the thiol concentration in the cuvette was $C_{thiol}^{exp} = 10 \pm 1 \mu\text{M}$ and the AuNP concentration in the cuvette was $C_{NP} = 0.64 \times 10^{-9} \text{ M}$. Injecting this C_{NP} value in Equation (3.2) gives $C_{thiol}^{sat} = 5.39 \mu\text{M}$.

The plateau observed for both curves of Figure 3.5 indicates that MUDA and MHDA no longer absorb after the 20 nmol threshold has been reached. This larger amount of thiol (compared to the one that was calculated) experimentally determined could be explained by other chemical and physical phenomena than those we considered: the formation of a molecular multilayer on the AuNP surface instead of the hypothesized monolayer, a larger reactive surface of the AuNP than calculated, or the oxidation of the thiol function of some molecules that prevents them to react with the gold surface. These phenomena will not be discussed here, nevertheless, it is safe to say that the formation of a multilayer is unlikely, the thickness of such a layer would greatly affect the value of the LSPR wavelength shift, which is not what was observed here. To conclude, we can say that Equations (3.2) and (3.3) are enough to get a correct estimation (the right order of magnitude) of the thiol amount necessary to reach the saturation of the AuNPs surface (full coverage).

II - Predictive analytical model for the LSPR peak wavelength shift

1 - Derivation of the model

a - Sensitivity factor of 22 nm spherical AuNPs and dependence of the LSPR on the solvent refractive index

For AuNPs dispersed in a solvent, as schematized in Figure 3.7 a), there is a dependence of the LSPR regarding the refractive index of the solvent $n_{solvent}$ which can be calculated with the electrostatic model in first approximation or with the Mie theory for a more accurate description¹³⁸ (see Figure 3.6 and Table 3.2). Spectra calculated with Mie theory for increasing values of $n_{solvent}$ are shown in Figure 3.6. If $n_{solvent}$ varies in the range 1.3 - 1.6, the refractive index can be written as $n_{solvent} = n_0 + \Delta n'$ and the wavelength shift can be expressed with the following linear relationship:

$$\Delta\lambda_{LSPR} = m \cdot \Delta n' \quad (3.4)$$

Where m is the sensitivity factor (dependent on the size, shape, and nature of the nanoparticle). For a 22 nm spherical gold nanoparticle, $m = 69 \text{ nm.RIU}^{-1}$ (Refractive Index Unit).

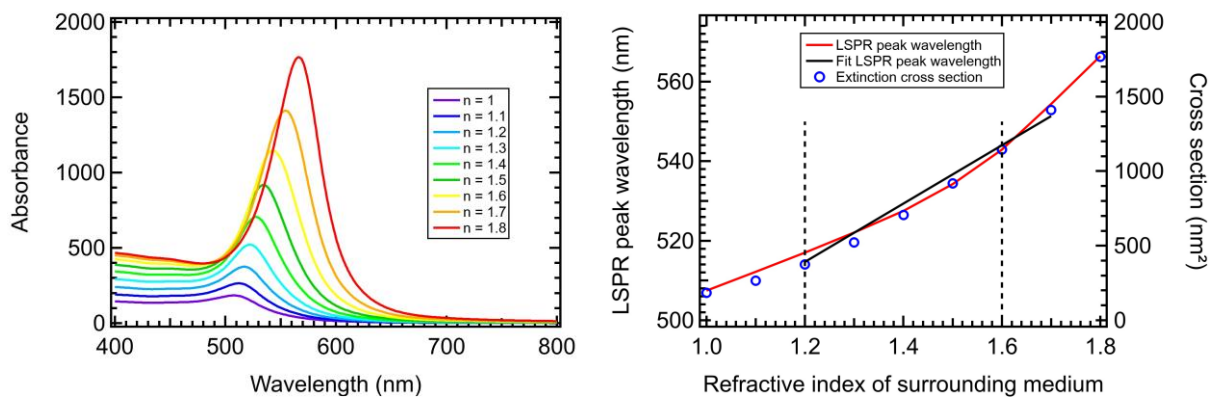


Figure 3.6: Evolution of the extinction cross section of 22 nm AuNP in a medium whose refractive index is increased from 1 to 1.8 (left). Calculations are done with the Mie theory. Plot of the extinction maximum (solid red line, left axis) as a function of the optical index of the surrounding solvent. Value of the max extinction cross section (blue open circles, right axis). Within the range of 1.3 - 1.6, the evolution is approximately linear with a slope of $m = 69 \text{ nm.RIU}^{-1}$. Bichromatics calculator was used¹⁵⁷.

Table 3.2: Values of the LSPR peak wavelength (λ_{LSPR}) and of the extinction cross section at λ_{LSPR} as a function of the index of the surrounding solvent.

Index (RIU)	λ_{LSPR} (nm)	Extinction cross section at λ_{LSPR} (nm ²)
1	507.42	183.26
1.1	512.17	264.38
1.2	517.03	374.80
1.3	522.02	521.45
1.4	527.53	705.21
1.5	534.22	916.80
1.6	542.93	1145.12
1.7	554.42	1410.65
1.8	566.43	1766.00

b - Calculation of the LSPR shift generated by the adsorption of a full monolayer of molecules

Let us consider the grafting of a monolayer of molecules of refractive index n_{molec} at the surface of a 22 nm spherical gold nanoparticle dispersed in a solvent of refractive index n_0 (schematized in Figure 3.7 b)). Equation 3.4 is not suitable for the calculation of $\Delta\lambda_{LSPR}$ induced by the grafting since the height of the molecular layer is inferior to the electromagnetic decay length l_d . The electromagnetic decay length represents the extension of the local electromagnetic field i.e., the length up to which the near field can probe the environment of the AuNP (in our case the molecular layer and a zone of the solvent around the AuNP + molecular layer).

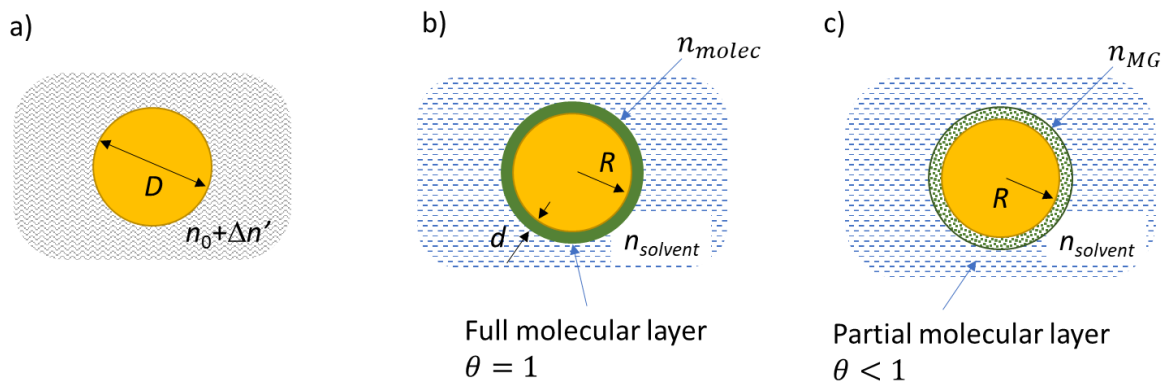


Figure 3.7: a) Spherical nanoparticle of diameter D in a medium of index $n_0 + \Delta n'$ b) the same nanoparticle bearing a molecular layer of thickness d , in a medium of index $n_{solvent}$ c) the same nanoparticle with a partial molecular coverage $\theta < 1$. The refractive index of the incomplete molecular layer n_{MG} is calculated with the Maxwell-Garnett formula.

The small LSPR shift generated by the functionalization of a nanoparticle by a molecular entity has been described and used for the first time by Englebienne to determine the affinity constants of biomolecules grafted on nanoparticles¹⁵⁸. Nevertheless, it is the work of Van Duyne in the field of biosensors¹⁵⁹ that led to the formula used calculate the LSPR shift^{153,160}:

$$\Delta\lambda_{LSPR} = m \cdot \Delta n \left[1 - \exp\left(-\frac{2d}{l_d}\right) \right] \quad (3.5)$$

Where m is the sensitivity factor ($m = 69 \text{ nm.RIU}^{-1}$, same explanation as for Equation 3.4), Δn is the difference between the refractive indices of the solvent and that of the molecular layer $\Delta n = n_{molec} - n_{solvent}$, d is the thickness of the molecular layer, and l_d is the electromagnetic field decay length.

A more complex set of non-linearized formulas was proposed by Pollit et al.¹⁶¹ to calculate $\Delta\lambda_{LSPR}$ while Messersmith et al.¹⁶² proposed an incorrect formula.

First, to be able to calculate values of the LSPR wavelength shift expected for the case of a full coverage of the AuNP surface using Equation 3.5 we need to evaluate l_d . A sphere of radius R excited by an electromagnetic field E_0 , radiates an optical near field that exponentially decays from the nanoparticle (see Figure 3.8). The electromagnetic decay length is related to this exponential decay, where the electric field can be expressed as¹⁶³:

$$E_x = E_0 + A \exp\left(-\frac{r-R}{l_d}\right) \quad (3.6)$$

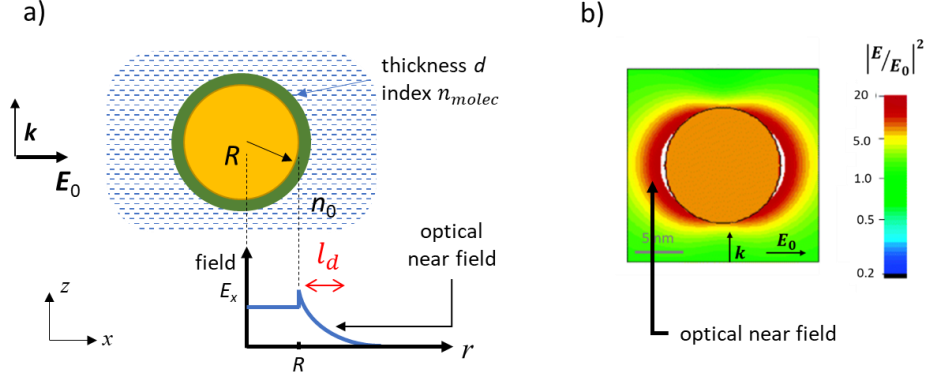


Figure 3.8: a) Spherical nanoparticle of radius R , bearing a molecular layer of thickness d , in a medium of index n_0 ; The near field radiated by the particle extends over a length l_d . b) 2D representation of the near-field enhancement by a gold nanoparticle in water upon excitation at its plasmon resonance ($\lambda = 520 \text{ nm}$). The intensity of electric field is enhanced of a factor of 20 in the vicinity of the nanoparticle surface and decay as $1/r^3$. Reprinted from ¹⁶⁴.

However, as can be seen in relations 3.7 the decrease of the near field is in $1/r^3$ and not exponential. The near field radiated by a metallic sphere along the xx' and zz' axis (see Figure 3.8), under an excitation $E_0 \mathbf{u}_x$ is:

$$E_{xx'} = E_0 \left(1 + 2 \frac{\alpha'}{x^3} \right) \text{ and } E_{zz'} = E_0 \left(1 - \frac{\alpha'}{x^3} \right) \quad (3.7)$$

where $x = r/R$ and α' is the reduced polarizability of the particle.

However, as shown in Figure 3.9, it is possible to fit Equations 3.7 by an exponential decay similar to that of Equation 3.6. For a spherical gold nanoparticle at the resonance, the reduced polarizability is $\alpha' = 2.63$ and the fit applied to relations 3.7 gives:

$$E_{xx'} = 1.04 \times E_0 + 4.83 \exp \left(-\frac{x-1}{0.45} \right)$$

$$E_{zz'} = 0.98 \times E_0 - 2.42 \exp \left(-\frac{x-1}{0.45} \right)$$

Which makes us arrive to the following linear relation to evaluate l_d :

$$l_d = 0.45 \times R \quad (3.8)$$

In the present case AuNPs have a radius $R = 11.0 \text{ nm}$, therefore, $l_d = 4.95 \text{ nm}$.

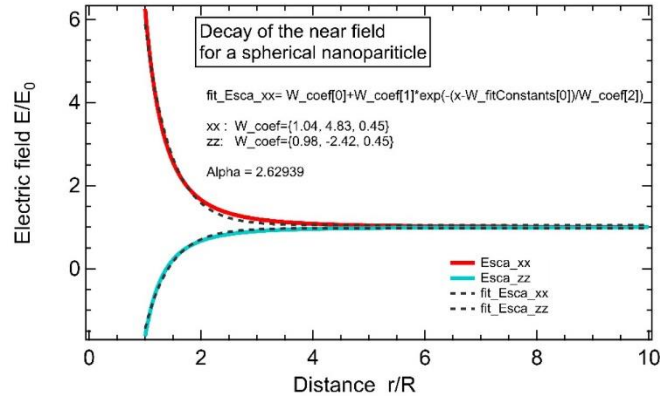


Figure 3.9: Decay of the radiated electric near field along the axis xx' and zz' for a gold nanoparticle in water.

Second, we need to determine the thickness d of the molecular layer. Since we know that on flat gold surfaces, molecules are attached to the surface at a tilt angle $\alpha = 30^\circ$ ¹⁵³, the effective thickness of the monolayer is smaller than the length l of the molecules and we have $d = l \cdot \cos(\alpha) = 1.32 \text{ nm}$ with ($l = 1.52 \text{ nm}$ for MUDA). We must then evaluate the refractive index of the molecular layer which is not trivial since it depends on the nature of the molecule and its compactness on the surface. We chose to use $n_{molec} = 1.46$ which is the value measured by Goldmann et al.¹⁵⁹ for a compact DDT monolayer and reported in other publications¹⁶². We now have the value of $\Delta n = n_{molec} - n_{solvent} = 1.46 - 1.33 = 0.13$. Finally, since we know the values of all the parameters required to use Equation 3.5, we can now calculate the value of the spectral shift expected for the grafting of a monolayer of MUDA or MHDA on the whole surface of the AuNPs (see Figure 3.7 b)). We find $\Delta\lambda_{LSPR}(MUDA) = 3.70 \text{ nm}$ and $\Delta\lambda_{LSPR}(MHDA) = 4.71 \text{ nm}$ ($l = 2.13 \text{ nm}$ and thus $d = 1.84 \text{ nm}$ for MHDA).

c - Evaluation of the coverage of the nanoparticle surface using the Maxwell-Garnett model

Up to this point, we always assumed a full coverage of the AuNP surface, but we now focus on the case of a partial coverage (schematized in Figure 3.7 c)). Partial coverage allows to describe what happens before full coverage is reached or not when working with an amount of thiol molecules inferior to the minimum amount required to reach full coverage. During kinetics experiments (similar to the one shown further in Figure 3.11), thiol molecules progressively cover the nanoparticle surface before full coverage is reached. We had to find a way to link the evolution with time of the LSPR wavelength (i.e., the shift $\Delta\lambda_{LSPR}$) to that of

the molecular coverage. In particular, we needed to verify if a linear relation exists between $\Delta\lambda_{LSPR}$ and θ (the coverage).

A partial coverage corresponds to a medium where solvent molecules are inserted in the free spaces that are not occupied by the molecules to graft (in our case the thiols). The refractive index of such a medium can be calculated with the Effective Medium Approximations (EMA) and the Maxwell-Garnett formula (MG)¹⁶⁵. The MG formula allows to calculate the dielectric permittivity ε_{MG} of an heterogenous medium, here the solvent (of dielectric permittivity $\varepsilon_{solvent}$) which contains inclusions of adsorbed thiol molecules (of dielectric permittivity ε_{molec}) quantified by the volume fraction f . In our case f corresponds to the coverage θ which varies between 0 (no grafted molecules) and 1 (full molecular coverage). Consequently, ε_{MG} can be expressed as:

$$\varepsilon_{MG} = \varepsilon_{solvent} \frac{\varepsilon_{molec}(1+2\theta)+2\varepsilon_{solvent}(1-\theta)}{\varepsilon_{molec}(1-\theta)+\varepsilon_{solvent}(2+\theta)} \quad (3.9)$$

Which simplifies into:

$$\varepsilon_{MG} = \varepsilon_{solvent} \frac{1+2q\theta}{1-q\theta} \text{ with } q = \frac{\varepsilon_{molec}-\varepsilon_{solvent}}{\varepsilon_{molec}+2\varepsilon_{solvent}} \quad (3.10)$$

If ε_{molec} is close to $\varepsilon_{solvent}$, then $q \ll 1$ and (3.10) can be linearized. In our case $\varepsilon_{solvent} = 1.33^2 = 1.77$ and $\varepsilon_{molec} = 1.46^2 = 2.13$, therefore $q = 0.064$ which satisfies $q \ll 1$. The linearization is reasonable, and the equivalent refractive index of the partially complete molecular layer n_{MG} is obtained:

$$n_{MG} = (\varepsilon_{MG})^{1/2} = n_{solvent} \left(1 + \frac{3}{2}q\theta\right) \quad (3.11)$$

This result confirms that in the case of an heterogenous medium composed of materials with refractive indices close to one another, the resultant effective index of this medium is simply proportional to the surface coverage θ .

d - Application to the case of spherical plasmonic nanoparticles

Let us combine Equation 3.11 with Equation 3.5, now we have $\Delta n = n_{MG} - n_{solvent}$ and it can be written as $\Delta n = \frac{3}{2}q \cdot \theta \cdot n_{solvent}$ using Equation (3.11). The LSPR wavelength shift can then be expressed as:

$$\Delta\lambda_{LSPR} = m \cdot \frac{3}{2}q \cdot \theta \cdot n_{solvent} \left[1 - \exp\left(-\frac{2d}{l_d}\right) \right] \quad (3.12)$$

Since all the parameters from Equation (3.12) have been previously calculated, in our conditions, the linear relation between the LSPR wavelength shift and the coverage can be written for each of the molecules as follows:

$$\Delta\lambda_{LSPR} = 3.63 \times \theta \text{ (nm) for MUDA} \quad (3.13)$$

$$\Delta\lambda_{LSPR} = 4.63 \times \theta \text{ (nm) for MHDA} \quad (3.14)$$

These two last equations are valid for 22 nm spherical gold nanoparticles in water with a partial coverage $\theta < 1$. The calculated and experimental results are summarized in Table 3.3.

Table 3.3: Calculated and measured values of the LSPR wavelength shift induced by the grafting of each molecule. The effective length of the molecules is given assuming a tilt angle from the normal to the surface $\alpha = 30^\circ$.

Molecule	Effective length - d (nm)	$n_{solvent}$	$\Delta\lambda_{LSPR}$ (nm) calculated for $\theta = 1$	$\Delta\lambda_{LSPR}$ (nm) calculated for $\theta < 1$	$\Delta\lambda_{LSPR}$ (nm) measured
MUDA	1.32	1.33	3.70	$3.63 \times \theta$	2.7
MHDA	1.84	1.33	4.71	$4.63 \times \theta$	3.9

2 - LSPR wavelength shift at full coverage: calculated versus measured

The experimentally obtained values of the LSPR wavelength shift at full coverage, respectively 2.7 nm and 3.9 nm for MUDA and MHDA, are inferior to the calculated values (3.70 nm and 4.71 nm, respectively). Several reasons can explain this discrepancy, first, the model we proposed relies on a set of three hypotheses. Firstly, we assumed that we had a compact layer of molecules, secondly, we assumed that these molecules were 30° tilted with respect to the normal of the surface and finally, we assumed that they had a refractive index $n_{molec} = 1.46$. All these assumptions, which were impossible to verify experimentally, are uncertainty sources that affect the accuracy of the model.

We are going to discuss the influence of these assumptions on the value of $\Delta\lambda_{LSPR}$. First, the molecular layer on the AuNPs is probably not as compact as hypothesized, its density is probably lower than that of well-organized SAM type layer on a flat gold surface, decreasing

the value of $\Delta\lambda_{LSPR}$. Second, regarding the tilt angle of the molecules, if we consider that the molecules are perpendicular to the surface (no tilting angle, $\alpha = 0$), for a full coverage of MUDA molecules, the effective monolayer thickness would be 1.52 nm and we would have a much larger $\Delta\lambda_{LSPR}$ of 6.65 nm. This effect would be even stronger for MHDA whose carbon chain is longer than that of MUDA. However, this configuration is highly unlikely for molecules possessing such a long carbon chain. Conversely, if we consider a larger tilt angle than we did of 50° as reported elsewhere¹⁶⁶ instead of 30° , the values of $\Delta\lambda_{LSPR}$ become smaller, respectively 2.9 nm and 3.8 nm for MUDA and MHDA, which corresponds better to our experimental values. Finally, if we consider a larger value of the refractive index of the molecules, the values of $\Delta\lambda_{LSPR}$ decreases. To sum up, we can say that the model corresponding to Equation 3.5 is precise enough to give a correct idea of the trend for the values of $\Delta\lambda_{LSPR}$ of different molecules. Its limit is set by the accuracy of the parameter values used to calculate $\Delta\lambda_{LSPR}$ using aforementioned Equation 3.5. As previously said, this model will be particularly useful to calculate the expected $\Delta\lambda_{LSPR}$ values for a set of molecules to compare.

III - Functionalization kinetics

1 - Adsorption reaction kinetics measurements

Kinetics measurements were carried out, they consisted in adding a volume of MUDA solution of known concentration at $t = 0$ to a volume of AuNPs of known concentration. The functionalization of the AuNPs by the thiol molecules was monitored by successive acquisition of UV-visible spectra (shown in Figure 3.10) that were then fitted.

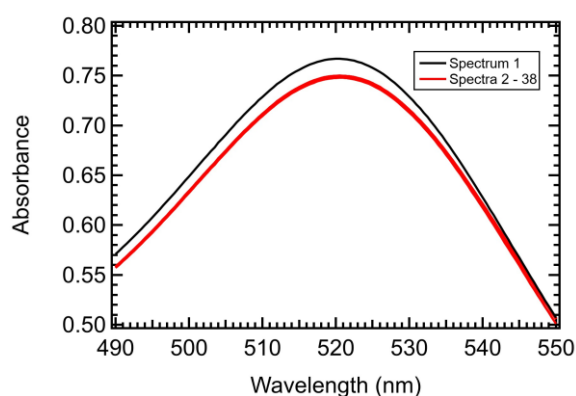


Figure 3.10: UV-visible spectra recorded during the kinetics measurements.

As shown in Figure 3.11, the value of the LSPR wavelength was extracted from each fitted spectrum and plotted versus the time to monitor the progressive evolution of the functionalization with time and hence gaining information on the functionalization kinetics. More details about the experimental procedure and the treatment of the acquired data are given in Chapter 2.II.1.c.

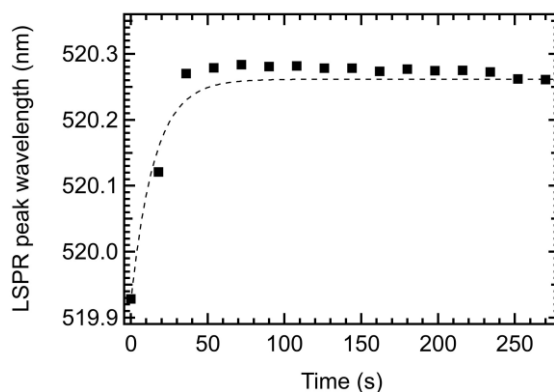


Figure 3.11: Evolution of the LSPR peak wavelength upon functionalization of the AuNPs surface with MUDA plotted versus the time (to elucidate the functionalization kinetics). The solution was not stirred during the acquisition of the spectra. 50 μL of MUDA at 35 μM were added to 2 mL of AuNPs at 0.66×10^{-9} mol/L, leading to a final MUDA concentration of 0.86 μM in the reacting solution (in the cuvette). The dotted line corresponds to a fit of the data with a single exponential.

The total LSPR wavelength shift measured in this experiment is 0.33 nm (λ_{LSPR} evolved from 519.93 to 520.26 nm) which is consistent with the shift observed during the saturation experiments at the point for which we had the same MUDA concentration in the reacting solution. It is no surprise to find a smaller shift value since the amount of MUDA introduced in the solution is inferior to that required to attain the full coverage of the AuNPs surface. The set of points corresponding to the evolution of λ_{LSPR} with the time were fitted with a single exponential with a time constant $\tau = 15$ s. The reaction completion time was thus estimated to be $t_{\text{reac}} = 3 \times \tau = 45$ s. Since the experiment was performed without stirring, the reaction occurred by diffusion which rendered it slow enough to be monitored by the method we chose. If the experiment was carried out with stirring, the reaction would occur much faster, rendering it impossible to monitor with our method (the main limit being the acquisition time of a spectrum).

2 - Functionalization time and adsorption reaction kinetics

As shown in Figure 3.11, the reaction occurring in the total 2.05 mL of solution with a concentration of 0.008 μM in MUDA and 0.64×10^{-9} in AuNPs, induced a progressive spectral shift of the LSPR peak which follows an exponential law with a time constant $\tau = 15$ s. According to the demonstration given in II.1 (see Equation 3.9 to 3.11), the LSPR peak wavelength shift is proportional to the coverage, the latter should then follow the same temporal evolution than the LSPR peak wavelength i.e, an exponential law. Since both the LSPR peak wavelength and the coverage present an exponential evolution, it is safe to assume that the adsorption reaction follows a classical Langmuir kinetics law^{167,168}.

According to the Langmuir model, the rate constant $k = 1/\tau$ is a combination of two components: the intrinsic rate constant of adsorption k_a and the intrinsic rate constant of desorption k_d . In our case, $k = k_a \cdot C_{thiol} + k_d$ however, the desorption of any thiol molecule will be neglected, rendering the rate constant k directly proportional to the thiol concentration: $k \approx k_a \cdot C_{thiol}$.

Our kinetics measurements gave a reaction completion time $t_{reac} = 3 \times \tau = 45$ s for a thiol concentration of $C_{thiol} = 0.86 \mu\text{M}$. This result greatly differs from that of other studies which reports a much larger reaction time (an “overnight” reaction is often performed)^{123,169}. To be fair, our approach only brings an insight on the functionalization kinetics and especially the evolution time since it actually depends on many factors. The first one is the amount of thiol introduced in the AuNPs solution, if we have $C_{thiol} > 0.86 \mu\text{M}$, full saturation of the AuNPs surface will be reached and the temporal evolution will stop. In doing so, the reaction completion time value t_{reac} only constitutes an upper limit of the completion time. The second one is the thiol adsorption mechanism which, as Pan et al.¹⁶⁷ reported, the Langmuir model does not suffice to describe. It is important to note that the adsorption mechanism of MUDA on a flat gold surface has been studied and described by Damos et al.¹⁷⁰ who showed that for certain thiol concentrations, the kinetics mechanism consists of two steps (a first rapid adsorption step followed by a slower reorganization step). In the end, we can say that the approach we proposed allows to obtain information on the most adequate experimental conditions for the functionalization of gold nanoparticles with thiol molecules regarding the concentration in thiols and the immersion time.

Conclusion

To summarize this chapter, the progressive functionalization of spherical 22 nm gold nanoparticles by thiol molecules was monitored with UV-visible spectroscopy which gave us access to the LSPR peak wavelength evolution. The absorption of MUDA and MHDA induced a LSPR peak wavelength shift of 2.7 nm (from 520.2 nm to 522.9 nm) and 3.9 nm (from 520.2 to 524.1 nm) respectively. The LSPR peak wavelength value reached a plateau indicating that full coverage was reached as soon as the thiol amount added to the 2 mL of AuNPs solution (at 0.66×10^{-9} M) equaled or overpassed 20 nmol. This quantity of thiol corresponds to 15 000 molecules, forming a layer on the surface of each AuNP, a number of molecules superior to that given by the geometrical calculation (8400). This calculated result can however be used as a lower limit for a design of an experiment aiming at full functionalizing AuNPs. An analytical model was derived to predicting the value of the LSPR peak wavelength shift. The values calculated with that model corresponded well to the experimentally measured ones. Finally, an insight on the kinetics of the functionalization reaction was given, it would follow a Langmuir kinetic law and using a MUDA solution of 0.86 μ M, the reaction was completed in less than 45 s, a much shorter time than many reported in the literature.

In the following chapters, the analytical predictive model in particular will be reused to predict the shift expected for the functionalization of supported spherical nanoparticles of various sizes by thiol-terminated diarylethene molecules.

Chapter 4: Switching kinetics of diarylethenes C5HT-di-PSAc and Cl-C5HT-PSAc in solution

The aims of this chapter are to introduce the diarylethene molecules that were used for this PhD work. The structure of the molecules is commented and linked to the properties and spectral features it confers them⁵⁰. A photokinetic study of the aforementioned molecules in solution is presented. The reversibility and symmetry of the switching is investigated as well as the fatigue resistance of the molecules. The quantum yields for both photo-induced reactions are calculated as well as the switching ratio associated to each molecule.

All the UV-visible spectroscopy measurements presented in this chapter are made with approximately 2 mL of a 1.25×10^{-5} M solution in degassed dimethylformamide (DMF) under 600 rpm stirring. This concentration is within the range of concentrations usually employed to carry out this type of photochemistry studies with DAEs^{50,51,56,59,116,171,172}. A stock solution was prepared for each molecule so that all the experiments are made with the exact same solution. Before every measurement, the aliquot of solution to be used is illuminated with visible light (505 nm) for 10 minutes to always start with all the molecules in the open state.

I - Structure and related properties of the molecular switches

The semi-developed formula of the two diarylethenes that were studied are presented in Figure 4.1. The names of these molecules according to the IUPAC formalism are S,S'-((cyclopent-1-ene-1,2-diylbis(5-methylthiophene-4,2-diyl))-bis(4,1-phenylene)) diethanethioate which will be designated as C5HT-di-PSAc and S-(4-(4-(2-(5-chloro-2-methylthiophen-3-yl)cyclopent-1-en-1-yl)-5-methylthiophen-2-yl)phenyl) ethanethioate which will be designated as Cl-C5HT-PSAc.

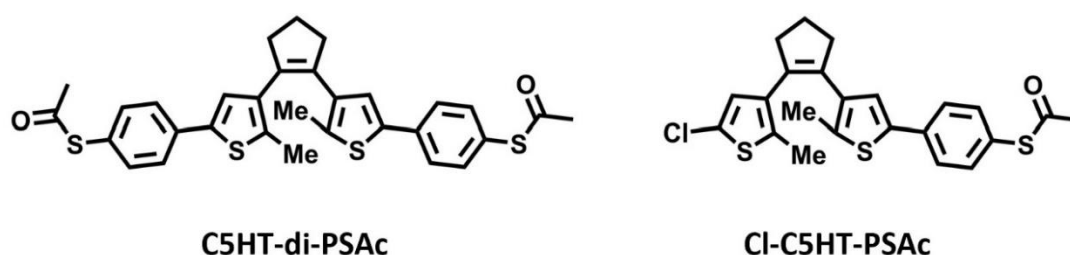


Figure 4.1: Semi-developed formula of the two diarylethenes molecules.

These diarylethene molecules are dithienylethenes i.e., diarylethenes with thiophene rings as aryl moieties. They are dithienylperhydrocyclopentene derivatives since their bridging unit is a perhydrocyclopentene. The role and influence on the properties and spectral characteristics of each component of the molecules is going to be discussed.

1 - Impact of each component of the molecules on its properties

Each subunit of the molecules is represented in Figure 4.2 below for C5HT-di-PSAc.

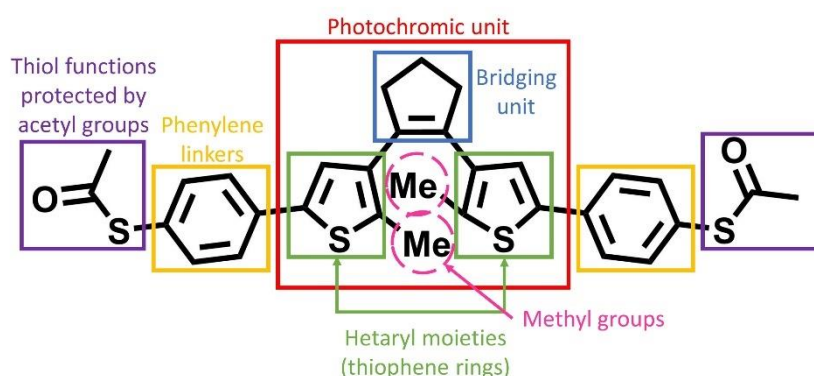


Figure 4.2: Subunits of diarylethene molecule C5HT-di-PSAc.

a - The photochromic unit

The photochromic unit is composed of the hetaryl moieties (thiophene rings) and the bridging unit (perhydrocyclopentene ring). Its role is the most important since it is the part where the photochromism happens, it requires extensive description.

The cyclization of diarylethenes, triggered by UV light, is a 6π -electron electrocyclic reaction. It follows the Woodward-Hoffman principle of molecular orbital symmetry conservation (applied to the π orbitals of the central ring). The cyclization is therefore only permitted in the excited state and occurs as a conrotatory process. Consequently, the substituents on each side of the new bond formed through the photocyclization are in trans-configuration. It is generally considered as a barrierless one-step reaction involving a one-photon excitation that takes place in a unique singlet excited state ($S_1 - 2A$) in the ps time range. The closed form is fully conjugated with a π -system extended to the whole molecule since all of its components are in the same plane.^{26,29,45,46,51,55,173}

The cycloreversion reaction, triggered by visible light in our case, also follows the Woodward-Hoffman principle and a conrotatory path. However, it must overcome an energy barrier (which is the same as for the symmetry forbidden thermal reaction) corresponding to the difference of energy between the ground state ($S_0 - 1A$) of the closed form and that of the open form. One more singlet state is involved ($S_1 - 1B$) which is in this reaction the lowest excited state near the Franck-Condon transition.^{26,29,45,46,55,173}

A complete description based on theoretical calculations of the mechanisms of these two reactions is given in Chapter 1.II.1, the main transitions occurring during these reactions are reminded in a simplified Jablonski diagram (see Figure 4.3).

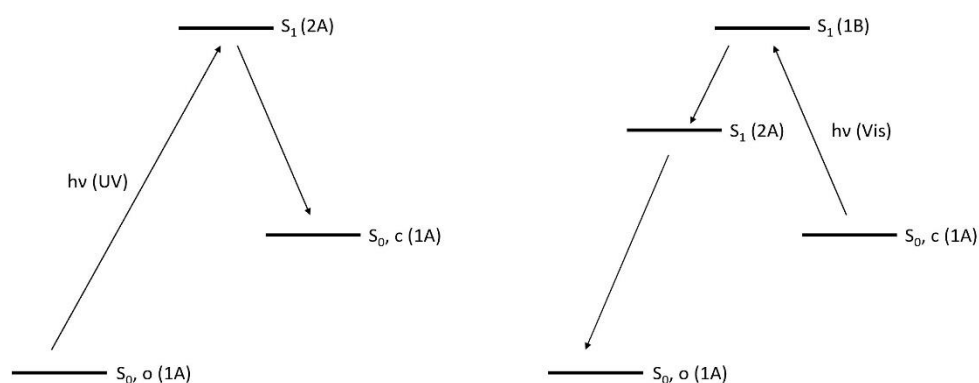


Figure 4.3: Simplified Jablonski diagram summarizing the transitions occurring during the cyclization reaction (left) and cycloreversion (right). Note that ‘o’ stands for opened and ‘c’ for closed, referring to the opened or closed isomer of the molecule.

A minor photocyclization channel via the triplet state (T_1) can also be present, it can be detected by making experiments in absence of oxygen: if the quantum yield of the cyclization reaction is reduced in absence of oxygen (no possible quenching of the triplet state which then cannot contribute to the reaction), it proves the existence of this channel¹⁷².

In order to elucidate all the transitions occurring during the photochromic reactions of our molecule, measurements with time-resolved ultra-fast spectroscopy techniques (femtosecond transient spectroscopy^{30,174}, or nanosecond flash photolysis^{56,116}, for example) would be required. Quantum chemistry calculations could also be made, they are usually made using the distance between the carbon atoms at positions 2 and 6 of the central ring i.e. the carbons in between which the bond is formed upon the cyclization reaction as the reaction coordinate while following the evolution of the potential energy surfaces (PESs)^{44-47,175}.

b - The hetaryl moieties (thiophene rings)

To justify the use of thienyl as heterocyclic aryl group, thermal stability must be considered⁵⁰. Indeed, this heterocyclic aryl group prevents a disrotatory thermally induced reaction (predictable using Woodward-Hoffman rules) to happen in the ground state i.e the opening of the molecule induced by heat^{29,50,173}. In the S_0 state the opened and closed forms of the DAE are separated by a potential energy barrier that guaranties their thermal stability (all diarylethenes with heterocyclic aryls are thermally irreversible P-type photochromes) and define the kinetics of the ring-opening thermic reaction. The barrier height is related to the energy difference between the ground state of the open and the closed state, it depends on the type of aromatic nuclei of the molecule. The larger the energy difference, the lower the barrier on the closed form and the lower the stability of the closed form. Diarylethenes containing aromatic nuclei with the lowest aromatic stabilization energy are the most thermally stable, they are the ones with heterocyclic aryl group. The ones we use, thienyls, with an aromatic stabilization energy of 4.7 kcal/mol, lower than that of furyl (9.1), pyrrolyl (13.8) and phenyl (27.7) are the most stable. The same trend is observed for the values of the relative ground state energy difference between the open and close ring form. It is of -3.3 kcal/mol (for the conrotatory mode) for 1,2-di(3-thienyl)ethene, lower than that of 1,2-di(3-furyl)ethene (9.2), 1,2-di(3-pyrrolyl)ethene (15.5), and 1,2-diphenylethene (27.3)^{29,46}. Thiophene rings also mean a more effective conjugation (lower aromaticity and lower inter-ring torsional angle)⁵⁹.

c - The bridging unit (perhydrocyclopentene ring)

The cyclopentene is the bridging ring between the two aryl groups, the three of them forming the photochromic unit. First of all, one of the main role of this cyclopentene is to prevent the photoisomerization (which is an unwanted side process) reaction by blocking the molecule in cis-configuration^{46,56}. Inserting an ethylene group in a third additional ring is the most efficient way to achieve that, this is what is done here with the perhydrocyclopentene while in most cases the perfluorocyclopentene is used. We will then justify why the use of the former is more beneficial than the use of the latter.

The synthesis of the perhydrocyclopentene is easier than that of the perfluorocyclopentene, it can be synthesized on a large scale and the basic switch can easily be derivatized³⁰. Regarding the photochromism properties, the perhydrocyclopentene facilitates the tuning of the switch properties, especially the choosing of the desired excitation wavelength. Indeed, the λ_{\max}

position of the band of the closed form in the visible region on the UV-visible spectrum of the molecule can be shifted according to the functional groups that are put in para¹⁷⁶. For example, a highly electro-attractive group will make the band redshift. The influence of the substituents is also visible on the chemical shift of the ¹H NMR spectrum of the molecule³⁰. For the perfluorocyclopentene, the position of the band in the visible area for the closed form is always redshifted no matter what the substituents are, the electron-withdrawing properties of the fluorine atoms dominate the absorption properties. Changing the functional groups has no effect on the position of the band on the UV-visible spectrum nor on the chemical shift on the ¹H spectrum. In our case, a tunable DAE was required since we wanted to have an overlap between the absorption band in the visible of the switch and the LSPR peak of gold nanoparticles.

Some claim the presence or absence of fluorine atoms on the cyclopentene ring does not have any effect on the quality of the switching (fatigue)³⁰, others claim it does⁵⁹. Nevertheless, the electron-withdrawing effect of the fluorine atoms stabilizes the thienyl groups, reflecting on the thermal stability of the compounds (absence of ring-opening when exposed to heat). The perhydro derivatives do not have this extra stabilization, the heterocyclic aryl groups and the terminal functional groups must therefore be chosen carefully to preserve high thermal stability^{30,176}.

d - The methyl groups (on the photochromic unit)

Regarding the presence of the methyl groups in trans configuration in position 2' of the thiophene rings (or 2 and 6 of the central phenyl ring), they guarantee the chemical stability of the DAE molecule against oxidation. It was also demonstrated that these methyl groups (2'-position) improve fatigue resistance⁵⁹, then again, the use of benzothiophene units could also improve fatigue resistance, although both thiophene and benzothiophene are acknowledged as the best options regarding the choice of the aryl groups considering the high fatigue resistance they provide¹⁷¹.

Replacing the methyl groups on the photochromic unit by bulkier substituents could help improve the quantum yields of the reactions. Let us remind that the open form of a dithienylethene molecule exist in two conformations: parallel (P), with the thiophene rings in mirror symmetry; and antiparallel (AP), with the thiophene rings in C₂ symmetry⁵¹. It is possible to evaluate the relative percentage of each conformation with ¹H NMR measurements⁵⁶. The photocyclization only happens in the antiparallel conformation, obeying Woodward-Hoffman

rules. The lifetime of the excited state being shorter than the time required for the interconversion between the P to the AP conformer, only the molecules already in the AP conformation can undergo cyclization upon light absorption⁵⁰. For unsubstituted dithienylethenes, there is as many molecules in the parallel conformation as in the antiparallel conformation thus restricting the photocyclization quantum yield to 0.5 maximum. Both emission (luminescence) and photocyclization happen, the former from the molecules in P conformation, the latter from the molecules in AP conformation. There are ways to favorize the AP conformation (and thus increase the cyclization yield) by attaching (π -donor) substituents to the reactive carbons of the thiophene rings^{29,46,51,55}. Other strategies exist to maximize the AP population, one of the most employed is to include the DAEs in a crystalline or polymeric matrix which only permit the AP conformation, the quantum yields can be increased up to 1 if a population of AP conformers exclusively is achieved^{55,56}.

e - The phenylene linkers

Choosing the right substituents to put on each side of the photochromic unit allows to tune the absorbance properties to select the desired excitation wavelength of the molecule or rendering the molecule more adapted to a specific application^{55,56,116}. However, the effects of the different substituents on the photochromic properties must be carefully studied since they can lead to their degradation or even their loss¹⁷¹.

f - The thiol functions protected by acetyl groups

At the extremity of the phenylene linkers we find thiol functions protected by acetyl groups. These protecting groups prevent the oxidation of the thiol functions (see Chapter 2.I.1.c for the deprotection procedure of the thiol functions). Thiols functions were chosen for their affinity with gold since the plan always was to attach the diarylethene molecules to gold nanoparticles. Nevertheless, the electronic effect (electron-donating group, -M effect) of the acetyl groups must be considered when reflecting on the properties of the molecules.

2 - UV-Visible spectral characteristics of the opened and closed form of the molecules

The ring-opening/ring-closing reaction of both molecules is presented in Figure 4.4, as well as the adsorption spectra in solution of their opened and closed forms. The spectra designated as those of the closed isomers, corresponds to spectra recorded at the PSS after irradiation of the solution with UV light at $\lambda_{exc}(UV) = 300$ nm. The spectra of the open isomers

were recorded after 10 minutes of irradiation of the DAE solution with visible light at $\lambda_{\text{exc}}(\text{Vis}) = 505 \text{ nm}$.

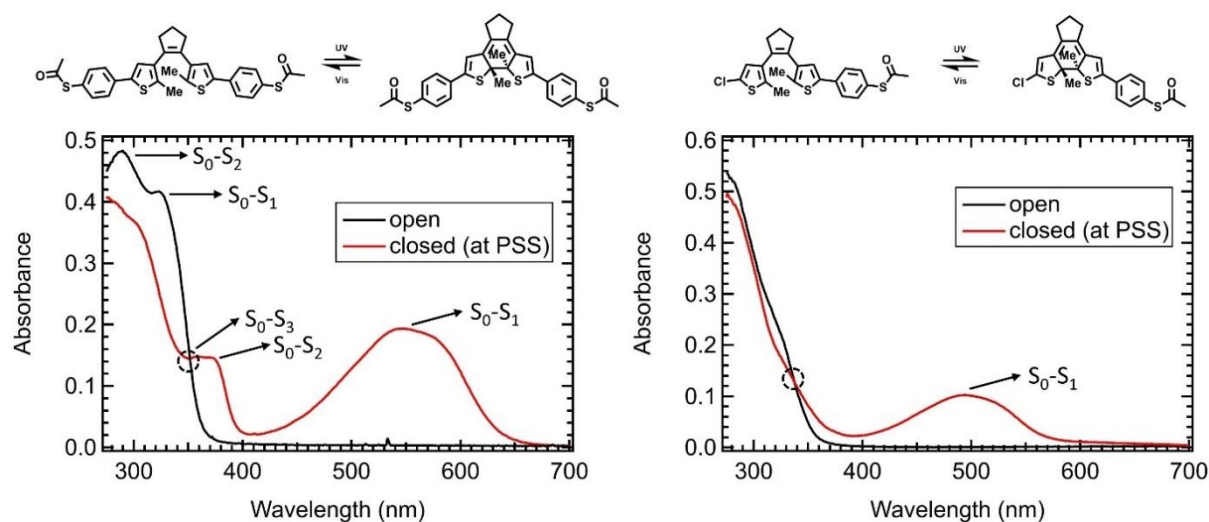


Figure 4.4: Photocyclization and photocycloreversion reaction and the spectra corresponding to the opened and closed form of each molecule. The isosbestic point are circled in dotted line. The spectral transitions corresponding to each band are indicated. The molecules are solubilized in DMF at a concentration of $1.25 \times 10^{-5} \text{ M}$ in a 1 cm cuvette.

It should be noted that the spectra of both molecules present an isosbestic point i.e., a point for which the absorbance remains constant under irradiation of any kind (these points are circled on Figure 4.4). This isosbestic point is located at 352 nm for C5HT-di-PSAc and at 334 nm for Cl-C5HT-PSAc. Both molecules also display a characteristic absorption band in the UV range, a band with two features at 290 and 323 nm for C5HT-di-PSAc and a single band at approximately 272 nm (just before the solvent cut-off) for Cl-C5HT-PSAc.

The opened forms of the molecules do not absorb in the visible while the closed forms of the molecules display a broad absorption band in the visible region. C5HT-di-PSAc's band is located in the 400 - 650 nm range with a maximum absorbance at 546 nm. Cl-C5HT-PSAc's band is in the 400 - 550 nm range with a maximum absorbance at 492 nm. Cl-C5HT-PSAc's band maxima are blue-shifted because its conjugated system is smaller (the molecule possess less electronic density) than that of C5HT-di-PSAc⁵⁹.

The transitions were associated to each band based on the assignments made for analogous molecules found in the literature^{173,177}. The most important transitions are the two $S_0 \rightarrow S_1$ since they are the transitions involved in the photochromic reactions (see 4.1.a). The λ_{max} of each band, its associated transition, absorbance value, and molar absorption coefficient are summarized in Table 4.1.

Table 4.1: Characteristics of each absorption band present on the UV-visible spectra of the two molecules.

Molecule 1 (C5HT-di-PSAc)			
λ_{\max} (nm)	Absorbance	ϵ (L.mol ⁻¹ .cm ⁻¹)	Transition
290 (o)	0.4834	38 700	S ₀ → S ₂
323 (o)	0.4167	33 300	S ₀ → S ₁
356 (c)	0.1470	11 800	S ₀ → S ₃
373 (c)	0.1456	11 600	S ₀ → S ₂
546 (c)	0.1934	15 500	S ₀ → S ₁
Molecule 2 (Cl-C5HT-PSAc)			
λ_{\max} (nm)	Absorbance	ϵ (L.mol ⁻¹ .cm ⁻¹)	Transition
492 (c)	0.0970	7760	S ₀ → S ₁

The position of the absorbance bands is particularly important regarding the choice of the LEDs. The emission wavelength of the LEDs must correspond as much as possible to the absorbance maxima of the bands corresponding to the transitions involved in the photochromic reactions (photocyclization and photocycloreversion) of the molecules. Regarding the wavelength of the visible LED it is not that important since it was demonstrated that the quantum yield of the ring-opening reaction was independent from the excitation wavelength when it is in the visible^{59,171}. However, with a LED producing light at 505 nm we are roughly located in the middle of the absorption band of both molecules in their closed form. Regarding the wavelength of the UV LED, it is more determinant since the quantum yield of the photocyclization depends on the excitation wavelength. Many choose to irradiate the molecules at the wavelength of the isosbestic points to make sure the influence of changes in the part of incident light absorbed in the sample are negligible^{116,172}. We chose to use a UV LED emitting at 300 nm i.e., between the band at 323 nm of C5HT-di-PSAc and the band at approximately 272 nm of Cl-C5HT-PSAc. We remind that these two bands are those corresponding to the transitions involved in photocyclization. This LED is therefore adapted to both our molecules. The absorbance value, and molar absorption coefficient at $\lambda_{\text{exc}}(\text{UV} - 300 \text{ nm})$ and $\lambda_{\text{exc}}(\text{Vis} - 505 \text{ nm})$ for both the opened and closed forms of the molecules and at λ_{iso} (wavelength of the isosbestic point) are summarized in Table 4.2.

Table 4.2: Absorbance value, and molar absorption coefficient at $\lambda_{\text{exc}}(\text{UV} - 300 \text{ nm})$, $\lambda_{\text{exc}}(\text{Vis} - 505 \text{ nm})$ and λ_{iso} .

Molecule 1 (C5HT-di-PSAc)		
	Absorbance	ϵ (L.mol ⁻¹ .cm ⁻¹)
$\lambda_{\text{exc}}(\text{UV} - 300 \text{ nm}) - \text{o}$	0.4546	36367
$\lambda_{\text{exc}}(\text{Vis} - 505 \text{ nm}) - \text{o}$	0	0
$\lambda_{\text{exc}}(\text{UV} - 300 \text{ nm}) - \text{c}$	0.3688	29506
$\lambda_{\text{exc}}(\text{Vis} - 505 \text{ nm}) - \text{c}$	0.1377	11017
$\lambda_{\text{iso}} (352 \text{ nm})$	0.1447	11574
Molecule 2 (Cl-C5HT-PSAc)		
	Absorbance	ϵ (L.mol ⁻¹ .cm ⁻¹)
$\lambda_{\text{exc}}(\text{UV} - 300 \text{ nm}) - \text{o}$	0.3738	29903
$\lambda_{\text{exc}}(\text{Vis} - 505 \text{ nm}) - \text{o}$	0	0
$\lambda_{\text{exc}}(\text{UV} - 300 \text{ nm}) - \text{c}$	0.3472	27772
$\lambda_{\text{exc}}(\text{Vis} - 505 \text{ nm}) - \text{c}$	0.0940	7520
$\lambda_{\text{iso}} (334 \text{ nm})$	0.1516	12130

II - Kinetics of the ring closing reaction: irradiation of the switches with UV light

In this second part, UV-visible spectroscopy measurements conducted following UV light irradiation to study the ring-closing reaction kinetics of the molecules as well as their resistance to fatigue are presented.

1 - Steady-state UV-visible spectroscopy measurements

a - Spectral features corresponding to the closed form

The evolution of the light absorption spectrum of the molecules for the ring-closing reaction is shown in Figure 4.5. We can see that the absorption band in the visible region increases upon UV light irradiation: the molecules are progressively switched to their closed form. In the meantime, the absorbance of the UV bands decreases. The solution goes from colorless to purple, which is usual for DAEs¹⁷². At some point, the absorbance bands no longer evolve, the photostationary state - an equilibrium between ring-opening/ring-closing reactions - has been reached¹⁷¹. For the ring-opening reaction, i.e., under visible light irradiation, the reverse evolution is expected but not necessarily in the same time range. The closed form also absorbs in the UV region, both ring-closing and ring-opening occur after photoexcitation, explaining why a photostationary state (equilibrium situation) will always be reached^{30,172}.

Indeed, a UV photon can be absorbed by the open-ring form inducing the expected ring-closing (switching) reaction, but it can also be absorbed by the closed-ring form inducing the opposite reaction i.e., the ring-opening (backswitching) reaction. This situation explains why the photostationary state is an equilibrium state between two reactions in competition, it is reached when the probability for any of these both reactions to occur is the same.

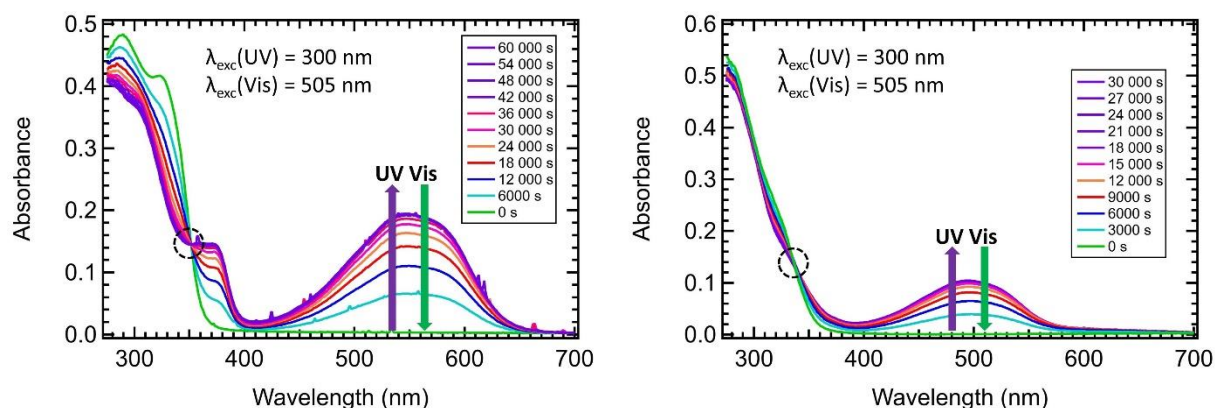


Figure 4.5: Evolution of the spectra under UV and visible irradiation for C5HT-di-PSAc (on the left) and Cl-C5HT-PSAc (on the right). The isosbestic points are circled in dotted line.

b - Photostationary state (PSS)

At first, the kinetics of the ring-closing reaction of both molecules was studied. The solution was exposed to UV light (see Table 4.3), 1000 consecutive short (30 s) irradiations were performed until the photostationary state was reached. Here, we want to assess the duration of the UV light exposure required to make the maximum amount of molecules switch. We also want to know if after the maximum number of molecules underwent photocyclization, we reached the PSS, or if the molecules are degrading i.e., a side product is formed.

Table 4.3: UV LED ($\lambda_{\text{exc}}(\text{UV}) = 300 \text{ nm}$) parameters for the ring-closing reaction monitoring.

Molecule 1 (C5HT-di-PSAc)						
LED	I (A)	P (mW)	Φ (mW/cm ²)	Φ_{photons} (photons/s/cm ²)	Irradiation time (s)	Irradiation number
UV	0.5	5.5×10^{-2}	0.194	2.93×10^{14}	30	1000
Molecule 2 (Cl-C5HT-PSAc)						
LED	I (A)	P (mW)	Φ (mW/cm ²)	Φ_{photons} (photons/s/cm ²)	Irradiation time (s)	Irradiation number
UV	0.5	5.5×10^{-2}	0.194	2.93×10^{14}	60	1000

The kinetics of the ring-closing reaction was monitored at the wavelengths chosen as follows:

_ 450 nm and 600 nm are located at the extremities of the absorption band in the visible corresponding to the transition involved in the photocycloreversion of both molecules.

_ 520 nm and 537 nm respectively correspond to the LSPR wavelength of 25 nm and 50 nm gold nanoparticles.

520 nm is chosen as monitoring wavelength for most of the experiments presented in this chapter. The choice of the monitoring wavelength does not appear determinant as long as it is chosen somewhere on the absorbance band in the visible where the absorbance is high enough. Indeed, as shown in Figure 4.6 the evolution of the absorbance is extremely similar whether it is monitored at 520, 537 or even 600 nm.

The monitoring at λ_{\max} of the band in the visible corresponding to the transition involved in the photocycloreversion is presented and used further in this chapter (see 4.IV) for the calculations of quantum yields.

The evolution of the absorbance monitored at the different wavelengths is presented in Figure 4.6.

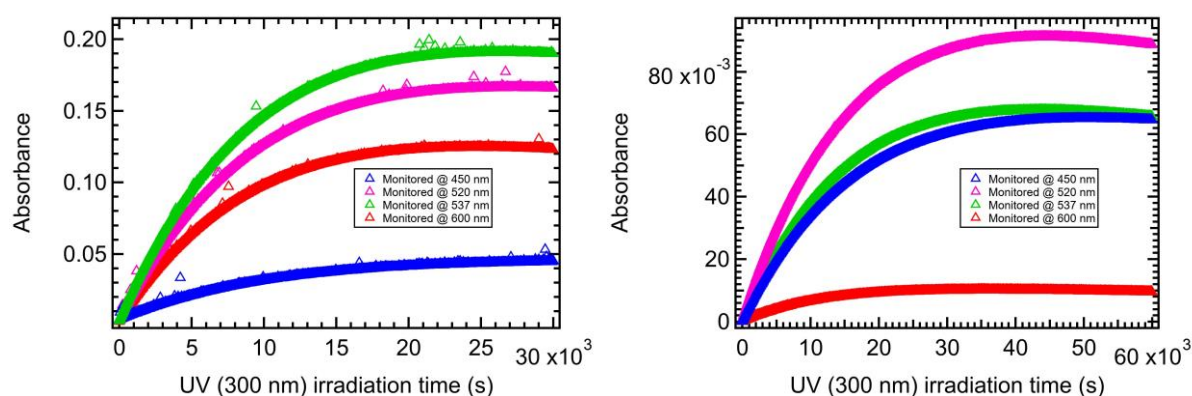


Figure 4.6: Evolution of the absorbance under UV irradiation monitored at various wavelength for C5HT-di-PSAc (on the left) and Cl-C5HT-PSAc (on the right).

It is easily noticeable that C5HT-Di-PSAc switches faster than Cl-C5HT-PSAc. For C5HT-di-PSAc, it takes 23 100 s (6 h 25 minutes) to reach the plateau corresponding to the PSS. For Cl-C5HT-PSAc it takes 36 660 s (10 h 11 minutes) to reach a plateau before the absorbance starts to decrease (using data at 520 nm). The time it takes to reach the PSS was calculated as follows: all data points that clearly belonged to the PSS were averaged (between 24 990 and 30 000 s, 168 points, for C5HT-di-Ac), this mean value (0.166173 for C5HT-di-Ac) was then subtracted to all absorbance value. The first value with a difference strictly inferior to 0.001 to the mean value was considered to correspond to the first point of the PSS. The calculation was made slightly differently for Cl-C5HT-PSAc since at some point the absorbance starts decreasing. The average value (0.086853) was calculated on a constant part of the curve (between 40 980 s and 47 040 s, 102 points).

There seemed to be some differences in the evolution according to the monitored wavelength. Each curve was therefore normalized by its maximum values, and they were all plotted in Figure 4.7.

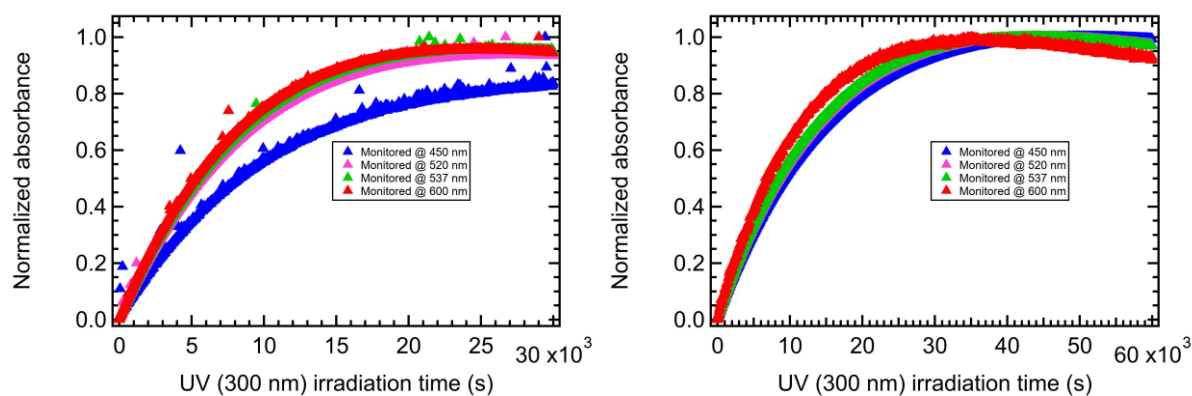


Figure 4.7: Evolution of the normalized absorbance under UV irradiation monitored at various wavelengths for C5HT-di-PSAc (on the left) and Cl-C5HT-PSAc (on the right).

The UV LED is operating at its maximum power for these measurements (see Table 4.3). It was chosen not to measure the development to the PSS using lower power considering it already takes a very long time using maximal power. However, using lower power, we would expect the PSS to appear at the same absorbance value, it would just take longer to reach it.

2 - Assessment of the fatigue resistance of the molecules

a - Evolution of the absorbance at a specific wavelength and at the isosbestic point

At 520 nm

The presence of degradation is investigated using the absorbance evolution under UV irradiation data monitored at 520 nm presented in Figure 4.6. Pariani et al.⁵⁹ showed that the by-product formation (fatigue) occurred preferentially during the photocyclization reaction under prolonged UV irradiation due to the irradiation of closed form molecules after this reaction has occurred. The fact that the absorbance decreases after reaching a plateau indicates that there is degradation i.e. generation of a side-product¹⁷¹.

If we look at the spectra of Cl-C5HT-PSAc, shown in Figure 4.8, at the time the absorbance starts to decrease after reaching a plateau i.e., at $t = 36\ 660$ s, and at the last spectra of the experiment at $t = 60\ 000$ s, we can distinguish a small hypsochromic shift of the band maximum indicating the production of a by-product^{59,171}. It is typical for thiophene derivatives, and more pronounced for electron-deficient ones¹⁷¹. Both the ring-closed molecules and the side-product display remarkably similar absorbances in the visible region since the π -conjugation pathways throughout their molecular backbone are the same. However, the absorbance of the byproduct is significantly lower explaining the typical decrease of the absorption band upon prolonged UV irradiation⁵⁹.

This experimentally observed hypsochromic shift was also shown in theoretical results and explained: the dihedral angle θ between thiophenes and phenyl rings in dithienylethenes derivatives is large. It increases upon formation of the by-product from the ring-closed molecule due to increased steric repulsion caused by the expansion of the former thiophene/thiazole 5-membered ring to a 6-membered ring. A significant increase of the dihedral angle due to the strong steric repulsion leads to a more complicated delocalization of the π -electron density, requiring a stronger twisting of the phenyl group resulting in the experimentally observed hypsochromic shift of the absorbance maximum of the byproduct¹⁷¹.

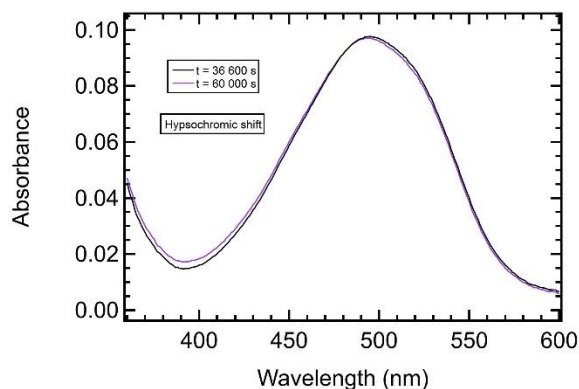


Figure 4.8: Spectra allowing to demonstrate the presence of a small hypsochromic shift for prolonged UV irradiation of Cl-C5HT-PSAc.

At the isosbestic points

A particularly useful feature to confirm that there is fatigue or not is the evolution of the isosbestic points^{56,116}. This evolution is shown in Figure 4.9, we can see that Cl-C5HT-PSAc's isosbestic point is not well defined: it starts shifting after 12 000 s of UV irradiation, confirming the degradation of the molecules towards a side-product throughout the measurement. In contrast, C5HT-Di-PSAc's isosbestic point is perfectly defined and is not modified by the UV irradiation during the measurement. This indicates that C5HT-di-PSAc molecules are not degrading.

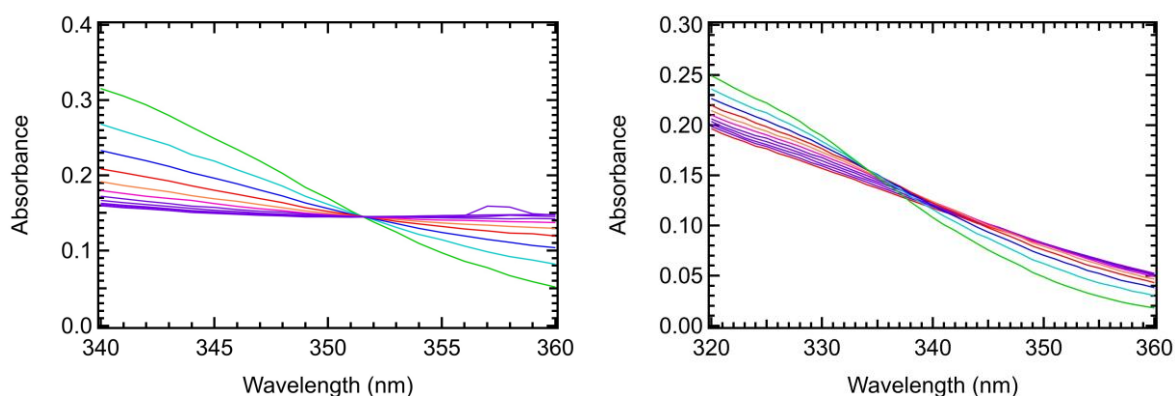


Figure 4.9: Isosbestic points for a UV irradiation of 30 000 s (C5HT-di-PSAc, on the left) and of 60 000 s (Cl-C5HT-PSAc, on the right).

The evolution of the absorbance at the isosbestic points is shown in Figure 4.10.

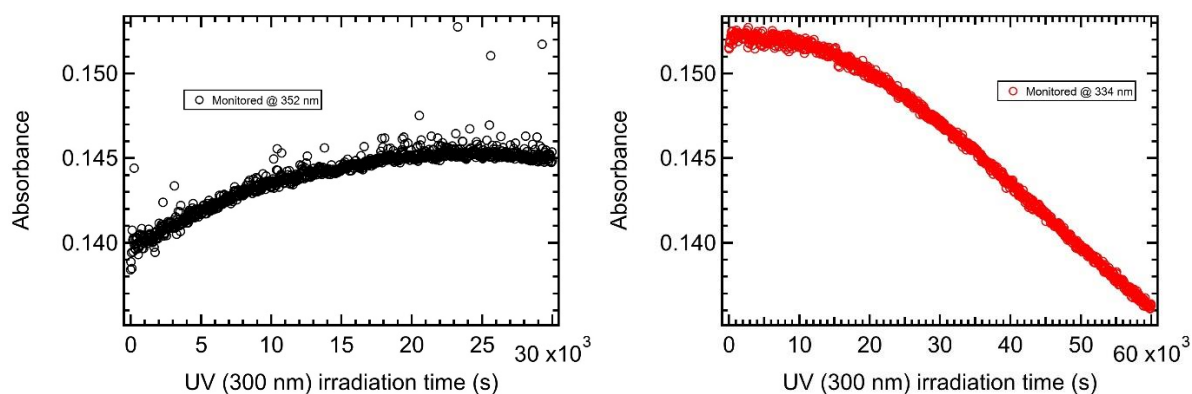


Figure 4.10: Evolution of the absorbance at the isosbestic point throughout the UV illumination, for C5HT-di-PSAc (left) and Cl-C5HT-PSAc (right).

In the case of Cl-C5HT-PSAc, the absorbance at the isosbestic point is steadily decreasing and almost immediately after the beginning of the UV irradiation (about 200 s), the fatigue of this molecule is clearly established. In the case of C5HT-di-PSAc, the value seems to slightly increase before stabilizing but the interval in which the value evolves is very tight, inferior to the resolution of the spectrophotometer so much that it would not be unreasonable to consider the absorbance as constant throughout the measurement. Another hypothesis is that a 3.5% thermal drift of the spectrophotometer occurred over the 8.5 hours duration of the experiment.

b - Potential origins of the degradation in Cl-C5HT-PSAc and nature of its by-product (BP)

The photochemical mechanisms (origin, steps, nature of the by-products) of degradation occurring upon photoconversion of DAEs was studied both theoretically and experimentally^{45,59,116,171,172,178,179}.

Different groups of DAEs undergo different photodegradation reactions: oxidation and elimination reactions from the molecules in the closed form. However, the formation of an annulated isomer (a condensed ring system) upon UV irradiation of the closed-ring molecules as a side-product has been reported for both perfluorocyclopentenes and perhydrocyclopentenes bridged dithienylethenes derivatives with quite different structures. It would occur according to a formal 1,2-dyotropic rearrangement following a concerted mechanism or a mechanism involving radical or ionic intermediates¹⁷¹.

Mendive-Tapia et al.⁴⁵ elucidated the formation mechanism of this BP with theoretical calculations, it is reminded here in a few words but a more complete description is available in Chapter 1.II.2.b. For the ring-opening reaction a transition state on the covalent excited state $S_1(2A)$ involving bond breaking of the penta-ring leads to a low energy $S_1(2A)/S_0(1A)$ conical intersection seam, which lies above one of the transition states leading to the by-product isomer on the ground state. Radiationless decay from the former to the latter occur leading to formation of the by-product.

Pariani et al.⁵⁹ also observed the apparition of this by-product for the series of 1,2-dithienyloctafluorocyclopentenes they studied. Oplachko et al.¹⁷² also reported that the asymmetrical diarylcyclopentenone (DCP) bearing benzothiophene units they studied undergoes photodegradation in two ways : the well-known formal 1,2-dyotropic rearrangement (no oxygen involved) and oxidation of the DCP molecule (whether it is opened or closed) by singlet oxygen produced via the quenching of the excited triplet state of the molecule by the dissolved oxygen in the solution.

The first time this BP was isolated and analyzed, its structure was determined by X-ray crystallography. Herder et al. isolated it for all the DAEs they studied by UPLC coupled to MS and characterized it by ^1H NMR. Performing this kind of analysis for our molecule would probably confirm that the by-product is also the same in our case. Nevertheless, considering all the characteristics shared by our molecules and some of the molecules they studied (bridging unit, heteroaryl moieties, phenyl rings), it is safe to make the hypothesis we have the same kind of by-product. It is represented in Figure 4.11 for Cl-C5HT-PSAc. The terminal substituents beard by the phenyl rings are different but they would rather influence the quantity of side-product formed than its nature¹⁷¹.

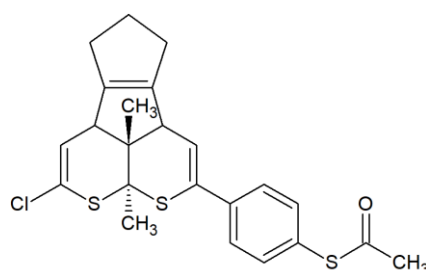


Figure 4.11: Hypothetic by-product of Cl-C5HT-PSAc.

c - Strategies to prevent degradation: introducing specific substituents

According to Herder et al.¹⁷¹, the most electron-rich DTEs bearing perhydrocyclopentene bridges and electron-donating or electron-neutral substituents on the adjacent phenyl rings, are almost quantitatively converted to the byproduct. For these molecules the rate of the BP formation (and thus its QY) is in the same order of magnitude as the rate of the ring-opening reaction (and thus its QY), which explains the decrease of the amounts photochromes under continuous UV irradiation and high irreversibility during cycle measurements. Some changes in the structure of the molecule could however reduce the fatigue.

The possibility to fully block this undesired reaction only exist for pentafluorocyclopentene derivatives. It consists in introducing methyl group on the 4-position (β -position) of the thiophene ring, but since the suppression of this reaction (reduction of fatigue) demonstrated for perfluorocyclopentenenes comes from the steric hindrance between the methyl groups in β -position and the fluorine atoms which prevent the breaking of the C-S bond in the thiophene ring and subsequent formation of the annulated ring molecules it does not work for perhydrocyclopentenenes⁴⁵.

Introducing a perfluorocyclopentene bridge strongly reduces byproduct formation by a factor 15 (on the QY of BP formation reaction) for donor- or electron-neutral substituted compounds of a factor 15. However, it was explained in 4.I that introducing this type of bridging unit involved a loss of the tunability of the molecules¹⁷¹.

For perhydrocyclopentenenes compounds, introducing substituents with sufficient acceptor strength ($-M$ effect) on the adjacent phenyl rings (in para position) can reduce the formation of byproduct up to the amount brought by the introduction of the perfluorocyclopentene ring (in our case the terminal -Ac is rather acceptor)¹⁷¹.

Other solutions are to use benzothiophenes or thiazoles as hetaryl moieties although Oplachko et al.¹⁷² demonstrated the improvement was not guaranteed for the former and Pariani et al.⁵⁹ demonstrated the improvement was not guaranteed for the latter. It can also be envisioned to oxidize the sulfur atom in the thiophene ring or to replace it with an acetyl group¹⁷¹.

Finally, an interesting solution would be to use chemically inert CF_3 or SF_5 groups (strong $-I$ effect) as terminal substituents at the meta positions of the phenyl rings instead of Cl

in para (or leaving the Cl in para, it should not make a big difference) since it does not modify the photoconversion rates nor the absorption spectrum and can reduce by-product formation by a factor 20 to 30 compared to unsubstituted or donor-substituted DTEs¹⁷¹.

d - Prediction of fatigue resistance

After underlining the role of the UV light adsorption by the closed form (C) in the fatigue resistance, Pariani et al.⁵⁹ proposed to calculate the ratio of the relative absorbance cross-section of the two forms (ϵ_C/ϵ_O) at the UV irradiation wavelength. They found a correlation between this ratio and the fraction of degraded molecules. A low ratio means a dominant absorption cross-section of the open-ring molecules, these molecules are the ones that will absorb most of the UV light leading to the photocyclization reaction. Reciprocally, a high ratio means a dominant absorption cross-section of the ring-closed molecules, these molecules are the ones that will absorb most of the UV light leading to an enhancement of the degradation⁵⁹.

In the case of our molecules, the ratio for Cl-C5HT-PSAc is worth 0.93, it is superior to that of C5HT-di-PSAc (0.81), which is consistent with the measurements that showed the presence of degradation for Cl-C5HT-PSAc and did not for C5HT-di-PSAc.

To obtain smaller values of this ratio, the wavelengths of the absorbance band in the UV of the two different forms must be as separated as possible or present the lowest absorbance band in the UV as possible for the closed form. Such tuning of the absorbance bands is achievable by introducing the relevant building-blocks in the structure of the molecule⁵⁹ (see 4.I).

Pariani et al.⁵⁹ showed that there is also a correlation between the dose of UV photons absorbed by the closed molecules and the number of degraded molecules. They also demonstrate that the formation rate of the side-product is proportional to the number of UV photons absorbed multiplied by the quantum yield of the side reaction.

All these correlations show how important the spectral characteristics of the molecules at the UV illumination wavelength are. The ratio ϵ_C/ϵ_O is a very useful tool to predict the fatigue resistance for different UV irradiation wavelength since the fatigue resistance will depend on the spectral characteristics of the molecule at this wavelength and not simply of the energy of the photons: lower photon energy does not necessarily mean higher fatigue resistance and vice

versa. If the absorption of the closed molecules at a low irradiation wavelength (i.e., high photon energy) is weak, the degradation will not be promoted⁵⁹.

III - Switching in both directions: reversibility, symmetry, and stability

The crucial characteristics of the switching that are its reversibility and symmetry were determined using UV-visible spectroscopy measurements recorded following luminous irradiation of the molecules. The ability of the molecules to undergo a large number of switching cycles was also tested.

1 - Reversibility: back-switching (ring-closing reaction)

The reversibility of the switching was then evaluated. We now use both LEDs with the parameters given in Table 4.4.

Table 4.4: LEDs ($\lambda_{\text{exc}}(\text{UV}) = 300 \text{ nm}$ and $\lambda_{\text{exc}}(\text{Vis}) = 505 \text{ nm}$) parameters for the reversibility measurements.

Molecule 1 (C5HT-di-PSAc)						
LED	I (A)	P (mW)	Φ (mW/cm ²)	Φ_{photons} (photons/s/cm ²)	Irradiation time (s)	Irradiation number
UV	0.5	5.5×10^{-2}	0.194	2.93×10^{14}	30	100 (3000 s)
Vis	1.3	1.30	2.65	6.74×10^{15}	30	500 (15 000 s)
Molecule 2 (Cl-C5HT-PSAc)						
LED	I (A)	P (mW)	Φ (mW/cm ²)	Φ_{photons} (photons/s/cm ²)	Irradiation time (s)	Irradiation number
UV	0.5	5.5×10^{-2}	0.194	2.93×10^{14}	30	100 (3000 s)
Vis	1.3	1.30	2.65	6.74×10^{15}	30	200 (6000 s)

Only a fraction of the molecules is switched to reduce the duration of the experiment. We need to know if the molecules switch back, then if they all switch back (full reversibility) and finally, the duration of the ring-opening reaction. These reversibility measurements are shown in Figure 4.12. Note that a single switching cycle was performed, it consisted in a 3000 s UV light irradiation (subdivided in 100 consecutive short 30 s UV light irradiation) followed by a 15 000 s visible light (subdivided in 500 consecutive short 30 s visible light irradiation).

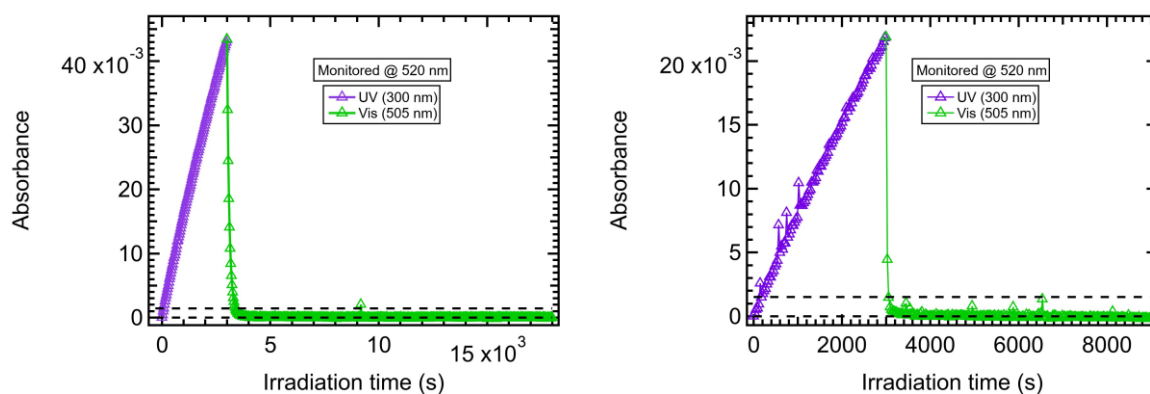


Figure 4.12: Reversibility measurements for C5HT-di-PSAc (on the left) and Cl-C5HT-PSAc (on the right). The molecules are illuminated with UV light for 3000 s and then with visible light until they all switch back to their opened form.

Both molecules display full and reversible back-switching: it is possible to switch all the molecules back to the starting (absorbance) point. For C5HT-Di-PSAc, 840 s of visible irradiation are necessary to make the molecules that have been switched by the previous 3 000 s of UV irradiation switch back to the open-ring state. For Cl-C5HT-PSAc, 660 s of visible irradiation are necessary to make the molecules that have been switched by the previous 3 000 s of UV irradiation switch back to the open state. However, it is necessary to take into account the drastic difference of power between the UV and the visible LED. As shown in Table 4.4, the visible LED is much more powerful than the UV LED. If we look at Φ_{photons} , the visible LED is 23 times more powerful than the UV LED, the UV illumination time must then be divided by 23, which gives 130 s.

The dotted lines in Figure 4.12 are used to define an even smaller portion of molecules able to switch fully reversibly in a much smaller amount of time, required to conduct switching cycles experiments. The irradiation times required to make it switch in both directions are determined; these values are going to be used for the fatigue resistance cycles measurements presented further in Figure 4.14.

The method to define this smaller portion is described for C5HT-di-PSAc. The first dotted line is drawn at $t_{0, \text{UV}} = 0$ s (starting point of UV irradiation) and crosses the absorbance data of visible irradiation at $t_{f, \text{vis}} = 3930$ s, for safety the end point is chosen to be $t_{f, \text{vis}} = 4200$ s. The second dotted line is drawn at $t_{f, \text{UV}} = 90$ s (of UV irradiation), it crosses the absorbance data of the visible irradiation part just below $t_{0, \text{vis}} = 3390$ s (starting point of visible irradiation). The times corresponding to the starting and the end point on both sides (UV on the left, visible

on the right) are subtracted: $\Delta t_{UV} = t_{f, UV} - t_{0, UV} = 90 - 0 = 90$ s and $\Delta t_{Vis} = t_{f, Vis} - t_{0, Vis} = 4200 - 3390 = 810$ s. We chose to subdivide the UV irradiation time in 3 steps of 30 s and the visible irradiation time in 6 steps of 135 s. All these values are summarized in Table 4.4. It is important to note that it has been demonstrated that subdividing an irradiation time in several steps does not affect the number of molecules that are switched¹⁸⁰.

2 - Symmetry of the switching

The symmetry of the switching was also studied with the results of the measurements presented in Figure 4.12.

The data were replotted (see Figure 4.13) in order to follow the evolution of the absorbance according to the number of photons the solution receives: the time is simply multiplied by the photon flux $\Phi_{photons}$. This $\Phi_{photons}$ is obtained by dividing the luminous flux in mW/cm² by the energy of one photon (hc/λ) in J.

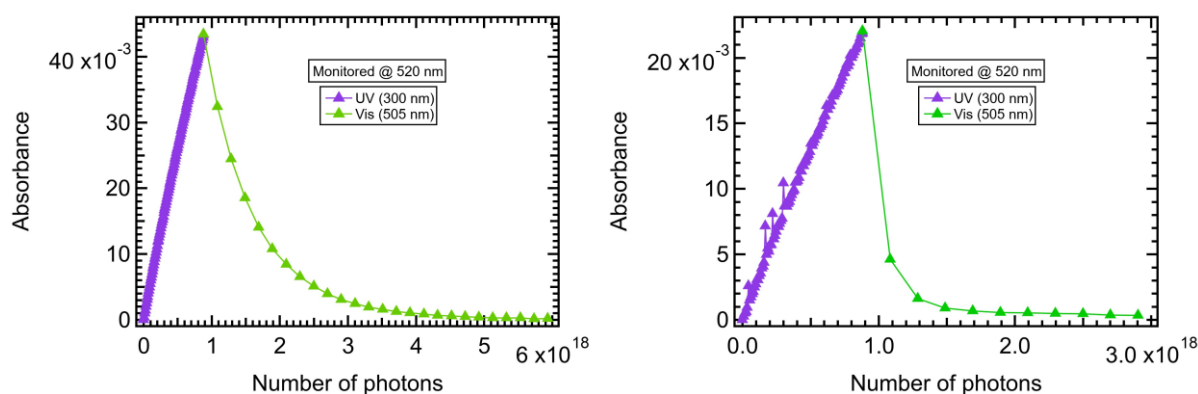


Figure 4.13: Reversibility measurements according to the number of photons for C5HT-di-PSAc (on the left) and Cl-C5HT-PSAc (on the right).

It appears immediately that the switching is not symmetrical, the photocyclization (triggered by UV illumination) being faster than the photocycloreversion (triggered by visible light). In both cases, the solution receives 8.82×10^{17} UV photons during the 3 000 s of irradiation (100 % of the molecules of the small portion are switched). For C5HT-di-PSAc, 5.658×10^{18} photons are required to make all the molecules switch back to the open state. In Cl-C5HT-PSAc's case, 4.45×10^{18} photons are necessary to make all the molecules switch back.

3 - Stability of the molecular switches under consecutive UV/visible exposure (cycles)

Cycling measurements are a usual method to study the fatigue resistance of photochromic compounds⁵⁹. They consist in subsequent illuminations with UV and visible light (the following procedure is repeated a certain number of times): the uncolored solution is exposed to UV light and then to visible light up to the total color bleaching. We want to know if the molecules can sustain their fully reversible switching over a certain number of switching cycles (40). The parameters used for these measurements are presented in Table 4.5.

Table 4.5: LEDs ($\lambda_{exc}(UV) = 300$ nm and $\lambda_{exc}(Vis) = 505$ nm) parameters for the cycles measurements.

Molecule 1 (C5HT-di-PSAc)						
LED	I (A)	P (mW)	Φ (mW/cm ²)	$\Phi_{photons}$ (photons/s/cm ²)	Irradiation time (s)	Irradiation number
UV	0.5	5.5×10^{-2}	0.194	2.93×10^{14}	30	3 (90 s)
Vis	1.3	1.30	2.65	6.74×10^{15}	135	6 (810 s)
Molecule 2 (Cl-C5HT-PSAc)						
LED	I (A)	P (mW)	Φ (mW/cm ²)	$\Phi_{photons}$ (photons/s/cm ²)	Irradiation time (s)	Irradiation number
UV	0.5	5.5×10^{-2}	0.194	2.93×10^{14}	90	3 (270 s)
Vis	1.3	1.30	2.65	6.74×10^{15}	165	6 (990 s)

The cycles are performed with the very small portion that had been previously defined (see Figure 4.12). The results are shown in Figure 4.14.

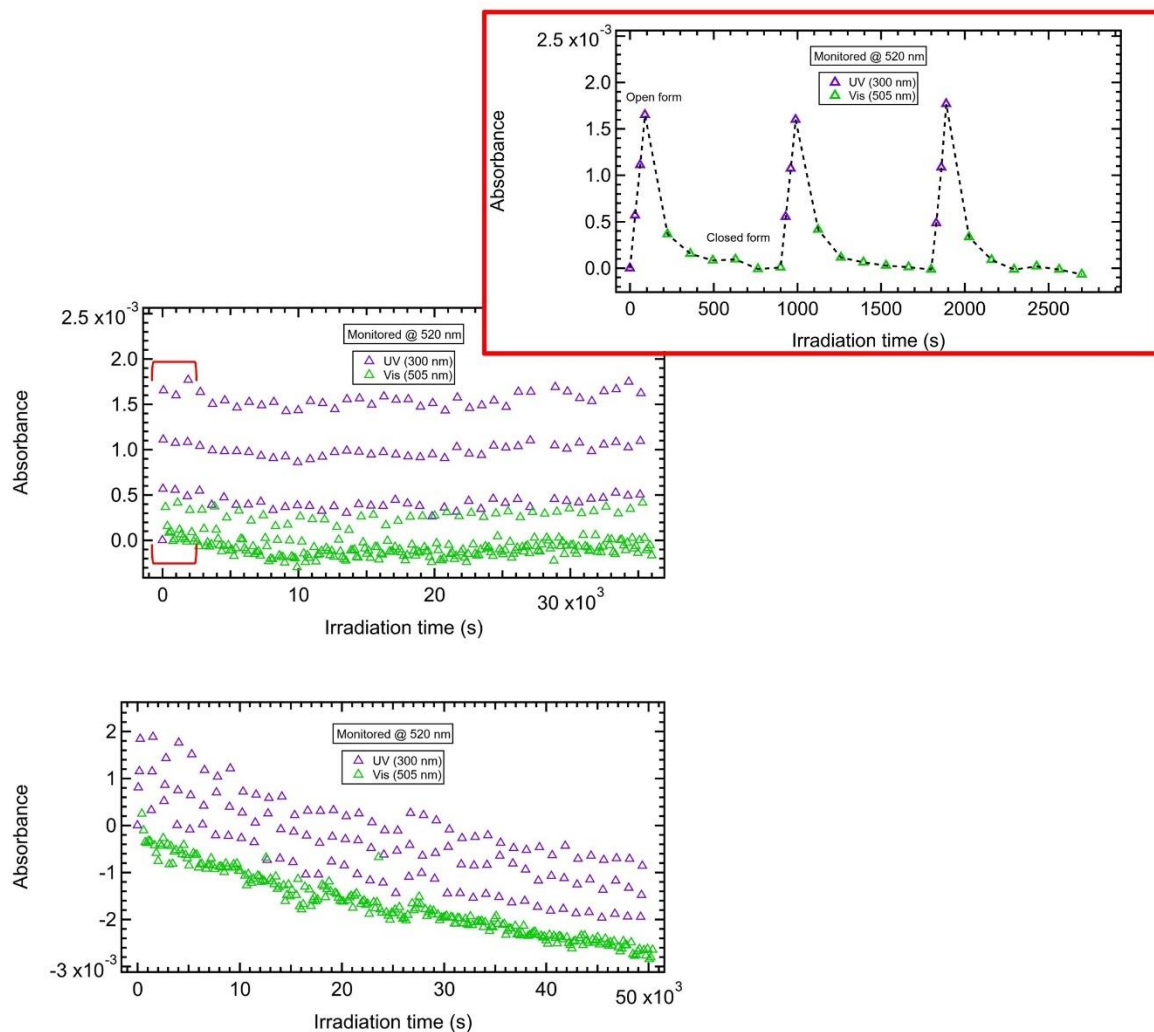


Figure 4.14: Evolution of the absorbance over 40 switching cycles for C5HT-di-PSAc (on the left) and Cl-C5HT-PSAc (on the right). In the case of C5HT-di-PSAc, each cycle consists in 3 consecutive UV light irradiations of 30 s followed by 6 consecutive visible light irradiations of 135s. In the case of Cl-C5HT-PSAc, each cycle consists in 3 consecutive UV light irradiations of 90 s followed by 6 consecutive visible light irradiations of 165s. The insert is a zoom on the three first cycles for C5HT-di-PSAc.

C5HT-di-PSAc is able to switch fully reversibly over 40 switching cycles: the absorbance increases and decreases to the same absorbance values for each cycle. If it were not the case, we would observe a progressive reduction of the amplitude of the variations of the absorbance. Globally, the absorbance slightly fluctuates, these fluctuations are attributed to the spectrophotometer. Regarding Cl-C5HT-PSAc, the absorbance globally decreases, further indicating fatigue of the molecules but a contribution to this decrease could be due to an instrumental issue. In order to free us from absorbance variations of instrumental origin, the difference between the maximal and minimal value of the absorbance for each cycle was plotted in Figure 4.15.

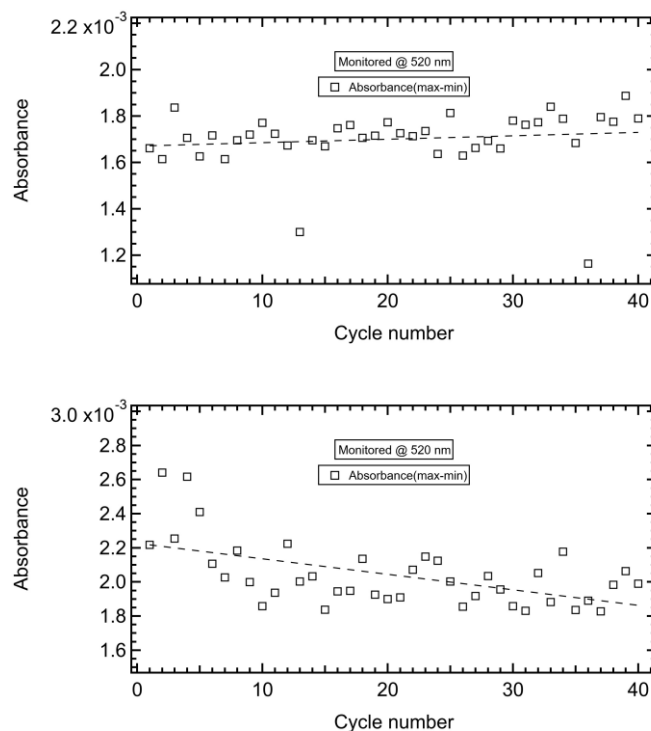


Figure 4.15: Absorbance amplitude of each of the 40 cycles for C5HT-di-PSAc (top) and Cl-C5HT-PSAc (bottom).

The consistency of the absorbance amplitude for C5HT-di-PSAc confirms the absence of degradation. A slight decrease of the absorbance amplitude is still observed for Cl-C5HT-PSAc confirming the degradation of the molecules.

A comment on the effect of the oxygen can be made consecutively to these measurements, Pariani et al.⁵⁹ observed no difference for up to 100 cycles regarding the degradation in the presence or absence of oxygen. They underline it is consistent with the fact that a single major by product is formed upon short irradiations, no matter the presence of oxygen. This side-product is likely the condensed derivative found for similar compounds (the version of this side-product for our molecules has been shown in Figure 4.11). According to them, side-products resulting from oxidation or elimination were found in aerated solutions only for long illuminations. This rules out the presence of this kind of product in our case since the total duration of our cycle mode fatigue experiments is shorter than that of the aforementioned 100 cycles.

The studies conducted by Cipolloni et al.^{56,116} could help understanding the differences observed for our two molecules. Their first study⁵⁶ showed that replacing thiophene rings with

benzothiophene rings significantly improved the fatigue resistance of the DAEs. Our molecules have thiophene rings but also phenylene linkers that could be considered to play the stabilizing role that the benzothiophene play here on fatigue resistance. To explain the low fatigue resistance of the unsymmetric molecule, we should have a look at the actual effect of this asymmetry. It is what they did in their next study¹¹⁶.

They studied two DAE molecules which are the symmetrical and asymmetrical version of the same molecule (as it is the case for us). The symmetrical one contains benzothieryl substituents on both sides of the central ring, the asymmetrical one has a benzothieryl substituent on one side and a thienyl substituent on the other. Both compounds are switching reversibly, but the unsymmetrical one demonstrates fatigue after a few ring-opening/ring-closing processes, which is exactly what is happening in our case. They studied the influence of structure modification that represents going from the symmetric to the unsymmetric form, by doing a steady state and a time-resolved spectroscopy study as well as a photokinetics study of both cyclization and cycloreversion reactions.

In their case, the absorption spectra of both opened and closed forms were almost similar for both molecules. In our case, the spectra presented more differences except for the main absorption band in the visible. For the closed form, we observe the same factor 2 between the molar absorption coefficient at λ_{max} of the absorption band in the visible, the value for the unsymmetrical form being about half of the value of the symmetrical form.

For the symmetrical molecule, the photocycloreversion to the open form was total. Regarding the unsymmetrical molecule, both photochemical reactions occur in both molecules but for the unsymmetrical one, consecutive switching cycles are not reproducible due to the formation of side-products materialized by appearance of residual absorption. They showed that the main side-product was the usual ring-condensed one from the formal 1,2-dyotropic rearrangement.

So, in the end, their symmetrical molecule has lower quantum yield but high fatigue resistance whereas the unsymmetrical molecule has higher quantum yield but no resistance to fatigue¹¹⁶. The benzothiophene units are known to increase fatigue resistance, removing one of these substituents would be the simplest explanation to the suppressed fatigue resistance of the asymmetrical compound. The same probably happens in our molecule with the phenylene linkers.

IV - Quantum yield and switching ratio calculations

Finally, the quantum yields of both reactions were calculated from previously shown UV-visible spectroscopy measurements using a method from the literature. The switching ratios of both reactions were also calculated using our own method based on the evolution of the absorbance in function of the number of photons received by the molecules. The calculated quantum yield and conversion values are summarized in Table 4.6 at the end of 4.IV.1. The calculated switching ratio values are summarized in Table 4.7 at the end of 4.IV.2.

1 - Quantum yields (QYs) calculations

The quantum yields of the ring-closing and ring-opening reactions are calculated using the model developed by Cipolloni et al.⁵⁶ who carried out steady state UV-visible measurements in solution (in 3-methylpentane, with concentrations in the 1 to 5 x 10⁻⁵ mol.L⁻¹ range) and used the resulting absorbance-time data to calculate the quantum yield of both cyclization and cycloreversion reactions with an accuracy of +/- 10 %. This model was then widely reused^{59,172} and enriched^{9,181}. The model to study the photokinetics of both reactions and to calculate the quantum yields is the following:

A first equation describes the kinetics of the reversible photo-induced reactions:

$$\frac{d[C]}{dt} = I_O \Phi_{O \rightarrow C} - I_C \Phi_{C \rightarrow O} \quad (4.1)$$

$d[C]/dt$ is the rate of formation of the closed colored form expressed as a function of the monochromatic light intensity (number of photons by unit of volume by unit of time) absorbed by the opened (I_O) and the closed (I_C) forms, and the quantum yield of the ring closing ($\Phi_{O \rightarrow C}$) and ring opening ($\Phi_{C \rightarrow O}$).

A second equation describes what happens at the photostationary state, reached after illumination with I^0 intensity:

$$[C] \Phi_{C \rightarrow O} = [O] \Phi_{O \rightarrow C} \quad (4.2)$$

From which the open to closed conversion at PSS can be extracted from the ratio $\Phi_{O \rightarrow C}/(\Phi_{O \rightarrow C} + \Phi_{C \rightarrow O})$.

They finally arrive at a third equation which is a rearrangement of the first one but adapted to the case of a 1 cm cell-path, it is also the equation linked to $\Phi_{O \rightarrow C}$:

$$\frac{dA_C}{dt} = \epsilon_C \Phi_{O \rightarrow C} I^0 F A^0 - A_C [I^0 F \epsilon_{iso} (\Phi_{O \rightarrow C} + \Phi_{C \rightarrow O})] \quad (4.3)$$

this time, the formation rate of the closed form (and thus the color appearance and increase) is expressed as a function of its absorbance A_C and molar absorption coefficient ϵ_C at the monitored wavelength (in their study 445 nm), $F = A_{total}/(1 - 10^{-A_{total}})$ is the photokinetic factor, A^0 is the initial absorbance at the irradiation wavelength, and ϵ_{iso} is the molar absorption coefficient at the isosbestic point.

According to the third equation, by plotting dA_C/dt versus A_C a line is obtained, its slope is the sum of the quantum yields ($\Phi_{O \rightarrow C} + \Phi_{C \rightarrow O}$) and its intercept is the quantum yield of the ring closing reaction $\Phi_{O \rightarrow C}$.

A fourth equation is given for the calculation of the quantum yield of the ring opening reaction $\Phi_{C \rightarrow O}$, this reaction takes place by irradiation of a solution at the PSS (or a colored solution of pure closed molecules):

$$-\frac{dA_C}{dt} = \epsilon_C \Phi_{C \rightarrow O} I^0 (1 - 10^{-A_{C'}}) \quad (4.4)$$

With $A_{C'}$ the absorbance of the closed colored form at the irradiation wavelength. By plotting $-dA_C/dt$ versus $10^{-A_{C'}}$ a line is obtained, its slope and intercept are equal and correspond to the value of the ring-opening reaction $\Phi_{C \rightarrow O}$.

This model was used to calculate the QYs. The conversion was also calculated using the ratio derived from the second equation, Conversion = $\Phi_{O \rightarrow C}/(\Phi_{O \rightarrow C} + \Phi_{C \rightarrow O})$.

The quantum yields were calculated the reversibility experiment data (presented in 4.III) allowing us to calculate the values of the QYs using the same data than for the calculations of the switching ratios (SRs) presented further.

The UV irradiation part of the data had to be replotted at λ_{max} of the absorption band in the visible range for both molecules, 546 nm for C5HT-di-PSAc and 492 nm for Cl-C5HT-PSAc. The visible irradiation part of the data had to be replotted at $\lambda_{exc(Vis)} = 505$ nm for both molecules. The plots are shown in Figure 4.16 for C5HT-di-PSAc and Figure 4.17 for Cl-

C5HT-PSAc. The third equation (4.3) is still used to determine the ring-closing reaction quantum yield but for the ring-opening reaction quantum yield, since this time we have the data corresponding to the irradiation of the solution with visible light until full photocycloreversion, we can use the fourth equation (4.4).

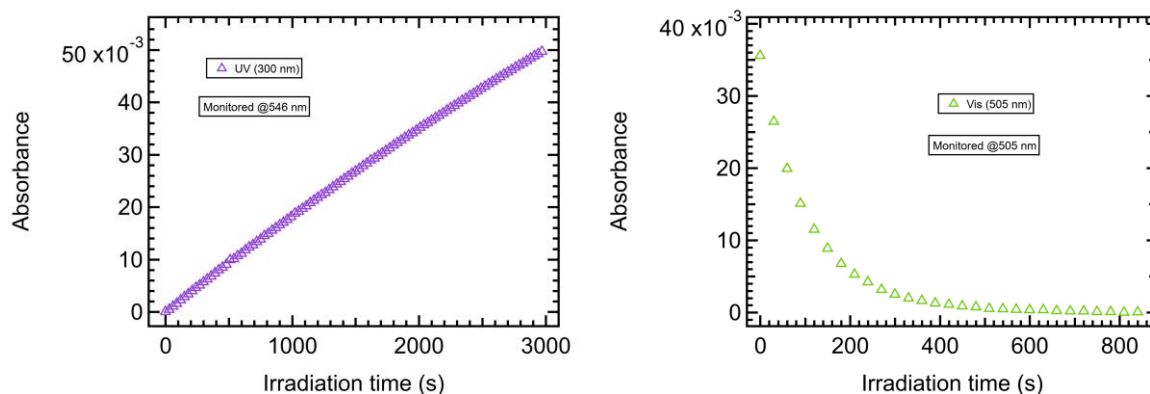


Figure 4.16: Evolution of the absorbance of C5HT-di-PSAc under UV irradiation monitored at $\lambda_{\max} = 546$ nm (band in the visible range corresponding to the maximum absorbance of the closed-ring molecules) (left) and then visible light irradiation monitored at $\lambda_{\text{exc}}(\text{Vis}) = 505$ nm (right).

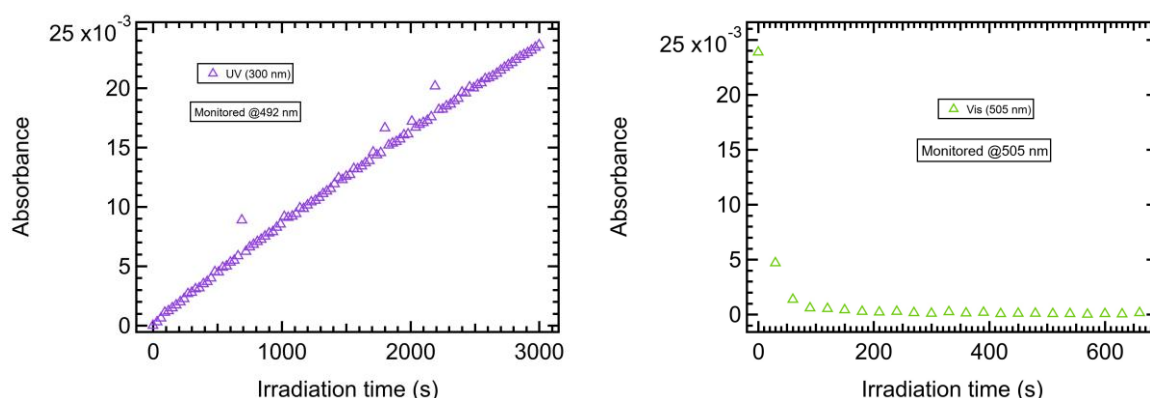


Figure 4.17: Evolution of the absorbance of Cl-C5HT-PSAc under UV irradiation monitored at $\lambda_{\max} = 492$ nm (band in the visible range corresponding to the maximum absorbance of the closed-ring molecules) (left) and then visible light irradiation monitored at $\lambda_{\text{exc}}(\text{Vis}) = 505$ nm (right).

Let us start with C5HT-di-PSAc, the temporal derivative of the absorbance of the closed form dA_{closed}/dt was plotted versus the absorbance of the closed form A_{closed} ; it was then fitted with a linear regression of equation: $y = -9.5648\text{e-}05 x + 1.9197\text{e-}05$, the intercept value is 0.2 it corresponds to $\Phi_{O \rightarrow C}$. Then, the opposite of the derivative of the absorbance of the open form $-dA_{\text{open}}/dt$ was plotted versus $10^{-A_{\text{open}}}$, it was then fitted with a linear regression of equation

$y = - 0.0037582 x + 0.0037553$, the value of the slope and the intercept is the same and corresponds to $\Phi_{C \rightarrow O} = 0.038$. The aforementioned graphs are presented in Figure 4.18.

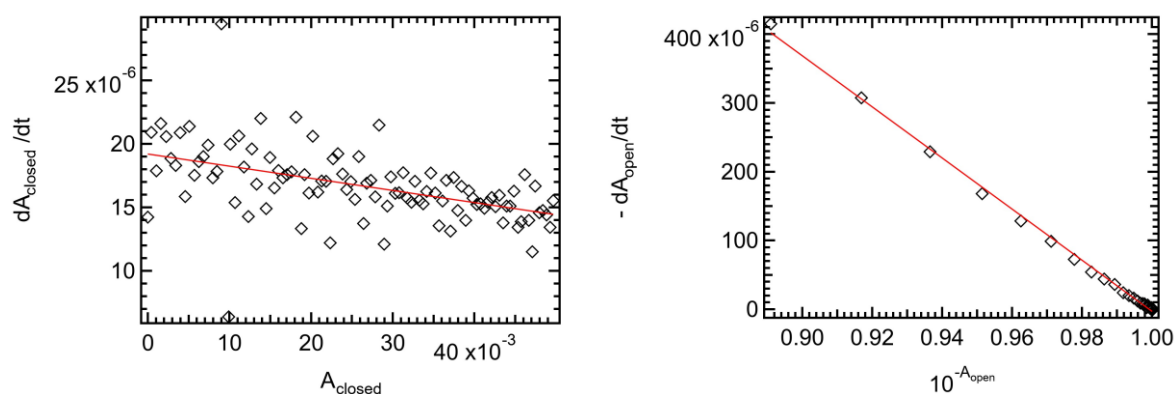


Figure 4.18: Temporal derivative of the absorbance evolution of the C5HT-di-PSAc closed-ring molecules (dA_{closed}/dt) versus the absorbance of the closed-ring molecules (A_{closed}) (left) opposite of the temporal derivative of the absorbance of the open form ($-dA_{open}/dt$) versus $10^{-A_{open}}$ (right).

We proceed the same way for Cl-C5HT-PSAc, the temporal derivative of the absorbance of the closed form dA_{closed}/dt was plotted versus the absorbance of the closed form A_{closed} ; it was then fitted with a linear regression of equation: $y = - 0.00022721 x + 1.0703e-05$, the intercept value is 0.047 it corresponds to $\Phi_{O \rightarrow C}$. Then, the opposite of the derivative of the absorbance of the open form $-dA_{open}/dt$ was plotted versus $10^{-A_{open}}$, it was then fitted with a linear regression of equation $y = - 0.011999 x + 0.011993$, the value of the slope and the intercept is the same and corresponds to $\Phi_{C \rightarrow O} = 0.012$. The aforementioned graphs are presented in Figure 4.19.

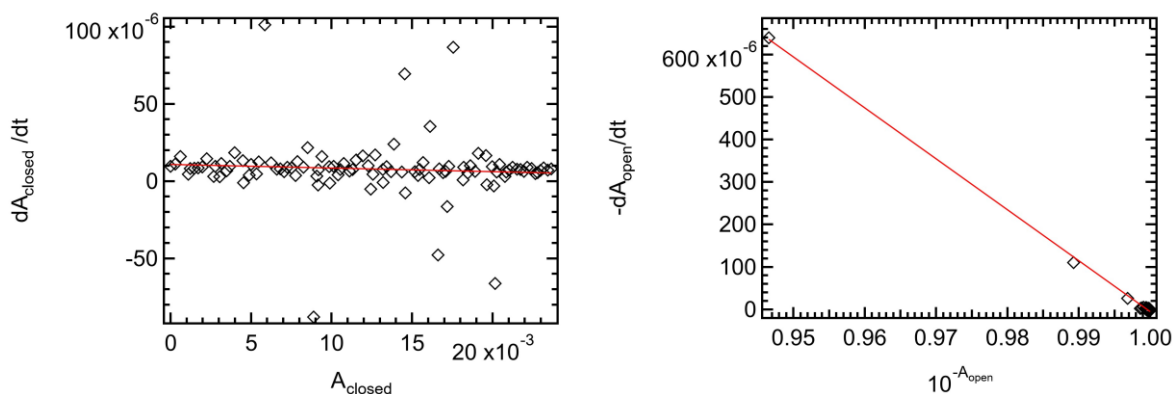


Figure 4.19: Temporal derivative of the absorbance evolution of the Cl-C5HT-PSAc closed-ring molecules (dA_{closed}/dt) versus the absorbance of the closed-ring molecules (A_{closed}) (left) opposite of the temporal derivative of the absorbance of the open form ($-dA_{\text{open}}/dt$) versus $10^{-A_{\text{open}}}$ (right).

For C5HT-di-PSAc, the same value of $\Phi_{O \rightarrow C}$ was obtained using the data (replotted at λ_{max} of the absorption band in the visible region, i.e., 546 nm) of the kinetics of the ring closing reaction (presented in 4.II) and the third equation (4.3). These data correspond to a solution that was irradiated until reaching the PSS, unlike the reversibility experiment data (presented in 4.III). It would indicate that the model of Cipolloni et al.⁵⁶ also works for a solution of molecules that did not reach the PSS.

Regarding the quantum yields, they show the typical photochemical behavior of diarylethenes, where the forward quantum yield is determined by the dynamic equilibrium between the parallel and antiparallel conformers (with a value comprised between 0 and 1) and the backward quantum yield is 2 or 3 orders of magnitude lower. Furthermore, their values are consistent with those found in the literature for analogous DAEs^{56,59,116,171}.

The QYs of both reactions and the conversion are larger for C5HT-di-PSAc than for Cl-C5HT-PSAc.

Table 4.6: Quantum yield and conversion values ($\lambda_{\text{exc}}(\text{UV}) = 300 \text{ nm}$ and $\lambda_{\text{exc}}(\text{Vis}) = 505 \text{ nm}$).

Molecule 1 (C5HT-di-PSAc)		
$\Phi_{\text{O} \rightarrow \text{C}}$	$\Phi_{\text{C} \rightarrow \text{O}}$	Conversion
0.20	0.038	0.84
Molecule 2 (Cl-C5HT-PSAc)		
$\Phi_{\text{O} \rightarrow \text{C}}$	$\Phi_{\text{C} \rightarrow \text{O}}$	Conversion
0.11	0.012	0.80

2 - Switching ratio (SRs) calculations

The switching ratios are calculated with the reversibility experiment data (presented in 4.III) for which the absorbance was monitored at 520 nm. It is important to note that the SRs can be calculated from the absorbance data monitored at any wavelength since we demonstrated in 4.I that no matter the wavelength chosen for the monitoring, the evolution to the PSS was quite similar (see Figure 4.7).

The same parts of the data are used than for calculating the QYs with Method 2; for the UV irradiation part from $t = 0 \text{ s}$ to $t = 3000 \text{ s}$ (for both molecules) and for the visible irradiation part from $t = 3000 \text{ (0 s)}$ to $t = 3840 \text{ s}$ (840 s) (C5HT-di-PSAc) and $t = 3000 \text{ s}$ to $t = 3640 \text{ s}$ (640 s) (Cl-C5HT-PSAc). The number of photons received by the solution is calculated using the photon flux (see Table 4.4) to multiply the time of irradiation which gives a number of photons per cm^2 corresponding to the total time of irradiation. The energy of the photon is taken into account since the photon flux is calculated by dividing the light flux in mW/cm^2 by the energy of one photon in J.

From the data plotted versus the number of photons received ($A = f(\text{number of photons})$), for C5HT-di-PSAc, it took 840 s to fully switch back a portion of molecules that has received UV light for 3000 s. In terms of photons, for C5HT-di-PSAc, it took 5.658×10^{18} visible light (505 nm) photons to fully switch back a portion of molecules that had received 8.82×10^{17} UV photons (300 nm).

$$\text{We obtain } SR(\text{UV}/\text{Vis}) = \frac{n_{\text{photons}}(\text{UV})}{n_{\text{photons}}(\text{Visible})} = \frac{8.82 \times 10^{17}}{5.658 \times 10^{18}} = 0.16,$$

$$\text{Or } SR(\text{Vis}/\text{UV}) = \frac{n_{\text{photons}}(\text{Visible})}{n_{\text{photons}}(\text{UV})} = \frac{5.658 \times 10^{18}}{8.82 \times 10^{17}} = 6.42.$$

For Cl-C5HT-PSAc, it took 4.45×10^{18} visible light (505 nm) photons to fully switch back a portion of molecules that had received 8.82×10^{17} UV photons (300 nm).

$$\text{We obtain } SR(UV/Vis) = \frac{n_{photons(UV)}}{n_{photons(Visible)}} = \frac{8.82 \times 10^{17}}{4.45 \times 10^{18}} = 0.20,$$

$$\text{Or } SR(Vis/UV) = \frac{n_{photons(Visible)}}{n_{photons(UV)}} = \frac{4.45 \times 10^{18}}{8.82 \times 10^{17}} = 5.06.$$

The same values of SRs are found whether we calculate them in function of the time or the number of photons. For C5HT-di-PSAc, the photocyclization is 6.5 times faster than the photocycloreversion. For Cl-C5HT-PSAc, it is 5.06 times faster, note that for this experiment the UV irradiation time did not exceed 3000 s so Cl-C5HT-PSAc should not have undergone degradation.

Table 4.7: Switching ratio values calculated for both molecules ($\lambda_{exc}(UV) = 300$ nm and $\lambda_{exc}(Vis) = 505$ nm).

Molecule 1 (C5HT-di-PSAc)	
SR (UV/Vis)	SR (Vis/UV)
0.16	6.42
Molecule 2 (Cl-C5HT-PSAc)	
SR (UV/Vis)	SR (Vis/UV)
0.2	5.06

If we look at the values of the quantum yields of C5HT-di-PSAc and at its value of switching ratio, we notice that they both indicate that the switching is asymmetric with the ring-opening reaction taking much longer than the ring-closing reaction. The same observation can be made for Cl-C5HT-PSAc

Finally if we compare the switching ratios of the two molecules, we notice that the asymmetry of the switching is more pronounced for C5HT-di-PSAc than for Cl-C5HT-PSAc.

Conclusion

In the end, one must remember that all the results presented in this chapter only corresponds to the experimental parameters chosen here. Indeed, changing the concentration of the solution or the LEDs (i.e., the illumination wavelengths) would have an impact on the time it takes to make the molecules switch and the quantum yields of the reactions. Considering the long time it takes to make our molecules switch, better illumination parameters would be useful to reduce the duration of experiments involving to make all the molecules in solution switch.

We did not study the effect of temperature on the switching of our molecules, Cipolloni et al.^{56,116} demonstrated that temperature effects are small and undetectable by quantum yield measurements on a wide interval around room temperature. Nevertheless and quite interestingly, Kudernac et al.¹⁸² showed it was possible to tune the temperature dependence of the switching of dithienylethenes.

We did not study the influence of the solvent on the spectral characteristics and on the quantum yields of our molecules by making experiments with other solvents. The influence of the solvent is more important for fluorescence than for absorption properties but still; a significant solvatochromic effect that is to say a redshift can appear with increasing value of the solvent polarity parameter $E_T(30)$. Our molecules possess a perhydrocyclopentene ring so very low polarity and no atom susceptible to form hydrogen bonds with a protic solvent. We used dimethylformamide (DMF) which is a polar aprotic solvent so no significant solvatochromic effect on the absorption properties would be expected. Even less, since our molecules don't possess a donor and an acceptor group that would trigger a push-pull effect and increase the sensibility to the solvent^{183,184}. Regarding the effect of the solvent on the QY values, Herder et al. showed that using solvents with lower polarity than acetonitrile, which is the case of DMF¹⁸⁵ can slightly increase the ring-closing reaction quantum yield but has no effect on the ring-opening and by-product formation reaction¹⁷¹.

The effect the structure of the molecule can have on its properties (photochromism, configuration, thermal stability, tunability, fatigue resistance) and its spectral characteristics (localization and evolution of the absorbance bands) was explained. Particular attention was given to the bands corresponding to the transitions involved in the photoconversion reactions, and to specific points on the spectra: at $\lambda_{exc}(UV - 300 \text{ nm})$ and $\lambda_{exc}(Vis - 505\text{nm})$ and the isosbestic points.

A photokinetic study of both molecules allowed us to assess the time it took for them to reach the PSS, if they suffered degradation (fatigue), the reversibility and symmetry of their switching and to calculate their quantum yields and switching ratios.

C5HT-di-PSAc needs 23 100 s to reach the PSS under the experimental conditions that we used. It is resistant to fatigue, as the clean evolution of its isosbestic point under UV light irradiation shows as well as the preservation of the same absorbance amplitude throughout the cycles measurements. Its switching is fully reversible but asymmetric. The quantum yield and of its ring-closing and ring-opening reaction are worth 0.20 and 0.038 respectively. Its switching ratio (ratio of the time it takes for both reactions to occur) is worth 6.5.

Cl-C5HT-PSAc takes 36 660 s to reach a plateau before the absorbance starts to decrease under the experimental conditions that we used. This molecule suffers fatigue, it was indicated by the decrease in the absorbance under UV light irradiation which was accompanied by an hypsochromic shift on the spectra. It was confirmed by the evolution of its isosbestic point under UV light irradiation (it shifts) and by the decrease in the absorbance amplitude throughout the cycles measurements. The switching of the Cl-C5HT-PSAc molecules that are not degraded is fully reversible but asymmetric. The quantum yield of its ring-closing and ring-opening reaction are worth 0.047 and 0.012 respectively. Its switching ratio (ratio of the time it takes for both reactions to occur) is worth 5.1.

It what follows, we will investigate if the nanoantenna effect provided by supported gold nanoparticles on which the molecules will be grafted have an impact on the quantum yields of one or both reactions and on their switching ratios.

Chapter 5: Influence of the plasmonic antenna effect on the switching kinetics of the diarylethenes grafted on supported gold nanoparticles

In this chapter, both diarylethene molecules (C5HT-di-PSH and Cl-C5HT-PSH) are grafted on spherical 28 nm gold nanoparticles deposited on ITO substrates. The adsorption of C5HT-di-PSH and Cl-C5HT-PSH on 28 nm gold nanoparticles is expected to cause a shift of the LSPR wavelength. This shift will be predicted using the model developed in Chapter 3 and compared to the experimentally obtained value. Then, we will try to observe the switching (previously observed in solution) of both diarylethene molecules grafted on the AuNPs. The switching was monitored by optical spectroscopy following the evolution of LSPR peak position. The conservation of the properties of a molecule (in our case, the fully reversible switching) upon attachment to the metallic surface of an electrode (in our case, the gold nanoparticle) is not guaranteed due to the potential excessive strength of the coupling between the molecule and the metal^{33,97}. The reversibility and symmetry (by mean of the calculation of the switching ratios) of the switching will be assessed as well as the fatigue undergone by the molecules when they are connected to the gold nanoparticles.

As can be seen in Figure 5.1, the absorption band in the visible of the DAE molecules corresponding to a transition involved in the photochromic reaction (switching) is located in the same spectral area than the LSPR peak of the gold nanoparticles. We can therefore expect an influence of the plasmon on the photocyclization and photocycloreversion reactions of the molecules. Indeed, AuNPs act like plasmonic antenna: the electromagnetic field around them can be amplified up to 10 times in response to incident light. We will see if this LSPR enhancement is present in our case and contributes to increase the QY and thus the speed of the photochromic reactions, especially that of the photocycloreversion reaction. An acceleration of this latter reaction would result in a more symmetrical photoconversion, indicated by a value of the SR closer to 1. Let us remind that for C5HT-di-PSAc in DMF, the SR is equal to 6.5 meaning that 6.5 times more visible light photons are needed to trigger the photocycloreversion after the molecules were switched by the UV light photons.

It is important to note that since we work with ITO, we cannot access the absorbance peak in the UV region corresponding to the other transition involved in the photochromic

reactions (switching). Indeed, the transmittance of ITO drops to 0 below 380 nm. Note that the band observed between 600 nm and 800 nm on the spectrum of 28 nm AuNPs on ITO on Figure 5.1 is due to the presence of AuNPs aggregates on the ITO substrate.

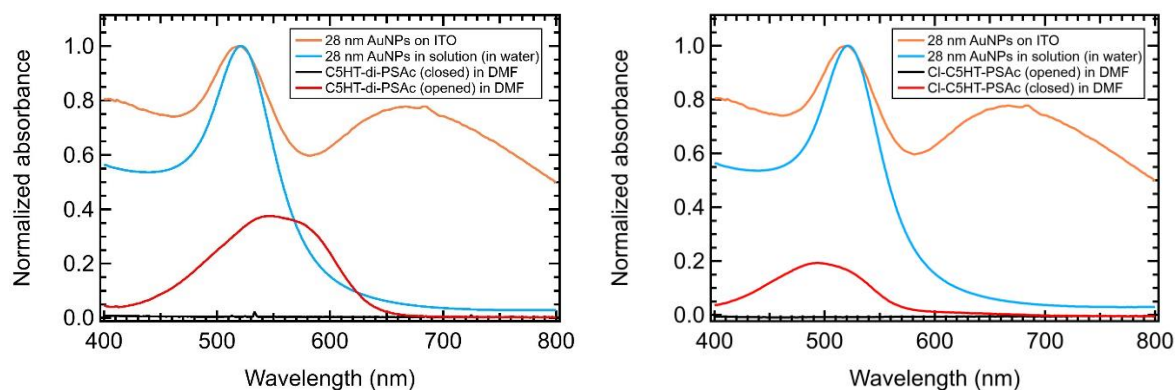


Figure 5.1: Normalized UV-visible spectrum of 28 nm AuNPs in water, 28 nm AuNPs deposited on ITO and C5HT-di-PSAc (left) in DMF or Cl-C5HT-PSAc (right).

I - Adsorption and switching of Cl-C5HT-PSH and C5HT-di-PSH on 28 nm AuNPs deposited on ITO

In this first part of Chapter 5, the results presented were obtained with samples prepared following the DAE grafting protocol 1 described in Chapter 2.I.3.a. However, as shown in Table 2.3, some preparation steps slightly differ from a sample to the other. We are going to study the effect the variation of some preparation steps has on the switching ability of the molecules once grafted on the AuNPs.

1 - Cl-C5HT-PSH

a - Stepwise UV-visible spectroscopy monitoring and subsequent switching measurements

As can be seen in Figure 5.2, the preparation of sample ADITO69 (see Table 2.3 in Chapter 2.I.3. for the details of every preparation step) was monitored step by step by recording a UV-visible spectra after the two main steps of the preparation. The position of the LSPR peak was extracted and compared to that of the preceding step.

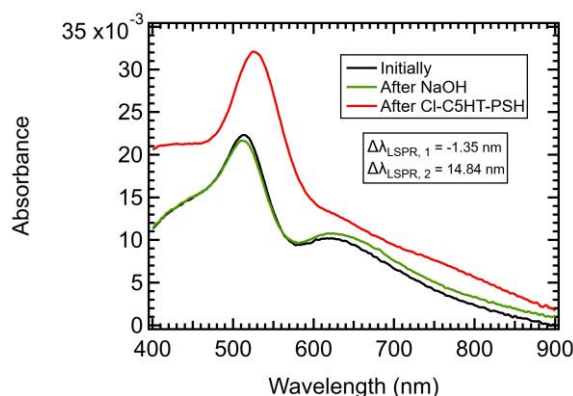


Figure 5.2: UV-visible spectra recorded after the deposition of the AuNPs, after the desilanzation and after the adsorption of the Cl-C5HT-PSH molecules.

Initially, $\lambda_{\text{LSPR}} = 512.7 \text{ nm}$, after the desilanzation step, a $\Delta\lambda_{\text{LSPR}, 1}$ of -1.35 nm is measured and a small decrease of the absorbance is observed, probably due to the removal of APTES molecules in the vicinity of the AuNPs since a simultaneous decrease of the absorbance and blueshift of the LSPR indicate a local decrease of the optical index (which is the case when molecules are removed) a few AuNPs must have detached from the surface during this step. After the DAE molecules adsorption step, a $\Delta\lambda_{\text{LSPR}, 2}$ of 14.84 nm is measured, and a large increase of the absorption is observed. This value of the LSPR wavelength shift is slightly superior to the one calculated for the formation of a full molecular monolayer using the predictive model from Chapter 3, $\Delta\lambda_{\text{LSPR}} = 11.98 \text{ nm}$, using Equation 3.4 with the following parameters $m = 73$ (calculated for 28 nm AuNPs with the same method than that presented in Chapter 3), $\Delta n = n_{\text{molec}} - n_{\text{air}} = 1.46 - 1 = 0.46$ (the spectra are recorded with the substrate placed in the spectrophotometer at air, hence the use of the refractive index of air), $d = 13.9 \text{ \AA}$ (length of Cl-C5HT-PSAc in its open form, as given in Chapter 2) and $l_d = 0.45 \times R = 0.45 \times 14 = 6.3$ (with R the radius of the AuNPs, for 28 nm AuNPs, $R = 14 \text{ nm}$, see Chapter 3 for the derivation of the expression used to calculate l_d). A full layer of Cl-C5HT-PSH must be present at the surface of the gold nanoparticles, which is not surprising since the samples were prepared working with a large excess of molecules (see Table 2.3).

This monitoring was not carried out for all the samples, indeed, recording a spectrum of the sample after different steps requires to dry it between the preparation steps which is not recommended according to Cha et al.¹²⁴. For the rest of the samples, the presence of DAE molecules at the surface was confirmed by the observation of switching. The type of samples obtained using this first grafting protocol is schematized in Figure 5.3.

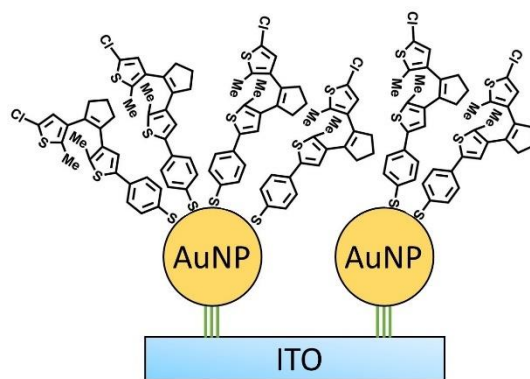


Figure 5.3: Scheme of the type of sample obtained with grafting protocol 1: ITO/AuNPs(28 nm)/Cl-C5HT-PSH. The green sticks are silanes (APTES). Note that this sketch is not on scale since the size of the DAE molecules is 1.39 nm, that of the APTES molecules is 0.5 nm and that of the AuNPs in 28 nm.

Switching measurements (cycles measurements) were carried out as described in Chapter 2.II.2.b, the sample was successively irradiated with UV (300 nm) and visible (505 nm) light. The parameters used for each type of illumination are reminded in Table 5.1.

Table 5.1: LEDs parameters used for the switching measurements made on the samples prepared with grafting protocol 1.

LED	I (A)	P (mW)	Φ (mW/cm ²)	Φ_{photons} (photons/s/cm ²)
UV	0.24	0.178	0.251	3.79×10^{14}
Vis	0.7	2.26	3.19	8.10×10^{15}

The results of the switching cycles measurements performed on ADITO69 are presented in Figure 5.4.

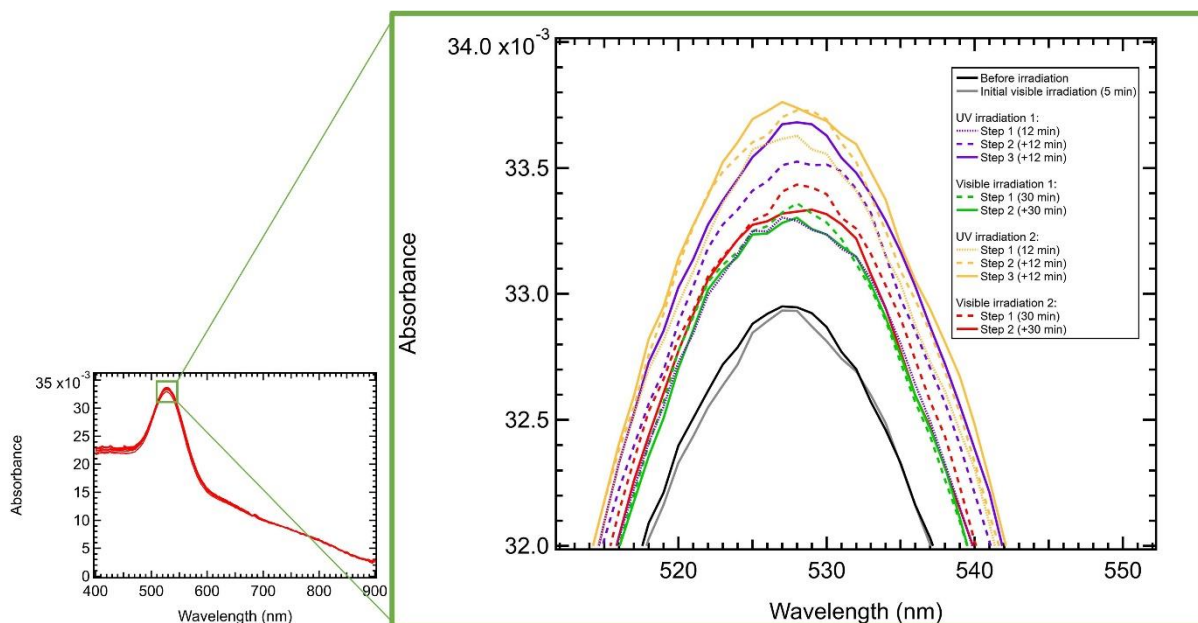


Figure 5.4: UV-visible spectra corresponding to the switching measurements on ADITO69 (28 nm AuNPs).

An increase of the LSPR peak absorbance occurs upon ring-closing of the molecules (in response to UV light exposure) grafted on the AuNPs, while a decrease of the LSPR peak absorbance occurs upon ring-closing of the molecules (in response to visible light exposure). The variation in absorbance occurring upon the switching is 7×10^{-4} which corresponds to a relative increase of 2 %. This behavior was observed in comparable proportions by Snegir et al.¹⁸⁶ for furan-based diarylethene molecules grafted on 17 nm gold nanoparticle deposited on glass substrates.

It is important to note that control switching measurements (switching measurements on AuNPs deposited on ITO without DAE molecules grafted on them) were made using two ITO substrates: one with 28 nm AuNPs deposited on it (ADITO55), the other one with 35 nm AuNPs deposited on it (ADITO56), see Chapter 2.I.2.d for more details about their preparation. The results of these control switching measurements are shown in the Appendix (see Figure A.5.1 and Figure A.5.2), the evolution of the LSPR peak absorbance in response to the UV and visible irradiations is random and much weaker (2×10^{-4}), demonstrating that the systematic absorbance increase upon UV irradiation and absorbance decrease upon visible irradiation corresponds to the switching of the DAE molecules.

The LSPR peak absorbance and wavelength were then extracted by fitting the peaks (of Figure 5.4) with a Lorentzian function (see Chapter 2.II.1.d for more details) and the evolution of the absorbance at λ_{LSPR} and that of λ_{LSPR} were plotted versus the time (see Figure 5.5).

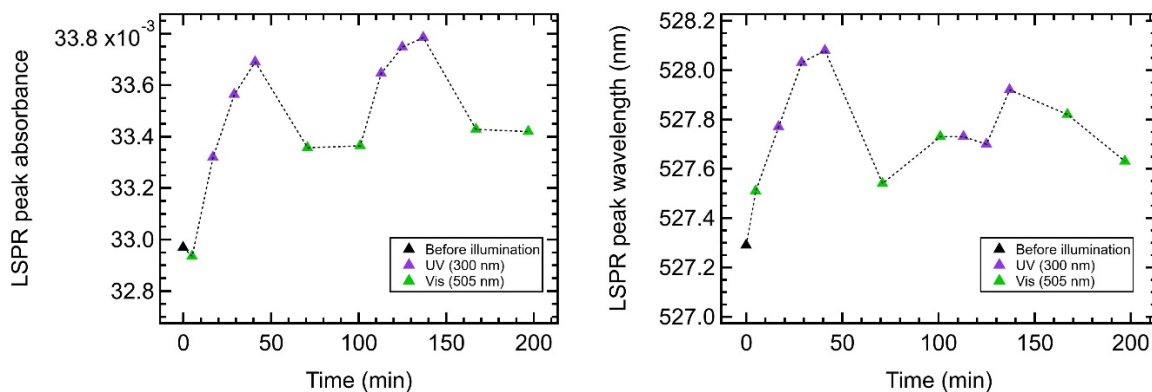


Figure 5.5: Evolution of the LSPR peak absorbance (left) and wavelength (right) of ADITO69 as a function of time upon irradiation. The dotted line is a guide for the eyes.

The relevant physical quantity to consider appears to be the absorbance. Indeed, even if the modifications of the absorbance are small, they are still (and always) large enough to be above the spectrophotometer sensibility. Regarding the modifications of the wavelength, it is rarely the case, for most samples (as it is the case here). The evolution of the λ_{LSPR} values is below the spectrophotometer sensibility, usually resulting in erratic variations of λ_{LSPR} .

As can be seen in Figure 5.5 by looking at the evolution of the absorbance at λ_{LSPR} ADITO69 can switch reversibly but not fully. Indeed, the second step of the visible irradiation from the first switching cycle (Step 2 of Visible irradiation 1 in Figure 5.4) does not allow to make the molecules switch back any further. Only half of the molecules were switched back by the preceding first step of the first switching cycle (Step 1 of Visible irradiation 1 in Figure 5.4).

b - Influence of the gold nanoparticles size: 28 nm and 35 nm

We are going to focus on two samples prepared with 28 nm AuNPs (ADITO49 and ADITO46) and on two samples prepared with 35 nm AuNPs (ADITO47 and ADITO48).

ADITO49 and ADITO46 only differed in the DAE molecule adsorption step: two different solution and immersion time were used. ADITO49 was immersed for 3 hours in a 3.21

$\times 10^{-4}$ ethanolic DAE solution while ADITO46 was immersed in a 6.36×10^{-4} ethanolic DAE for 15 hours. In a few words, ADITO49 underwent a short immersion in a solution roughly two times more concentrated than that of ADITO46 that underwent a long immersion. The rest of the preparation steps were the same for the two samples, similar to those described below for the second couple of samples. In both cases, the samples were prepared with DAE molecules in excess so that it could be considered that a full coverage of the AuNPs was reached.

ADITO47 and ADITO48 were prepared the exact same way: same baking step (120 °C for an hour), same desilanization step (immersion in a 0.8 mM NaOH solution), same AuNPs deposition (immersion for an hour) and finally, aliquots from the same ethanolic DAE solution at 6.36×10^{-4} with an immersion time of 15 hours (same solution than for ADITO46).

For ADITO46 the septum popped out during the DAE grafting step resulting in slow evaporation of the solution in which the substrate was immersed. This sample thus has a thick layer of crystallized molecules on it (evidenced by AFM measurements, see Figure A.5.3).

Switching measurements were performed as described in Chapter 2.II.2.b, the sample was successively irradiated with UV (300 nm) and visible (505 nm) light. The parameters used for each type of illumination are the ones previously reported in Table 5.1.

The results of the switching measurements performed on ADITO49 are presented in Figure 5.6.

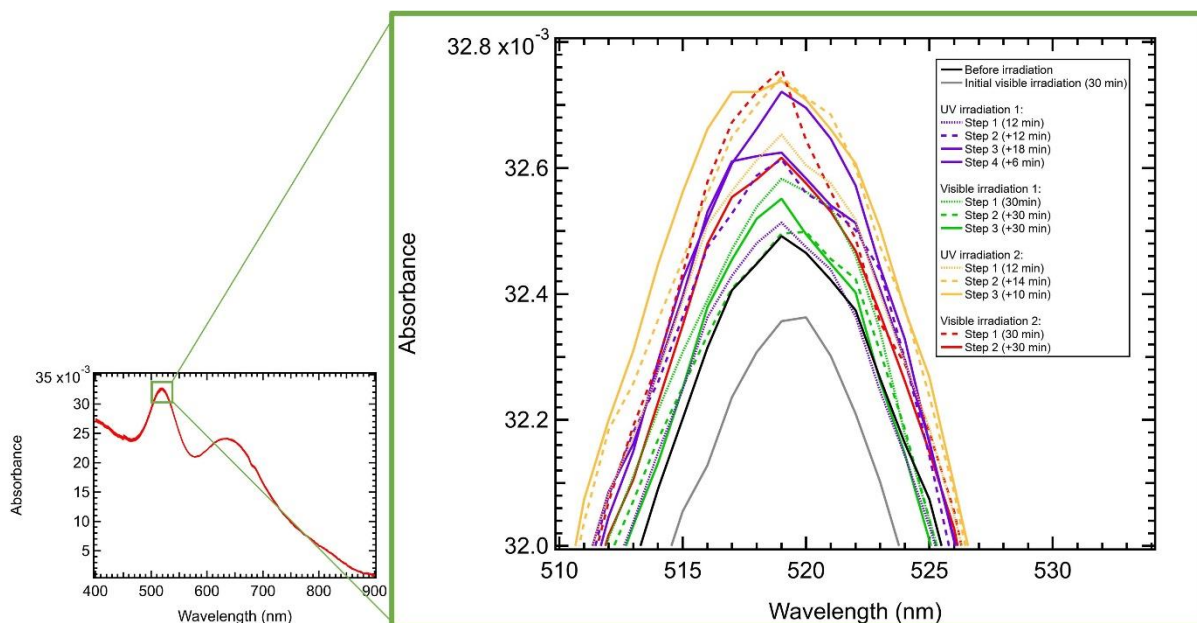


Figure 5.6: UV-visible spectra corresponding to the switching measurements on ADITO49 (28 nm AuNPs).

The LSPR peak absorbance and wavelength were then extracted by fitting the peaks (of Figure 5.6) with a Lorentzian function (see Chapter 2.II.1.d for more details) and the evolution of the absorbance at λ_{LSPR} and that of λ_{LSPR} were plotted versus the time (see Figure 5.7).

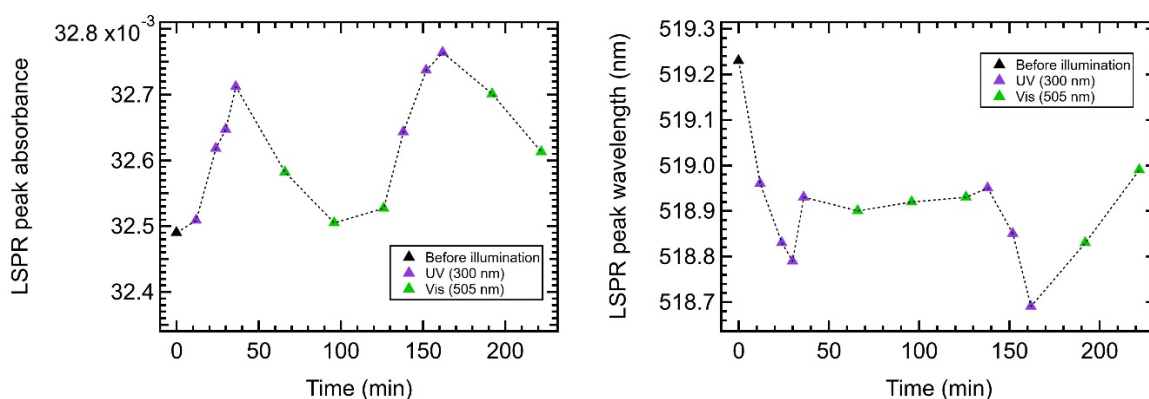


Figure 5.7: Evolution of the LSPR peak absorbance (left) and wavelength (right) of ADITO49 as a function of time upon irradiation. The dotted line is a guide for the eyes.

As can be seen in Figure 5.7 by looking at the evolution of the absorbance at λ_{LSPR} for the first switching cycle (UV irradiation 1 + Visible irradiation 1, see Figure 5.6) ADITO49 can switch fully reversibly since the second step of Visible irradiation 1 allows to make switch back all the molecules that had switched. However, if we look at the second switching cycle (UV

irradiation 2 + Visible irradiation 2, see Figure 5.6) we observe that the first step of Visible irradiation 2 does not allow to make as many molecules switch back as the first step of Visible irradiation 1 (taking into account that both steps had the same duration). The reversible switching is already compromised at the second switching cycle for which longer visible irradiation steps may be required. Regarding the evolution of the LSPR wavelength values, it is erratic since we are below the spectrophotometer sensitivity.

The same measurements and exploitation were made for ADITO46 (28 nm AuNPs, see Figure 5.8 and Figure 5.9), ADITO47 (35 nm AuNPs, see Figure 5.10 and Figure 5.11) and ADITO48 (28 nm AuNPs, see Figure A.5.4 and A.5.5).

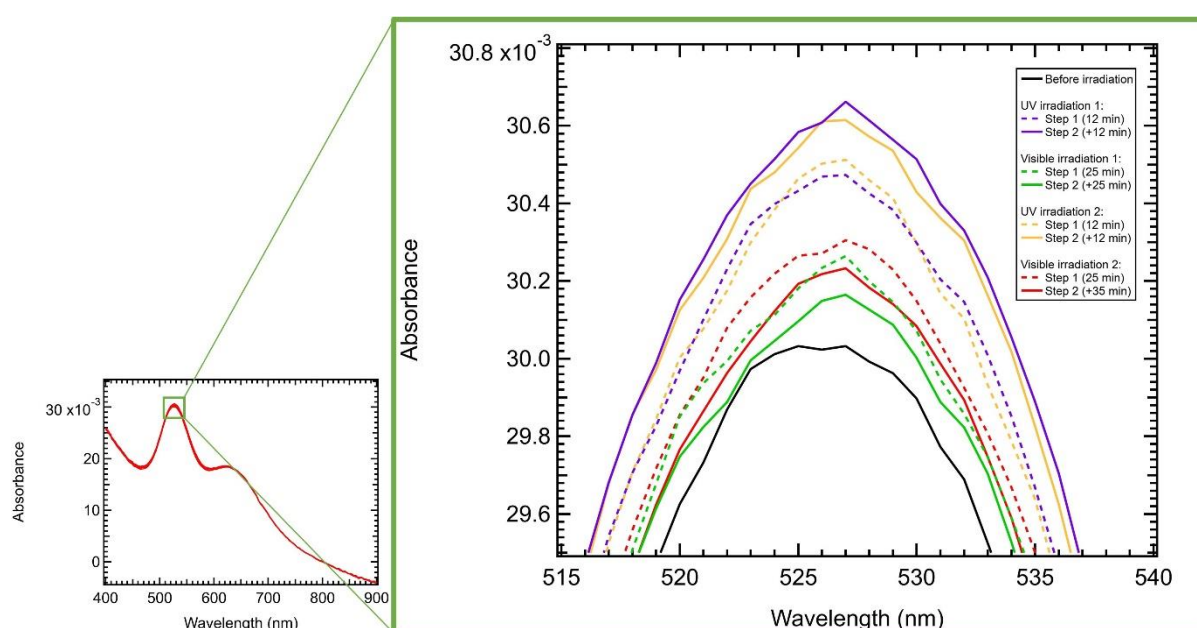


Figure 5.8: UV-visible spectra corresponding to the switching measurements on ADITO46 (28 nm AuNPs).

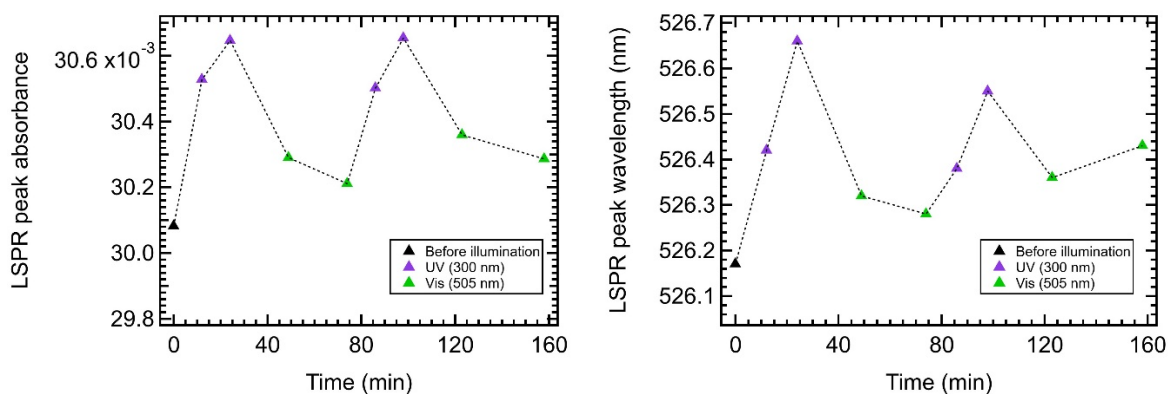


Figure 5.9: Evolution of the LSPR peak absorbance (left) and wavelength (right) of ADITO46 as a function of time upon irradiation. The dotted line is a guide for the eyes.

As can be seen in Figure 5.9 by looking at the evolution of the absorbance at λ_{LSPR} ADITO46 can switch reversibly. The amplitude of its absorbance variation is twice that of ADITO49. The duration of the visible irradiation is not sufficient to assess if ADITO46 can switch fully reversibly however if we look at the first step of each visible irradiation, the first step of Visible irradiation 2 make less molecules switch than the first step of Visible irradiation 1. Regarding the evolution of the LSPR wavelength values, since ADITO46 presents a thick crystallized layer of molecules, the larger quantity of molecules increases the values of the variations of λ_{LSPR} which are slightly above the sensitivity limit of the spectrophotometer and thus more consistent with that of the absorbance.

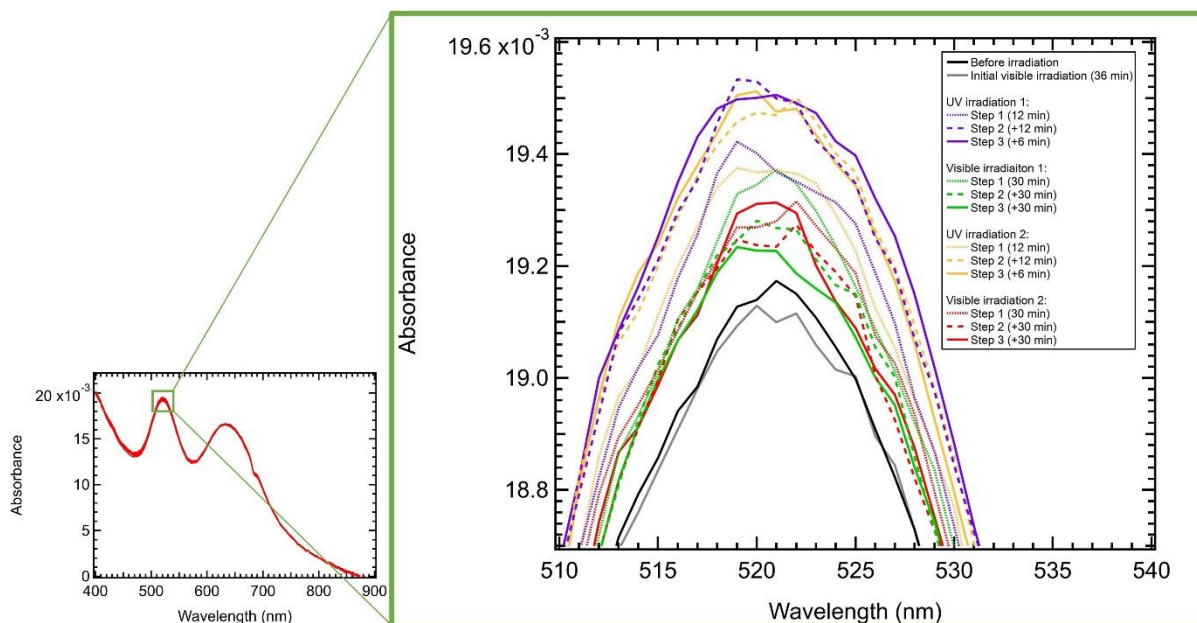


Figure 5.10: UV-visible spectra corresponding to the switching measurements on ADITO47 (35 nm AuNPs).

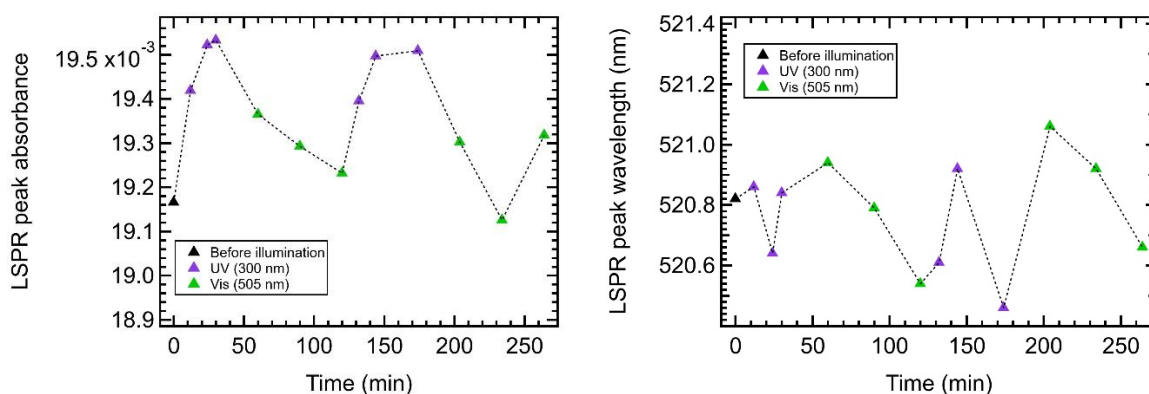


Figure 5.11: Evolution of the LSPR peak absorbance (left) and wavelength (right) of ADITO47 as a function of time upon irradiation. The dotted line is a guide for the eyes.

As can be seen in Figure 5.11 by looking at the evolution of the absorbance at λ_{LSPR} ADITO47 can switch fully reversibly. Regarding the evolution of the LSPR wavelength values, it is erratic since we are below the spectrophotometer sensitivity.

At this point, it is important to underline that the switching ability of the DAE molecules was preserved upon their grafting on the AuNPs. Reversible switching was observed for samples prepared with AuNPs of both sizes (28 nm and 35 nm) indicating that this increase of the AuNPs' size does not influence the switching or the possibility to detect it.

c - Influence of the deprotection method and suppression of the desilanization step

We are now going to focus on ADITO60 and ADITO61 that were prepared with a solution deprotected by adding a few drops of ammonia directly in the solution (unlike for the previous samples that were deprotected using a N_2/NH_3 flow, see procedure described in Chapter 2.I.1.c) and more importantly without a desilanization step, meaning that some silanes remain everywhere on the surface of the ITO substrate (as schematized in Figure 5.12) and not only under the attached 28 nm AuNPs (as previously schematized in Figure 5.3). They were prepared with the same AuNPs than ADITO46 and 49 (previously described). Both samples were immersed in an aliquot of the same DAE solution at 6.38×10^{-4} but ADITO61 was immersed twice longer (8h versus 4h). The same measurements and exploitation than for the previous samples were made for ADITO60 (see Figure 5.13 and Figure 5.15) and ADITO61 (see Figure 5.14 and Figure 5.15).

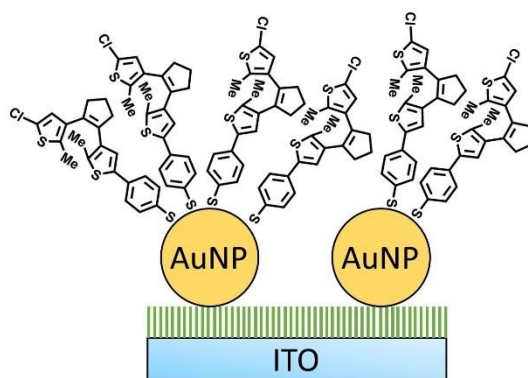


Figure 5.12: Scheme of the type of sample obtained with grafting protocol 1 without the desilanization step: ITO/AuNPs(28 nm)/Cl-C5HT-PSH. The green sticks are silanes (APTES). Note that this sketch is not on scale since the size of the DAE molecules is 1.39 nm, that of the APTES molecules is 0.5 nm and that of the AuNPs is 28 nm.

Regarding the deprotection method, we can already confirm that it does not have an influence on the switching, indeed, for all the previous samples (deprotected with the ammonia/argon gas flux), we obtained comparable switching to that obtained by Snegir et al.¹⁸⁶ who had deprotected their DAE solutions with liquid ammonia.

Switching cycles measurements were performed as described in Chapter 2.II.2.b, the sample was successively irradiated with UV (300 nm) and visible (505 nm) light. The parameters used for each type of illumination are the ones previously reported in Table 5.1. The results of the switching measurements performed on ADITO60 and ADITO61 are presented in

Figure 5.13 and Figure 5.14. The typical switching times are around 45 minutes for the switching and 120 minutes for the back switching.

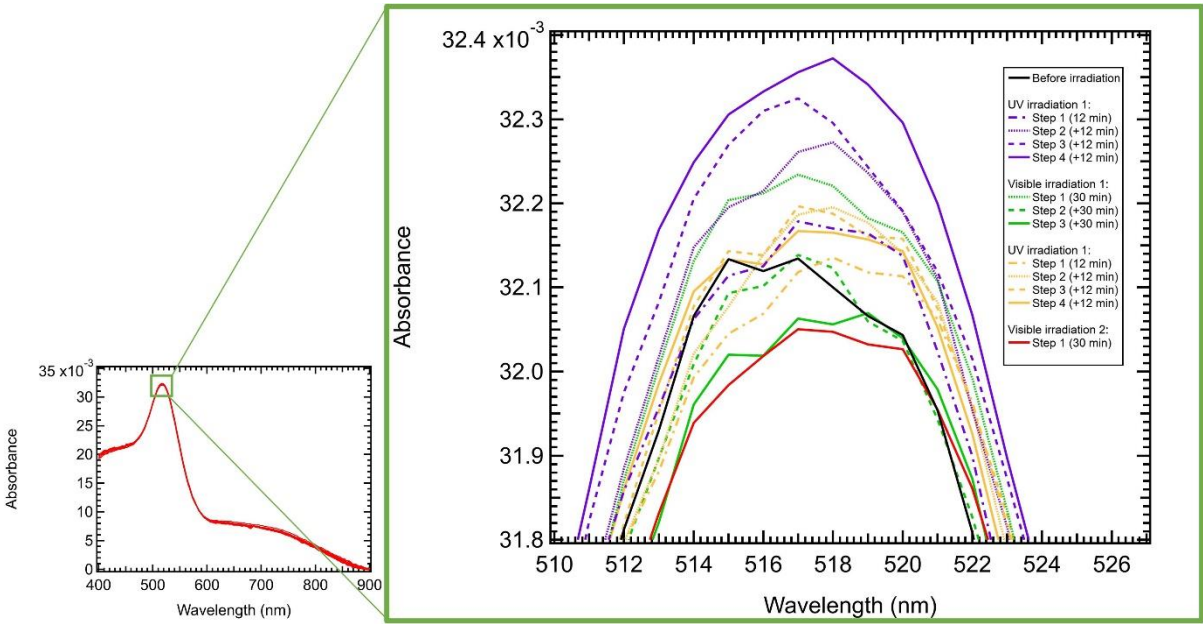


Figure 5.13: UV-visible spectra corresponding to the switching measurements on ADITO60.

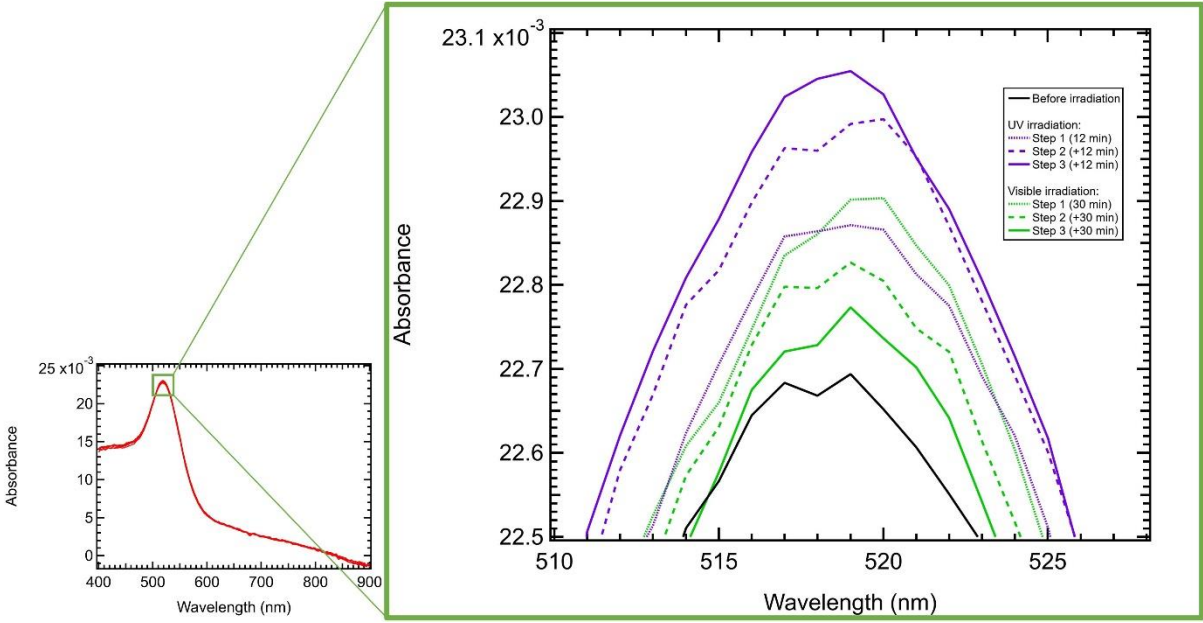


Figure 5.14: UV-visible spectra corresponding to the switching measurements on ADITO61.

The LSPR peak absorbance and wavelength were then extracted by fitting the LSPR peaks with a Lorentzian function (see Chapter 2.II.1.d for more details) and the evolution of the absorbance at λ_{LSPR} were plotted versus the time for both samples (see Figure 5.15).

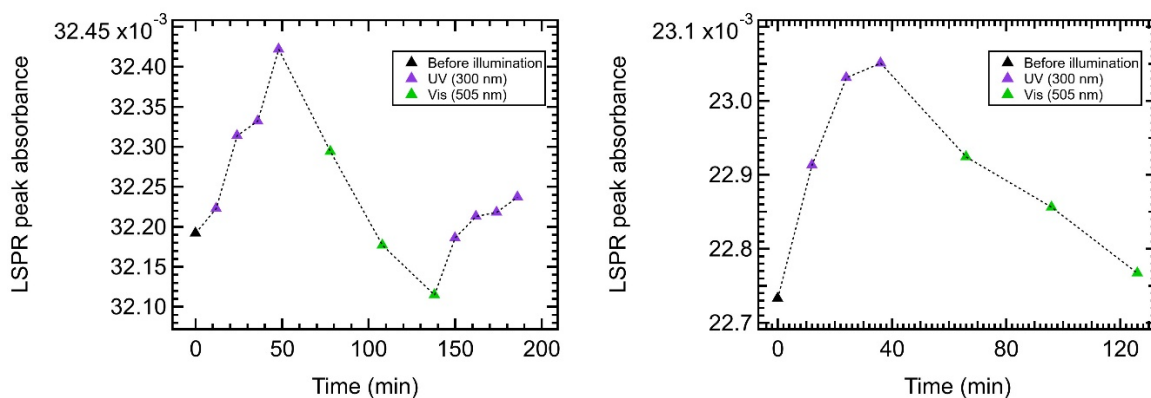


Figure 5.15: Evolution of the LSPR peak absorbance of ADITO60 (left) and ADITO61 (right) as a function of time upon irradiation. The dotted line is a guide for the eyes.

Both samples display reversible switching, however fatigue appear at the second switching cycle for ADITO60 (the second UV irradiation does not allow to make as many molecules switch than the first one had). This fatigue that appears very soon, after only one switching cycle was also observed by Toyama et al.¹⁸⁷ and Van der Molen et al.³³ when monitoring the switching of DAEs via the conductance evolution (in high vacuum for the former and in ambient conditions for the latter) connected in a network of AuNPs.

Van der Molen et al.³³ provide two explanations for this drop in efficiency of visible photons for triggering the ring opening (cycloreversion photoreaction): it could be due to a strong electronic coupling between the molecules and the metallic nanoparticles that leads to a charge transfer so that the electron excited in the molecule is captured by the AuNP, instead of switching the molecule. The second reason is that some molecules are sterically hindered in their switching process.

Toyama et al.¹⁸⁷ were working with DAE molecules that exhibit strong geometrical reorganization upon switching and assign the fatigue to the large geometrical changes that progressively lead the molecule network into a more and more blocked configuration, where the system could not easily accommodate new movements.

2 - C5HT-di-PSH

We are now focusing on samples ADITO64 and ADITTOVI that were still prepared with 28 nm AuNPs following DAE grafting protocol 1 described in Chapter 2.I.3.a. but with a solution of C5HT-di-PSH. The preparation steps were the same for both samples, the duration

of some steps was just a bit longer for ADITTOVI (see Table 2.4 in Chapter 2.I.3.a). The same switching measurements and exploitation than for the samples with Cl-C5HT-PSH (see LEDs parameters of Table 5.1) were made for ADITO64 (see Figure 5.16 and Figure 5.17) and ADITTOVI (see Figure 5.A.5 and Figure 5.A.6).

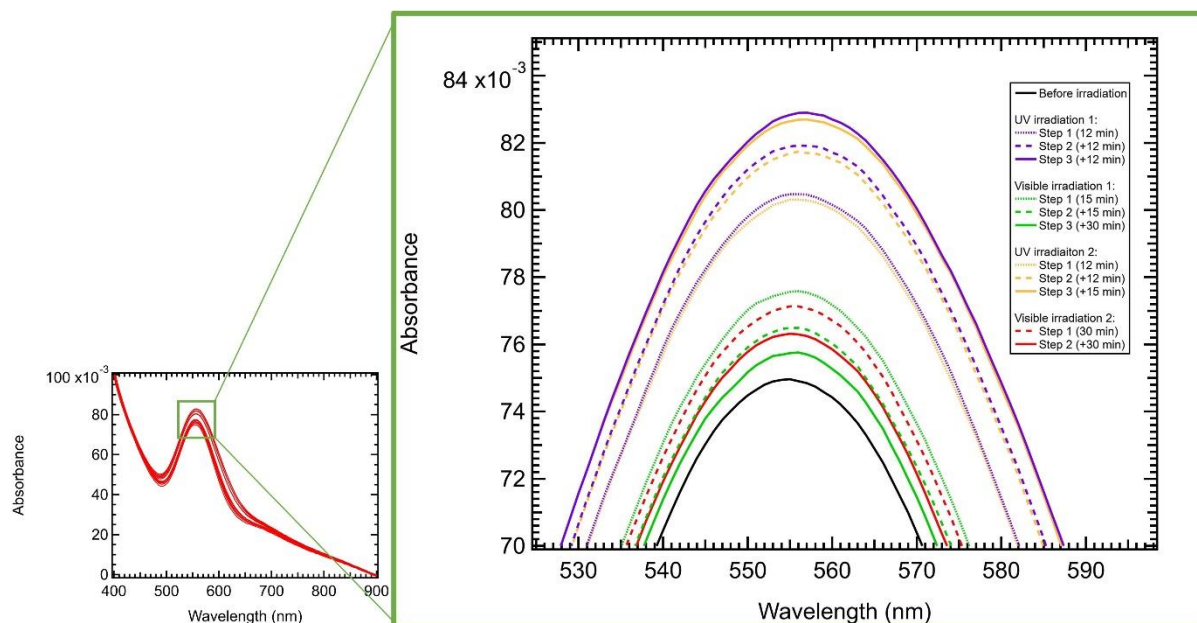


Figure 5.16: UV-visible spectra corresponding to the switching measurements on ADITO64.

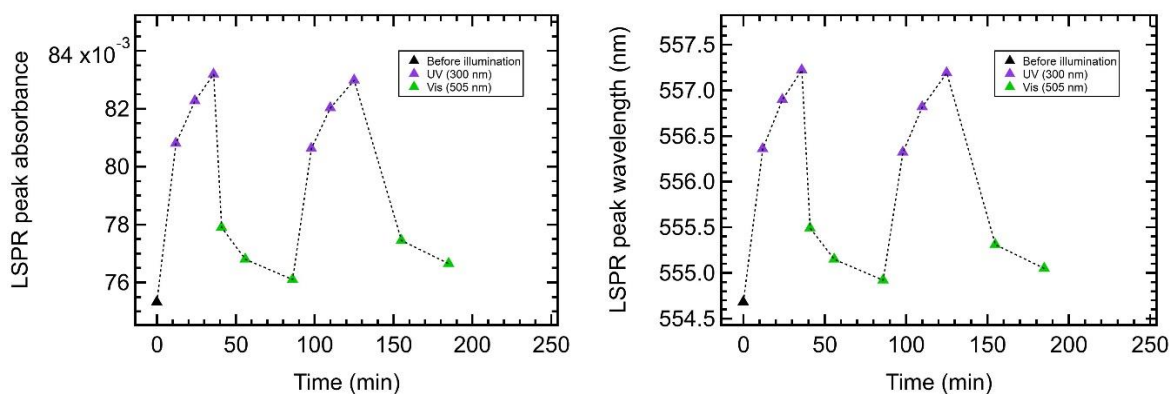


Figure 5.17: Evolution of the LSPR peak absorbance (left) and wavelength (right) of ADITO64 as a function of time upon irradiation. The dotted line is a guide for the eyes.

Reversible switching was measured for both samples, it was fully reversible in the case of ADITTOVI (see Figure A.5.6 and A.5.7) and it would probably have been the case for ADITO64 with a longer visible irradiation. For both these sample, a very thick layer of molecules was present at the surface of the AuNPs, either because some air entered during the

adsorption of the molecules inducing some crystallization or because the large excess of molecules that was used favored the formation of di sulfur bridges and therefore C5HT-di-PSH molecules chains.

Indeed, in these experiments, the LSPR peak shows up at a wavelength of 555 nm (compared to 525 nm for Cl-C5HT-PSH), which indicates a thicker molecular layer. And the absorbance values are also greater: around 85×10^{-3} abs. units (compared to 30×10^{-3} for Cl-C5HT-PSH). As a result, the kinetics are also easier to monitor.

For both cycles of each sample, it was possible to calculate a value of switching ratio using Equation 5.1 (see Table 5.2 for ADITO64 and Table A.5.1 for ADITIVI). The number of photons received by the sample is calculated using the photon flux to multiply the time of irradiation which gives a number of photons per cm^2 corresponding to the total time of irradiation. The energy of the photon is taken into account since the photon flux is calculated by dividing the light flux in mW/cm^2 by the energy of one photon in J.

$$SR(Vis/UV) = \frac{n_{photons(Visible)}}{n_{photons(UV)}} = \frac{\Delta t_{Vis} \times \Phi_{photons_Vis}}{\Delta t_{UV} \times \Phi_{photons_UV}} \quad (5.1)$$

The calculated values of switching ratio are given with a 6% precision. The uncertainty on the values of switching ratio was calculated using a formula expressing the propagation of uncertainty on the relevant parameters (see the section “Calculation of the uncertainty on the values of the switching ratios” in the Appendix).

For ADITO64, Δt_{vis} is determined graphically so that it corresponds to the difference between the time required to reach the absorbance value after the UV irradiation and the time required to go back to the initial value of the absorbance before the UV irradiation. The example of the determination of Δt_{UV} and Δt_{vis} is given in Figure 5.1 for the 2 cycles of ADITO64:

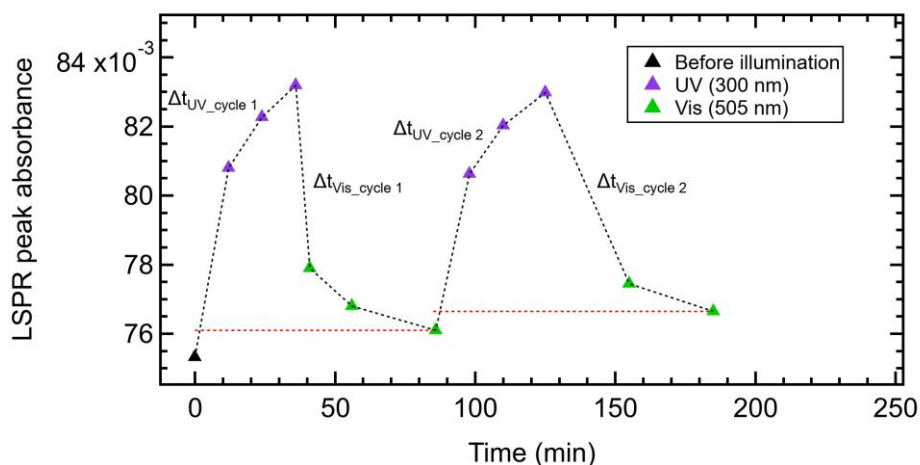


Figure 5.18: Example of the determination of Δt_{UV} and Δt_{Vis} for the calculations of the switching ratios with the data from the cycling measurements made on ADITO64. The time value corresponding to the absorbance value at the crossing of the black and the red dotted line is the one used to delimit Δt_{UV} . The black dotted line is a guide for the eyes.

Table 5.2: Values of the switching ratios calculated for the two cycles the measurements made on ADITO64.

ADITO64	Δt_{UV} (min)	Δt_{Vis} (min)	SR(UV/Vis)	SR(Vis/UV)
Cycle 1	34	50	0.032	31.4
Cycle 2	38	60	0.030	33.7

These switching ratio values will be discussed further.

For all the samples studied in this first part, the reversibility (and even full reversibility for some samples) of the switching that was observed can be attributed to the relevant choice of phenylene group as the DAE molecules linker (called “spacer” in the field of molecular electronics). Indeed, all the studies reporting reversible switching for diarylethenes connected to gold whether it was flat gold surfaces^{64,94,188–191}, gold nanoparticles^{33,62,63,95,96,187} or both^{62,63,96,187} (one leg of the molecule being connected to a flat gold electrode and the other one to a gold nanoparticle) regarded diarylethenes with a phenylene group as a spacer^{33,62–64,94–96,187–192}. This short spacer ensures sufficient decoupling of the molecules and the metal so that the photocyclization and photocycloreversion are not completely quenched and reversible switching is conserved as well as the capacity of the molecule to electrically conduct. Dulić et

al.⁹⁷ showed quite early that using thiophene rings as linker (or spacer) did not allow to have reversible switching once the molecule was connected to gold.

As an intermediate result, we can confirm that our two molecules exhibit a reversible switching even when they are chemically linked to AuNPs. This is due to the thiophene and phenylene linkers that connect the active photochromic unit to the thiol anchoring group. The ~ 0.6 nm decoupling length of these linkers avoids a total quenching of the photocycloreversion reaction. The question we need to address now is whether the quantum yield of the photocycloreversion is increased due to the plasmonic effect of the AuNPs or not.

In what follows, the samples are prepared with C5HT-di-PSH using grafting protocol 2 (see Chapter 2.I.3.b) which allows to have a monolayer of molecules at the surface of the AuNPs and not a thick layer as it was the case for the samples prepared with grafting protocol 1 (see Chapter 2.I.3.a).

II - Adsorption and switching of a monolayer of C5HT-di-PSH on 28 nm AuNPs deposited on ITO

In this second part of Chapter 5, the results presented were obtained with samples prepared following DAE grafting protocol 2 described in Chapter 2.I.3.b. We are going to study the effect the variation of some preparation steps has on the grafting of the molecules on the AuNPs. Then, the switching of the molecules for that type of samples will be investigated.

1 - Adsorption of C5HT-di-PSH on 28 nm gold nanoparticles deposited on ITO: in situ UV-visible spectroscopy monitoring

In this part, the adsorption of C5HT-di-PSH on the 28 nm has been monitored in situ with the ITO substrates immersed in solvent (stabilization phase) and in DAE solution (adsorption phase), see Chapter 2.I.3.b for the full description of the experimental procedure. All the $\Delta\lambda_{\text{LSPR}}$ were calculated by averaging the values of λ_{LSPR} of the last fifty spectra of the stabilization phase and averaging the values of λ_{LSPR} of the last two hundred spectra of the adsorption phase, the value obtained for the stabilization phase is then subtracted to that obtained for the adsorption phase.

We must start by explaining that the value of λ_{LSPR} is not the same whether the sample is in air (ambient conditions) or immersed in a solvent, in our case DMF, due to the different refractive index of these two media. This difference is illustrated in Figure 5.19, which shows the experimentally obtained UV-visible spectra and associated λ_{LSPR} of the same sample (ADITOC, ITO/AuNPs(28 nm)) in air ($\lambda_{\text{LSPR}} = 511.7$ nm) and in DMF ($\lambda_{\text{LSPR}} = 532.4$ nm). This figure also shows the spectra that were calculated with an online calculator based on Mie theory⁷⁴. These spectra were calculated for 28 nm AuNPs in air ($\lambda_{\text{LSPR}} = 499.3$ nm) and in an effective medium ($\lambda_{\text{LSPR}} = 518.4$ nm) of refractive index 1.38 corresponding to an effective medium made of ITO and DMF ($n_{\text{DMF}} = 1.4305$ at 20°C), respectively the substrate and the solvent with whom the AuNPs are in contact).

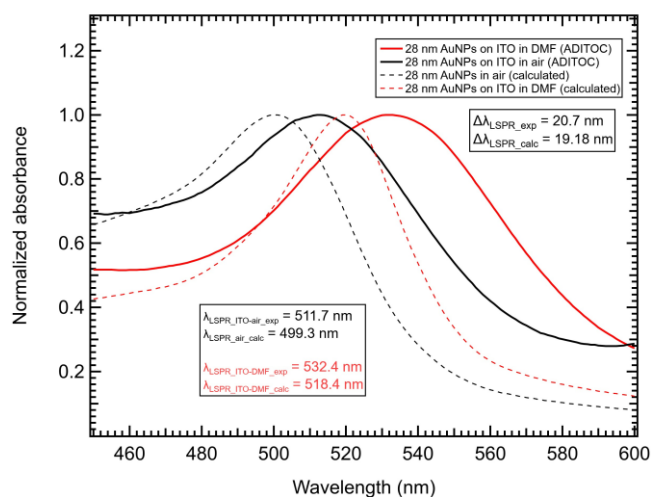


Figure 5.19: UV-visible spectrum of sample ADITOC (ITO/AuNPs(28 nm)) in air ($\lambda_{\text{LSPR}} = 511.7$ nm) and in DMF ($\lambda_{\text{LSPR}} = 532.4$ nm) and associated calculated spectra of 28 nm AuNPs in air ($\lambda_{\text{LSPR}} = 499.3$ nm) and in an effective medium ITO/DMF ($\lambda_{\text{LSPR}} = 518.4$ nm).

a - Control experiments: Evolution of λ_{LSPR} upon injection of solvent

First, two control experiments were made, they consisted in injecting solvent (DMF) at the end of the stabilization phase instead of injecting a DAE molecules solution to start the adsorption phase. The goal of these control experiments is to confirm that the small variations of λ_{LSPR} measured during the experiment is really due to the grafting of the molecules. In the first (control experiment 1) case the DMF had been degassed (ADITOB) but in the second case (control experiment 2) it had not been degassed (ADITO8). The evolution of the LSPR peak wavelength during the two phases of the experiment is shown in Figure 5.20.

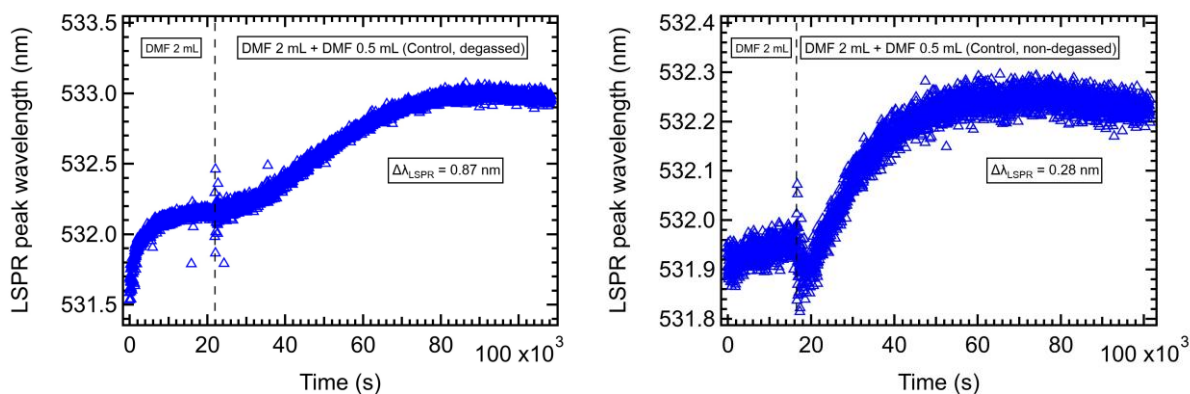


Figure 5.20: Control experiments conducted with sample ADITOB in degassed solvent (control experiment 1, on the left) and sample ADITO8 in non-degassed solvent (control experiment 2, on the right).

As expected, small values of $\Delta\lambda_{\text{LSPR}}$ are obtained for both samples, 0.87 nm for ADITOB (degassed) and 0.28 nm for ADITO8 (non-degassed). The origin of these values is a combination of the maximum values that had been measured in Chapter 2.II.b for the drift of λ_{LSPR} over time and the modification of the value of λ_{LSPR} induced by the repositioning of the custom sample holder in the cuvette after the injection.

For both ADITOB and ADITO8, two UV-visible spectra are shown for both phases of the experiment, the stabilization phase (before the injection, on the left part of the dotted line in Figure 5.20) and the adsorption phase (after the injection, on the right part of the dotted line in Figure 5.20). These spectra, shown in Figure 5.21 (for the stabilization phase) and Figure 5.22 (for the adsorption phase), allow to ensure that there is no degradation of the AuNPs layer (and therefore of the LSPR peak) during the experiment.

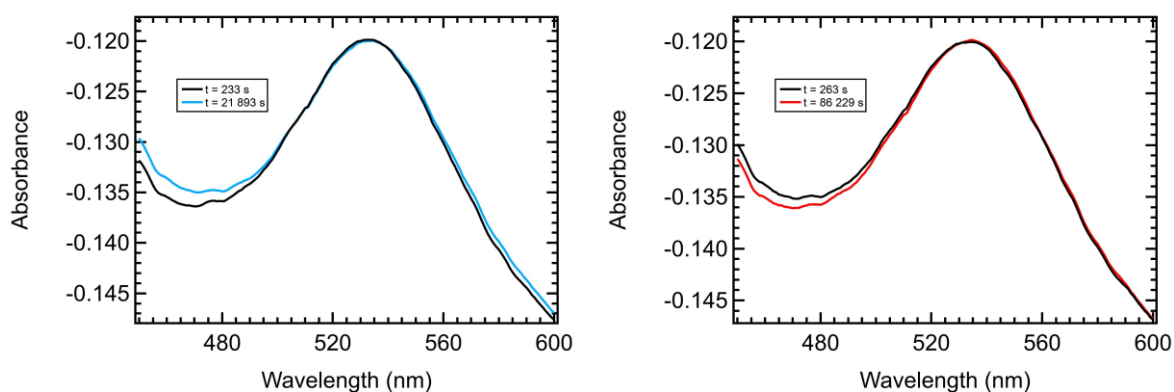


Figure 5.21: Two UV-visible spectra from each phase of the experiment (control) made with ADITOB. On the left, spectrum 10/800 (in black) and spectrum 800/800 ($t = 21893$ s) of the stabilization phase. On the right, spectrum 10/2808 (in black) and spectrum 2800/2808 ($t = 86480$ s) of the adsorption phase (in red).

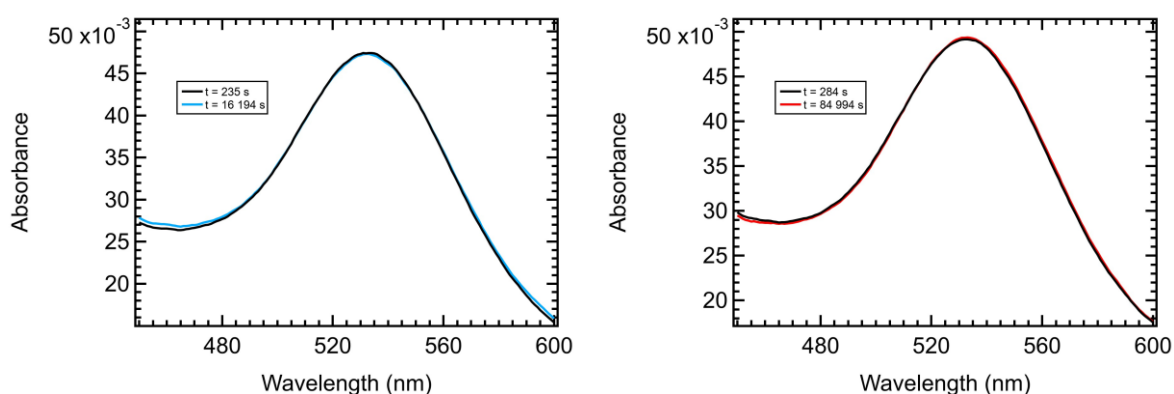


Figure 5.22: Two UV-visible spectra from each phase of the experiment (control) made with ADITO8. On the left, spectrum 10/611 (in black) and spectrum 600/611 ($t = 16503$ s) of the stabilization phase. On the right, spectrum 10/2800 (in black) and spectrum 2800/2800 ($t = 84964$ s) of the adsorption phase (in red).

The observation is the same for both samples and correspond to the behavior that was expected, the two spectra from the two phases of the experiment are superimposable, proving the absence of degradation of the AuNPs layer (no AuNPs detachment from the surface) and of any significant modification of λ_{LSPR} during the control experiments.

b - Influence of the solvent degassing

L. Ruf reported in his Master thesis that degassing the solvent allowed to drastically reduce the drift of λ_{LSPR} during both phases of the experiment¹²⁶. We decided to test this affirmation. First, we studied the influence of degassing the solvent on the drift of λ_{LSPR} during the stabilization phase. The evolution of λ_{LSPR} during three different stabilization phases (two for which the solvent was degassed, one for which it was not) is presented in Figure 5.23.

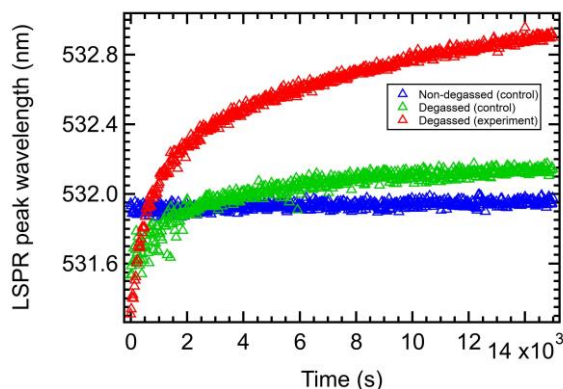


Figure 5.23: Evolution of λ_{LSPR} during three different stabilization phases, two with degassed solvent (one from the control experiment made with sample ADITOB in green, one from the experiment made with sample ADITOC, in red) and one with non-degassed solvent (from the control experiment made with sample ADITO8).

The stabilization phase presenting the smallest λ_{LSPR} drift is the one made with non-degassed solvent. This observation is further confirmed by plotting the data from the two control experiments (one had been made with degassed solvent and the other with non-degassed solvent) on the same graph (see Figure 5.24). It appears clearly that the control experiment displaying the smallest $\Delta\lambda_{\text{LSPR}}$ between the beginning and the end of the adsorption phase is the one conducted with non-degassed solvent with a $\Delta\lambda_{\text{LSPR}}$ value of 0.28 nm versus 0.81 nm for the control experiment made with degassed solvent. At a first sight it is unexpected that the degassed solvent is the one that causes the most variation for $\Delta\lambda_{\text{LSPR}}$. However, since the initial sample is in non-degassed DMF, DMF contains dissolved oxygen and nitrogen. The addition of an equal amount (2 mL) of degassed solvent changes significantly the local optical index around the nanoparticles which causes the 0.81 nm shift over 60 s as shown in Figure 5.24 (left panel).

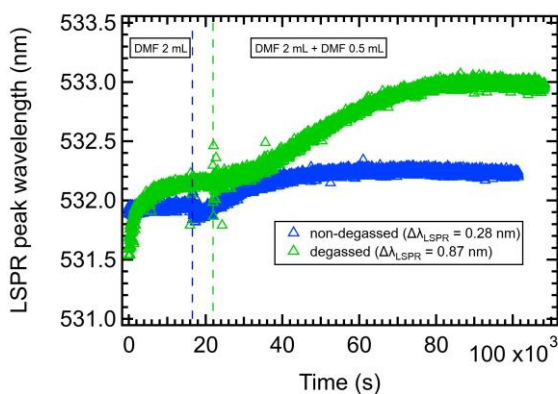


Figure 5.24: Control experiments made with degassed (in green) and non-degassed (in blue) solvent.

Degassing the solvent and preparing DAE solutions with degassed solvent is inconvenient, it takes a lot more time and requires more precautions to avoid reoxygenation/rehydration of the solvent. We demonstrated that using degassed solvent did not ensure to significantly and reproducibly limit the drift of λ_{LSPR} during the grafting protocol and that it could actually create a drift due to the reoxygenation/rehydration of the solvent during the experiment. In what follows, the grafting protocol has been conducted without degassing the solvent, except for the experiment with sample ADITOC (whose stabilization phase has been previously shown in Figure 5.23).

c - Influence of the deprotection of the molecules on the grafting

In the literature, it has been claimed that since the Au-S bond formation is so favored, the S-Ac bond (i.e., the bond between the thiol function and its protecting acetyl group) spontaneously cleaves upon chemisorption on gold^{64,94,188}, rendering deprotection useless¹⁹³. It is important to note that both Katsonis et al.⁹⁴ and Arramel et al.⁶⁴ worked with DAE molecules very similar to the ones we are using, rendering the comparison between their work and ours particularly relevant.

To test if the grafting of our protected molecule (C5HT-di-PSAc) took place to the same extent or at all compared to when it is deprotected (C5HT-di-PSH), we carried out the grafting procedure and monitored it without deprotecting C5HT-di-PSAc (sample ADITO1). The test was also made with Cl-C5HT-PSAc (sample ADITO5). The results are presented in Figure 5.25.

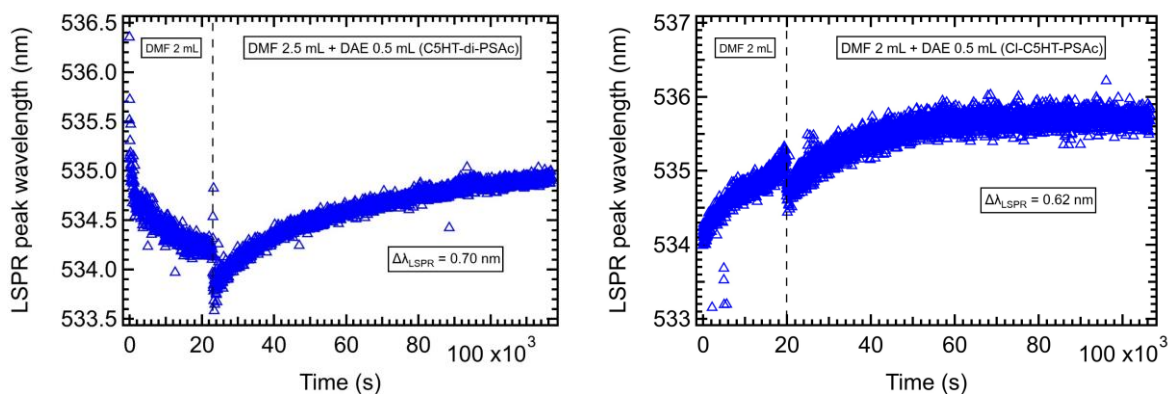


Figure 5.25: Tentative of grafting of the protected molecules C5HT-di-PSAc (on the left, sample ADITO1) and Cl-C5HT-PSAc (on the right, sample ADITO5) on 25 nm gold nanoparticles deposited on ITO.

The values of $\Delta\lambda_{LSPR}$ obtained are similar to that obtained for the control experiment (without injecting DAE molecules), indicating that no grafting took place. In our case, the deprotection of the molecules is necessary. In the three previously cited references, SAMs on flat gold surfaces, flamed Au(111) surfaces in the case of Katsonis et al. and Arramel et al., 60 nm thermally evaporated gold layer on a 500 nm silicon oxide layer with a 1 nm Cr adhesion layer on top of it and a p-type silicon wafer beneath it in the case of Kronemeijer et al. were prepared (with immersion times comparable to ours but non-protected molecules). In our case, spherical gold nanoparticles were used. The differences observed may be due to the geometry differences between both types of gold surfaces (flat and spherical).

For both ADITO1 and ADITO5, two UV-visible spectra are shown for both phases of the experiment, the stabilization phase (before the injection, on the left part of the dotted line in Figure 5.25) and the adsorption phase (after the injection, on the right part of the dotted line in Figure 5.25). These spectra, shown in Figure 5.26 (for the stabilization phase) and Figure 5.27 (for the adsorption phase), allow to ensure that there is no degradation of the AuNPs layer (and therefore of the LSPR peak) during the experiment.

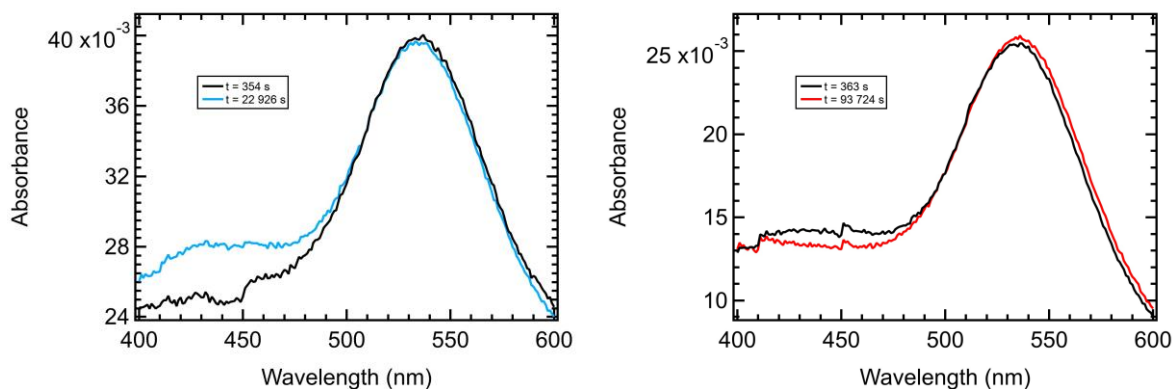


Figure 5.26: Two UV-visible spectra from each phase of the experiment made with ADITO1. On the left, spectrum 10/572 (in black) and spectrum 570/572 ($t = 23009$ s) of the stabilization phase. On the right, spectrum 10/2182 (in black) and spectrum 2180/2182 ($t = 93807$ s) of the mixing phase (in red).

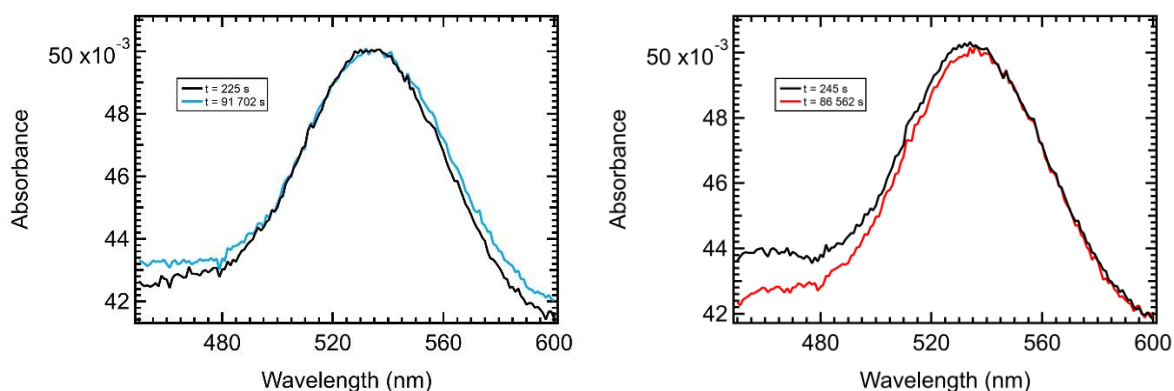


Figure 5.27: Two UV-visible spectra from each phase of the experiment made with ADITO5. On the left, spectrum 10/757 (in black) and spectrum 750/757 ($t = 19894$ s) of the stabilization phase. On the right, spectrum 10/2904 (in black) and spectrum 2900/2904 ($t = 86680$ s) of the mixing phase (in red).

The observation is the same for both samples and correspond to the behavior that was expected, the two spectra from the two phases of the experiment are almost superimposable, proving the absence of degradation of the AuNPs layer and of any significant modification of λ_{LSPR} during the grafting without deprotection tests. The noise present on the spectra is due to the stirring bar hitting the cuvette.

d - Evolution of λ_{LSPR} upon injection of C5HT-di-PSH solution: grafting

The evolution of λ_{LSPR} of the AuNPs upon injection of 0.5 mL of C5HT-di-PSH is presented in Figure 5.28 for a sample prepared in non-degassed solvent (ADITOI) and a solvent prepared in degassed solvent (ADITOC). The expected value of the shift for the formation of a full molecular monolayer was calculated with the predictive model from Chapter 3 using Equation 3.4, $\Delta\lambda_{\text{LSPR}} = 2.53$ nm with the following parameters $m = 73$ (calculated for 28 nm AuNPs with the same method than that presented in Chapter 3), $q = 0.064$, $\Delta n = 0.08$ ($n_{\text{molec}} = 1.46 - n_{\text{effective medium ITO-DMF}} = 1.38$), $l_d = 6.3$ (calculated for AuNPs with a radius $R = 14$ nm with Equation 3.8) and the length of the molecules in the open form: $d = 1.91$ nm.

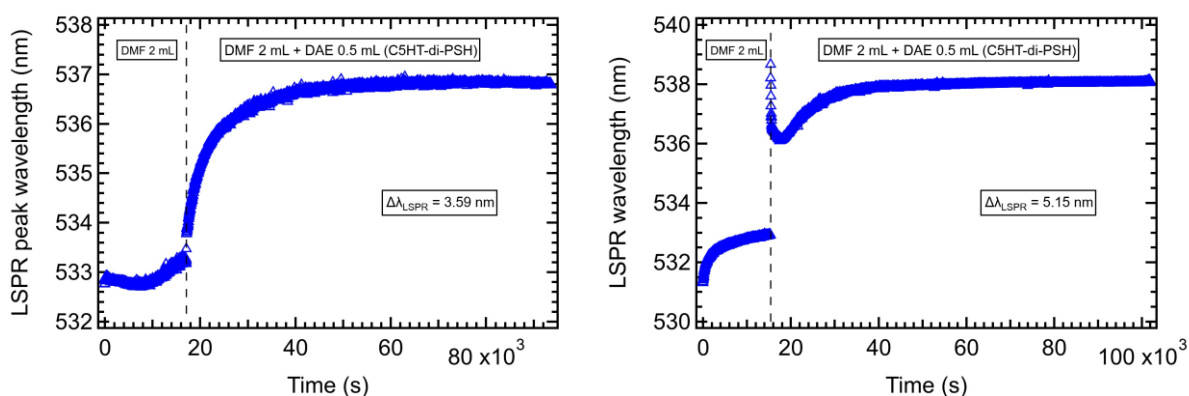


Figure 5.28: Grafting of C5HT-di-PSH on 25 nm gold nanoparticles deposited on ITO. Deposition carried out in a DAE solution prepared with non-degassed DMF for sample ADITOI (on the left) and in a DAE solution prepared with degassed DMF for sample ADITOC (on the right).

A $\Delta\lambda_{\text{LSPR}}$ of 3.59 nm (between the end of the stabilization phase and that of the adsorption phase) is obtained for ADITOI and a $\Delta\lambda_{\text{LSPR}}$ of 5.15 nm is obtained for ADITOC. ADITOI, whose $\Delta\lambda_{\text{LSPR}}$ value is a bit superior to the calculated one, must be covered by a full layer of molecules or slightly more and ADITOC, whose $\Delta\lambda_{\text{LSPR}}$ value is superior to the calculated one and to that of ADITOI is either covered by more than a monolayer of molecules or covered with a monolayer of molecules (or even a little less) and part of the shift value is due to the reoxygenation/rehydration of the degassed DMF during the experiment.

The evolution of λ_{LSPR} of the AuNPs upon injection of 0.5 mL of C5HT-di-PSH is presented for other samples ADITOD ($\Delta\lambda_{\text{LSPR}} = 2.41$ nm corresponding to a coverage of 95.3 %), ADITOG ($\Delta\lambda_{\text{LSPR}} = 3.34$ nm corresponding to more than a monolayer) and ADITOH ($\Delta\lambda_{\text{LSPR}} = 1.79$ nm corresponding to a coverage of 70.8 %) in the Appendix, respectively in Figure A.5.8 for ADITOD, in Figure A.5.9 for ADITOG and in Figure A.5.10 for ADITOH.

For both ADITOI and ADITOC, two UV-visible spectra are shown for both phases of the experiment, the stabilization phase (before the injection, on the left part of the dotted line in Figure 5.28) and the adsorption phase (after the injection, on the right part of the dotted line in Figure 5.28). These spectra shown in Figure 5.29 (for the stabilization phase) and Figure 5.30 (for the adsorption phase), allow to ensure that there is no degradation of the AuNPs layer (and therefore of the LSPR peak) during the experiment.

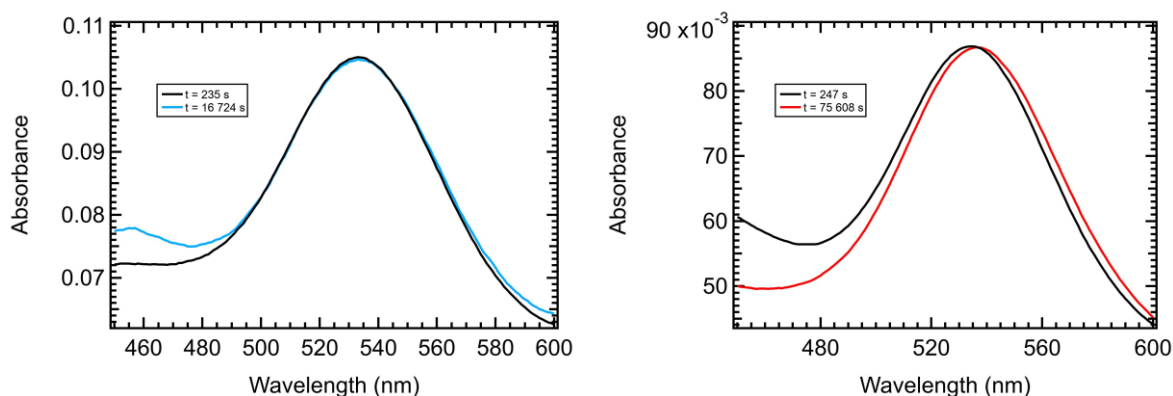


Figure 5.29: Two UV-visible spectra from each phase of the experiment made with ADITOI. On the left, spectrum 10/633 (in black) and spectrum 620/633 ($t = 17119$ s) of the stabilization phase. On the right, spectrum 10/2528 (in black) and spectrum 2500/2528 ($t = 76552$ s) of the adsorption phase (in red).

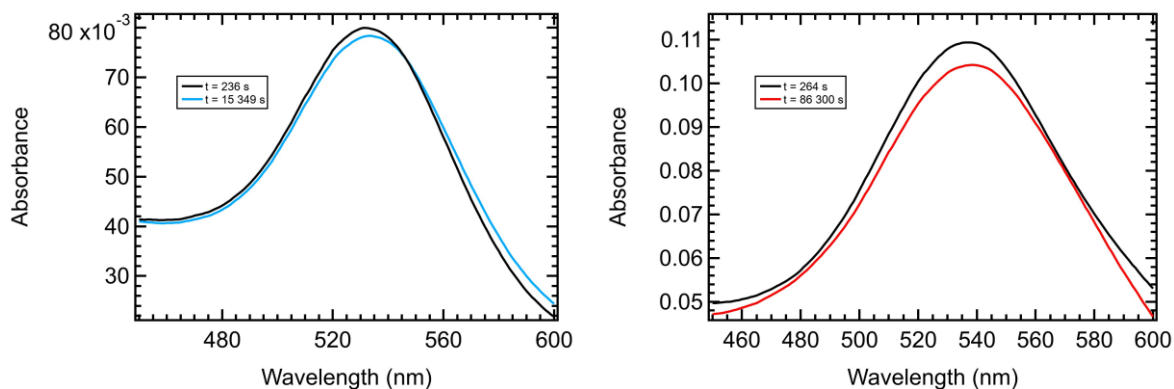


Figure 5.30: Two UV-visible spectra from each phase of the experiment made with ADITOC. On the left, spectrum 10/571 (in black) and spectrum 570/571 ($t = 15377$ s) of the stabilization phase. On the right, spectrum 10/2805 (in black) and spectrum 2800/2805 ($t = 86447$ s) of the adsorption phase (in red).

The observation is the same for both samples and correspond to the behavior that was expected for a successful grafting. The two spectra from the stabilization phase are perfectly (for ADITOI) and almost (for ADITOC) superimposable. A part of the shift can be seen on the graph containing the two spectra from the adsorption experiment. The aspect of the spectra does not change from the beginning to the end of the experiment ruling out any degradation of the AuNPs layer.

The type of samples obtained using this second grafting protocol is schematized in Figure 5.31.

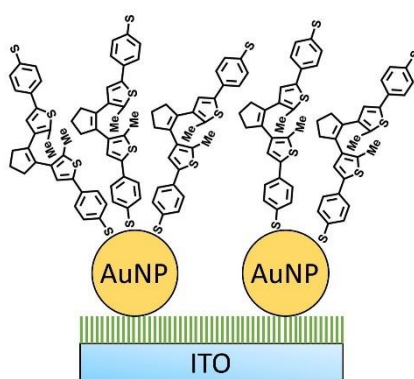


Figure 5.31: Scheme of the type of sample obtained with grafting protocol 2: ITO/AuNPs(28 nm)/C5HT-PSH. The green sticks are silanes (APTES). Note that this sketch is not on scale since the size of the DAE molecules is 1.79 nm, that of the APTES molecules is 0.5 nm and that of the AuNPs in 28 nm.

2 - Switching of C5HT-di-PSH grafted on 28 nm gold nanoparticles deposited on ITO

Switching measurements were carried out as described in Chapter 2.II.2.b, the sample was successively irradiated with UV (300 nm) and visible (505 nm) light. The parameters used for each type of illumination are reminded in Table 5.3.

Table 5.3: LEDs parameters used for the switching measurements made on the samples prepared with grafting protocol 2.

LED	I (A)	P (mW)	Φ (mW/cm ²)	Φ_{photons} (photons/s/cm ²)
UV	0.07	5.5×10^{-2}	0.194	2.93×10^{14}
Vis	0.67	1.30	2.65	6.74×10^{15}

The switching measurements presented in Figure 5.32 performed on ADITOI (on Day 1) consisted in 3 UV-visible irradiation cycles with irradiations of the same duration (30 minutes). These measurements were repeated the day after (Day 2, see Figure A.5.11 and A.5.12) and the day after (Day 3, see Figure A.5.13 and A.5.14) but with different irradiation durations (see the aforementioned figures for the duration values). The LSPR peak absorbance and wavelength were then extracted by fitting the LSPR peaks with a Lorentzian function (see Chapter 2.II.1.d for more details) and the evolution of the absorbance at λ_{LSPR} and that of λ_{LSPR} were plotted versus the time and versus the number of photons (see Figure 5.33 for the measurements of Day 1, Figure 5.A.11 for those of Day 2, Figure 5.A.13 for those of Day 3 and Figure 5.35 for the measurement of the three days).

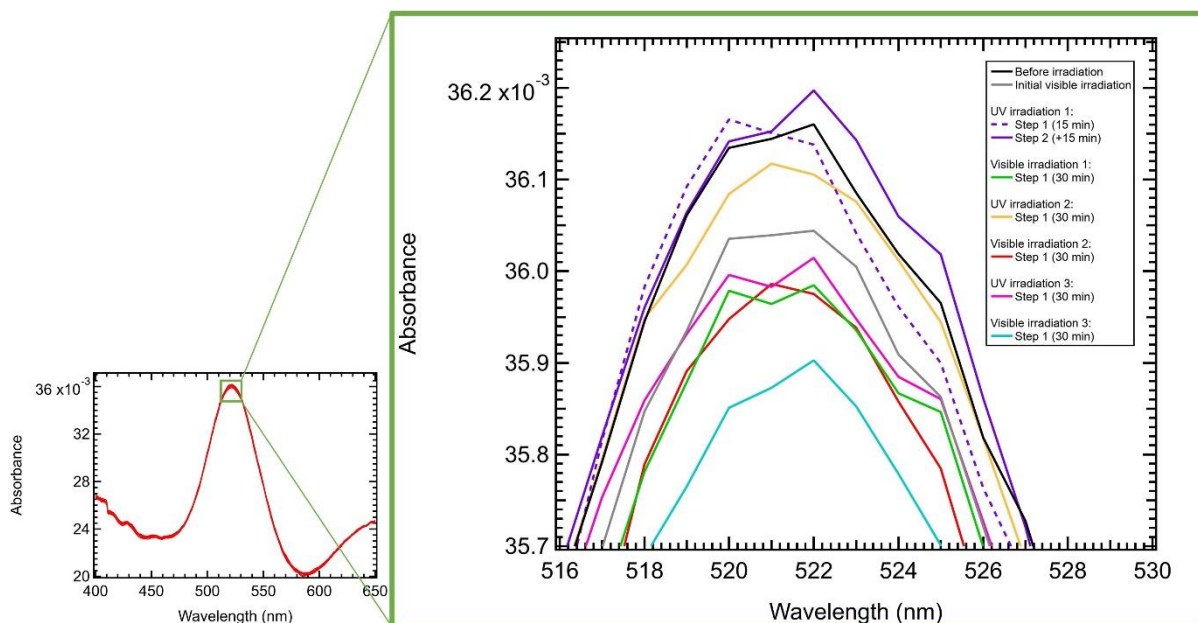


Figure 5.32: UV-visible spectra corresponding to the switching measurements on ADITOI (Day 1).

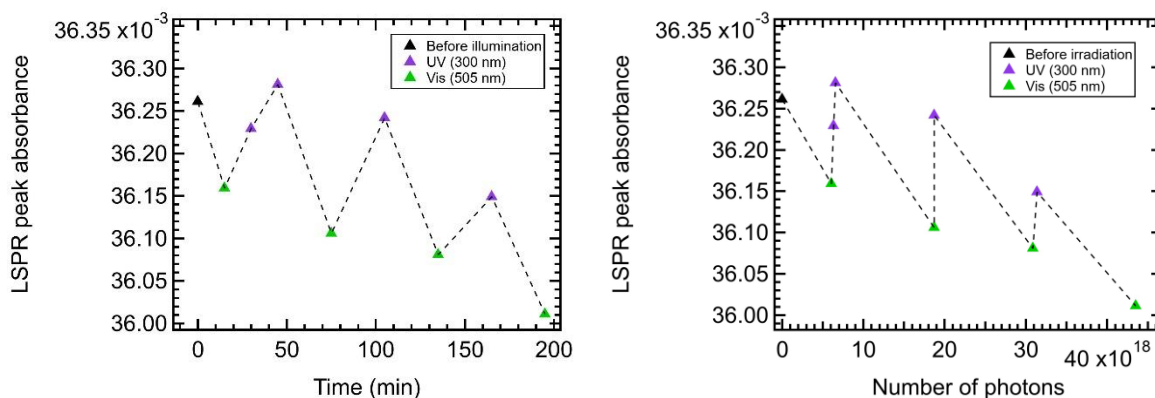


Figure 5.33: Evolution of the LSPR peak absorbance of ADITOI (Day 1) as a function of time (left) or number of photons (right) upon irradiation. The dotted line is a guide for the eyes.

Unlike for ADITO64, for ADITOI (but also ADITOC and ADITOEVI) Δt_{vis} (and not Δt_{UV}) is determined graphically so that it corresponds to the difference between the time required to reach the absorbance value after the UV irradiation and the time required to go back to the initial value of the absorbance before the UV irradiation. The example of the determination of Δt_{UV} and Δt_{vis} is given in Figure 5.34 for the 3 cycles of ADITOI.

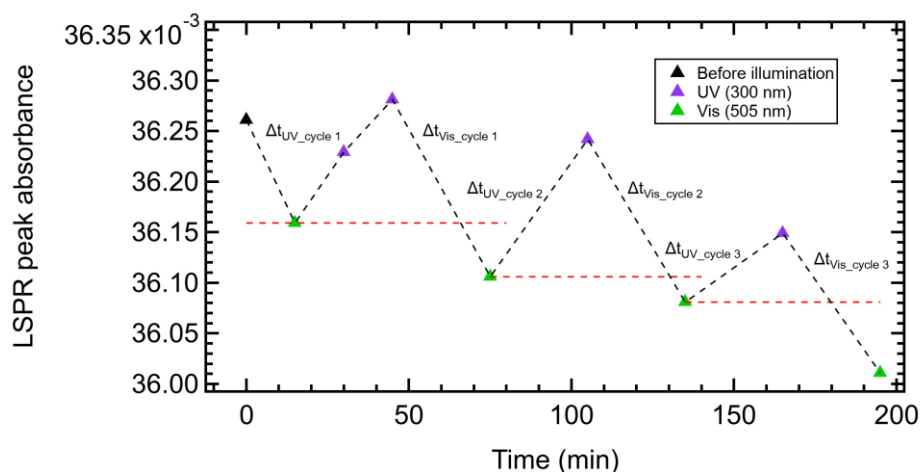


Figure 5.34: Example of the determination of Δt_{UV} and Δt_{vis} for the calculations of the switching ratios with the data from the cycling measurements made on ADITOI (Day 1). The time value corresponding to the absorbance value at the crossing of the black and the red dotted line is the one used to delimit Δt_{vis} . The black dotted line is a guide for the eyes.

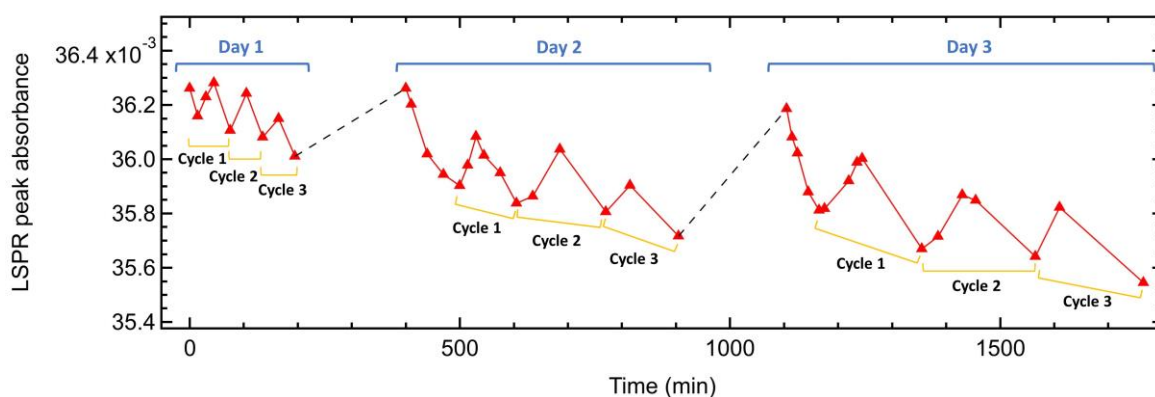


Figure 5.35: Evolution of the LSPR peak absorbance of ADITOI over 3 consecutive days of measurements as a function of time upon irradiation. The time scale between each measurement day (in the 2 dotted lines zone) was voluntarily shortened, it does not actually correspond to how much time passed in between the series of measurement.

ADITOI clearly displays fully reversible switching, its ability to switch reversibly is durable since it was possible to make it switch reversibly during measurement sessions carried out three days in a row. However, it also undergoes fatigue since always longer visible irradiations are necessary to make it switch back (it is particularly noticeable if we compare the durations of the visible irradiations on Day 1 and on Day 3).

For each switching cycle, it was possible to calculate a value of switching ratio (see Table 5.4) using the method explained in 5.I.2.

The calculated values of switching ratio are given with a 6% precision. The uncertainty on the values of switching ratio was calculated using a formula expressing the propagation of uncertainty on the relevant parameters (see the section “Calculation of the uncertainty on the values of the switching ratios” in the Appendix).

Table 5.4: Values of the switching ratios (Vis/UV above, UV/Vis in parenthesis below) calculated for each cycle of each measurement day of ADITOI.

ADITOI		Δt_{UV} (min)	Δt_{vis} (min)	SR(UV/Vis)	SR(Vis/UV)
Day 1	Cycle 1	30	21	0.062	16.1
	Cycle 2	30	25	0.052	19.2
	Cycle 3	30	15	0.087	11.5
Day 2	Cycle 1	29	56	0.023	44.42
	Cycle 2	80	73	0.048	21.0
	Cycle 3	45	47	0.042	24.0
Day 3	Cycle 1	79	63	0.055	18.3
	Cycle 2	75	118	0.028	36.2
	Cycle 3	45	101	0.019	51.63

The same measurements and exploitation were made on ADITOC (see Figure 5.36 and Figure 5.37). A value of switching ratio was calculated for both cycles (see Table 5.5). The values of the switching ratios are going to be discussed in the last part of this chapter.

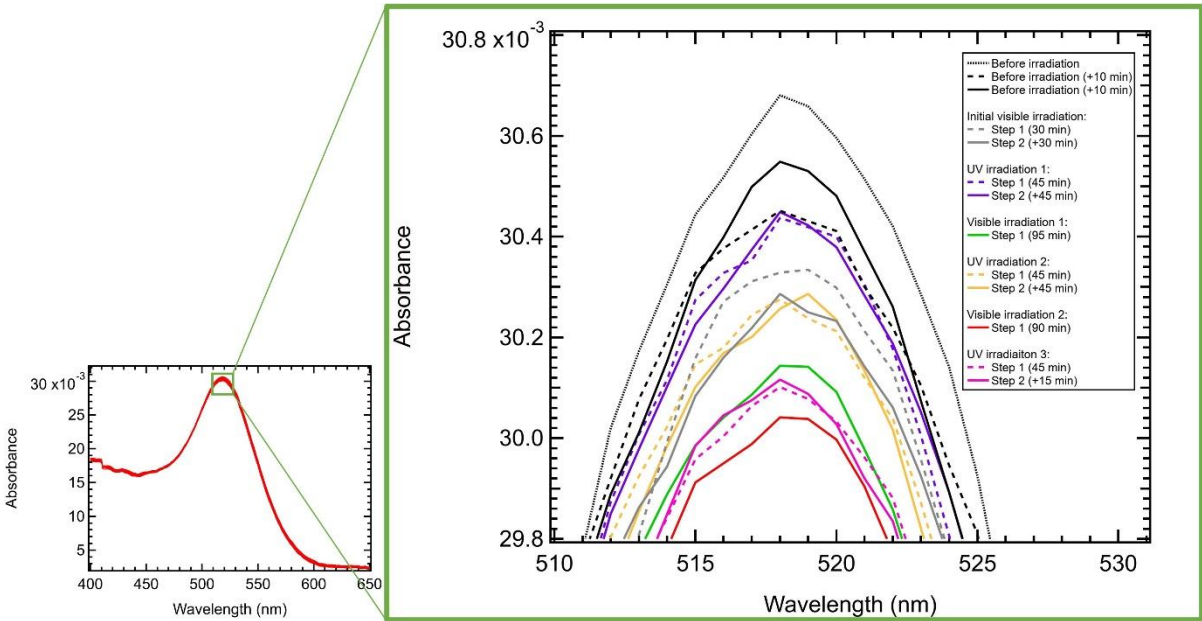


Figure 5.36: UV-visible spectra corresponding to the switching measurements on ADITOC.

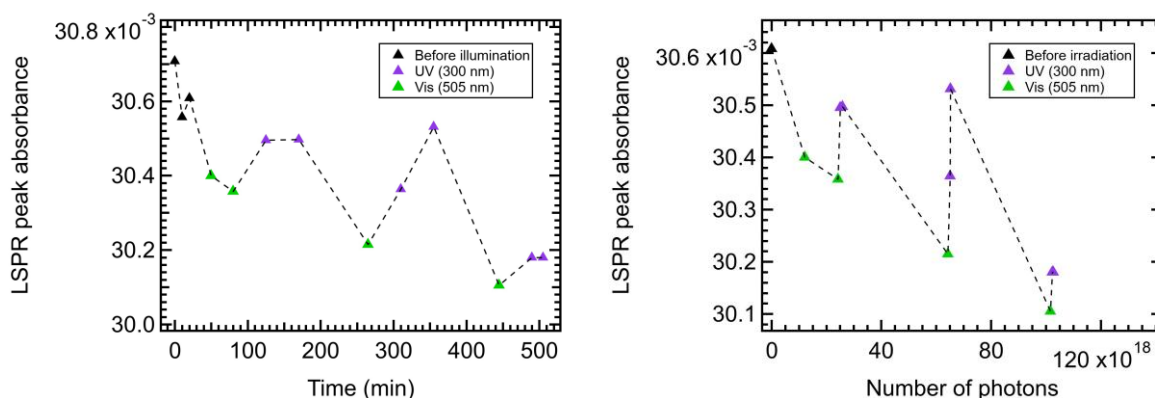


Figure 5.37: Evolution of the LSPR peak absorbance of ADITOC as a function of time (left) or number of photons (right) upon irradiation. The dotted line is a guide for the eyes.

ADITOC switches fully reversibly however it undergoes fatigue, indeed, the last UV irradiation that lasted 60 minutes only made a very low amount of molecules switch, much lower than for the two previous switching cycles.

Table 5.5: Values of the switching ratios (Vis/UV above, UV/Vis in parenthesis below) calculated for the two cycles the measurements made on ADITOC.

ADITOC	Δt_{UV} (min)	Δt_{Vis} (min)	SR(UV/Vis)	SR(Vis/UV)
Cycle 1	45	47	0.042	24.0
Cycle 2	90	67	0.058	17.1

It is important to note that at the end of each visible irradiation, we always reach a lower value of the absorbance at λ_{LSPR} , it is either due to the fact that not all the molecules were in their open form before the beginning of the measurements which would be surprising since initial visible irradiation were performed before the beginning of the switching cycles measurements precisely so that the measurements would start with all the molecules in their open form, or it is due to a drift of the spectrophotometer.

Both samples prepared with grafting protocol 2 (see Chapter 2.I.3.b) exhibit fully reversible switching. As previously explained at the end of the first part of this chapter, it is attributed to the relevant choice of phenylene group as the DAE molecules linker (see discussion of 5.I.2). Switching ratios values could be calculated for some of the switching cycles, they will be discussed and compared to the value calculated for another type of

switching measurements in the next part of this chapter. Here, the switching is computed with the DAE linked to the AuNPs and probed in air. The average SR is about 26 (average over the 11 values displayed in Table 5.4 and Table 5.5). This value is higher than the value of 6.4 (Table 4.7) computed for the same C5HT-di-PSH molecule when it is free and in the DMF solvent. It means that more visible photons are necessary for triggering the cycloreversion photoreaction when the molecule is linked to an AuNP, compared to the molecule in solution. We were expecting the opposite trend, and it is discussed in the following section.

III - Determination of the influence of the plasmonic nanoantenna effect on the reversible switching kinetics: comparison with the kinetics in solution

In the last part of this chapter, a last value of switching ratio will be calculated for the sample ADITOI based on more specific switching measurement. Then, this SR value and all the previously calculated values will be discussed and compared to the SR value calculated in Chapter 4 for the DAE molecules in solution. Finally, the presence and influence of the plasmonic nanoantenna effect, providing LSPR enhancement of the switching reaction will be discussed.

1 - Calculation of the switching ratio for C5HT-di-PSH grafted on 28 nm AuNPs deposited on ITO

Additional switching measurements, shown in Figure 5.38, were carried out to be able to calculate the switching ratio as precisely as possible. These measurements were intended only for that purpose unlike the previous cycles measurements used to assess the reversibility and the fatigue but from which it was possible to evaluate the SR. They were conducted in the same experimental conditions than all the other switching measurements presented in Chapter 5.II which are described in the last paragraph of Chapter 2.I.1.d. However, here, the UV irradiation was made particularly long to really make the plateau indicating that the full switching of the molecules took place appear. The measurements can be decomposed in five parts:

(1) From $t = 0$ to $t = 220$ min, three spectra were recorded every 10 minutes before any irradiation took place to make sure the spectrophotometer is stabilized and provides a reproducible spectrum of the sample. Then the sample was irradiated with visible light for 90 min so that we could start the experiment with all the molecules in the open form (OF). A

spectrum was recorded 20 min after this initial 90 min visible irradiation, then a second 90 min irradiation was made, and a spectrum was recorded immediately after. Since it was identical to the previously recorded one, we considered all the molecules were in the OF and the experiment could start.

(2) From $t = 220$ to $t = 431$ min, the sample is irradiated with UV light to make all the molecules switch to their closed form (CF). The absorbance increases until it reaches a plateau (for $\Delta t_{UV} = 60$ min) indicating that all the molecules are now in their CF.

(3) From $t = 431$ to $t = 446$ min, the sample is irradiated with visible light for 15 min, the absorbance decreases and goes back slightly below its value before the UV irradiation, which corresponds to the initial state for which we had all the molecules in the OF. In doing so, we can be sure that all the molecules were switched back to the OF for $\Delta t_{vis} = 15$ min. Furthermore, it confirms that the increase of the absorbance measured for the UV irradiation was significant (corresponded to the switching) and was not due to a measurement artefact that would make the absorbance increase. It would have been appreciable to have an intermediate value of the absorbance upon visible irradiation, however, it was hardly predictable that 15 minutes would be enough to make all the molecules switch back to the open state considering that it took much longer during the previous measurements made on this sample (and in general). The cycle measurements performed on Day 2 shown in Figure A.5.14 demonstrates it quite well.

(4) From $t = 466$ to $t = 547$ min, the sample is irradiated with UV light for 120 min ($2 \times \Delta t_{UV} = 60$ min) to make all the molecules switch to the CF once more. However, the absorbance value reached after this second UV irradiation is inferior to that reached after the first UV irradiation.

(5) From $t = 547$ to $t = 617$ min, the sample is irradiated with visible light for 50 minutes to make all the molecules switch back to the OF, which they do.

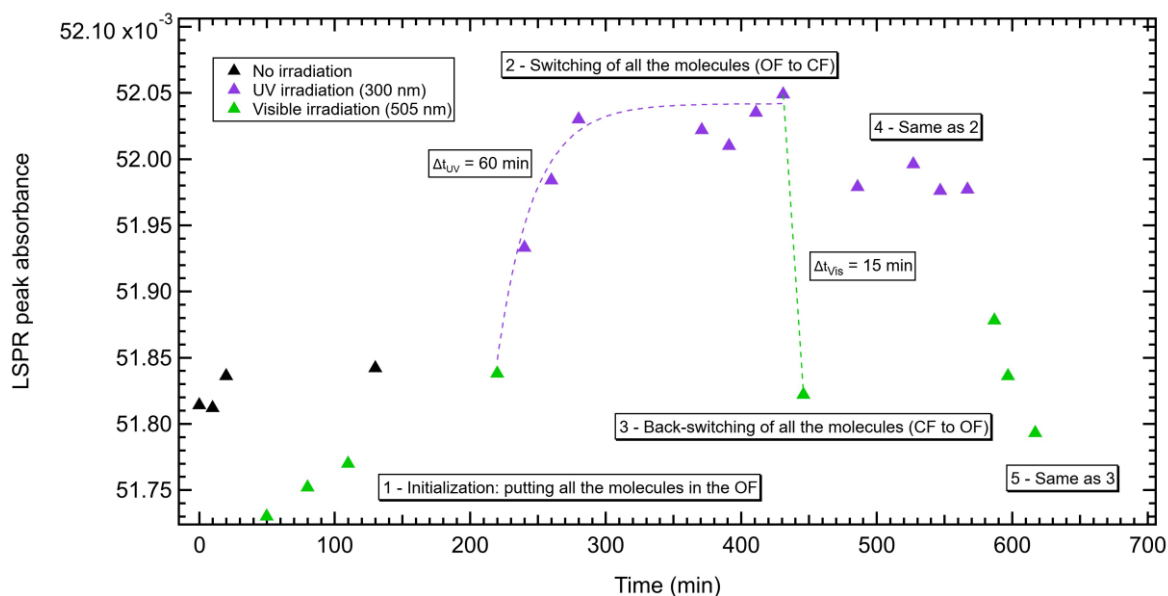


Figure 5.38: Evolution of the LSPR peak absorbance of ADITOI as a function of time.

The value of the switching ratio is calculated as previously explained using Equation 5.1 and the durations of the irradiations $\Delta t_{UV} = 60$ min and $\Delta t_{vis} = 15$ min required to make the molecules respectively switch and switch back. We obtain $SR(Vis/UV) = 5.76$. The much shorter irradiation times (especially regarding the visible light irradiation time) required to make the molecules switch and then used to calculate a switching ratio value inferior to those previously calculated could be explained by the fact that it was the fourth session of measurements on ADITOI. Some molecules may have been damaged or quenched during the previous measurement sessions. It means that a lower number of molecules able to switch was left, explaining why it took less time to make them switch than previously for a larger number of molecules.

2 - Comparison of the SR values obtained for molecules in solution and molecules grafted on 28 nm AuNPs deposited on ITO

Let us remind that the value of the switching ratio $SR(Vis/UV)$ obtained for C5HT-di-PSAc in solution, given in Chapter 4, is 6.42. The values obtained for C5HT-di-PSH grafted on 28 nm AuNPs with protocol 1 (ADITO64 and ADITОВI) or 2 (ADITOI, ADITOC) deposited on ITO are summarized in Table 5.6.

Table 5.6: Values of SR(Vis/UV) obtained for C5HT-di-PSH grafted on 28 nm AuNPs deposited on ITO.

Sample	λ_{LSPR}	Figure	Average SR(Vis/UV)
ADITO64	555.0	5.17	32.6
ADITОВI	551.3	A.5.6	22.9
ADITOI (Day 1)	522.0	5.33	15.6
ADITOI (Day 2)	521.8	A.5.11	29.8
ADITOI (Day 3)	521.8	A.5.13	35.4
ADITOC	518.0	5.37	20.6
ADITOI (Day 4)	524.8	5.38	5.8

As previously mentioned for ADITO69, a multilayer of molecules is probably present on top of the AuNPs of samples ADITO64 and ADITОВI that were prepared with grafting protocol 1 and thus a large excess of DAE molecules. It explains the larger value of their λ_{LSPR} compared to that of samples ADITOI and ADITOC prepared with grafting protocol 2 and thus a lower quantity of DAE molecules. For these two samples, a monolayer is likely present at the surface of the AuNPs.

It is delicate to make a direct comparison between molecules in solution and molecules on the AuNPs for several reasons: the number of molecules in the solution and on the AuNPs is not the same and some surface confinement effects appear for the molecules on the AuNPs⁶⁴. Regarding the number of molecules, very quick and simple order of magnitude calculations can be made. For 2 to 3 mL of C5HT-di-PSAc solution at $1.25 \times 10^{-5} \text{ mol.L}^{-1}$, we are dealing with about 10^{16} molecules, however the SR was calculated for measurements during which only about 13% of the potentially switchable molecules had been switched so roughly 10^{15} molecules. For the C5HT-di-PSH molecules grafted on the AuNPs, we injected 2.5 mL of solution at 5 μM so 7.5×10^{15} molecules, considering that every molecule takes 0.25 nm^2 on the surface of the AuNPs, that the surface of the ITO substrate is full covered by AuNPs and that the measured part of the substrate (considering the geometry of the sample holder) has a surface of 0.5 cm^2 , we are dealing with 10^{14} molecules.

Let us now calculate the expected absorption spectrum in the case of the absence of interaction between the AuNPs and the DAE molecules. First, we need to calculate the effective absorbance of a mixture of AuNPs and DAEs to evaluate the variation of the absorbance of the mixture when the DAEs switch between their OF and CF. Since both the AuNPs and the CF-DAEs exhibit a strong absorption band around 520 nm, it is important to know whether the

switching produce an important change in the absorption of the mixture or not. This calculation is based on the Beer-Lambert law and thus on the fact that the molar absorption coefficient is proportional to the absorbance. For 25 nm AuNPs, we can estimate that a full coverage with DAEs corresponds roughly to $N_{DAE} = 9000$ molecules per nanoparticle. The molar absorptivity of CF-C5HT-di-PSAc was previously measured (see Table 4.2), its maximum value is reached at 546 nm, and we have $\epsilon_{546} = 15\,500 \text{ M}^{-1}\text{cm}^{-1}$. The molar absorptivity of the AuNPs is linked to their cross section with:

$$\epsilon_{AuNP} = \frac{10^{-3}}{\ln 10} \cdot N_A \cdot \sigma_{ext AuNP}$$

$\sigma_{ext AuNP}$ can be calculated from the electrostatic approximation of the Mie theory⁷⁰ (see Figure 5.39). We obtain a value at LSPR of $\epsilon_{AuNP} = 2.7 \times 10^9 \text{ M}^{-1}\text{cm}^{-1}$. This value is in agreement with that of Liu et al.¹⁵² who obtained $\epsilon_{AuNP} = 2.9 \times 10^9 \text{ M}^{-1}\text{cm}^{-1}$ at $\sim 520 \text{ nm}$, the authors do not provide the values obtained for other wavelengths.

The molar absorbance coefficient of the mixture is:

$$\epsilon_{mix} = \epsilon_{DAE} \cdot C_{DAE} \cdot b + \epsilon_{AuNP} \cdot C_{AuNP} \cdot b = (\epsilon_{DAE} \cdot N_{DAE} + \epsilon_{AuNP}) C_{AuNP} \cdot b$$

In the following, we plot $\epsilon_{mix} = (\epsilon_{DAE} \cdot 9000 + \epsilon_{AuNP}) C_{AuNP} \cdot b$

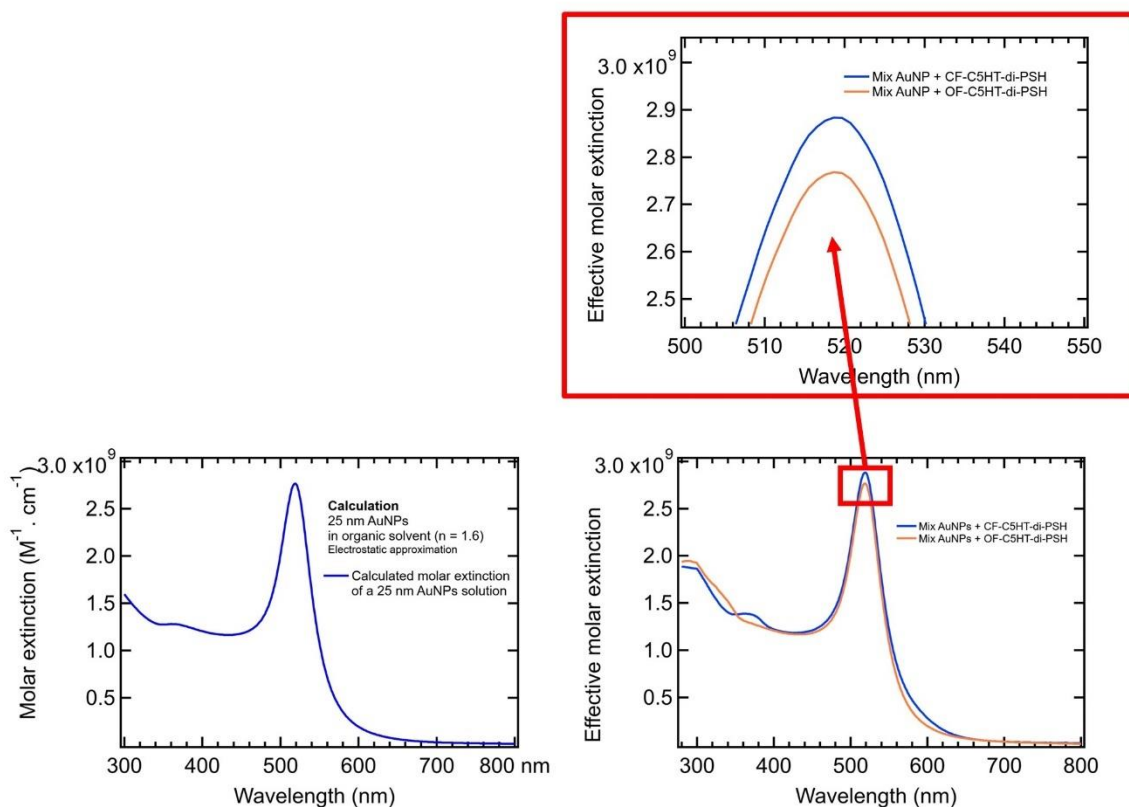


Figure 5.39: Calculation of the molar absorptivity for 25 nm AuNPs within the electrostatic approximation. The molar absorptivity is proportional to this curve, and we obtain $\epsilon_{AuNP} = 2.7 \times 10^9 \text{ M}^{-1} \cdot \text{cm}^{-1}$ at 520 nm (left). Calculated effective molar absorptivity ϵ_{mix} of a mixture of AuNP and DAE in the case there is no interaction between the two species (right).

This calculation was made considering a mix of AuNPs and DAEs with proportions corresponding to a monolayer of DAEs on 25 nm AuNPs. It does not take into account the local refractive index modulation induced by the DAEs nor the plasmonic nanoantenna effect or quenching resulting from the AuNPs. Only the spectra modulations of the first order are calculated. This calculation shows that the switching is not supposed to induce a shift of the LSPR and that the expected modulation of the absorbance at λ_{LSPR} upon switching of a full monolayer of DAEs is of 4%, which is readily detectable. Since the experimentally measured one is of 2%, the calculation confirms that this absorbance modulation is indeed coming from the switching of the diarylethenes molecules. This lower value comes from the fact that in our case the AuNPs deposited on ITO substrates and steric hindrance between the DAE molecules is present.

3 - Quenching due to the connection to the AuNPs versus LSPR enhancement provided by the nanoantenna effect of the AuNPs

The value of SR calculated for molecules in solution corresponded to the following irradiation time values: $\Delta t_{UV} = 50$ min and $\Delta t_{vis} = 14$ min, these values are very close to the ones from the experiment presented in 5.III.1 of this chapter for molecules on AuNPs $\Delta t_{UV} = 60$ min and $\Delta t_{vis} = 15$ min, indicating a similar switching rate (or at least a switching rate of the same order of magnitude) of the molecules whether they are in solution or grafted on the AuNPs. This result is in agreement with that of Arramel et al.⁶⁴ who measured the switching rate of comparable DAE molecules grafted on a flat gold surface and then compared it to that of the molecules in solution. They reported a switching time of respectively 1 to 3 s for the molecules in solution and 90 s for the molecules grafted on the gold surface (SAMs on flamed Au(111)).

The larger values of SRs obtained for the cycle measurements performed on ADITTOVI, ADITTOI and ADITTOC resulting from larger values of irradiation times Δt_{UV} and Δt_{vis} to make the molecules switch indicate a slower rate of the molecules once they are grafted on the AuNPs. This result is in agreement with many studies reporting slower switching rates for DAEs grafted on gold whether it was flat gold, supported gold nanoparticles or gold nanoparticles in solution (see Chapter 1.III.5).

According to both the studies of Tsuboi et al.¹⁰² and Nishi et al.¹⁰¹ (see Chapter 1.III.5) we would have three areas around the AuNPs, represented in Figure 5.40:

_ the quenching area: $0 \text{ nm} < d_{\text{quenching}} < 5 \text{ nm}$, with $d_{\text{quenching}}$ the distance at which the quenching of the ring-opening/ring-closing reactions is dominant.

_ the enhancement area: $5 \text{ nm} < d_{\text{LSPR enhancement}} < 12 \text{ nm}$, with d_{LSPR} the distance at which the plasmonic enhancement of the ring-opening/ring-closing reactions QY is dominant.

_ the non-enhancement area: $12 \text{ nm} < d_{\text{non-enhancement}} < \infty$, with $d_{\text{non-enhancement}}$ the distance at which the molecules are too far for plasmonic enhancement to occur.

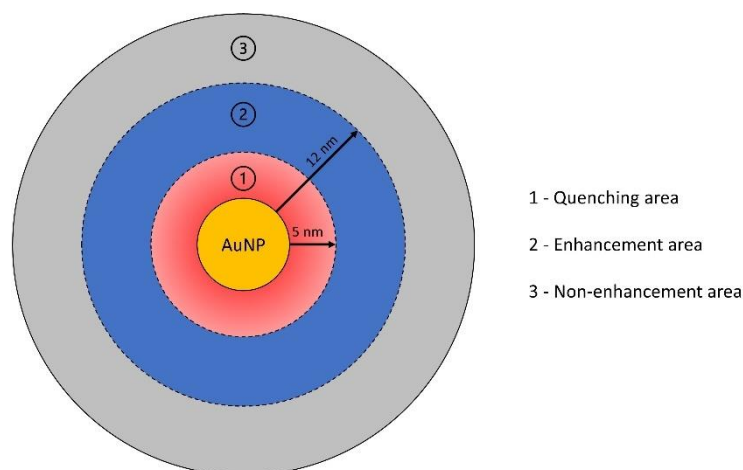


Figure 5.40: Scheme of the phenomena occurring in the areas around a spherical gold nanoparticle.

In our case, considering that our molecules are directly connected to the gold nanoparticles via their thiol anchor group and that their length is very short (1.91 nm for C5HT-di-PSH and 1.39 nm for Cl-C5HT-PSH, both in their open form), they are experiencing strong quenching, explaining why no acceleration of any of the photochromic reactions was observed. Even if some LSPR enhancement is present, it is completely dominated by quenching.

Conclusion

In conclusion, the monitoring of the adsorption of both diarylethene molecules on 28 nm AuNPs was presented. The monitoring was conducted either stepwise (when using grafting protocol 1) or in situ (when using grafting protocol 2). The value of the LSPR peak wavelength shift induced by the adsorption of the DAEs was calculated (2.53 nm) and compared to the experimentally obtained values (1.79 - 5.15 nm). For grafting protocol 2, the effect of several experimental parameters (degassing of the solvent and deprotection of the molecules) on the adsorption was described.

The switching measurements conducted on samples obtained with both grafting protocols were described. For the samples obtained with grafting protocol 1, the effect of several experimental parameters (AuNPs size, deprotection method and desilylation step) on the switching was commented. It resulted that the samples prepared with both grafting protocols displayed reversible switching, some of them fully, some other not. The switching, which was thus preserved upon grafting of the molecules on the AuNPs, corresponded to a variation of the

absorbance at λ_{LSPR} of 0.2 to 0.7×10^{-3} units. Some samples clearly underwent fatigue as soon as the second cycle.

The cycle switching measurements performed on the samples prepared with C5HT-di-PSH were used to calculate values of the switching ratio of the DAEs when grafted on AuNPs. Another switching ratio value was calculated with the data from more specific measurements. The values of switching ratio calculated for DAEs grafted on AuNPs were compared to the value calculated for DAEs in solution. The tuning of molecules i.e., the absorption band in the visible of the DAE molecules corresponding to a transition involved in the photochromic reactions (switching) located in the same spectral area than the LSPR peak of the gold nanoparticles, did not suffice to guarantee a LSPR enhancement effect. Indeed, the molecules, whose π -system is directly connected to the AuNPs undergo quenching, slowing down the photocyclization and photocycloreversion reactions, especially the latter. To further understand what is occurring at the molecular level, the energy levels corresponding to the molecular orbitals of C5HT-di-SH should be either measured (by STM or XPS) or theoretically calculated.

Nevertheless, when aiming at the fabrication of a molecular electronic device, regardless of the risk of quenching, the sulfur atom from the anchor group should be directly linked to the π system of the molecule to ensure sufficient conduction. Putting the thiol anchor group in meta instead of putting it in para could help reduce the coupling. However, to study the plasmonic enhancement, which does not involve conductance measurements, it appears better to not directly connect the DAE molecules to the noble metal NPs and to make sure they are located at the right distance from the NPs: not too close to avoid quenching and not far to still interact with the LSPR.

Chapter 6: Working at the single nanoparticle scale: coupled measurements of the optical response of neighbor and DAE-functionalized gold nanoparticles

In this last chapter, unlike for all the previous ones showing results corresponding to the average response of a very large number of AuNPs, we will be considering the response of single gold nanoparticles. Subsequently to their dark field microscopy and AFM characterization, the scattering spectrum of several single 51 nm gold nanoparticles deposited on ITO was recorded. Using techniques with a nanoscale resolution provides many advantages such as access to the uniqueness of the nanoparticle, elimination of bulk effects (inhomogeneous broadening, orientation averaging, and array effects)¹¹². The plasmonic interaction of some of these single 51 nm AuNPs with 28 nm AuNPs was studied. In particular, the modifications induced by these satellite AuNPs on the UV-visible spectra of the 51 AuNPs with which they form plasmonic dimers was studied. Then, the adsorption of diarylethene molecule C5HT-di-PSH was monitored on single 51 nm AuNPs. Finally, we tried to measure the switching of the DAE molecules on the 51 nm AuNPs on single nanoparticles.

I - Plasmonic spectra of single 51 nm gold nanoparticles

In this first part of Chapter 6, we will be working with an ITO substrate on which 51 nm AuNPs were deposited according to the AuNPs deposition protocol 3 described in Chapter 2.I.2.d.

1 - The zone of interest: dark field microscopy

A zone of interest (zone A of sample ADITO80) was isolated and a set of 22 single AuNPs was selected. The zone and the AuNPs selection are shown in Figure 6.1. The criterion for the selection of the AuNPs was that they were isolated, or at least that they seemed to be. The main objective after making the selection was to prove that the AuNPs were indeed “single AuNPs”, in doing so, for similar samples, we would be able to tell just by looking at the microscopy image which nanoparticle is isolated, and which is not.

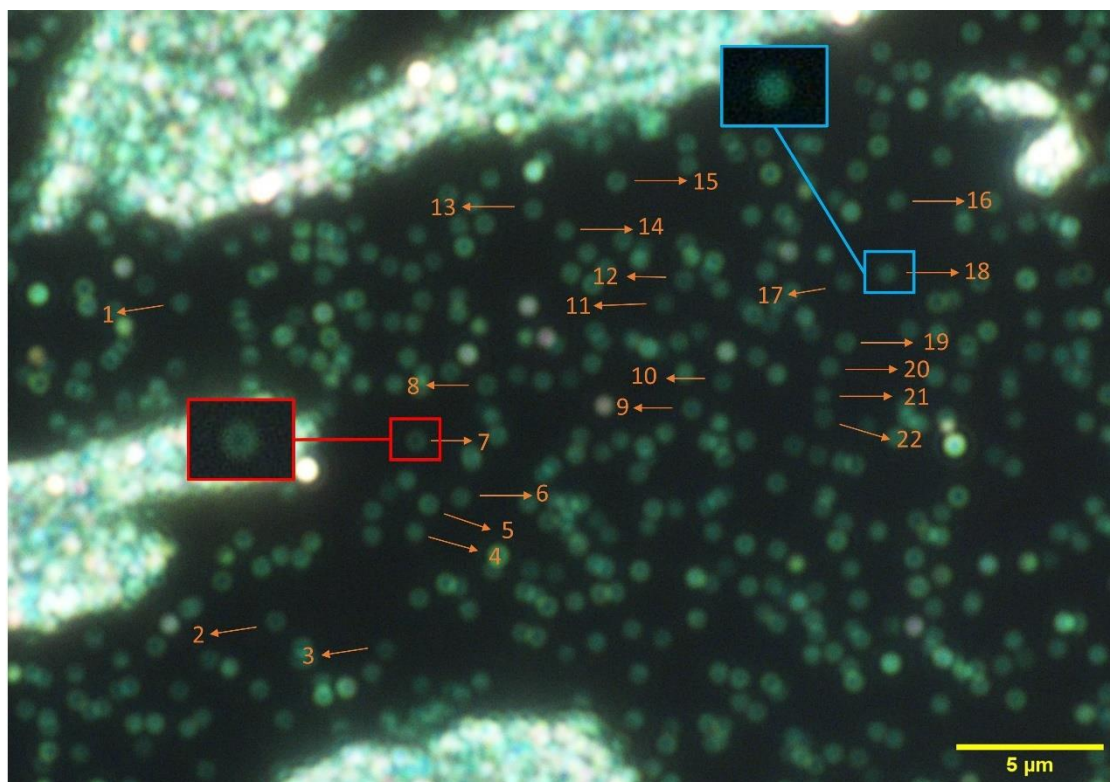


Figure 6.1: Dark field microscopy image of the zone of interest (zone A of ADITO80). The 22 AuNPs indicated in orange are part of a selection of single 51 nm AuNPs. Magnification 100x, exposure time 700 ms, gain 6.2. Red inset: doughnut shaped AuNP. Blue inset: bright dot AuNP.

Some of the AuNPs on the ITO substrate appear as green dots while some other appear as green circles, this aspect is due to the substrate^{75,194,195}. Chen et al.¹⁹⁴ investigated the effect of the dielectric properties of the substrate on the far field scattering pattern (spatial distribution of the scattered light) of 42 by 89 nm gold nanorods (AuNRs). To do so, they studied the electromagnetic interactions between the AuNRs and different substrates (metals, semiconductors, and insulators) possessing various dielectric constants. The differences observed regarding the pattern shape and the color for different substrates was assigned to the different image dipoles induced by the substrate. They demonstrated, both experimentally and with FDTD calculations that when the modulus of the dielectric constant of the substrate is superior to 7, the far field scattering pattern of the AuNRs has a doughnut shape. Conversely, when the modulus of the dielectric constant of the substrate is inferior to 7, the far field scattering pattern of the AuNRs has a solid bright spot/dot shape.

The presence of the substrate breaks the symmetry of the AuNR dielectric environment influencing the plasmonic properties of the supported AuNRs^{75,194}. Under external optical excitation, the substrate is polarized, and a non-uniform electric field is generated across the

metallic NP. This nonuniform electric field can excite the NP multipolar plasmon modes making their intrinsic electron oscillations interact with the substrate-induced electric field: image dipoles are induced in the substrate. Those image dipoles interact with the original plasmonic dipoles in the nanorods. These interactions among the different plasmon modes of the AuNRs, mediated by the substrate, triggers their hybridization, and strongly influence the far-field scattering patterns of the AuNRs. The total far-field intensity of the light scattered from the nanorod is a sum of the contributions from the in plane and normal dipoles. The observed scattering pattern depends on the relative magnitude of the net in-plane and normal dipoles. Since the magnitude of the induced image dipole depends on the dielectric properties of the substrate, the dielectric function of the substrate influences the far field scattering pattern of the supported Au nanorods. As demonstrated with a simple electrostatic model the ratio of the electric field intensity between the in-plane and normal dipole radiation is proportional to the dielectric constant of the substrate (proportional to $\frac{1}{4|\epsilon_{substrate}|^2}$ actually). The ratio is directly related to the experimentally observed scattering patterns of the AuNRs because the far-field scattering intensity is proportional to $|E|^2$ since the magnitudes of the in-plane and normal dipoles are fixed for a given Au nanorod under a fixed excitation condition¹⁹⁴.

In their case, the distance between the AuNR and the surface of the substrate was estimated to be 1.5 nm, which is roughly the same in our case. For the AuNRs on the ITO substrate, they observed red “solid bright spots”. For spherical AuNPs on an ITO substrate, we observe green dots (or as they call them “solid bright spots”) or partial rings (or as they call them “doughnut shapes”). Partial rings because unlike for substrates with higher dielectric constant modulus for which the center of the ring is clearly visible and appears the same color as the substrate and the ring is very thin, we have thick rings for which the center is not really visible and exhibit different color than the substrate. The shape is, as they explained, consistent with the value of the dielectric constant modulus of ITO, $|\epsilon_{ITO}| = 3.338 < 7$. The color is explained by the geometry of the NP, in our case a sphere, which possess an isotropic individual dipolar plasmon mode whose resonance is located at 539 nm on its scattering spectrum.

2 - Confirmation of the isolation: AFM characterization

The zone A of ADITO80 was characterized by AFM (the principle of this technique is reminded in Chapter 2.II.4) and a topographic image (see Figure 6.2) was recorded to show that the selected AuNPs were indeed isolated. When zooming on the AuNPs, one can notice that

they are not all exactly identical, the most obvious difference regards their shape as can be seen on the images of Figure 6.3. Their size also slightly varies as can be seen in Table 6.1 by looking at the values of their height and LSPR peak wavelength.

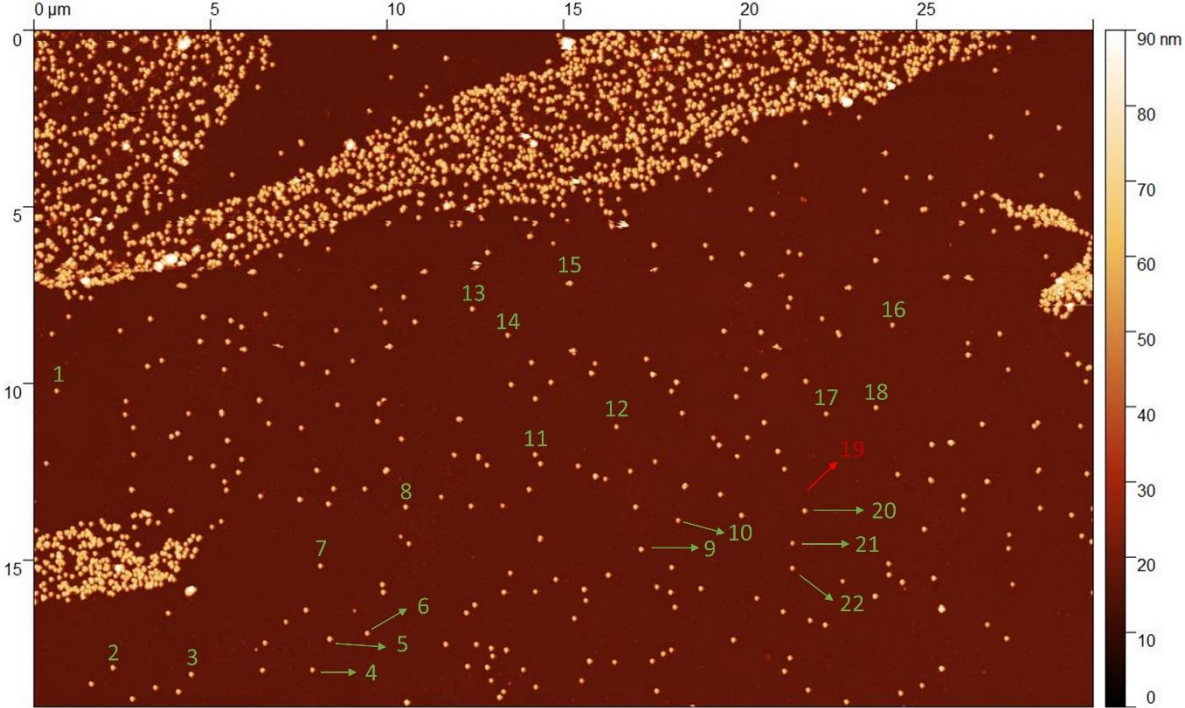


Figure 6.2: AFM image of the zone of interest. The 22 AuNPs indicated in green are those from the selection of single 51 nm AuNPs. The AuNP 19 that went missing is indicated in red.

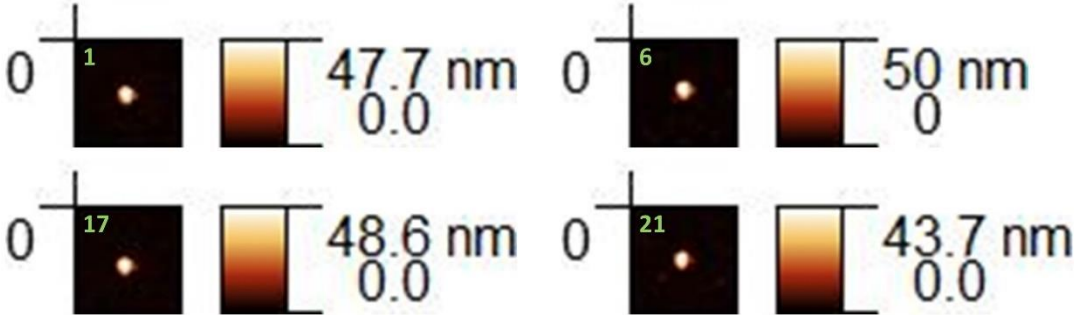


Figure 6.3: Zoomed images of AuNPs 1, 6, 17, and 21.

As can be seen on Figure 6.2, all the AuNPs from the selection are single gold nanoparticles (no dimers, trimers, or aggregates). It confirms our ability to directly identify single AuNPs using dark field microscopy. It can be noted that AuNP 19 is missing, it may have stayed stuck on the AFM tip.

3 - Dark field microscopy coupled to UV-visible spectroscopy: UV-visible spectrum of a single 51 nm AuNP

The scattering spectrum of each of the 22 AuNPs was recorded using the setup made of the UV-visible spectrophotometer coupled to the optical microscope described in Chapter 2.II.4, and then fitted by a Lorentzian between 500.14 and 580.74 nm. Working with individual AuNPs deposited on a substrate requires to make statistical comparisons of many measurements¹⁰³. All the spectra are presented in Figure 6.4, the average value of their λ_{LSPR} is 539.31 nm with a standard deviation of 4 nm. The small differences amongst the values of λ_{LSPR} are attributed to small size variations amongst the AuNPs⁶⁹. The example of AuNP 1 is also shown ($\lambda_{\text{LSPR, AuNP1}} = 536.09$ nm). This average value is in agreement with the value of 540 nm both calculated (FDTD simulations with a refractive index $n = 1.45$) and measured by Yoon et al.¹⁰⁴ for single non-ideal realistic (icosahedron) 51 nm AuNPs. For ideal (perfectly spherical) AuNPs they calculated and measured the position of the LSPR peak to be at 553 nm.

Table 6.1: LSPR peak wavelength and height (measured on the AFM images) of each AuNP of the selection.

#AuNP (51 nm)	λ_{LSPR} (nm)	Height (measured with the AFM) (nm)
1	536.09	42.3
2	538.54	53.1
3	540.97	54.3
4	540.04	49.8
5	542.74	58.3
6	546.95	49.1
7	543.21	50.8
8	536.54	49.8
9	537.46	55.0
10	538.78	47.5
11	531.42	51.3
12	539.69	46.9
13	541.65	51.8
14	539.51	43.1
15	541.93	52.4
16	537.02	45.5
17	545.92	47.3
18	537.15	45.6
19	541.79	/
20	541.69	48.2
21	531.72	42.2
22	534.03	46.9

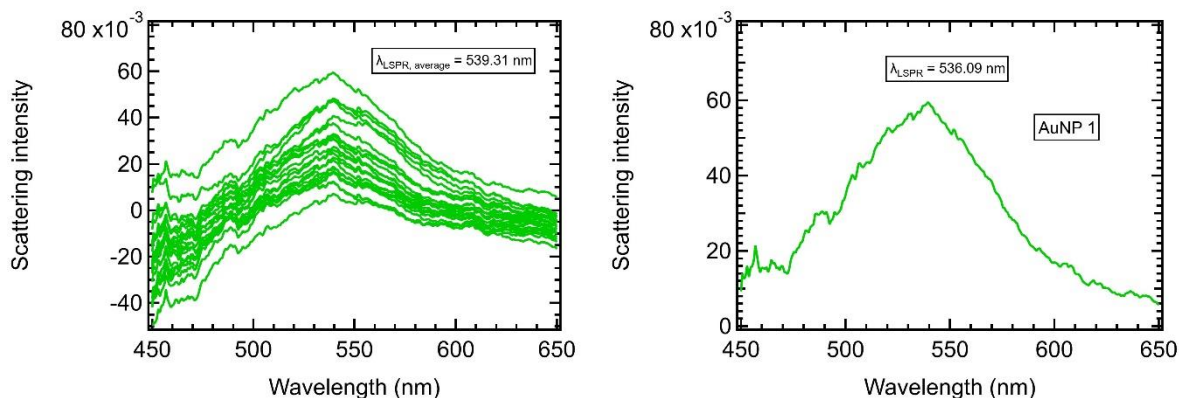


Figure 6.4: Scattering spectra of each of the 22 AuNPs from the selection of single 51 nm AuNPs (on the left). Example of a single 51 nm AuNP (AuNP 1) spectrum (on the right).

It can also be interesting to quickly compare the spectrum of a single 51 nm AuNP on ITO with the spectrum of the AuNP solution batch this AuNP came from, it was made with AuNP 1 and the YPOP57E batch in Figure 6.5.

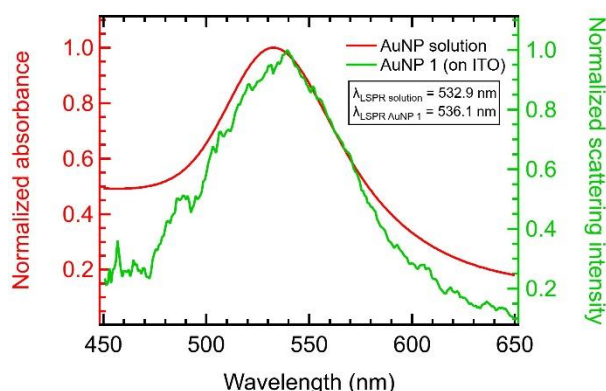


Figure 6.5: UV-visible spectrum of AuNP 1 and the AuNP batch it came from YPOP57E (AuNPs in aqueous solution).

The broadness of the peaks is comparable, but their position is slightly different because the LSPR does not peak at the same wavelength in extinction (AuNPs in solutions) and in scattering (AuNP deposited on ITO, measured by dark field microscopy coupled to UV-visible spectroscopy) and because the AuNPs are in media with different refractive indices⁶⁹. The peak of the AuNPs in aqueous solution ($n = 1.33$) is blueshifted compared to that of AuNP 1 deposited on ITO and measured in air ($n = 1$).

We are able to measure the scattering spectra of individual AuNPs, these spectra show (through the position of the LSPR peak) that the AuNPs are not all perfectly identical. As can

be seen in Table 6.1, their LSPR peak wavelengths range from 531.41 to 546.95 nm. Indeed, they are not perfectly spherical (some of them are elongated), they possess facets, a different amount of surfactant (citrate) may have remained on their surface, they may not all be attached to the surface the same way via the APTES molecules. It justifies the use of dark field microscopy coupled to UV-visible spectroscopy to take into account their individuality.

II - Elaboration of asymmetric dimers of gold nanoparticles

After the selection of 22 AuNPs from the zone A of sample ADITO80 was fully characterized and the AuNPs scattering spectra were recorded, we decided to introduce “satellite nanoparticles” of 28 nm on this sample. These 28 nm AuNPs were drop casted on ADITO80 (for 15 minutes). The objective is to study the influence of these 28 nm satellite nanoparticles on the scattering spectra of the original 51 nm nanoparticles.

This size of the satellite AuNPs was chosen for several reasons, first, this size is below the limit of detection of the optical microscope, it is therefore easier to identify the zone after the deposition of the second layer of AuNPs since the only AuNPs we can see are the 51 nm ones. This size difference also facilitated the AFM characterization since the zone containing the 51 nm AuNPs could still be readily identified, and no confusion could be made between the much smaller 28 nm AuNPs and the original 51 nm AuNPs.

1 - Assessment of the satellite nanoparticles presence and plasmonic dimers formation

After the deposition of the 28 nm satellite AuNPs, we went back to zone A of ADITO80 and took a dark field microscopy image which is shown in Figure 6.6.

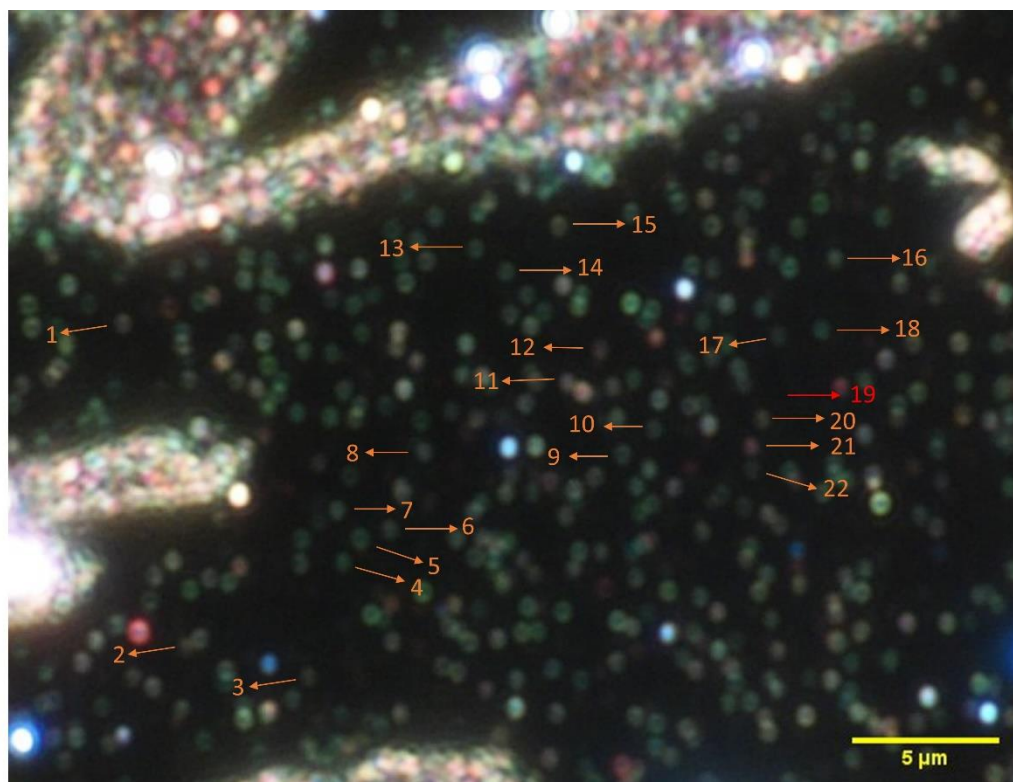


Figure 6.6: Dark field microscopy image of the zone of interest after the drop casting of 28 nm satellite AuNPs took place. The 22 AuNPs indicated in orange are those from the selection of single 51 nm AuNPs which might now possess a neighbor 28 nm AuNP. The AuNP 19 that went missing is indicated in red. Magnification 100x, exposure time 700 ms, gain 6.2.

The first immediately noticeable difference compared to the previously taken image of the zone (before the deposition of the 28 nm satellite AuNPs) regards the color of many AuNPs present on the image (included in the 22 AuNPs selection or not). Many AuNPs no longer appear green, they turned orange or red. This change is particularly visible for AuNP 21 that clearly turned red. These changes of color were obviously expected to reflect the modifications of the scattering spectra of the AuNPs that experienced them. Nevertheless, some AuNPs remained green, their spectra were expected to be the same as those measured the first time.

This change of color is in general a useful tool for detection applications, for example Liu et al.¹⁹⁶ developed a mercury ions (Hg^{2+}) colorimetric detection method with picomolar sensitivity based on single AuNPs analysis by dark field microscopy. On the one hand, citrated 70 nm AuNPs are immobilized on a glass slides, then modified with DNA oligonucleotides. On the other hand, a solution of 70 nm AuNPs modified with complementary DNA oligonucleotides is prepared. The principle of their method is schematized in Figure 6.7. To test a sample of industrial wastewater for example, the slide is immersed in the water sample and

some AuNPs solution is added to it. In the presence of mercury ions, a hybridization of the DNA oligonucleotides occurs leading to the formation of AuNPs aggregates. This formation is immediately visible on the dark-field microscopy images since single unmodified AuNPs appear green (no mercury contamination) while AuNPs aggregates in which mercury ions were trapped appear yellow.

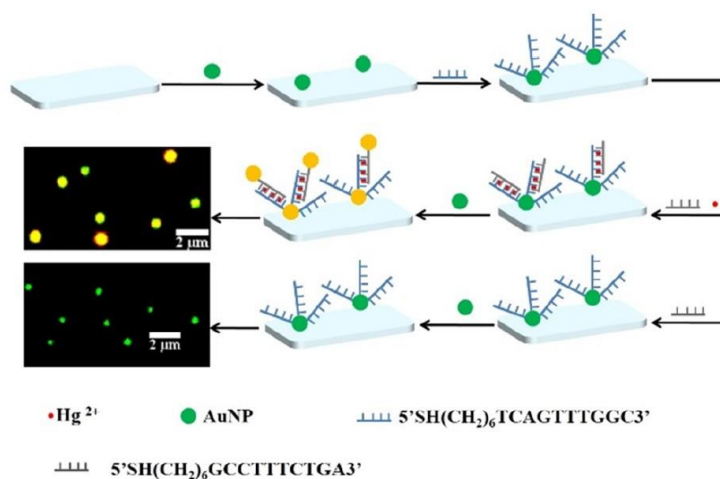


Figure 6.7: Scheme and dark field microscopy images of the Hg^{2+} sensor. Reprinted from¹⁹⁶.

Before recording the UV-visible spectra of all the AuNPs from the 22 AuNPs selection a second time, AFM topographic images were recorded. Two of these images are shown in Figure 6.8. and Figure 6.10, the rest of the images can be found in the Appendix in Figure A.6.1. They were expected to give us clear information about which 51 nm AuNP received a 28 nm satellite AuNP (or several) and is now part of a “neighbor AuNPs” system, and which 51 nm AuNP remained alone. It is particularly visible on the zoomed images given in Figure 6.9 and Figure 6.11.

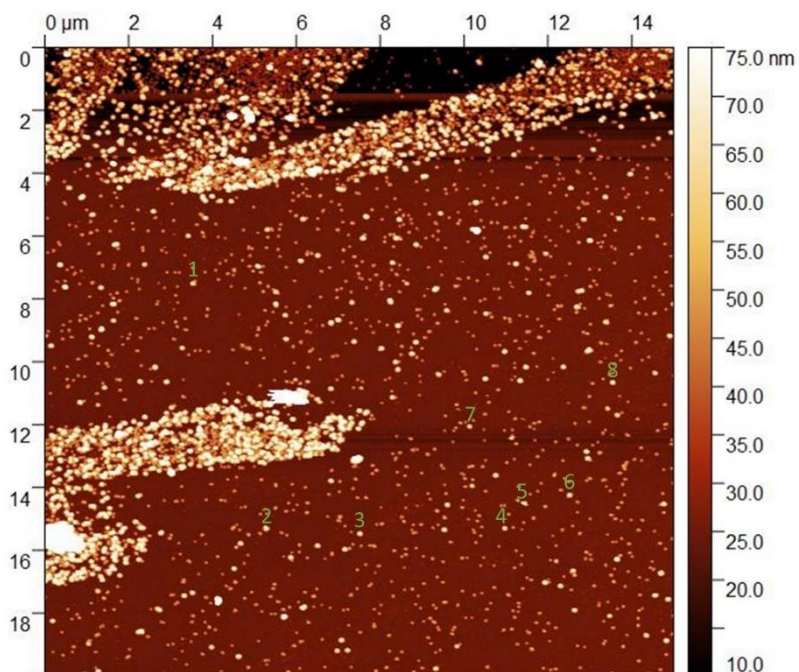


Figure 6.8: AFM image of AuNPs 1 to 8 (indicated in green) after the drop casting of 28 nm satellite AuNPs took place.

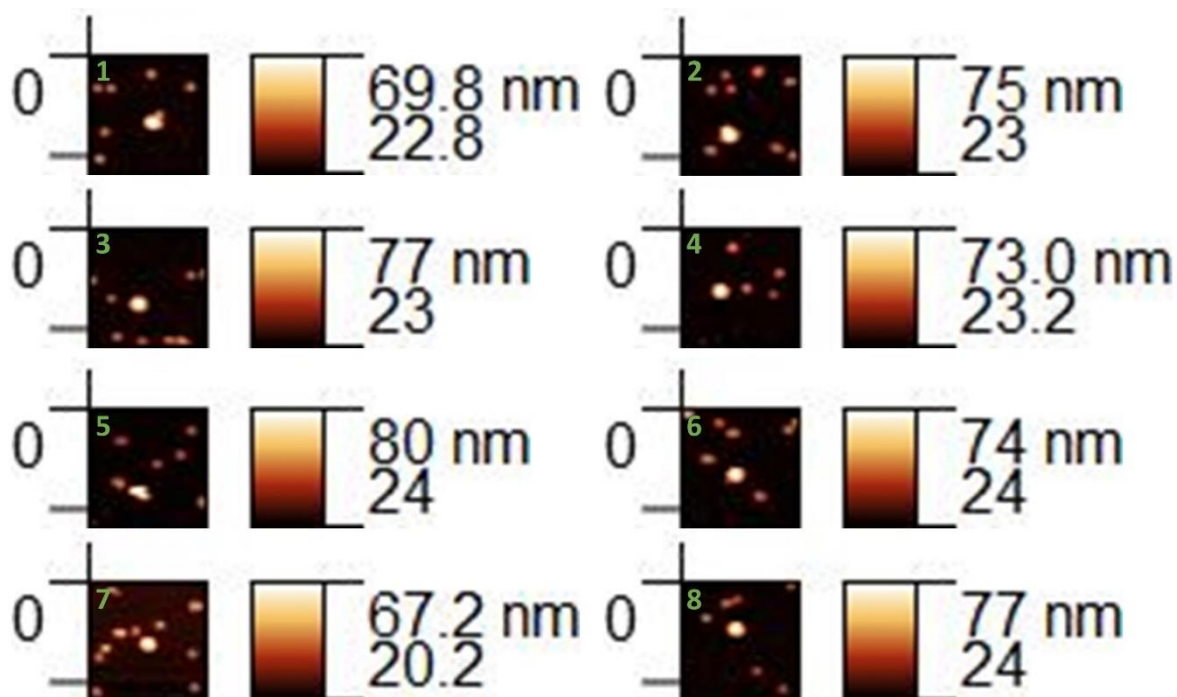


Figure 6.9: Zoomed images of AuNPs 1 to 8.

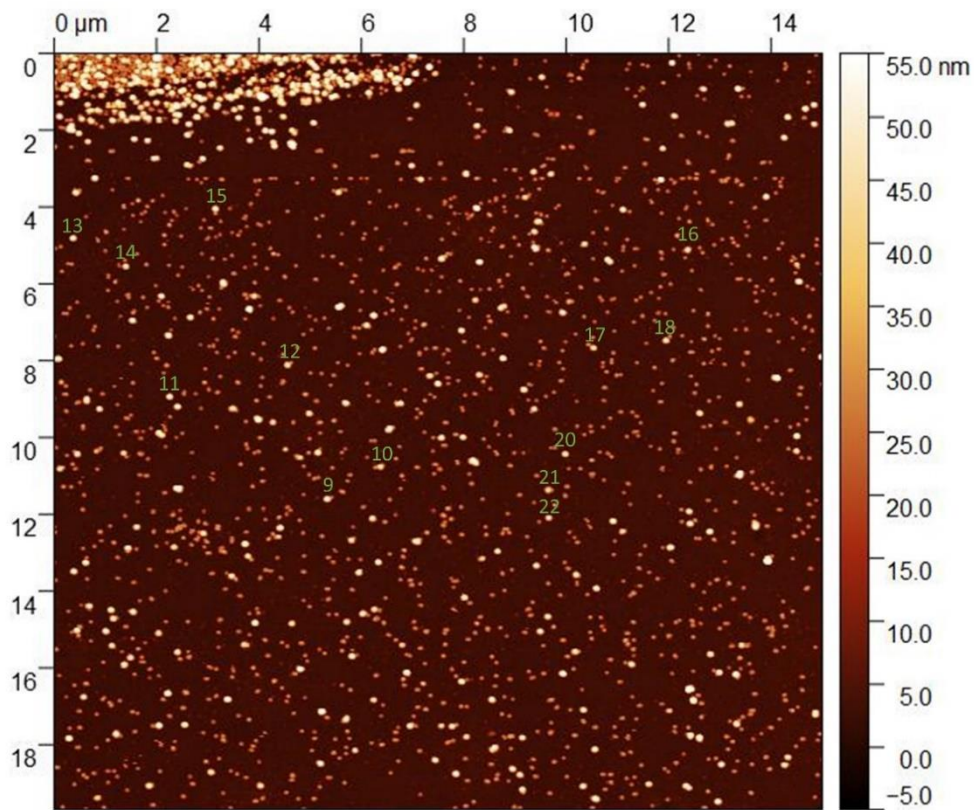
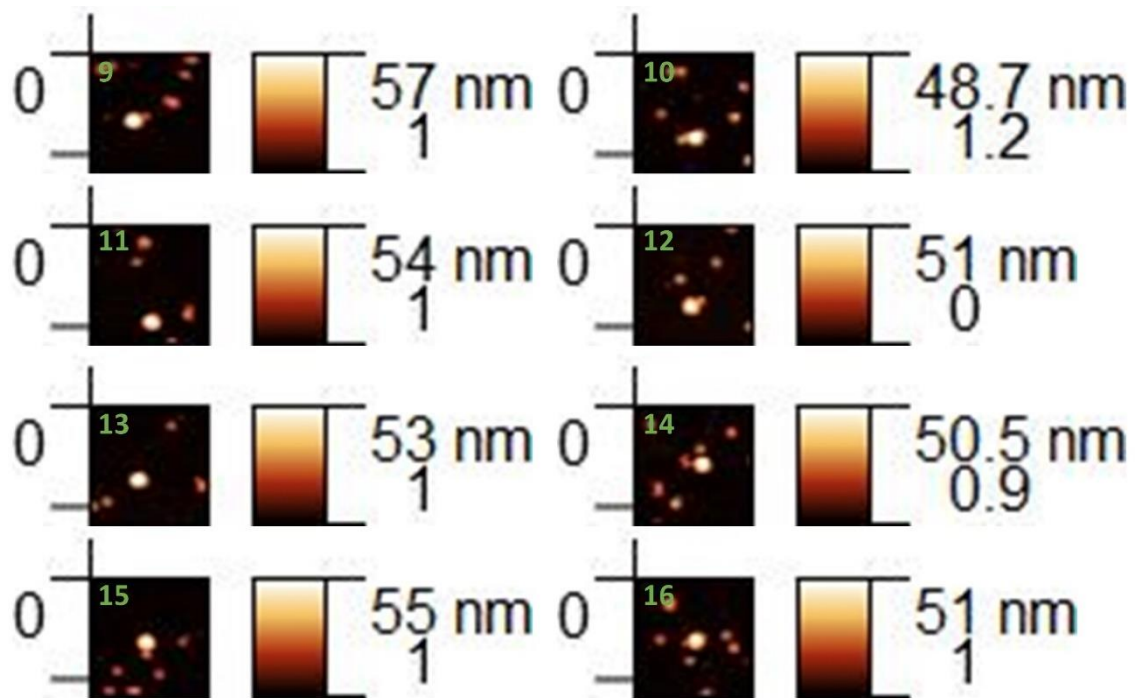


Figure 6.10: AFM image of AuNPs 9 to 22 (indicated in green) after the drop casting of 28 nm satellite AuNPs took place.



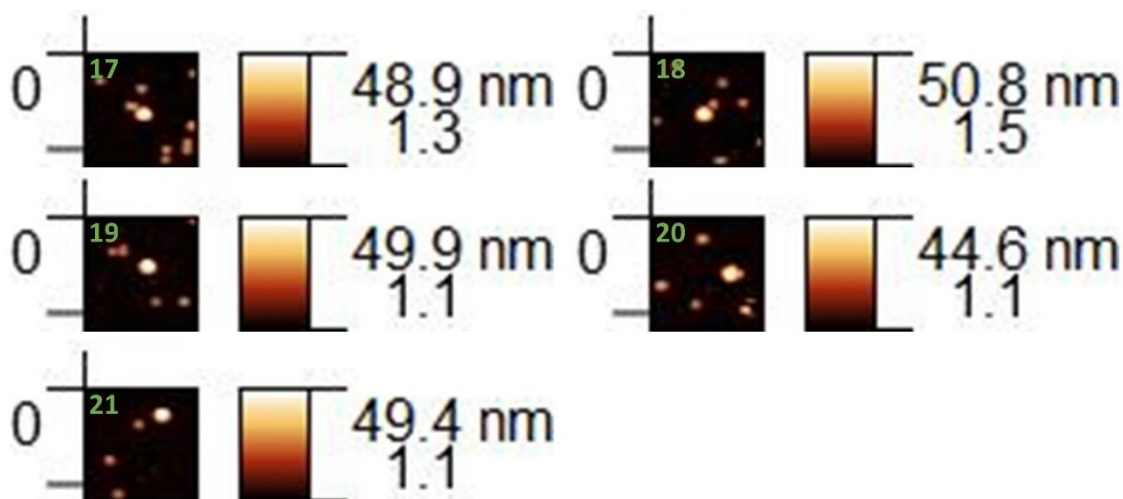


Figure 6.11: Zoomed images of AuNPs 9 to 21.

Based on the observations made on the AFM images, we can say that AuNPs 1, 9, 10, 12, 14, 15, 17, 18, 21 seem to have a satellite AuNP in contact with them or at least so close from them that it looks like they are in contact on the AFM image. Conversely, AuNPs 2, 3, 4, 5, 6, 7, 8, 11, 13, 19 and 20 are surrounded by satellite AuNPs that are clearly not in contact with them. The next step was to record the UV-visible spectra of each 51 nm AuNP from the selection and see which of them has had its spectrum modified by the presence of a satellite AuNP.

At this point, it is possible to assume that some asymmetric plasmonic dimers (see Chapter 1.IV), schematized in Figure 6.12 were assembled. The gap distance d_{gap} and the angle α between the dimer axis and the surface are indicated, we will see further in this chapter that they are important parameters due to their influence on the spectral features of the dimers. Regarding the angle α , note that for a gap distance d_{gap} of 1 nm, the value of the angle is 12° . However, the actual situation can be different than that represented in Figure 6.12, with the smaller nanoparticle on top of the bigger one, meaning that the angle α would be comprised between 12 and 90° . No chemical dimers (see Figure 1.25) were fabricated, this type of dimers will not be treated in this PhD manuscript.

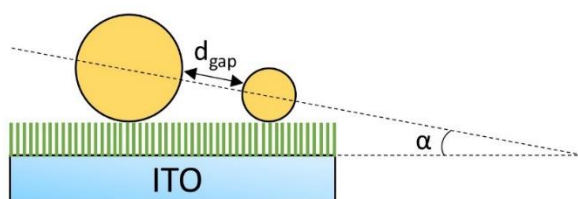


Figure 6.12: Asymmetric plasmonic dimer made of a 51 nm AuNP and a 28 nm AuNP separated by a gap distance d_{gap} . The dimer axis forms an angle α with the surface. The green sticks are silanes (APTES).

A dimer of metallic NPs is the simplest system to study plasmonic coupling, here we created asymmetric plasmonic dimers with the simplest, non-controlled, deposition method. It will be interesting to see if the plasmonic dimers self-assemble in a random manner or if some trends are observed.

2 - Dark field microscopy coupled to UV-visible spectroscopy measurements: effect of the 28 nm satellite nanoparticles on the initial 51 nm nanoparticles

The scattering spectrum of each 51 nm AuNP from the selection was recorded and then fitted by a Lorentzian between 500.14 and 580.74 nm for the spectra presenting a single LSPR peak and also between 599.82 and 687.01 nm for the spectra exhibiting two LSPR peaks.

a - Single 51 nm AuNPs

Let us start with the AuNPs from the selection whose spectrum (measured by dark field microscopy coupled to UV-visible spectroscopy) was poorly modified after the deposition of the second layer of AuNPs, it was the case for AuNPs 2, 4, 5, 7, 8, 10, 11, 13 and 14. These spectra only display one LSPR peak corresponding to an individual dipolar oscillation mode. The example of AuNP 8 scattering spectrum before (Measurement 1) and after (Measurement 2) the drop casting of 28 nm satellite AuNPs took place, is given in Figure 6.13. The scattering spectra of the other AuNPs are shown in the Appendix in Figure A.6.2.

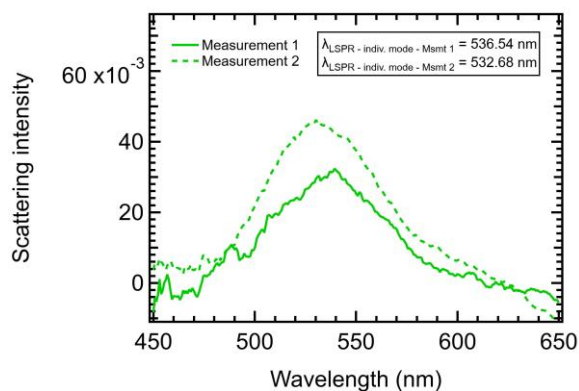


Figure 6.13: Scattering spectrum of AuNP 8 before (Measurement 1) and after (Measurement 2) the drop casting of 28 nm satellite AuNPs took place.

The values of the LSPR peak wavelength for both measurements and the values of the difference between them are given in Table 6.2. Although the shape of the LSPR peak was not modified in between the two measurements, globally we notice that the LSPR peaks of the second measurements are more intense than those of the first measurements. This intensity difference could contribute to explain the difference that is also observed regarding the position of the LSPR peak. The LSPR peaks of the second measurements are all blueshifted compared to the peaks of the first measurement. Since the former are more intense than the latter, the fit was probably more accurate for them, influencing the obtained value of LSPR peak wavelength. This effect combined to the uncertainty on the measurement of the spectrum (see Chapter 2.II.4) could explain the observed differences between the two measurements.

Table 6.2: Values of the LSPR peak wavelength of the AuNPs from the selection that do not possess a 28 nm AuNP neighbor before ($\lambda_{\text{LSPR single - individual mode Msmt 1}}$) and after ($\lambda_{\text{LSPR single - individual mode Msmt 2}}$) the drop casting of the 28 nm satellite AuNPs took place; difference between the LSPR peak wavelength values of the peak corresponding to the individual oscillation mode ($\Delta\lambda_{\text{LSPR single - individual mode}}$).

#AuNP (51 nm)	$\lambda_{\text{LSPR single - individual mode Msmt 1}}$ (nm)	$\lambda_{\text{LSPR single - individual mode Msmt 2}}$ (nm)	$\Delta\lambda_{\text{LSPR single - individual mode}}$ (nm)
2	538.54	518.08	-20.46
4	540.04	534.61	-5.43
5	542.74	527.76	-14.98
7	543.21	531.67	-11.54
8	536.54	532.68	-3.86
10	538.78	531.57	-7.21
11	531.42	525.52	-5.9
12	539.69	none	none
13	541.65	532.21	-9.44
14	539.51	529.74	-9.77
19	541.79	none	none

b - Neighbor AuNPs/asymmetric plasmonic dimers

The AuNPs whose spectra were modified are AuNPs 1, 3, 6, 9, 15, 16, 17, 18, 20, 21 and 22. The scattering spectra of AuNP 1 and AuNP 21 are shown in Figure 6.14, the spectra of the other AuNPs are shown in the Appendix in Figure A.6.3. They present two LSPR peaks arising from the lift of degeneracy of the dipolar oscillation mode, intrinsic to each 51 nm, occurring upon the interaction between the plasmonic modes of the neighbor nanoparticles i.e., the original 51 nm AuNP and a satellite 28 nm AuNP which form an asymmetric plasmonic dimer. Following the Nordlander model^{75,109} (see Chapter 1.IV.1), the first peak was attributed to the so-called transversal antibonding dipolar plasmon mode (TADP), it results from the excitation of the plasmonic dimer by light with a polarization perpendicular to the dimer axis. The second peak was attributed to the so-called longitudinal bonding dipolar plasmon mode (LBDP), it results from the excitation of the plasmonic dimer by light with a polarization parallel to the dimer axis. It should be noted that in our case, since the AuNPs have different sizes, the coupling is less efficient than for a dimer with same size entities. Another very important element to note and remember is that we used non-polarized incident light. We therefore measured the average optical response of the plasmonic dimer i.e., the response triggered by light polarized along the dimer axis (parallel polarization) and the response

triggered by light polarized along the normal to the dimer axis (transverse polarization). The positions of the peaks, the difference between the LSPR peak wavelength of the peaks respectively corresponding to the individual dipolar mode of the single AuNP and to the TADP mode of the plasmonic dimer, and the difference between the LSPR peak wavelength of the peaks respectively corresponding to the TADP mode and the LBDP mode of the plasmonic dimer are reported in Table 6.3.

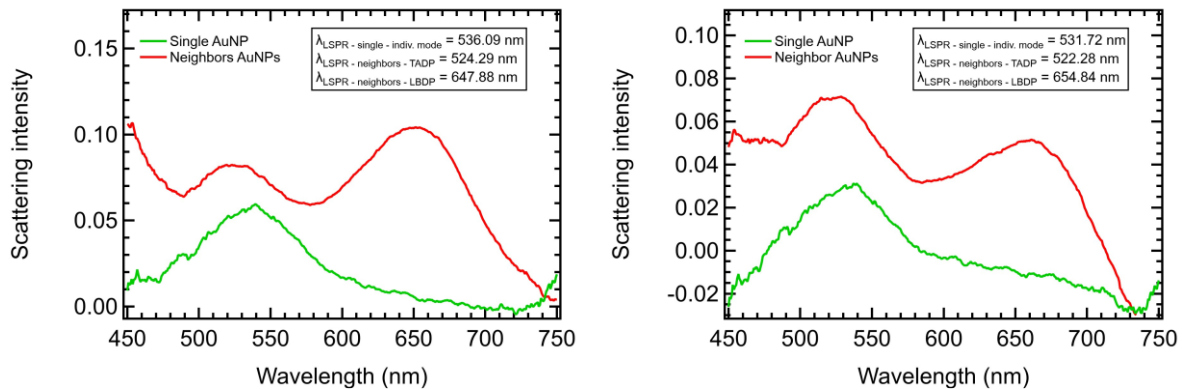


Figure 6.14: UV-visible spectrum of AuNP 1 (on the left) and AuNP 21 (on the right) before (single AuNP) and after (neighbor AuNPs) the drop casting of 28 nm satellite AuNPs took place.

The peak corresponding to the transverse mode of a dimer (no matter the gap distance) is always located at the same wavelength than the LSPR peak of an individual AuNP (of the same size than that composing the dimer)^{106,108}. In our case, we observe a small blueshift of this peak which could be attributed to the error on the measurement (see Chapter 2.II.4) but also to the variation of the angle between the axis dimer and the surface. The effect of the variation of this angle is discussed further in the chapter.

Table 6.3: Values of the LSPR peak(s) wavelength(s) of the AuNPs from the selection that possess a 28 nm AuNP neighbor before ($\lambda_{\text{LSPR single - individual mode}}$) and after ($\lambda_{\text{LSPR neighbors - individual mode}}$ and $\lambda_{\text{LSPR neighbors - collective mode}}$) the drop casting of the 28 nm satellite AuNPs took place; difference between the LSPR peak wavelength values of the peak corresponding to the individual ($\Delta\lambda_{\text{LSPR neighbors - individual mode}}$) and of that corresponding to the collective ($\Delta\lambda_{\text{LSPR neighbors - collective mode}}$) oscillation mode.

#AuNP (51 nm)	$\lambda_{\text{LSPR single - individual mode}}$ (nm)	$\lambda_{\text{LSPR neighbors - TADP}}$ (nm)	$\lambda_{\text{LSPR neighbors - LBDP}}$ (nm)	$\Delta\lambda_{\text{LSPR neighbors - individual - TADP}}$ (nm)	$\Delta\lambda_{\text{LSPR neighbors - TADP - LBDP}}$ (nm)
1	536.09	524.29	647.88	-11.8	123.59
3	540.97	531.91	660.87	-9.06	128.96
6	546.95	534.64	625.38	-12.31	90.74
9	537.46	522.35	648.85	-15.11	126.5
15	541.93	535.24	623.75	-6.69	88.51
16	537.02	531.00	661.88	-6.02	130.88
17	545.92	539.26	646.44	-6.66	107.18
18	537.15	527.11	685.59	-10.04	158.48
20	541.69	519.91	606.19	-21.78	86.28
21	531.72	522.28	654.84	-9.44	132.56
22	534.03	537.97	624.93	3.94	86.96

These results are globally in agreement with that of Yim et al.¹⁰⁵ (see Chapter 1.IV.2), as was observed in our case, the peaks corresponding to the dimers were always more intense than the peak of the monomer, and slight spectral differences due to the AuNPs morphology differences were also observed (see Figure 6.15). However, in our case, regarding the intensity of the peaks, the peak corresponding to the LBDP mode was sometimes more intense than the peak corresponding to the TADP mode (see AuNP 1 in Figure 6.14 for example), sometimes it was the opposite (see AuNP 21 in Figure 6.14 for example).

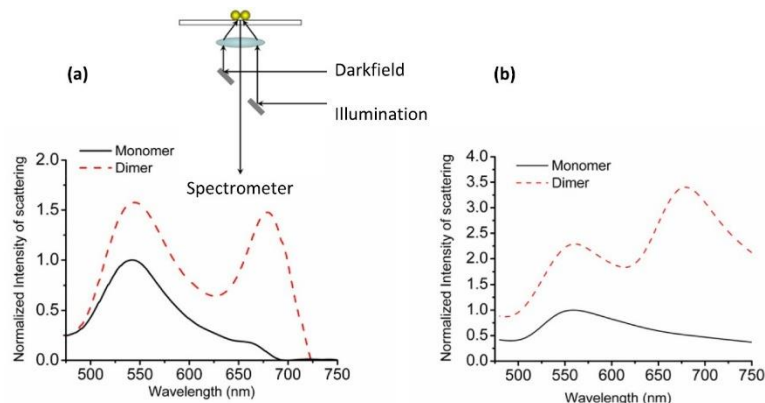


Figure 6.15: (a) Scattering spectra of a single Au nanoparticle monomer and a single dimer on ITO and scheme of the dark field spectroscopy setup used to record the spectra. (b) Simulated scattering spectra of a single Au nanoparticle monomer and a single dimer on ITO. Reprinted from¹⁰⁵.

Our results are also globally in agreement with that of Esashika et al.¹⁰⁶ (see Chapter 1.IV.2). Nevertheless, in their case, the intensity of the LBDP (located around 540 nm) was always inferior to that of the TADP (located around 640 nm) on their experimental spectra, whereas the intensity of the LBDP was always superior to that of the TADP on their calculated spectra. In our case, as previously mentioned and as can be seen in Figure 6.14 and A.6.3, on some of our spectra the LBDP peak is more intense than the TADP peak, on the other it is the opposite.

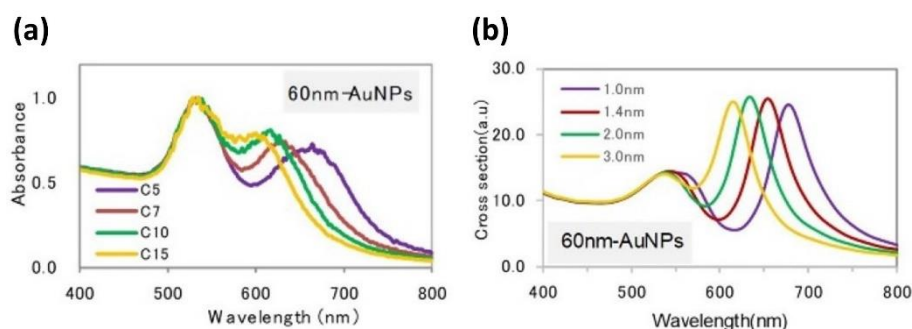


Figure 6.16: (a) Extinction spectra of 60 nm AuNPs dimers modified with C5 (5-carboxy-1-pentanethiol), C7 (7-carboxy-1-heptanethiol), C10 (10-carboxy-1-decanethiol) and C15 (15-carboxy-1-pentadecanethiol). (b) Simulated spectra of 60 nm AuNPs dimers with interparticle gaps of 1.0 nm, 1.4 nm, 2.0 nm and 3.0 nm. Adapted from¹⁰⁶.

c - The neighbor nanoparticles method to form plasmonic dimers

Dark field microscopy coupled to UV-visible spectroscopy measurements allow to detect and analyze the appearance of neighbor nanoparticles (after the deposition of satellite AuNPs) via the emergence of the peak corresponding to the plasmon coupling mode on the scattering spectra and of a new color on the microscopy images.

As previously mentioned, 11 AuNPs (n° 1, 3, 6, 9, 15, 16, 17, 18, 20, 21, and 22) acquired a neighbor versus 9 AuNPs (n° 2, 4, 5, 7, 8, 10, 11, 13, and 14) that remained isolated. The neighbor AuNPs can be divided in two groups according to the position of their LBDP peaks, located either around 655 nm or around 620 nm. On the one hand, it means that a strong tendency to form dimers exist spontaneously since the non-controlled deposition of the satellite 28 nm AuNPs led to the formation of 45% of dimers. On the other hand, it also means that the deposition does not occur in a random manner since recurrent values of the LBDP peak position appear.

III - Assessment of the interparticle distance in the asymmetric dimers

1 - Hybridization of the plasmonic modes: case of an asymmetric dimer

Now let us have a closer look on how the plasmonic modes of our asymmetric plasmonic dimers form. Their hybridization diagram is drawn in Figure 6.17 according to the Nordlander model (see Chapter 1.IV.1). It should be noted that in our case, since the AuNPs are not of the same size, the induced dipole moment (resulting from the anti-aligned dipoles of the constituent AuNPs) of the dark mode must be small but not zero. We would have “grey modes” instead of actual dark modes.

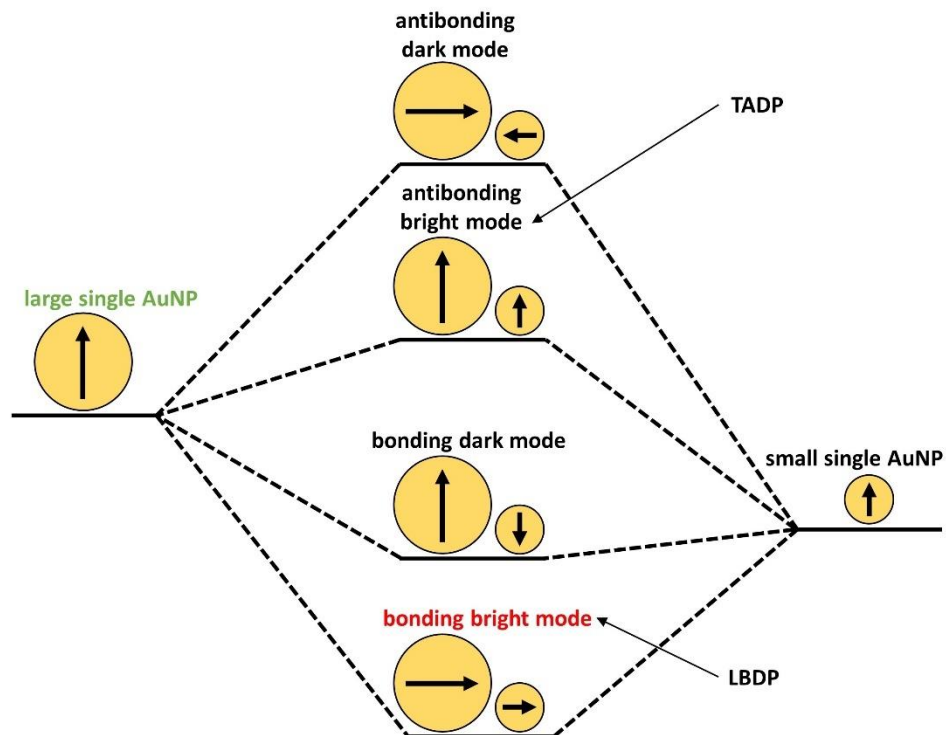


Figure 6.17: Plasmon hybridization diagram for an asymmetric plasmonic dimer of spherical gold nanoparticles. The arrows inside the AuNPs indicate the direction of the induced dipole moment corresponding to the charge separation occurring upon LSPR excitation.

2 - Calculation of the gap distance: application of the “plasmon ruler equation” to our results

Regarding the gap distance in our plasmonic dimers, by looking at the redshift values (see column $\Delta\lambda_{\text{LSPR neighbors - TADP - LBDP}}$ of Table 6.3) we notice that our AuNPs (except AuNPs 17 and 18) can be divided in two groups for which we find almost the same redshift values and thus for which we expect comparable gap distance values. For the first group i.e., AuNPs 6, 15, 20 and 22, with an average value of the redshift of 88.1 nm, it was possible to calculate an estimation of the gap distance value using a plasmon ruler equation⁶⁷ (Chapter 1.IV.4). For the second group, AuNPs 1, 3, 9, 16 and 21, with an average value of the redshift of 128.5 nm, it was not possible to calculate an estimation of the gap distance values: the shift values were too large. Several hypothesis can be made, the gap distance is actually the same as for the other group but the morphology of the gap (gap area and gap curvature) is different (and thus the degree of coupling is different) explaining the different average value of the redshift¹⁰⁴, or the gap distance is shorter than for the other group meaning that the AuNPs are in the nearly touching regime considering how large the values of the shift are^{75,113}.

Although this expression was calculated for an incident light polarized along the axis of the dimer, it was demonstrated that the effects of the polarization were very low for AuNPs with a diameter up to 40 nm and start becoming consequent for diameters superior to 87 nm⁶⁷. It means that it is reasonable to use it for our dimers even though we used non-polarized light.

We therefore decided to use this plasmon ruler equation (Equation 1.13) to calculate an estimation of the gap distance of our plasmonic dimers for which it was possible to do so, i.e., those containing AuNPs 6, 15, 20, and 22. Two different diameter values were used, the one obtained using the method of Haiss et al. and the measured on the TEM images. The results are shown in Table 6.4.

Table 6.4: Values of the gap distances calculated with the plasmon ruler equation.

#AuNP	S ($\Delta\lambda_{\text{LSPR neighbors - TADP - LBDP}}$) (nm)	s/D	d_{gap} (for D = 51 nm) (nm)	d_{gap} (for D = 60.2 nm) (nm)
6	90.74	0.0155	0.8	0.9
15	88.51	0.021	1.1	1.3
20	86.28	0.027	1.4	1.6
22	86.96	0.0255	1.3	1.5

The values of the gap distances are quite similar whether they were calculated with one value of the diameter or the other. The values are all close or superior to 1 nm, demonstrating that none of the AuNPs considered here are in the nearly touching regime^{75,113}. Instead, although they are very close from one another, the AuNPs would be separated by their respective citrate layer exerting electrostatic repulsion on each other.

3 - Simulation of the optical response of the asymmetric plasmonic dimers by BEM method (collaboration)

The simulations were performed by M. Maurice (PhD student at PROMES laboratory, CNRS/Université de Perpignan) with the Matlab toolbox MNPBEM. Regarding the dielectric permittivity of gold, the results given by Olmon et al.¹⁹⁷ were used in addition to a correction based on the Kreibig and Volmer model¹⁹⁸ to account for the specificities of a finite size nanoparticle.

The experimental values of gap distances are in agreement with the ones from the simulations that predicted gap distances inferior to 1.5 nm for all the plasmonic dimers. Indeed, when the gap is superior to 1.5 nm, it is no longer possible to distinguish the two peaks on the simulated spectra. The simulated results, shown further, are an average between those obtained with a parallel polarization and those obtained with a transverse polarization with respect to the plane of the substrate. Let us remind the configuration of the experimental setup used to record the spectra (see Chapter 2.II.4). The sample is illuminated by the microscope objective and with a numerical aperture of 0.9, corresponding to an incidence angle θ given by $\sin \theta = 0.9$ which gives $\theta = 64^\circ$. It results in a strong contribution of the p-polarized light. All the simulation results shown further are an average between those obtained with a parallel polarization and those obtained with a transverse polarization.

The simulations also allowed to study the influence on the spectra of the following parameters: the distance between the AuNPs and the substrate, the diameters of the AuNPs, the gap distance between the AuNPs, and the angle between the dimer axis and the surface (see Figure 6.12). The most influent parameters turned out to be the gap distance and the angle. A comparison of the spectral behavior of a symmetric and an asymmetric dimer was made for dimers in vacuum and supported dimers. First, it was noted that for both types of dimers, the distance from the substrate and the gap distance has no influence on the position of the peak corresponding to the TADP. It only influences the peak corresponding to the LBDP which

redshifts when the distance from the substrate and/or the gap distance decreases. The effect of the variation of the AuNPs diameter on the position of the peaks is quite low whereas the effect on the amplitude of the peaks is much more pronounced. This observation is in agreement with that of Romero et al.¹¹³ who obtained similar results for 60 nm AuNPs and for slightly larger or smaller nanoparticles.

For the spectra simulated in vacuum (see Figure 6.18), the following observations were made. The absorption cross section of the asymmetric dimer is smaller than that of the symmetric dimer. It is due to the smaller size of one of the AuNP from the asymmetric dimer. For the asymmetric dimer, the peak corresponding to the LBDP has a lower intensity, and the intensity decreases when the gap distance increases. The redshift observed for this peak upon reduction of the gap distance is less pronounced than for a symmetric dimer. When the gap distance reaches a value large enough, the peak completely disappears. This behavior is explained by the smaller size of one of the AuNPs from the asymmetric dimer. It reduces the efficiency of the coupling between the two AuNPs (it is optimal in the case of the symmetric dimers since both AuNPs have the same size).

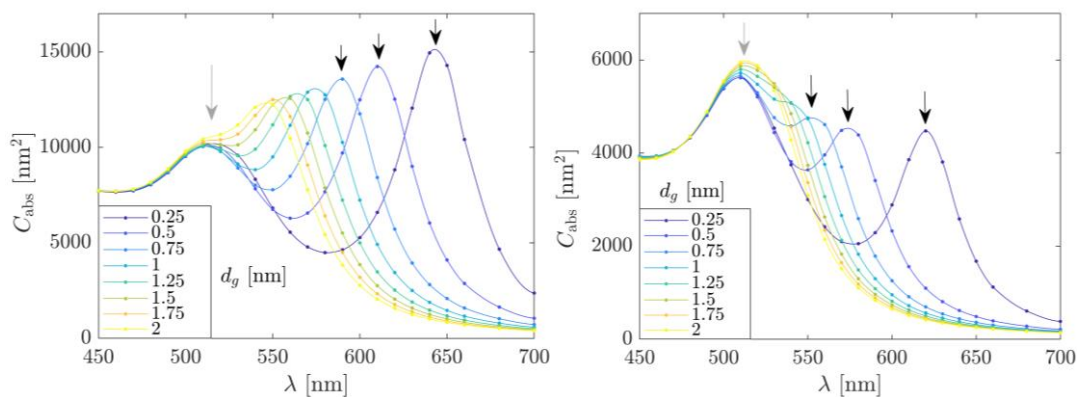


Figure 6.18: Simulated spectra of a symmetric (left) and an asymmetric dimer (right) in vacuum in function of their gap distance d_g . The symmetric dimer is made of two AuNPs of 60.2 nm whereas the asymmetric dimer is made of an AuNP of 60.2 nm and an AuNP of 29.1 nm.

For the spectra simulated for supported dimers (Figure 6.19), the following results were obtained. For the symmetric dimer, when the gap distance decreases, the intensity of the peak corresponding to the LBDP, unlike for a dimer in vacuum, it is not modified when the gap distance decreases. For the asymmetric dimer, unlike for a dimer in vacuum, the intensity of the peak corresponding to the LBDP decreases when the gap distance decreases. A blueshift of the

peak corresponding to the TADP is also observed upon reduction of the gap distance, in agreement with what was experimentally observed (see Table 6.3) but not with what is usually observed.

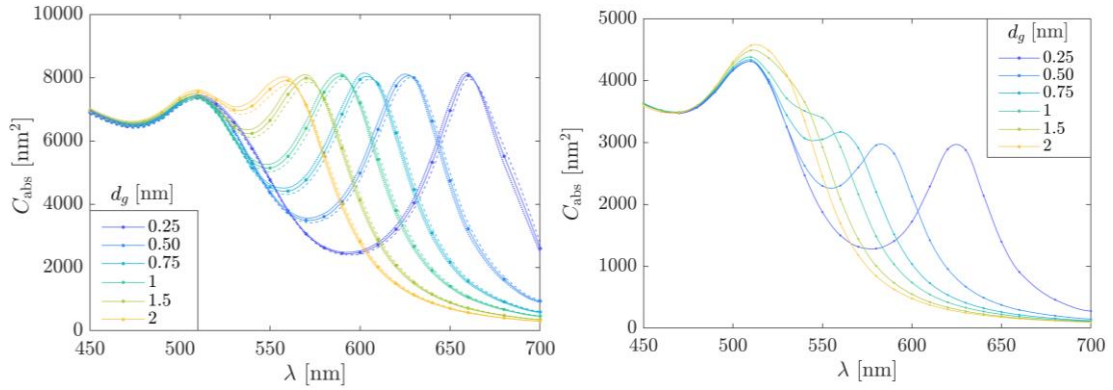


Figure 6.19: Simulated spectra of a symmetric (left) and an asymmetric dimer (right) deposited on ITO in function of their gap distance d_g . The symmetric dimer is made of two AuNPs of 60.2 nm whereas the asymmetric dimer is made of an AuNP of 60.2 nm and an AuNP of 29.1 nm. In both cases, the dimer axis is parallel to the substrate (no angle α). The following parameters were used, $e_s = 80$ nm (thickness of the substrate's ITO layer) $\epsilon_s = 3.6159$ (dielectric permittivity of the substrate's ITO layer), the layer of glass below that of ITO is considered infinite and with a dielectric permittivity of $\epsilon_{glass} = 2.3207$, the AuNPs are considered separated by a distance $d_s = 0.9729$ nm from the substrate (solid curves) corresponding to the size of an APTES molecule.

As shown in Figure 6.20, the importance of the influence of the angle between the dimer axis and the surface was demonstrated. The angle has an influence of the position on the peak corresponding to the LBDP. The redshift induced by the reduction of the gap distance decreases when the angle increases toward 90° . This trend can be explained by the combined influence of the distance from the substrate (when the distance from the substrate decreases, the peak corresponding to the LBDP redshifts) and of the polarization direction in relation to the dimer axis: when the angle goes towards 90° , a parallel polarization is felt like a transverse one and the AuNPs behave more and more like two independent AuNPs hence the lower redshift. In the simulations, the polarization is in the plane of the substrate so that when the angle between the axis dimer and the surface increases, the intensity of the LBDP peak decrease, until it disappears for an angle of 90° . In the experimental case, since we are working in dark field, the polarization is not in the plane of the substrate meaning that no matter the value of the angle, the peak of the LBDP could never disappear.

When the angle varies from -75° to 20° , and thus the distance from the surface varies, the position of the peak corresponding to the TADP varies of 6 nm, it could contribute to explain the blue shift observed after the deposition of the 28 nm AuNPs (see Table 6.3).

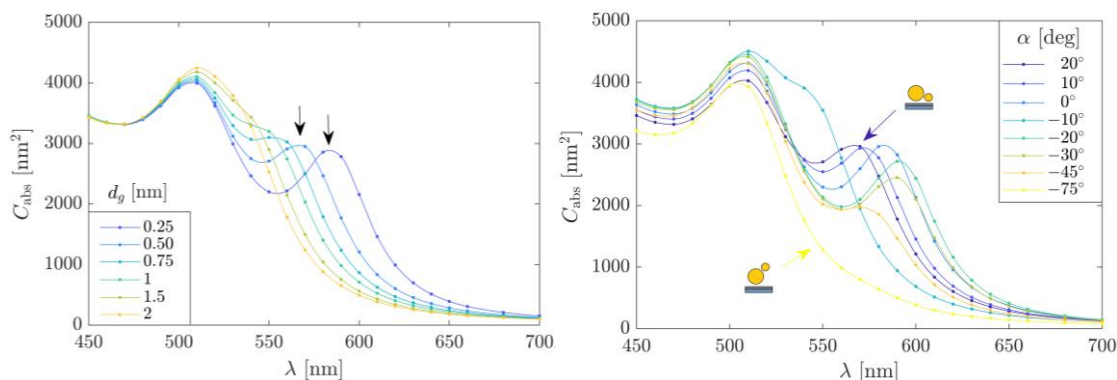


Figure 6.20: Simulated spectra of asymmetric dimers deposited on ITO with various gap distances d_g (left) or various angles α between the dimer axis and the substrate, for a fixed gap distance of 0.5 nm (right). The asymmetric dimer is made of an AuNP of 60.2 nm and an AuNP of 29.1 nm.

These simulations were very useful to detect general trends but are not adapted to more precise comparisons between the simulated dimers (with ideal perfectly spherical AuNPs) and the experimental ones (with realistic, faceted AuNPs without perfect monodispersity). As Yoon et al. pointed out, ideal and non-ideal dimers are not directly comparable and that the average properties of a group of non-ideal dimers do not correspond to that of an ideal dimer¹⁰⁴.

To summarize the preceding parts of this chapter, we demonstrated that we were able to visually identify a single gold nanoparticle on a dark field microscopy image and to record its scattering spectrum. We studied the evolution of that spectrum upon formation of asymmetric dimers: which peaks emerged, how they were shifted, which plasmonic modes they corresponded to, etc.. The gap distance of the dimers was estimated based on the position of the peaks using a plasmon ruler equation. We found out that the peak corresponding to the LBDP was mainly positioned around two values indicating that even though the deposition of the second layer of AuNPs leading to the formation of the dimers was not controlled, the formation of the plasmonic dimers does not occur randomly. Something, possibly the electrostatic repulsion, would define (or at least influence) the distance between the AuNPs. Although their gap distances are very small, it could be envisioned to post-functionalize the asymmetric plasmonic dimers (turning them into chemical dimers).

Plasmonic nanoparticles of other shapes are also of great interest, for example Grasseschi et al.⁶⁹ recorded the extinction spectra of individual hexagonal and triangular gold nanodisks (AuNDs) with a 50 nm diameter and 13 nm thickness deposited on glass by hyperspectral dark-field microscopy. These geometries are particularly interesting since NPs presenting sharp tips exhibit higher plasmonic enhancement⁶⁸. Large AuNDs (yellow), small hexagonal (snipped triangles) AuNDs (green), and small triangular AuNDs (red) were present on the DF microscopy image. These various AuNDs present different spectral profiles. Unlike our small or medium spherical nanoparticles which present an isotropic charge separation on the surface, generating a single dipolar mode, non-isotropic particles generate quadrupolar modes. In the case of flat nanoparticles, such as disks or triangles, two in-plane and two out-of-plane modes can be involved, from their corresponding dipoles and quadrupoles. The small triangular AuNDs presented one peak between 661 and 695 nm, the small hexagonal AuNDs presented one peak around 580 nm and most of the large AuNDs presented two peaks, the first one (in plane dipolar modes) in the range 562 - 633 nm and the second one in the range 622 - 709 nm (out-of-plane oscillations of the quadrupolar mode), some other only presented one peak in the range 623 - 637 nm. For the large AuNDs, to distinguish the triangular from the hexagonal ones, they made a deconvolution process of the peaks. The differences in the scattering spectra were associated with the degree of tip snipping of the AuNDs. When the triangular nanodisks are snipped (hexagonal), due to the electromagnetic field distribution at the metallic surface, the in-plane dipolar modes undergo blue shifts, while the quadrupole modes present a small or no shift. Consequently, large AuNDs whose peak corresponding to the in plane dipolar modes was blueshifted were identified as hexagonal whereas the large whose peak corresponding to the in plane dipolar modes was where it was expected to be based on theoretical calculations were identified as triangles.

IV - Measurement of the switching of 51 nm AuNPs functionalized by C5HT-di-PSH

1 - Adsorption of C5HT-di-PSH on single 51 nm AuNPs

A sample (ADITO82) with 51 nm AuNPs drop casted on ITO was prepared and three zones of interests were located on this sample. We will focus on zone B on which as previously done for the other sample, a selection of 31 AuNPs was made. Zone B and the AuNPs selection are shown in Figure 6.21.

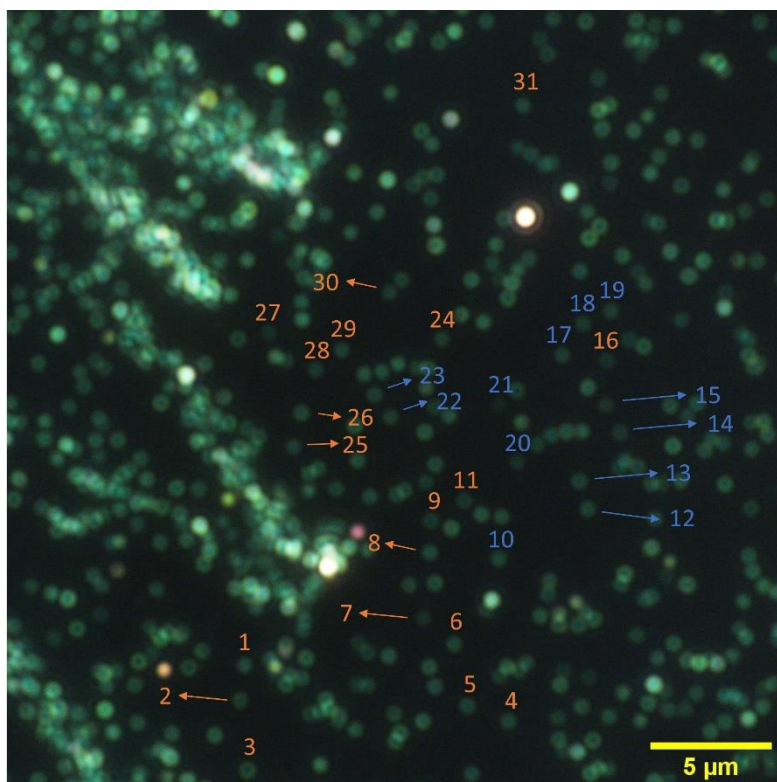


Figure 6.21: Dark field microscopy image of the zone of interest (zone B of ADITO82). The 22 AuNPs indicated in orange and blue are part of a selection of single 51 nm AuNPs. The AuNPs indicated in blue are those used for the switching measurements. Magnification 100x, exposure time 700 ms, gain 6.2.

The aim was to monitor the functionalization of each of these 31 AuNPs. First, the scattering spectra of each AuNP from the selection was recorded with the setup made of the UV-visible spectrophotometer coupled to the optical microscope and then fitted by a Gaussian between 500.14 and 592.19 nm. Second, the AuNPs were functionalized with C5HT-di-PSH following grafting protocol 1 (see Chapter 2.I.3.a) and their scattering spectrum was measured a second time and then fitted by a Gaussian between 500.14 and 592.19 nm. An example of spectra measured before and after the DAE functionalization corresponding to AuNP 6 is shown in Figure 6.23, and the scheme showing which type of sample is obtained is shown in Figure 6.22.

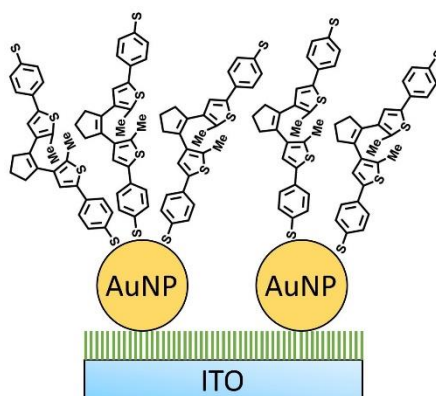


Figure 6.22: Scheme of the type of sample obtained with grafting protocol 1: ITO/AuNPs(28 nm)/C5HT-di-PSH. The green sticks are silanes (APTES). Note that this sketch is not on scale since the size of the DAE molecules is 1.79 nm, that of the APTES molecules is 0.5 nm and that of the AuNPs is 51 nm.

The value of the expected wavelength shift induced by the functionalization of the AuNPs by the C5HT-di-PSH molecules was calculated using the predictive model of Chapter 3 with Equation 3.4 and the following parameters $m = 116$ (calculated for 50 nm AuNPs with the same method than that presented in Chapter 3), $\Delta n = n_{\text{molec}} - n_{\text{air}} = 1.46 - 1 = 0.46$ (the spectra are recorded with the substrate placed in the spectrophotometer at air, hence the use of the refractive index of air), $d = 17.9 \text{ \AA}$ (length of C5HT-di-PSAc in its open form, as given in Chapter 2) and $l_d = 0.45 \times R = 0.45 \times 25.5 = 11.475$ (with R the radius of the AuNPs, for 51 nm AuNPs, $R = 25.5 \text{ nm}$, see Chapter 3 for the derivation of the expression used to calculate l_d). We obtained $\Delta\lambda_{\text{LSPR}} = 14.3 \text{ nm}$.

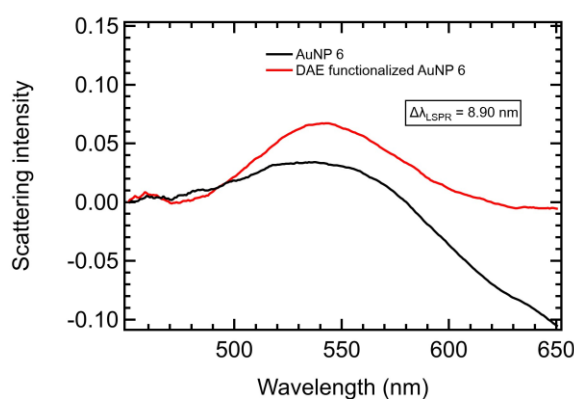


Figure 6.23: Spectrum of a single AuNP (AuNP 6) before and after DAE grafting.

As can be seen in Figure 6.24, for each pair of spectra (measured on each AuNP), the value of the LSPR peak wavelength before (AuNP) and after the DAE grafting (DAE functionalized AuNP) was extracted and plotted versus the AuNP number.

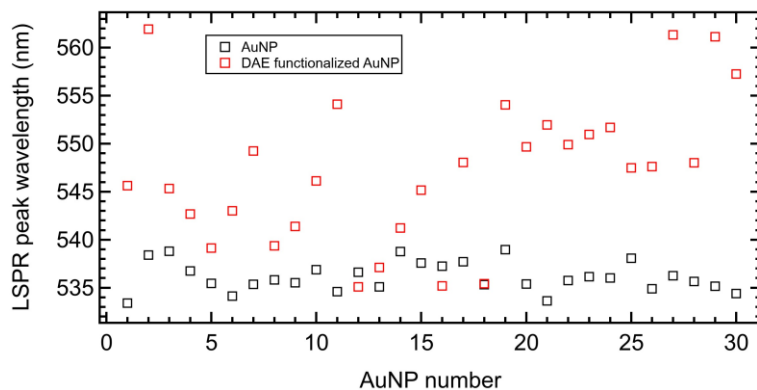


Figure 6.24: LSPR peak wavelength value before (AuNP) and after the DAE grafting (DAE functionalized AuNP) given for each AuNP.

As expected, the values of $\lambda_{\text{LSPR initial}}$ (in black, before the functionalization) are quite uniform. It is not the case for the values of $\lambda_{\text{LSPR DAE functionalized AuNP}}$ (in red, after the functionalization) that are very diverse, meaning that the functionalization of the AuNPs is inhomogeneous. The lack of uniformity of these values justifies the use of a technique to measure at the single nanoparticle scale rather than at a more global scale, as was done in Chapter 5. The values obtained in Chapter 5 correspond to the average response of a large number of AuNPs functionalized in an inhomogeneous fashion, rendering their interpretation more complicated.

All the values of the measured LSPR peak wavelength before the functionalization ($\lambda_{\text{LSPR initial}}$) and after it ($\lambda_{\text{LSPR DAE functionalized AuNP}}$) as well as the values of the difference between these LSPR peak wavelengths ($\Delta\lambda_{\text{LSPR}}$) are reported in Table 6.5.

Table 6.5: Values of the measured LSPR peak wavelength before the functionalization ($\lambda_{\text{LSPR initial}}$) and after it ($\lambda_{\text{LSPR DAE functionalized AuNP}}$); values of the difference between these LSPR peak wavelengths ($\Delta\lambda_{\text{LSPR}}$).

#AuNP (51 nm)	$\lambda_{\text{LSPR initial}}$ (nm)	$\lambda_{\text{LSPR after DAE functionalization}}$ (nm)	$\Delta\lambda_{\text{LSPR}}$ (nm)
1	533.40	545.64	12.24
2	538.40	561.94	23.54
3	538.81	545.34	6.53
4	536.73	542.69	5.96
5	535.44	539.14	3.70
6	534.12	543.02	8.90
7	535.36	549.24	13.88
8	535.80	539.35	3.55
9	535.52	541.37	5.85
10	536.88	546.13	9.25
11	534.57	554.12	19.55
12	536.61	535.07	-1.54
13	535.08	537.09	2.01
14	538.76	541.22	2.46
15	537.57	545.15	7.58
16	537.24	535.17	-2.07
17	537.71	548.05	10.34
18	535.33	535.41	0.08
19	538.95	554.05	15.10
20	535.39	549.66	14.27
21	533.63	551.96	18.33
22	535.76	549.89	14.13
23	536.13	550.96	14.83
24	536.02	551.70	15.68
25	538.07	547.50	9.43
26	534.90	547.61	12.71
27	536.24	561.35	25.11
28	535.65	548.03	12.38
29	535.14	561.13	25.99
30	534.39	557.28	22.89

The average value of the measured LSPR wavelength shift occurring upon functionalization of the AuNPs by the C5HT-di-PSH molecules is 11.01 nm with a standard deviation of 7.75 nm. This value is in global agreement with the calculated value of 14.3 nm confirming the grafting of the C5HT-di-PSH molecules at the surface of the AuNPs. However, when looking at the values of the experimentally measured $\Delta\lambda_{\text{LSPR}}$, we notice that the values are quite heterogenous which would mean that the grafting of the molecules also is. Let us remind that C5HT-di-PSH molecules are dithiol molecules, the AuNPs possessing a shift value superior to the calculated value for a full monolayer of molecules are probably covered with more than a monolayer due to the formation of short chains of C5HT-di-PSH molecules

connected by disulfide (S-S) bridges. Regarding the AuNPs possessing a shift value inferior to the calculated value, we can assume that they were simply covered with less than a monolayer of molecules. In the end, we were able to monitor the functionalization of a gold nanoparticle at the single nanoparticle scale using dark field microscopy coupled to UV-visible spectroscopy.

2 - Switching of C5HT-di-PSH molecules grafted on single 51 nm AuNPs

A simple UV irradiation setup, shown in Figure 6.25, was built directly on the optical microscope to make switching measurements on single 51 nm AuNPs functionalized with C5HT-di-PSH.

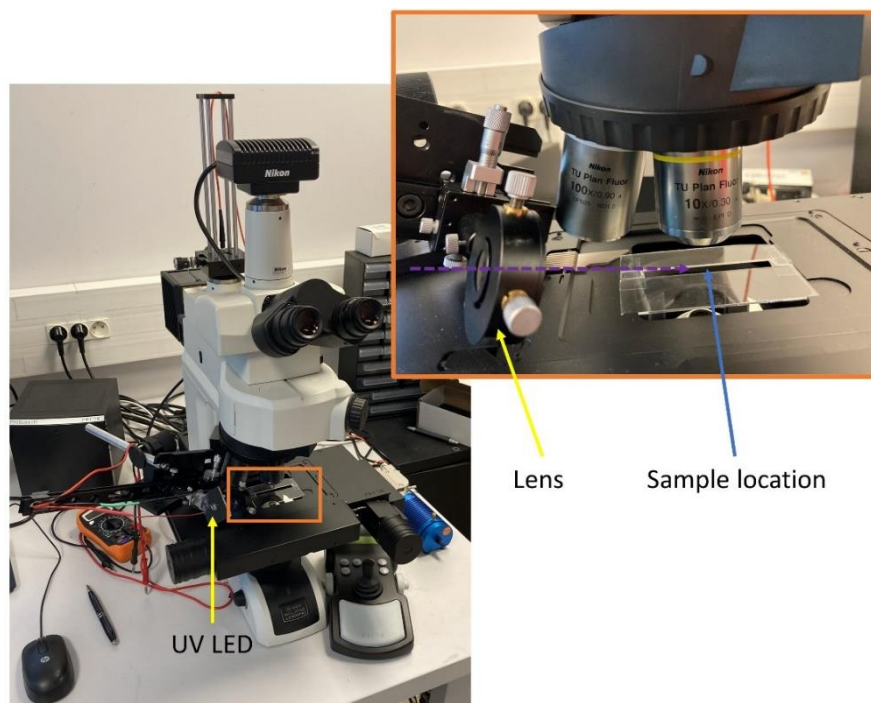


Figure 6.25: LED irradiation setup combined to the setup made of the UV-visible spectrophotometer coupled to the optical microscope. The UV light coming from the LED (trajectory indicated by the purple arrow) is focused on the sample by a lens of $f = 25$ mm yielding an illumination zone of 0.27 cm^2 .

The light flux received by the sample was measured the same way as for the other setups (see Chapter 2.II.2.b). All the parameters used for the irradiations are given in Table 6.6.

Table 6.6: LEDs parameters for the switching measurements.

LED	I (A)	P (mW)	Φ (mW/cm ²)	Φ_{photons} (photons/s/cm ²)
UV	0.25	0.302	0.933	1.41×10^{15}
Vis	0.7	2.26	3.19	8.10×10^{15}

Switching measurements were performed on 12 AuNPs from the selection of AuNPs from zone B (those indicated in blue on Figure 6.21). It should be noted that these measurements are particularly reliable especially regarding the measurement of the scattering intensity since all the spectra were recorded using the same baseline. The baseline remained stable throughout the whole measurement session, there was no need to re-record the “White” and the “Dark” (see Chapter 2.II.4) in between the irradiations.

First, the sample underwent an initial 90 minutes visible light irradiation to make sure to start the experiment with all the molecules in the open state. Then, the sample underwent two irradiation cycles consisting of a 45 minutes UV light irradiation followed by a 90 minutes visible light irradiation. A UV-visible spectrum of each AuNP was recorded after each irradiation (see the examples of AuNP 19 and 14 in Figure 6.26 and Figure 6.27) and at the end of the experiment, all the spectra were fitted by a Gaussian between 515.54 and 565.44 nm. The absorbance at λ_{LSPR} was extracted from the fit and plotted versus the time.

Out of the 12 AuNPs that were measured (AuNP 10, 12, 13, 14, 15, 17, 18, 19, 20, 21, 22, 23), 4 (AuNP 13, 14, 19, 20) clearly presented the expected behavior regarding the evolution of the scattering intensity at the LSPR peak i.e., an increase of the scattering intensity upon UV light irradiation and a decrease of the scattering intensity upon visible light irradiation. The spectra of the AuNPs presenting this evolution are shown in Figure 6.26 (AuNP 19) and Figure 6.27 (AuNP 14) and in the Appendix (see Figure A.6.4 and Figure A.6.5). The typical increase of the scattering intensity induced by the switching is of 5×10^{-3} units. By looking more closely at the values of the LSPR peak wavelength shift occurring upon functionalization (see Table 6.5), the quantity of molecules grafted on the AuNPs is not the factor determining its ability to switch. Indeed, in both groups of AuNPs, the ones that switch and the ones that do not switch, LSPR peak wavelength shift values of a few nm or around 15 nm are found. Instead, we can make the hypothesis that the factor determining the ability to switch of the molecules once they are grafted on the AuNPs is their geometry.

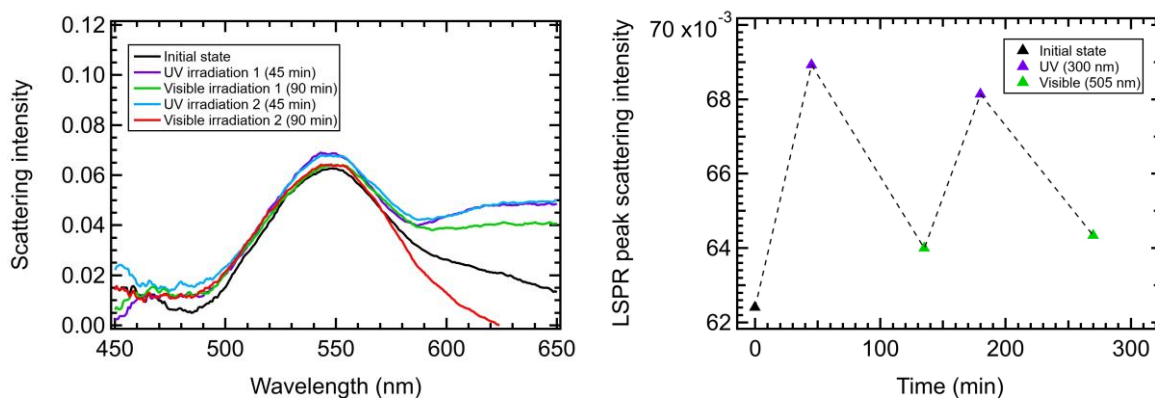


Figure 6.26: UV-visible spectra corresponding to the switching measurements on AuNP 19 (left). Evolution of the scattering intensity at λ_{LSPR} upon irradiation as a function of time.

As can be seen on the left part of Figure 6.26, the spectra corresponding to the AuNP after it received a UV irradiation (purple and blue) are almost superimposable, the same observation is made with the spectra corresponding to the AuNP after it received a visible irradiation (black, green and red). The two states, one for which the molecules are in the open form and the other one for which they are in the close form, are clearly distinguishable. Now if we look at the evolution of the absorbance at λ_{LSPR} , as it increases upon UV irradiation (and thus ring-closing of the molecules) and decreases upon visible irradiation (and thus ring-opening of the molecules). This behavior is consistent with the one observed in Chapter 5 when measuring the UV-visible spectra corresponding to the average response of many AuNPs with DAE grafted on them. The amplitude of the absorbance at λ_{LSPR} variations are also comparable to that of the samples presented in Chapter 5. It confirms that we are capable of measuring the switching of DAE molecules on individual gold nanoparticles, which in itself is a major result of this work.

A value of switching ratio was calculated with the method explained in Chapter 5.I.2 for the first switching cycle of AuNP 19. In this case we have $\text{SR} = 15.2$. This switching ratio is in agreement with the ones previously calculated in Chapter 5 (see Table 5.6).

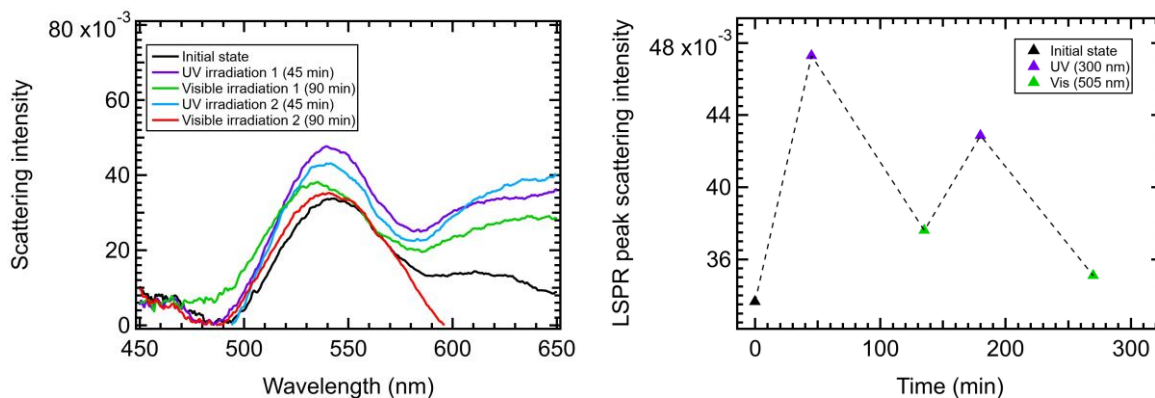


Figure 6.27: UV-visible spectra corresponding to the switching measurements on AuNP 14 (left). Evolution of the scattering intensity at λ_{LSPR} upon irradiation as a function of time.

Conclusion

In this last chapter, we started by studying the optical response of single 51 nm AuNPs deposited on ITO by coupled measurements (optical dark field microscopy and spectroscopy), the average position of the LSPR peak is 539.1 nm. The same approach was used to study the optical response of single asymmetric dimers made of a 51 nm AuNP and a 28 nm AuNP (also on ITO). The position of the TADP is close from that of the original LSPR peak of the individual AuNPs. The position of the LBDP was either around 655 nm (shifted of 128.5 nm with respect to the TADP) for a group of AuNPs or around 620 nm (shifted of 88.1 nm with respect to the TADP) for another group of AuNPs. For this latter group, it was possible to calculate the gap distance using a plasmon ruler equation, in average the gap distance is 1.2 nm. The hybridization of the plasmonic modes of the constituent AuNPs was experimentally shown (peak corresponding to the LBDP on the scattering spectrum) and then explained using the Nordlander model. General trends regarding the behavior of our asymmetric plasmonic dimers compared to symmetric ones were unraveled by BEM based simulations.

In the second half of the chapter, the functionalization of 51 nm AuNPs deposited on ITO by C5HT-di-PSH diarylethene molecules was studied at the single nanoparticle scale. An average value of the LSPR peak wavelength shift upon the functionalization of 11.01 nm was measured, close from the calculated value of 14.3 nm. We showed that it was possible to monitor the grafting of the molecules at the surface of the AuNPs through the evolution of the LSPR peak wavelength of the AuNP exactly the same way it had been done in the previous chapter for a large number of AuNPs. This latter point was demonstrated by calculating the

average LSPR wavelength shift induced by the functionalization of all the individual AuNPs and showing it was very close to the value calculated with the predictive model developed in Chapter 3. This agreement between the experimental and calculated values had been shown for measurements on a large number of AuNPs (see Chapter 5). Finally, after making sure the AuNPs were bearing DAE molecules, we measured the switching of these molecules still at the single nanoparticle scale (switching of the molecules beard by one single AuNP) using an irradiation setup combined to the setup made of the UV-visible spectrophotometer coupled to the optical microscope. We managed to measure this switching corresponding to an increase of the scattering intensity of 5×10^{-3} units at λ_{LSPR} , on several AuNPs. We noticed that this switching was analogous to that previously measured in Chapter 5 for a large number of functionalized AuNPs. Indeed, the amplitude of the variations of the absorbance (in Chapter 5) were comparable to that of the scattering intensity (in the present chapter) and the switching ratio of 15.2 calculated in the present chapter is in agreement with those calculated in Chapter 5.

Conclusion

Measurement of the switching ratio of diarylethenes molecules

In solution

A photokinetic study of the diarylethene molecules in solution (in DMF) was conducted by UV-visible spectroscopy coupled to an irradiation setup. This study allowed us to calculate their switching ratio (ratio of the time it takes for both photo-induced reactions to occur) which were respectively 6.4 for C5HT-di-PSAc and 5 for Cl-C5HT-PSAc. The time it took for the molecules to reach the PSS was also measured: 23 100 s for C5HT-di-PSAc and 36 660 s for Cl-C5HT-PSAc. This study also permitted to investigate the reversibility and symmetry of the switching as well as the fatigue resistance of the molecules. C5HT-di-PSAc is resistant to fatigue while Cl-C5HT-PSAc is susceptible to it. The switching of both molecules is reversible yet asymmetrical. One of the possibilities to solve this asymmetrical switching issue was to use the nanoantenna effect of AuNPs on which the molecules would be grafted: it has been explored.

Grafted on AuNPs deposited on ITO

The functionalization of 28 nm AuNPs deposited on ITO by C5HT-di-PSH molecules was monitored in situ by UV-visible spectroscopy. Values of the LSPR wavelength shift induced by the functionalization experimentally measured were comprise in the range 1.79 - 5.15 nm, while the theoretical value for a full coverage of the AuNPs with a monolayer of DAEs was calculated to be 2.53 nm. The switching of the DAEs grafted on the AuNPs was then measured in order to figure out if the nanoantenna effect provided by the gold nanoparticles generates an acceleration of the photocycloreversion reaction. This acceleration (or any effect coming from the nanoantenna effect) would have an impact on the switching ratio (it would be closer to 1 for a more symmetrical switching). An effect was expected since the absorption band in the visible of the DAE molecules corresponding to a transition involved in the photochromic reaction (switching) is located in the same spectral area than the LSPR peak of the gold nanoparticles. The switching of the DAEs grafted on the AuNPs was monitored by optical spectroscopy following the evolution of LSPR peak position: a 2% modification of the absorbance at λ_{LSPR} corresponding to the switching was measured. Reversible switching was preserved for all the samples upon grafting of the DAE molecule on the gold AuNP but fully reversible switching was only preserved for some of them. Fatigue quickly appeared after a

couple of switching cycles. The average switching ratio was calculated to be 22, it is about 3 times superior to the switching ratio obtained for DAEs in solution. This increase of the switching ratio value means that the asymmetry of the switching was increased, instead of reduced as intended. The photocycloreversion reaction was slowed down upon grafting of the DAEs on the AuNPs and not accelerated. It would be due to the presence of strong quenching since the π -system of the diarylethene molecule is directly connected to the AuNPs

Grafted on a single AuNP

We showed that it was possible to monitor the adsorption of DAE molecules at the single AuNP scale using dark field microscopy coupled to UV-visible spectroscopy. An average LSPR wavelength shift value of 11 nm was measured for the grafting of C5HT-di-PSH on individual 51 nm AuNPs. This value is close from the calculated one (14.3 nm) for a full coverage of an AuNP with a monolayer of C5HT-di-PSH. The switching of the DAE molecules present on an individual AuNP was then measured using the irradiation setup combined to the setup made of the UV-visible spectrophotometer coupled to the optical microscope. This switching was similar to the one previously measured for a large number of 28 nm AuNPs bearing C5HT-di-PSH molecules. It corresponded to a variation of the scattering intensity at λ_{LSPR} of 5×10^{-3} units, comparable to the variations of the absorbance measured for the switching of the DAEs on a large number of AuNPs. The value of the switching ratio calculated from the switching measurements at the single AuNP scale is 15, also comparable to the switching ratio values calculated for the switching of the DAEs on a large number of AuNPs.

Asymmetric plasmonic dimers

Asymmetric plasmonic dimers made of a 51 nm AuNP and a 28 nm AuNP were prepared: 45 % of the 28 nm AuNPs that were drop-casted on the ITO substrate with 51 nm AuNPs already deposited on it spontaneously formed dimers with the 51 nm AuNPs. These dimers were characterized individually by AFM and dark field microscopy coupled to UV-visible spectroscopy. Their scattering spectrum was recorded giving us access to the position of their hybridized plasmonic modes, especially that of the TADP which is close from that of the original LSPR peak of the individual AuNPs, and that of the LBDP. The latter was either around 655 nm (shifted of 128.5 nm with respect to the TADP) for a group of dimers or around 620 nm (shifted of 88.1 nm with respect to the TADP) for another group of dimers with an average gap distance of 1.2 nm, calculated with a plasmon ruler equation.

Perspectives: Towards the fabrication of dimers with gold nanoparticles connected by a diarylethene molecule

The preparation of dimers with different diarylethene molecules less susceptible to quenching is the main perspective of this PhD work. One of the possibilities would be to use monosubstituted diarylethenes with different a photochromic unit and different linkers/spacers (see Figure P.1). Another possibility would be to use disubstituted diarylethenes with eventually a different photochromic unit and/or different linkers/spacers (see Figure P.1). The biphenyl substituted dithienylethenes used by Hassan et al.¹⁹⁹ could be envisioned. A less explored yet interesting option would be to prepare a “double dimer” i.e., two nanoparticles connected by a diarylethene dyad^{200,201} (see Figure P.1). Note that the possibility to improve the photochromism of diarylethene dyads by connecting them to gold nanoparticles has been theoretically investigated by Fihey et al.²⁰²

Regarding the strategy of dimer fabrication, a solution to obtain chemical dimers prepared via a chemical bottom-up technique would be to implement the methods of Yoon et al.^{104,124} to diarylethenes, and then to deposit the dimers on a substrate (see Figure P.1). Otherwise, the fabrication of dimers via top down lithography techniques²⁰³ (see Figure P.1) could be considered, followed by a post-fabrication functionalization of the dimers gap²⁰⁴, as it is done with SERS substrates²⁰⁵.

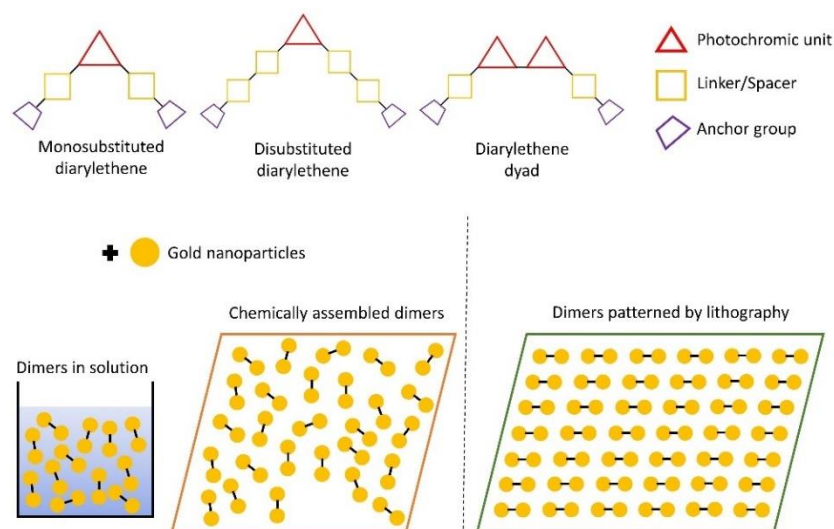


Figure P.1: Scheme of the different types diarylethene structures (monosubstituted DAE, disubstituted DAE, DAE dyad) that could be used to obtain dimers (top). Illustration of the different types of dimers that can be fabricated. (bottom).

Following the obtention of the dimers, the two conductive states of the diarylethene molecules would have to be measured by conductive AFM.

References

- (1) Kim, Y.; Hellmuth, T. J.; Sysoiev, D.; Pauly, F.; Pietsch, T.; Wolf, J.; Erbe, A.; Huhn, T.; Groth, U.; Steiner, U. E.; Scheer, E. Charge Transport Characteristics of Diarylethene Photoswitching Single-Molecule Junctions. *Nano Lett.* **2012**, *12* (7), 3736–3742. <https://doi.org/10.1021/nl3015523>.
- (2) Kim, Y.; Bahoosh, S. G.; Sysoiev, D.; Huhn, T.; Pauly, F.; Scheer, E. Inelastic Electron Tunneling Spectroscopy of Difurylethene-Based Photochromic Single-Molecule Junctions. *Beilstein J. Nanotechnol.* **2017**, *8*, 2606–2614. <https://doi.org/10.3762/bjnano.8.261>.
- (3) Kim, D.; Jeong, H.; Lee, H.; Hwang, W.-T.; Wolf, J.; Scheer, E.; Huhn, T.; Jeong, H.; Lee, T. Flexible Molecular-Scale Electronic Devices Composed of Diarylethene Photoswitching Molecules. *Adv. Mater.* **2014**, *26* (23), 3968–3973. <https://doi.org/10.1002/adma.201306316>.
- (4) Kim, D.; Jeong, H.; Hwang, W.-T.; Jang, Y.; Sysoiev, D.; Scheer, E.; Huhn, T.; Min, M.; Lee, H.; Lee, T. Reversible Switching Phenomenon in Diarylethene Molecular Devices with Reduced Graphene Oxide Electrodes on Flexible Substrates. *Adv. Funct. Mater.* **2015**, *25* (37), 5918–5923. <https://doi.org/10.1002/adfm.201502312>.
- (5) Benner, D.; Boneberg, J.; Nürnberger, P.; Waitz, R.; Leiderer, P.; Scheer, E. Lateral and Temporal Dependence of the Transport through an Atomic Gold Contact under Light Irradiation: Signature of Propagating Surface Plasmon Polaritons. *Nano Lett.* **2014**, *14* (9), 5218–5223. <https://doi.org/10.1021/nl502165y>.
- (6) Guhr, D. C.; Rettinger, D.; Boneberg, J.; Erbe, A.; Leiderer, P.; Scheer, E. Influence of Laser Light on Electronic Transport through Atomic-Size Contacts. *Phys. Rev. Lett.* **2007**, *99* (8), 086801. <https://doi.org/10.1103/PhysRevLett.99.086801>.
- (7) Ghafoori, G.; Boneberg, J.; Leiderer, P.; Scheer, E. Tuning the Transmission of Surface Plasmon Polaritons across Nano and Micro Gaps in Gold Stripes. *Opt. Express* **2016**, *24* (15), 17313. <https://doi.org/10.1364/OE.24.017313>.
- (8) Zotti, L. A.; Kirchner, T.; Cuevas, J.-C.; Pauly, F.; Huhn, T.; Scheer, E.; Erbe, A. Revealing the Role of Anchoring Groups in the Electrical Conduction Through Single-Molecule Junctions. *Small* **2010**, *6* (14), 1529–1535. <https://doi.org/10.1002/smll.200902227>.
- (9) Sysoiev, D.; Fedoseev, A.; Kim, Y.; Exner, T. E.; Boneberg, J.; Huhn, T.; Leiderer, P.; Scheer, E.; Groth, U.; Steiner, U. E. Synthesis and Photoswitching Studies of Difurylperfluorocyclopentenes with Extended π -Systems. *Chem. - Eur. J.* **2011**, *17* (24), 6663–6672. <https://doi.org/10.1002/chem.201003716>.
- (10) Sysoiev, D.; Yushchenko, T.; Scheer, E.; Groth, U.; Steiner, U. E.; Exner, T. E.; Huhn, T. Pronounced Effects on Switching Efficiency of Diarylcycloalkenes upon Cycloalkene Ring Contraction. *Chem. Commun.* **2012**, *48* (92), 11355. <https://doi.org/10.1039/c2cc35726g>.
- (11) Sendler, T.; Luka-Guth, K.; Wieser, M.; Lokamani; Wolf, J.; Helm, M.; Gemming, S.; Kerbusch, J.; Scheer, E.; Huhn, T.; Erbe, A. Light-Induced Switching of Tunable Single-Molecule Junctions. *Adv. Sci.* **2015**, *2* (5), 1500017. <https://doi.org/10.1002/advs.201500017>.
- (12) Khodko, A. A.; Khomenko, V. V.; Mamuta, O. D.; Mukha, Iu. P.; Sysoiev, D. O.; Huhn, T.; Snegir, S. V.; Kachalova, N. M. Picosecond Cyclization Reaction Dynamics of Furan-Based Diarylethene with Thiosemicarbazone Side-Chain Groups. *Mol. Cryst. Liq. Cryst.* **2016**, *639* (1), 64–70. <https://doi.org/10.1080/15421406.2016.1254524>.
- (13) Khodko, A.; Khomenko, V.; Shynkarenko, Y.; Mamuta, O.; Kapitanchuk, O.; Sysoiev, D.; Kachalova, N.; Huhn, T.; Snegir, S. Ultrafast Ring-Closing Reaction Dynamics of a Photochromic Furan-Based Difurylethene. *Chem. Phys. Lett.* **2017**, *669*, 156–160. <https://doi.org/10.1016/j.cplett.2016.12.034>.

- (14) Reecht, G.; Lotze, C.; Sysoiev, D.; Huhn, T.; Franke, K. J. Visualizing the Role of Molecular Orbitals in Charge Transport through Individual Diarylethene Isomers. *ACS Nano* **2016**, *10* (11), 10555–10562. <https://doi.org/10.1021/acsnano.6b06559>.
- (15) Reecht, G.; Lotze, C.; Sysoiev, D.; Huhn, T.; Franke, K. J. Disentangling Electron- and Electric-Field-Induced Ring-Closing Reactions in a Diarylethene Derivative on Ag(1 1 1). *J. Phys. Condens. Matter* **2017**, *29* (29), 294001. <https://doi.org/10.1088/1361-648X/aa75c1>.
- (16) Wolf, J.; Huhn, T.; Steiner, U. E. Large Protonation-Gated Photochromism of an OPE-Embedded Difurylperfluorocyclopentene. *Phys. Chem. Chem. Phys.* **2015**, *17* (8), 6066–6075. <https://doi.org/10.1039/C4CP05258G>.
- (17) Wolf, J.; Eberspächer, I.; Groth, U.; Huhn, T. Synthesis and Photoswitching Studies of OPE-Embedded Difurylperfluorocyclopentenes. *J. Org. Chem.* **2013**, *78* (17), 8366–8375. <https://doi.org/10.1021/jo401065b>.
- (18) Bossard-Giannesini, L.; Cruguel, H.; Lacaze, E.; Pluchery, O. Plasmonic Properties of Gold Nanoparticles on Silicon Substrates: Understanding Fano-like Spectra Observed in Reflection. *Appl. Phys. Lett.* **2016**, *109* (11), 111901. <https://doi.org/10.1063/1.4962731>.
- (19) Caillard, L.; Seitz, O.; Campbell, P. M.; Doherty, R. P.; Lamic-Humblot, A.-F.; Lacaze, E.; Chabal, Y. J.; Pluchery, O. Gold Nanoparticles on Oxide-Free Silicon–Molecule Interface for Single Electron Transport. *Langmuir* **2013**, *29* (16), 5066–5073. <https://doi.org/10.1021/la304971v>.
- (20) Caillard, L.; Sattayaporn, S.; Lamic-Humblot, A.-F.; Casale, S.; Campbell, P.; Chabal, Y. J.; Pluchery, O. Controlling the Reproducibility of Coulomb Blockade Phenomena for Gold Nanoparticles on an Organic Monolayer/Silicon System. *Nanotechnology* **2015**, *26* (6), 065301. <https://doi.org/10.1088/0957-4484/26/6/065301>.
- (21) Zhang, Y.; Pluchery, O.; Caillard, L.; Lamic-Humblot, A.-F.; Casale, S.; Chabal, Y. J.; Salmeron, M. Sensing the Charge State of Single Gold Nanoparticles via Work Function Measurements. *Nano Lett.* **2015**, *15* (1), 51–55. <https://doi.org/10.1021/nl503782s>.
- (22) Snegir, S. V.; Marchenko, A. A.; Yu, P.; Maurel, F.; Kapitanchuk, O. L.; Mazerat, S.; Lepeltier, M.; Léaustic, A.; Lacaze, E. STM Observation of Open- and Closed-Ring Forms of Functionalized Diarylethene Molecules Self-Assembled on a Au(111) Surface. *J. Phys. Chem. Lett.* **2011**, *2* (19), 2433–2436. <https://doi.org/10.1021/jz200875c>.
- (23) Snegir, S. V.; Yu, P.; Maurel, F.; Kapitanchuk, O. L.; Marchenko, A. A.; Lacaze, E. Switching at the Nanoscale: Light- and STM-Tip-Induced Switch of a Thiolated Diarylethene Self-Assembly on Au(111). *Langmuir* **2014**, *30* (45), 13556–13563. <https://doi.org/10.1021/la5029806>.
- (24) *The IUPAC Compendium of Chemical Terminology: The Gold Book*, 4th ed.; Gold, V., Ed.; International Union of Pure and Applied Chemistry (IUPAC): Research Triangle Park, NC, 2019. <https://doi.org/10.1351/goldbook>.
- (25) Merino, E.; Ribagorda, M. Control over Molecular Motion Using the *Cis* – *Trans* Photoisomerization of the Azo Group. *Beilstein J. Org. Chem.* **2012**, *8*, 1071–1090. <https://doi.org/10.3762/bjoc.8.119>.
- (26) Irie, M.; Fukaminato, T.; Matsuda, K.; Kobatake, S. Photochromism of Diarylethene Molecules and Crystals: Memories, Switches, and Actuators. *Chem. Rev.* **2014**, *114* (24), 12174–12277. <https://doi.org/10.1021/cr500249p>.
- (27) Andréasson, J.; Pischel, U. Light-Stimulated Molecular and Supramolecular Systems for Information Processing and Beyond. *Coord. Chem. Rev.* **2021**, *429*, 213695. <https://doi.org/10.1016/j.ccr.2020.213695>.
- (28) Huang, C.; Huang, R.; Zhang, S.; Sun, H.; Wang, H.; Du, B.; Xiao, Y.; Yu, T.; Huang, W. Recent Development of Photodeformable Crystals: From Materials to Mechanisms. *Research* **2021**, *2021*, 1–26. <https://doi.org/10.34133/2021/9816535>.

- (29) Irie, M. Diarylethenes for Memories and Switches. *Chem. Rev.* **2000**, *100* (5), 1685–1716. <https://doi.org/10.1021/cr980069d>.
- (30) Lucas, L. N. Dithienylcyclopentene Optical Switches: Towards Photoresponsive Supramolecular Materials, s.n.], S.I., 2001.
- (31) Perrier, A.; Aloise, S.; Olivucci, M.; Jacquemin, D. Inverse versus Normal Dithienylethenes: Computational Investigation of the Photocyclization Reaction. *J. Phys. Chem. Lett.* **2013**, *4* (13), 2190–2196. <https://doi.org/10.1021/jz401009b>.
- (32) Bandara, H. M. D.; Burdette, S. C. Photoisomerization in Different Classes of Azobenzene. *Chem Soc Rev* **2012**, *41* (5), 1809–1825. <https://doi.org/10.1039/C1CS15179G>.
- (33) van der Molen, S. J.; Liao, J.; Kudernac, T.; Agustsson, J. S.; Bernard, L.; Calame, M.; van Wees, B. J.; Feringa, B. L.; Schönenberger, C. Light-Controlled Conductance Switching of Ordered Metal–Molecule–Metal Devices. *Nano Lett.* **2009**, *9* (1), 76–80. <https://doi.org/10.1021/nl802487j>.
- (34) Kortekaas, L.; Browne, W. R. The Evolution of Spiropyran: Fundamentals and Progress of an Extraordinarily Versatile Photochrome. *Chem. Soc. Rev.* **2019**, *48* (12), 3406–3424. <https://doi.org/10.1039/C9CS00203K>.
- (35) Berkovic, G.; Krongauz, V.; Weiss, V. Spiropyrans and Spirooxazines for Memories and Switches. *Chem. Rev.* **2000**, *100* (5), 1741–1754. <https://doi.org/10.1021/cr9800715>.
- (36) Klajn, R. Spiropyran-Based Dynamic Materials. *Chem Soc Rev* **2014**, *43* (1), 148–184. <https://doi.org/10.1039/C3CS60181A>.
- (37) *The Nobel Prize in Chemistry 2016*. <https://www.nobelprize.org/prizes/chemistry/2016/press-release/> (accessed 2022-10-06).
- (38) Sauvage, J.-P. From Chemical Topology to Molecular Machines (Nobel Lecture). *Angew. Chem. Int. Ed.* **2017**, *56* (37), 11080–11093. <https://doi.org/10.1002/anie.201702992>.
- (39) Abendroth, J. M.; Bushuyev, O. S.; Weiss, P. S.; Barrett, C. J. Controlling Motion at the Nanoscale: Rise of the Molecular Machines. *ACS Nano* **2015**, *9* (8), 7746–7768. <https://doi.org/10.1021/acsnano.5b03367>.
- (40) Stoddart, J. F. Mechanically Interlocked Molecules (MIMs)-Molecular Shuttles, Switches, and Machines (Nobel Lecture). *Angew. Chem. Int. Ed.* **2017**, *56* (37), 11094–11125. <https://doi.org/10.1002/anie.201703216>.
- (41) Bruns, C. J.; Stoddart, J. F. Rotaxane-Based Molecular Muscles. *Acc. Chem. Res.* **2014**, *47* (7), 2186–2199. <https://doi.org/10.1021/ar500138u>.
- (42) Feringa, B. L. The Art of Building Small: From Molecular Switches to Motors (Nobel Lecture). *Angew. Chem. Int. Ed.* **2017**, *56* (37), 11060–11078. <https://doi.org/10.1002/anie.201702979>.
- (43) Feringa, B. L. The Art of Building Small: From Molecular Switches to Molecular Motors. *J. Org. Chem.* **2007**, *72* (18), 6635–6652. <https://doi.org/10.1021/jo070394d>.
- (44) Boggio-Pasqua, M.; Ravaglia, M.; Bearpark, M. J.; Garavelli, M.; Robb, M. A. Can Diarylethene Photochromism Be Explained by a Reaction Path Alone? A CASSCF Study with Model MMVB Dynamics. *J. Phys. Chem. A* **2003**, *107* (50), 11139–11152. <https://doi.org/10.1021/jp036862e>.
- (45) Mendive-Tapia, D.; Perrier, A.; Bearpark, M. J.; Robb, M. A.; Lasorne, B.; Jacquemin, D. New Insights into the By-Product Fatigue Mechanism of the Photo-Induced Ring-Opening in Diarylethenes. *Phys Chem Chem Phys* **2014**, *16* (34), 18463–18471. <https://doi.org/10.1039/C4CP03001J>.
- (46) Budyka, M. F. Diarylethylene Photoisomerization and Photocyclization Mechanisms. *Russ. Chem. Rev.* **2012**, *81* (6), 477–493. <https://doi.org/10.1070/RC2012v081n06ABEH004274>.

- (47) Nakamura, S.; Uchida, K.; Hatakeyama, M. Potential Energy Surfaces and Quantum Yields for Photochromic Diarylethene Reactions. *Molecules* **2013**, *18* (5), 5091–5103. <https://doi.org/10.3390/molecules18055091>.
- (48) Stadler, E.; Eibel, A.; Fast, D.; Freißmuth, H.; Holly, C.; Wiech, M.; Moszner, N.; Gescheidt, G. A Versatile Method for the Determination of Photochemical Quantum Yields via Online UV-Vis Spectroscopy. *Photochem. Photobiol. Sci.* **2018**, *17* (5), 660–669. <https://doi.org/10.1039/c7pp00401j>.
- (49) Higashiguchi, K.; Yotsuji, H.; Matsuda, K. Determination of Quantum Yield of Photoreaction in Solution and in Suspension by Global Fitting of Prolonged Change of Concentration. *Chem. Lett.* **2017**, *46* (10), 1564–1566. <https://doi.org/10.1246/cl.170673>.
- (50) Micheau, J.-C.; Coudret, C.; Kobeleva, O. I.; Barachevsky, V. A.; Yarovenko, V. N.; Ivanov, S. N.; Lichitsky, B. V.; Krayushkin, M. M. Quantitative Study of Photochromic Transformations of Diarylethene Derivatives with Either Perhydrocyclopentene or Oxazolone or Lactone Units. *Dyes Pigments* **2014**, *106*, 32–38. <https://doi.org/10.1016/j.dyepig.2014.02.013>.
- (51) Ribeiro, A.; Ballardini, R.; Belser, P.; Gandolfi, M. T.; Iyer, V. M.; Moggi, L. Photochemical Investigation of a Photochromic Diarylethene Compound That Can Be Used as a Wide Range Actinometer. *Photochem. Photobiol. Sci.* **2009**, *8* (12), 1734–1742. <https://doi.org/10.1039/b9pp00037b>.
- (52) Stranius, K.; Börjesson, K. Determining the Photoisomerization Quantum Yield of Photoswitchable Molecules in Solution and in the Solid State. *Sci. Rep.* **2017**, *7* (1), 41145. <https://doi.org/10.1038/srep41145>.
- (53) Ichikawa, T.; Morimoto, M.; Irie, M. Diastereoselective Photocyclization of a Photochromic Diarylethene Having a Benzo[b]Phosphole P-Oxide Group. *Dyes Pigments* **2017**, *137*, 214–220. <https://doi.org/10.1016/j.dyepig.2016.10.010>.
- (54) Uno, K.; Bossi, M. L.; Konen, T.; Belov, V. N.; Irie, M.; Hell, S. W. Asymmetric Diarylethenes with Oxidized 2-Alkylbenzothiophen-3-yl Units: Chemistry, Fluorescence, and Photoswitching. *Adv. Opt. Mater.* **2019**, *7* (6), 1801746. <https://doi.org/10.1002/adom.201801746>.
- (55) Jukes, R. T. F.; Adamo, V.; Hartl, F.; Belser, P.; De Cola, L. Photochromic Dithienylethene Derivatives Containing Ru(II) or Os(II) Metal Units. Sensitized Photocyclization from a Triplet State. *Inorg. Chem.* **2004**, *43* (9), 2779–2792. <https://doi.org/10.1021/ic035334e>.
- (56) Cipolloni, M.; Ortica, F.; Bougdid, L.; Moustrou, C.; Mazzucato, U.; Favaro, G. New Thermally Irreversible and Fluorescent Photochromic Diarylethenes. *J. Phys. Chem. A* **2008**, *112* (21), 4765–4771. <https://doi.org/10.1021/jp711110d>.
- (57) Murata, R.; Yago, T.; Wakasa, M. Photocyclization Reactions of Diarylethenes via the Excited Triplet State. *J. Phys. Chem. A* **2015**, *119* (45), 11138–11145. <https://doi.org/10.1021/acs.jpca.5b08205>.
- (58) Fredrich, S.; Morack, T.; Sliwa, M.; Hecht, S. Mechanistic Insights into the Triplet Sensitized Photochromism of Diarylethenes. *Chem. – Eur. J.* **2020**, *26* (34), 7672–7677. <https://doi.org/10.1002/chem.202000877>.
- (59) Pariani, G.; Quintavalla, M.; Colella, L.; Oggioni, L.; Castagna, R.; Ortica, F.; Bertarelli, C.; Bianco, A. New Insight into the Fatigue Resistance of Photochromic 1,2-Diarylethenes. *J. Phys. Chem. C* **2017**, *121* (42), 23592–23598. <https://doi.org/10.1021/acs.jpcc.7b04848>.
- (60) Cheng, H.; Yoon, J.; Tian, H. Recent Advances in the Use of Photochromic Dyes for Photocontrol in Biomedicine. *Coord. Chem. Rev.* **2018**, *372*, 66–84. <https://doi.org/10.1016/j.ccr.2018.06.003>.

- (61) Pischel, U.; Andréasson, J. A Simplicity-Guided Approach toward Molecular Set-Reset Memories. *New J. Chem.* **2010**, *34* (12), 2701. <https://doi.org/10.1039/c0nj00498g>.
- (62) Matsuda, K. Photochromic Diarylethene as an Information Processing Unit: Magnetic and Electric Switching. *Pure Appl. Chem.* **2008**, *80* (3), 555–561. <https://doi.org/10.1351/pac200880030555>.
- (63) Matsuda, K.; Yamaguchi, H.; Sakano, T.; Ikeda, M.; Tanifuji, N.; Irie, M. Conductance Photoswitching of Diarylethene–Gold Nanoparticle Network Induced by Photochromic Reaction. *J. Phys. Chem. C* **2008**, *112* (43), 17005–17010. <https://doi.org/10.1021/jp807479g>.
- (64) Arramel; Pijper, T. C.; Kudernac, T.; Katsonis, N.; van der Maas, M.; Feringa, B. L.; van Wees, B. J. Reversible Light Induced Conductance Switching of Asymmetric Diarylethenes on Gold: Surface and Electronic Studies. *Nanoscale* **2013**, *5* (19), 9277. <https://doi.org/10.1039/c3nr00832k>.
- (65) Willets, K. A.; Van Duyne, R. P. Localized Surface Plasmon Resonance Spectroscopy and Sensing. *Annu. Rev. Phys. Chem.* **2007**, *58* (1), 267–297. <https://doi.org/10.1146/annurev.physchem.58.032806.104607>.
- (66) Petryayeva, E.; Krull, U. J. Localized Surface Plasmon Resonance: Nanostructures, Bioassays and Biosensing—A Review. *Anal. Chim. Acta* **2011**, *17*.
- (67) Jain, P. K.; Huang, W.; El-Sayed, M. A. On the Universal Scaling Behavior of the Distance Decay of Plasmon Coupling in Metal Nanoparticle Pairs: A Plasmon Ruler Equation. *Nano Lett.* **2007**, *7* (7), 2080–2088. <https://doi.org/10.1021/nl071008a>.
- (68) Ross, M. B.; Mirkin, C. A.; Schatz, G. C. Optical Properties of One-, Two-, and Three-Dimensional Arrays of Plasmonic Nanostructures. *J. Phys. Chem. C* **2016**, *120* (2), 816–830. <https://doi.org/10.1021/acs.jpcc.5b10800>.
- (69) Grasseschi, D.; Lima, F. S.; Nakamura, M.; Toma, H. E. Hyperspectral Dark-Field Microscopy of Gold Nanodisks. *Micron* **2015**, *69*, 15–20. <https://doi.org/10.1016/j.micron.2014.10.007>.
- (70) Louis, C.; Pluchery, O. *Gold Nanoparticles for Physics, Chemistry, and Biology*, Second edition.; World Scientific: New Jersey, 2017.
- (71) Coronado, E. A.; Encina, E. R.; Stefani, F. D. Optical Properties of Metallic Nanoparticles: Manipulating Light, Heat and Forces at the Nanoscale. *Nanoscale* **2011**, *3* (10), 4042. <https://doi.org/10.1039/c1nr10788g>.
- (72) Schumacher, L.; Jose, J.; Janoschka, D.; Dreher, P.; Davis, T. J.; Ligges, M.; Li, R.; Mo, M.; Park, S.; Shen, X.; Weathersby, S.; Yang, J.; Wang, X.; Meyer zu Heringdorf, F.; Sokolowski-Tinten, K.; Schlücker, S. Precision Plasmonics with Monomers and Dimers of Spherical Gold Nanoparticles: Nonequilibrium Dynamics at the Time and Space Limits. *J. Phys. Chem. C* **2019**, *123* (21), 13181–13191. <https://doi.org/10.1021/acs.jpcc.9b01007>.
- (73) Jain, P. K.; Lee, K. S.; El-Sayed, I. H.; El-Sayed, M. A. Calculated Absorption and Scattering Properties of Gold Nanoparticles of Different Size, Shape, and Composition: Applications in Biological Imaging and Biomedicine. *J. Phys. Chem. B* **2006**, *110* (14), 7238–7248. <https://doi.org/10.1021/jp057170o>.
- (74) Saviot, L. <https://saviot.cnrs.fr/mie/index.html>. <https://saviot.cnrs.fr/mie/index.html> (accessed 2022-07-21).
- (75) Halas, N. J.; Lal, S.; Chang, W.-S.; Link, S.; Nordlander, P. Plasmons in Strongly Coupled Metallic Nanostructures. *Chem. Rev.* **2011**, *111* (6), 3913–3961. <https://doi.org/10.1021/cr200061k>.
- (76) Noguez, C. Surface Plasmons on Metal Nanoparticles: The Influence of Shape and Physical Environment. *J. Phys. Chem. C* **2007**, *111* (10), 3806–3819. <https://doi.org/10.1021/jp066539m>.

- (77) Pluchery, O.; Bryche, J.-F. *An Introduction to Plasmonics*; Advanced textbooks in physics; World Scientific: New Jersey, 2023.
- (78) Rodríguez-Fernández, J.; Pérez-Juste, J.; García de Abajo, F. J.; Liz-Marzán, L. M. Seeded Growth of Submicron Au Colloids with Quadrupole Plasmon Resonance Modes. *Langmuir* **2006**, *22* (16), 7007–7010. <https://doi.org/10.1021/la060990n>.
- (79) Habib, A.; Zhu, X.; Fong, S.; Yanik, A. A. Active Plasmonic Nanoantenna: An Emerging Toolbox from Photonics to Neuroscience. *Nanophotonics* **2020**, *9* (12), 3805–3829. <https://doi.org/10.1515/nanoph-2020-0275>.
- (80) Giannini, V.; Fernández-Domínguez, A. I.; Heck, S. C.; Maier, S. A. Plasmonic Nanoantennas: Fundamentals and Their Use in Controlling the Radiative Properties of Nanoemitters. *Chem. Rev.* **2011**, *111* (6), 3888–3912. <https://doi.org/10.1021/cr1002672>.
- (81) Zamora-Perez, P.; Tsoutsis, D.; Xu, R.; Rivera_Gil, P. Hyperspectral-Enhanced Dark Field Microscopy for Single and Collective Nanoparticle Characterization in Biological Environments. *Materials* **2018**, *11* (2), 243. <https://doi.org/10.3390/ma11020243>.
- (82) Shannahan, J. H.; Sowrirajan, H.; Persaud, I.; Podila, R.; Brown, J. M. Impact of Silver and Iron Nanoparticle Exposure on Cholesterol Uptake by Macrophages. *J. Nanomater.* **2015**, *2015*, 1–12. <https://doi.org/10.1155/2015/127235>.
- (83) Zhang, Y.; He, S.; Guo, W.; Hu, Y.; Huang, J.; Mulcahy, J. R.; Wei, W. D. Surface-Plasmon-Driven Hot Electron Photochemistry. *Chem. Rev.* **2018**, *118* (6), 2927–2954. <https://doi.org/10.1021/acs.chemrev.7b00430>.
- (84) Smith, J. G.; Faucheaux, J. A.; Jain, P. K. Plasmon Resonances for Solar Energy Harvesting: A Mechanistic Outlook. *Nano Today* **2015**, *10* (1), 67–80. <https://doi.org/10.1016/j.nantod.2014.12.004>.
- (85) Tahir, M.; Tahir, B.; Amin, N. A. S. Synergistic Effect in Plasmonic Au/Ag Alloy NPs Co-Coated TiO₂ NWs toward Visible-Light Enhanced CO₂ Photoreduction to Fuels. *Appl. Catal. B Environ.* **2017**, *204*, 548–560. <https://doi.org/10.1016/j.apcatb.2016.11.062>.
- (86) Mukherjee, S.; Libisch, F.; Large, N.; Neumann, O.; Brown, L. V.; Cheng, J.; Lassiter, J. B.; Carter, E. A.; Nordlander, P.; Halas, N. J. Hot Electrons Do the Impossible: Plasmon-Induced Dissociation of H₂ on Au. *Nano Lett.* **2013**, *13* (1), 240–247. <https://doi.org/10.1021/nl303940z>.
- (87) Zheng, Z.; Tachikawa, T.; Majima, T. Plasmon-Enhanced Formic Acid Dehydrogenation Using Anisotropic Pd–Au Nanorods Studied at the Single-Particle Level. *J. Am. Chem. Soc.* **2015**, *137* (2), 948–957. <https://doi.org/10.1021/ja511719g>.
- (88) Cortés, E.; Xie, W.; Cambiasso, J.; Jermyn, A. S.; Sundararaman, R.; Narang, P.; Schlücker, S.; Maier, S. A. Plasmonic Hot Electron Transport Drives Nano-Localized Chemistry. *Nat. Commun.* **2017**, *8* (1), 14880. <https://doi.org/10.1038/ncomms14880>.
- (89) Schlücker, S. Surface-Enhanced Raman Spectroscopy: Concepts and Chemical Applications. *Angew. Chem. Int. Ed.* **2014**, *53* (19), 4756–4795. <https://doi.org/10.1002/anie.201205748>.
- (90) Verma, P. Tip-Enhanced Raman Spectroscopy: Technique and Recent Advances. *Chem. Rev.* **2017**, *117* (9), 6447–6466. <https://doi.org/10.1021/acs.chemrev.6b00821>.
- (91) Sharma, B.; Frontiera, R. R.; Henry, A.-I.; Ringe, E.; Van Duyne, R. P. SERS: Materials, Applications, and the Future. *Mater. Today* **2012**, *15* (1–2), 16–25. [https://doi.org/10.1016/S1369-7021\(12\)70017-2](https://doi.org/10.1016/S1369-7021(12)70017-2).
- (92) Zrimsek, A. B.; Chiang, N.; Mattei, M.; Zaleski, S.; McAnally, M. O.; Chapman, C. T.; Henry, A.-I.; Schatz, G. C.; Van Duyne, R. P. Single-Molecule Chemistry with Surface- and Tip-Enhanced Raman Spectroscopy. *Chem. Rev.* **2017**, *117* (11), 7583–7613. <https://doi.org/10.1021/acs.chemrev.6b00552>.

- (93) Ding, S.-Y.; Yi, J.; Li, J.-F.; Ren, B.; Wu, D.-Y.; Panneerselvam, R.; Tian, Z.-Q. Nanostructure-Based Plasmon-Enhanced Raman Spectroscopy for Surface Analysis of Materials. *Nat. Rev. Mater.* **2016**, *1* (6), 16021. <https://doi.org/10.1038/natrevmats.2016.21>.
- (94) Katsonis, N.; Kudernac, T.; Walko, M.; van der Molen, S. J.; van Wees, B. J.; Feringa, B. L. Reversible Conductance Switching of Single Diarylethenes on a Gold Surface. *Adv. Mater.* **2006**, *18* (11), 1397–1400. <https://doi.org/10.1002/adma.200600210>.
- (95) Yamaguchi, H.; Ikeda, M.; Matsuda, K.; Irie, M. Photochromism of Diarylethenes on Gold and Silver Nanoparticles. *Bull. Chem. Soc. Jpn.* **2006**, *79* (9), 1413–1419. <https://doi.org/10.1246/bcsj.79.1413>.
- (96) Ikeda, M.; Tanifuji, N.; Yamaguchi, H.; Irie, M.; Matsuda, K. Photoswitching of Conductance of Diarylethene-Au Nanoparticle Network. *Chem. Commun.* **2007**, No. 13, 1355. <https://doi.org/10.1039/b617246f>.
- (97) Dulić, D.; van der Molen, S. J.; Kudernac, T.; Jonkman, H. T.; de Jong, J. J. D.; Bowden, T. N.; van Esch, J.; Feringa, B. L.; van Wees, B. J. One-Way Optoelectronic Switching of Photochromic Molecules on Gold. *Phys. Rev. Lett.* **2003**, *91* (20), 207402. <https://doi.org/10.1103/PhysRevLett.91.207402>.
- (98) Nishi, H.; Kobatake, S. Photochromism and Optical Property of Gold Nanoparticles Covered with Low-Polydispersity Diarylethene Polymers. *Macromolecules* **2008**, *41* (11), 3995–4002. <https://doi.org/10.1021/ma702882t>.
- (99) Nishi, H.; Asahi, T.; Kobatake, S. Light-Controllable Surface Plasmon Resonance Absorption of Gold Nanoparticles Covered with Photochromic Diarylethene Polymers. *J. Phys. Chem. C* **2009**, *113* (40), 17359–17366. <https://doi.org/10.1021/jp906371k>.
- (100) Nishi, H.; Asahi, T.; Kobatake, S. Enhanced One-Photon Cycloreversion Reaction of Diarylethenes near Individual Gold Nanoparticles. *J. Phys. Chem. C* **2011**, *115* (11), 4564–4570. <https://doi.org/10.1021/jp111807k>.
- (101) Nishi, H.; Asahi, T.; Kobatake, S. Plasmonic Enhancement of Gold Nanoparticles on Photocycloreversion Reaction of Diarylethene Derivatives Depending on Particle Size, Distance from the Particle Surface, and Irradiation Wavelength. *Phys. Chem. Chem. Phys.* **2012**, *14* (14), 4898. <https://doi.org/10.1039/c2cp23820a>.
- (102) Tsuboi, Y.; Shimizu, R.; Shoji, T.; Kitamura, N.; Takase, M.; Murakoshi, K. Acceleration of a Photochromic Ring-Opening Reaction of Diarylethene Derivatives by Excitation of Localized Surface Plasmon. *J. Photochem. Photobiol. Chem.* **2011**, *221* (2–3), 250–255. <https://doi.org/10.1016/j.jphotochem.2011.04.016>.
- (103) Loumagne, M.; Midelet, C.; Doussineau, T.; Dugourd, P.; Antoine, R.; Stamboul, M.; Débarre, A.; Werts, M. H. V. Optical Extinction and Scattering Cross Sections of Plasmonic Nanoparticle Dimers in Aqueous Suspension. *Nanoscale* **2016**, *8* (12), 6555–6570. <https://doi.org/10.1039/C6NR00918B>.
- (104) Yoon, J. H.; Selbach, F.; Schumacher, L.; Jose, J.; Schlücker, S. Surface Plasmon Coupling in Dimers of Gold Nanoparticles: Experiment and Theory for Ideal (Spherical) and Nonideal (Faceted) Building Blocks. *ACS Photonics* **2019**, *6* (3), 642–648. <https://doi.org/10.1021/acsphotonics.8b01424>.
- (105) Yim, T.-J.; Wang, Y.; Zhang, X. Synthesis of a Gold Nanoparticle Dimer Plasmonic Resonator through Two-Phase-Mediated Functionalization. *Nanotechnology* **2008**, *19* (43), 435605. <https://doi.org/10.1088/0957-4484/19/43/435605>.
- (106) Esashika, K.; Ishii, R.; Tokihiro, S.; Saiki, T. Simple and Rapid Method for Homogeneous Dimer Formation of Gold Nanoparticles in a Bulk Suspension Based on van Der Waals Interactions between Alkyl Chains. *Opt. Mater. Express* **2019**, *9* (4), 1667. <https://doi.org/10.1364/OME.9.001667>.

- (107) Lereu, A. L.; Sanchez-Mosteiro, G.; Ghenuche, P.; Quidant, R.; Van Hulst, N. F. Individual Gold Dimers Investigated by Far- and near-Field Imaging. *J. Microsc.* **2008**, *229* (2), 254–258. <https://doi.org/10.1111/j.1365-2818.2008.01895.x>.
- (108) Dickreuter, S.; Kern, D. P.; Fleischer, M. Single Particle Dark-Field Spectroscopy of Spherical Dimers with down to Sub-10 Nm Gaps Fabricated by the Annealing of Nano-Pillars. *Nanophotonics* **2018**, *7* (7), 1317–1324. <https://doi.org/10.1515/nanoph-2018-0016>.
- (109) Nordlander, P.; Oubre, C.; Prodan, E.; Li, K.; Stockman, M. I. Plasmon Hybridization in Nanoparticle Dimers. *Nano Lett.* **2004**, *4* (5), 899–903. <https://doi.org/10.1021/nl049681c>.
- (110) Yang, S.-C.; Kobori, H.; He, C.-L.; Lin, M.-H.; Chen, H.-Y.; Li, C.; Kanehara, M.; Teranishi, T.; Gwo, S. Plasmon Hybridization in Individual Gold Nanocrystal Dimers: Direct Observation of Bright and Dark Modes. *Nano Lett.* **2010**, *10* (2), 632–637. <https://doi.org/10.1021/nl903693v>.
- (111) Deng, T.-S.; Parker, J.; Yifat, Y.; Shepherd, N.; Scherer, N. F. Dark Plasmon Modes in Symmetric Gold Nanoparticle Dimers Illuminated by Focused Cylindrical Vector Beams. *J. Phys. Chem. C* **2018**, *122* (48), 27662–27672. <https://doi.org/10.1021/acs.jpcc.8b10415>.
- (112) Fan, J. A.; Bao, K.; Lassiter, J. B.; Bao, J.; Halas, N. J.; Nordlander, P.; Capasso, F. Near-Normal Incidence Dark-Field Microscopy: Applications to Nanoplasmonic Spectroscopy. *Nano Lett.* **2012**, *12* (6), 2817–2821. <https://doi.org/10.1021/nl300160y>.
- (113) Romero, I.; Aizpurua, J.; Bryant, G. W.; García De Abajo, F. J. Plasmons in Nearly Touching Metallic Nanoparticles: Singular Response in the Limit of Touching Dimers. *Opt. Express* **2006**, *14* (21), 9988. <https://doi.org/10.1364/OE.14.009988>.
- (114) Lucas, L. N.; Jong, J. J. D. de; Esch, J. H. van; Kellogg, R. M.; Feringa, B. L. Syntheses of Dithienylcyclopentene Optical Molecular Switches. *Eur. J. Org. Chem.* **2003**, *2003* (1), 155–166. [https://doi.org/10.1002/1099-0690\(200301\)2003:1<155::AID-EJOC155>3.0.CO;2-S](https://doi.org/10.1002/1099-0690(200301)2003:1<155::AID-EJOC155>3.0.CO;2-S).
- (115) Browne, W. R.; de Jong, J. J. D.; Kudernac, T.; Walko, M.; Lucas, L. N.; Uchida, K.; van Esch, J. H.; Feringa, B. L. Oxidative Electrochemical Switching in Dithienylcyclopentenes, Part 2: Effect of Substitution and Asymmetry on the Efficiency and Direction of Molecular Switching and Redox Stability. *Chem. - Eur. J.* **2005**, *11* (21), 6430–6441. <https://doi.org/10.1002/chem.200500163>.
- (116) Cipolloni, M.; Ortica, F.; El Yahyaoui, A.; Heynderickx, A.; Moustrou, C.; Favaro, G. New Photochromic Symmetrical and Unsymmetrical Bis(Heteroaryl)Maleimides: A Spectrokinetic Study. *Chem. Phys.* **2009**, *358* (3), 258–264. <https://doi.org/10.1016/j.chemphys.2009.02.011>.
- (117) Turkevich, J. Colloidal Gold. Part I: Historical and Preparative Aspects, Morphology and Structure. *Gold Bull.* **1985**, *18* (3), 86–91. <https://doi.org/10.1007/BF03214690>.
- (118) Turkevich, J. Colloidal Gold. Part II: Colour, Coagulation, Adhesion, Alloying and Catalytic Properties. *Gold Bull.* **1985**, *18* (4), 125–131. <https://doi.org/10.1007/BF03214694>.
- (119) Frens, G. Controlled Nucleation for the Regulation of the Particle Size in Monodisperse Gold Suspensions. *Nat. Phys. Sci.* **1973**, *241* (105), 20–22. <https://doi.org/10.1038/physci241020a0>.
- (120) Ji, X.; Song, X.; Li, J.; Bai, Y.; Yang, W.; Peng, X. Size Control of Gold Nanocrystals in Citrate Reduction: The Third Role of Citrate. *J. Am. Chem. Soc.* **2007**, *129* (45), 13939–13948. <https://doi.org/10.1021/ja074447k>.
- (121) Bastús, N. G.; Comenge, J.; Puentes, V. Kinetically Controlled Seeded Growth Synthesis of Citrate-Stabilized Gold Nanoparticles of up to 200 Nm: Size Focusing versus Ostwald Ripening. *Langmuir* **2011**, *27* (17), 11098–11105. <https://doi.org/10.1021/la201938u>.
- (122) Haiss, W.; Thanh, N. T. K.; Aveyard, J.; Fernig, D. G. Determination of Size and Concentration of Gold Nanoparticles from UV–Vis Spectra. *Anal. Chem.* **2007**, *79* (11), 4215–4221. <https://doi.org/10.1021/ac0702084>.

- (123) Perera, G. S.; Athukorale, S. A.; Perez, F.; Pittman, C. U.; Zhang, D. Facile Displacement of Citrate Residues from Gold Nanoparticle Surfaces. *J. Colloid Interface Sci.* **2018**, *511*, 335–343. <https://doi.org/10.1016/j.jcis.2017.10.014>.
- (124) Cha, H.; Yoon, J. H.; Yoon, S. Probing Quantum Plasmon Coupling Using Gold Nanoparticle Dimers with Tunable Interparticle Distances Down to the Subnanometer Range. *ACS Nano* **2014**, *8* (8), 8554–8563. <https://doi.org/10.1021/nn5032438>.
- (125) Xie, Z.; Bâldea, I.; Oram, S.; Smith, C. E.; Frisbie, C. D. Effect of Heteroatom Substitution on Transport in Alkanedithiol-Based Molecular Tunnel Junctions: Evidence for Universal Behavior. *ACS Nano* **2017**, *11* (1), 569–578. <https://doi.org/10.1021/acsnano.6b06623>.
- (126) Ruf, L. *Adsorption Kinetics of Short Alkanethiols on Gold Nanoparticles Precipitated on Quartz Slides: A Spectrophotometric Study*; Universität Konstanz: Germany, 2021.
- (127) <https://jascoinc.com/learning-center/theory/spectroscopy/uv-vis-spectroscopy/>. <https://jascoinc.com/learning-center/theory/spectroscopy/uv-vis-spectroscopy/> (accessed 2022-07-01).
- (128) <https://jascoinc.com/learning-center/theory/spectroscopy/uv-vis-spectroscopy/instrumentation/>. <https://jascoinc.com/learning-center/theory/spectroscopy/uv-vis-spectroscopy/instrumentation/> (accessed 2022-07-01).
- (129) <https://jascoinc.com/products/spectroscopy/uv-visible-nir-spectrophotometers/specifications/>. <https://jascoinc.com/products/spectroscopy/uv-visible-nir-spectrophotometers/specifications/> (accessed 2022-07-07).
- (130) Gao, P. F.; Lei, G.; Huang, C. Z. Dark-Field Microscopy: Recent Advances in Accurate Analysis and Emerging Applications. *Anal. Chem.* **2021**, *93* (11), 4707–4726. <https://doi.org/10.1021/acs.analchem.0c04390>.
- (131) <https://www.microscopyu.com/techniques/stereomicroscopy/darkfield-illumination>. <https://www.microscopyu.com/techniques/stereomicroscopy/darkfield-illumination> (accessed 2022-07-04).
- (132) <https://www.edmundoptics.com/knowledge-center/application-notes/microscopy/optical-microscopy-application-darkfield-illumination/>. <https://www.edmundoptics.com/knowledge-center/application-notes/microscopy/optical-microscopy-application-darkfield-illumination/> (accessed 2022-07-04).
- (133) Shere, L.; Zhang, Z. J.; Preece, J. A. Application of Atomic Force Microscopy in Formulation Engineering. *Johns. Matthey Technol. Rev.* **2018**, *62* (4), 438–452. <https://doi.org/10.1595/205651318X15342609861275>.
- (134) Villarreal, E.; Li, G. G.; Zhang, Q.; Fu, X.; Wang, H. Nanoscale Surface Curvature Effects on Ligand–Nanoparticle Interactions: A Plasmon-Enhanced Spectroscopic Study of Thiolated Ligand Adsorption, Desorption, and Exchange on Gold Nanoparticles. *Nano Lett.* **2017**, *17* (7), 4443–4452. <https://doi.org/10.1021/acs.nanolett.7b01593>.
- (135) Kimling, J.; Maier, M.; Okenve, B.; Kotaidis, V.; Ballot, H.; Plech, A. Turkevich Method for Gold Nanoparticle Synthesis Revisited. *J. Phys. Chem. B* **2006**, *110* (32), 15700–15707. <https://doi.org/10.1021/jp061667w>.
- (136) Park, J.-W.; Shumaker-Parry, J. S. Structural Study of Citrate Layers on Gold Nanoparticles: Role of Intermolecular Interactions in Stabilizing Nanoparticles. *J. Am. Chem. Soc.* **2014**, *136* (5), 1907–1921. <https://doi.org/10.1021/ja4097384>.
- (137) Basu, S.; Ghosh, S. K.; Kundu, S.; Panigrahi, S.; Praharaj, S.; Pande, S.; Jana, S.; Pal, T. Biomolecule Induced Nanoparticle Aggregation: Effect of Particle Size on Interparticle Coupling. *J. Colloid Interface Sci.* **2007**, *313* (2), 724–734. <https://doi.org/10.1016/j.jcis.2007.04.069>.

- (138) Bard, A.; Rondon, R.; Marquez, D. T.; Lanterna, A. E.; Scaiano, J. C. How Fast Can Thiols Bind to the Gold Nanoparticle Surface? *Photochem. Photobiol.* **2018**, *94* (6), 1109–1115. <https://doi.org/10.1111/php.13010>.
- (139) Kassam, A.; Bremner, G.; Clark, B.; Ulibarri, G.; Lennox, R. B. Place Exchange Reactions of Alkyl Thiols on Gold Nanoparticles. *J. Am. Chem. Soc.* **2006**, *128* (11), 3476–3477. <https://doi.org/10.1021/ja057091q>.
- (140) Wang, Y.; Zeiri, O.; Neyman, A.; Stellacci, F.; Weinstock, I. A. Nucleation and Island Growth of Alkanethiolate Ligand Domains on Gold Nanoparticles. *ACS Nano* **2012**, *6* (1), 629–640. <https://doi.org/10.1021/nn204078w>.
- (141) Englebienne, P.; Verhas, M.; Van Hoonacker, A. High-Throughput Screening Using the Surface Plasmon Resonance Effect of Colloidal Gold Nanoparticles. *The Analyst* **2001**, *126* (10), 1645–1651. <https://doi.org/10.1039/b105252g>.
- (142) Sardar, R.; Funston, A. M.; Mulvaney, P.; Murray, R. W. Gold Nanoparticles: Past, Present, and Future. *Langmuir* **2009**, *25* (24), 13840–13851. <https://doi.org/10.1021/la9019475>.
- (143) Pluchery, O.; Caillard, L.; Dollfus, P.; Chabal, Y. J. Gold Nanoparticles on Functionalized Silicon Substrate under Coulomb Blockade Regime: An Experimental and Theoretical Investigation. *J. Phys. Chem. B* **2018**, *122* (2), 897–903. <https://doi.org/10.1021/acs.jpcc.7b06979>.
- (144) Unser, S.; Bruzas, I.; He, J.; Sagle, L. Localized Surface Plasmon Resonance Biosensing: Current Challenges and Approaches. *Sensors* **2015**, *15* (7), 15684–15716. <https://doi.org/10.3390/s150715684>.
- (145) Stuart, D. A.; Haes, A. J.; Yonzon, C. R.; Hicks, E. M.; Van Duyne, R. P. Biological Applications of Localised Surface Plasmonic Phenomena. *IEE Proc. - Nanobiotechnology* **2005**, *152* (1), 13. <https://doi.org/10.1049/ip-nbt:20045012>.
- (146) Zahid, A. A. S. M.; Hanif, Md. A.; Lee, I.; Islam, Md. A.; Hahn, J. R. Effect of Amino, Hydroxyl, and Carboxyl Terminal Groups of Alkyl Chains of Self-assembled Monolayers on the Adsorption Pattern of Gold Nanoparticles. *Surf. Interface Anal.* **2019**, *51* (11), 1102–1112. <https://doi.org/10.1002/sia.6697>.
- (147) Taladriz-Blanco, P.; Buurma, N. J.; Rodríguez-Lorenzo, L.; Pérez-Juste, J.; Liz-Marzán, L. M.; Hervés, P. Reversible Assembly of Metal Nanoparticles Induced by Penicillamine. Dynamic Formation of SERS Hot Spots. *J. Mater. Chem.* **2011**, *21* (42), 16880. <https://doi.org/10.1039/c1jm12175h>.
- (148) Stein, B.; Zopes, D.; Schmutte, M.; Schneider, R.; Mohsen, A.; Goroncy, C.; Mathur, S.; Graf, C. Kinetics of Aggregation and Growth Processes of PEG-Stabilised Mono- and Multivalent Gold Nanoparticles in Highly Concentrated Halide Solutions. *Faraday Discuss.* **2015**, *181*, 85–102. <https://doi.org/10.1039/C5FD00024F>.
- (149) Vanderkooy, A.; Chen, Y.; Gonzaga, F.; Brook, M. A. Silica Shell/Gold Core Nanoparticles: Correlating Shell Thickness with the Plasmonic Red Shift upon Aggregation. *ACS Appl. Mater. Interfaces* **2011**, *3* (10), 3942–3947. <https://doi.org/10.1021/am200825f>.
- (150) Haes, A. J.; Van Duyne, R. P. A Nanoscale Optical Biosensor: Sensitivity and Selectivity of an Approach Based on the Localized Surface Plasmon Resonance Spectroscopy of Triangular Silver Nanoparticles. *J. Am. Chem. Soc.* **2002**, *124* (35), 10596–10604. <https://doi.org/10.1021/ja020393x>.
- (151) Dahlin, A. B.; Tegenfeldt, J. O.; Höök, F. Improving the Instrumental Resolution of Sensors Based on Localized Surface Plasmon Resonance. *Anal. Chem.* **2006**, *78* (13), 4416–4423. <https://doi.org/10.1021/ac0601967>.
- (152) Liu, X.; Atwater, M.; Wang, J.; Huo, Q. Extinction Coefficient of Gold Nanoparticles with Different Sizes and Different Capping Ligands. *Colloids Surf. B Biointerfaces* **2007**, *58* (1), 3–7. <https://doi.org/10.1016/j.colsurfb.2006.08.005>.

- (153) Vericat, C.; Vela, M. E.; Salvarezza, R. C. Self-Assembled Monolayers of Alkanethiols on Au(111): Surface Structures, Defects and Dynamics. *Phys. Chem. Chem. Phys.* **2005**, *7* (18), 3258. <https://doi.org/10.1039/b505903h>.
- (154) Badia, A.; Singh, S.; Demers, L.; Cuccia, L.; Brown, G. R.; Lennox, R. B. Self-Assembled Monolayers on Gold Nanoparticles. *Chem. - Eur. J.* **1996**, *2* (3), 359–363. <https://doi.org/10.1002/chem.19960020318>.
- (155) Chen, S.; Kimura, K. Synthesis and Characterization of Carboxylate-Modified Gold Nanoparticle Powders Dispersible in Water. *Langmuir* **1999**, *15* (4), 1075–1082. <https://doi.org/10.1021/la9812828>.
- (156) Hinterwirth, H.; Kappel, S.; Waitz, T.; Prohaska, T.; Lindner, W.; Lämmerhofer, M. Quantifying Thiol Ligand Density of Self-Assembled Monolayers on Gold Nanoparticles by Inductively Coupled Plasma–Mass Spectrometry. *ACS Nano* **2013**, *7* (2), 1129–1136. <https://doi.org/10.1021/nn306024a>.
- (157) <https://bichromatics.com/calculator/>.
- (158) Cho, C.-Y.; Lee, S.-J.; Song, J.-H.; Hong, S.-H.; Lee, S.-M.; Cho, Y.-H.; Park, S.-J. Enhanced Optical Output Power of Green Light-Emitting Diodes by Surface Plasmon of Gold Nanoparticles. *Appl. Phys. Lett.* **2011**, *98* (5), 051106. <https://doi.org/10.1063/1.3552968>.
- (159) Goldmann, C.; Lazzari, R.; Paquez, X.; Boissière, C.; Ribot, F.; Sanchez, C.; Chanéac, C.; Portehault, D. Charge Transfer at Hybrid Interfaces: Plasmonics of Aromatic Thiol-Capped Gold Nanoparticles. *ACS Nano* **2015**, *9* (7), 7572–7582. <https://doi.org/10.1021/acsnano.5b02864>.
- (160) Sannomiya, T.; Dermutz, H.; Hafner, C.; Vörös, J.; Dahlin, A. B. Electrochemistry on a Localized Surface Plasmon Resonance Sensor. *Langmuir* **2010**, *26* (10), 7619–7626. <https://doi.org/10.1021/la9042342>.
- (161) Pollitt, M. J.; Buckton, G.; Piper, R.; Brocchini, S. Measuring Antibody Coatings on Gold Nanoparticles by Optical Spectroscopy. *RSC Adv.* **2015**, *5* (31), 24521–24527. <https://doi.org/10.1039/C4RA15661G>.
- (162) Messersmith, R. E.; Nusz, G. J.; Reed, S. M. Using the Localized Surface Plasmon Resonance of Gold Nanoparticles To Monitor Lipid Membrane Assembly and Protein Binding. *J. Phys. Chem. C* **2013**, *117* (50), 26725–26733. <https://doi.org/10.1021/jp406013q>.
- (163) Novotny, L.; Hecht, B. *Principles of Nano-Optics*, 2nd ed.; Cambridge University Press: Cambridge, 2012.
- (164) Rodríguez-Fernández, J.; Pérez-Juste, J.; Liz-Marzán, L. M. Seeded Growth of Submicron Au Colloids with Quadrupole Plasmon Resonance Modes. 4.
- (165) Maxwell-Garnett, J. C. XII. Colours in Metal Glasses and in Metallic Films. *Philos. Trans. R. Soc. Lond. Ser. Contain. Pap. Math. Phys. Character* **1904**, *203* (359–371), 385–420. <https://doi.org/10.1098/rsta.1904.0024>.
- (166) Techane, S. D.; Gamble, L. J.; Castner, D. G. Multitechnique Characterization of Self-Assembled Carboxylic Acid-Terminated Alkanethiol Monolayers on Nanoparticle and Flat Gold Surfaces. *J. Phys. Chem. C* **2011**, *115* (19), 9432–9441. <https://doi.org/10.1021/jp201213g>.
- (167) Pan, W.; Durning, C. J.; Turro, N. J. Kinetics of Alkanethiol Adsorption on Gold. *Langmuir* **1996**, *12* (18), 4469–4473. <https://doi.org/10.1021/la9408634>.
- (168) Swenson, H.; Stadie, N. P. Langmuir's Theory of Adsorption: A Centennial Review. *Langmuir* **2019**, *35* (16), 5409–5426. <https://doi.org/10.1021/acs.langmuir.9b00154>.
- (169) Cárdenas, M.; Barauskas, J.; Schillén, K.; Brennan, J. L.; Brust, M.; Nylander, T. Thiol-Specific and Nonspecific Interactions between DNA and Gold Nanoparticles. *Langmuir* **2006**, *22* (7), 3294–3299. <https://doi.org/10.1021/la0530438>.

- (170) Damos, F. S.; Luz, R. C. S.; Kubota, L. T. Determination of Thickness, Dielectric Constant of Thiol Films, and Kinetics of Adsorption Using Surface Plasmon Resonance. *Langmuir* **2005**, *21* (2), 602–609. <https://doi.org/10.1021/la0487038>.
- (171) Herder, M.; Schmidt, B. M.; Grubert, L.; Pätzelt, M.; Schwarz, J.; Hecht, S. Improving the Fatigue Resistance of Diarylethene Switches. *J. Am. Chem. Soc.* **2015**, *137* (7), 2738–2747. <https://doi.org/10.1021/ja513027s>.
- (172) Oplachko, M. V.; Smolentsev, A. B.; Magin, I. M.; Pozdnyakov, I. P.; Nichiporenko, V. A.; Grivin, V. P.; Plyusnin, V. F.; Vyazovkin, V. V.; Yanshole, V. V.; Parkhats, M. V.; Yadykov, A. V.; Shirinian, V. Z.; Glebov, E. M. Mechanism of Photochromic Transformations and Photodegradation of an Asymmetrical 2,3-Diarylcyclopentenone. *Phys. Chem. Chem. Phys.* **2020**, *22* (9), 5220–5228. <https://doi.org/10.1039/C9CP05744G>.
- (173) Ern, J.; Bens, A. T.; Martin, H.-D.; Mukamel, S.; Schmid, D.; Tretiak, S.; Tsiper, E.; Kryschi, C. Reaction Dynamics of Photochromic Dithienylethene Derivatives. *Chem. Phys.* **1999**, *246* (1–3), 115–125. [https://doi.org/10.1016/S0301-0104\(99\)00183-4](https://doi.org/10.1016/S0301-0104(99)00183-4).
- (174) Ishibashi, Y.; Fujiwara, M.; Umesato, T.; Saito, H.; Kobatake, S.; Irie, M.; Miyasaka, H. Cyclization Reaction Dynamics of a Photochromic Diarylethene Derivative as Revealed by Femtosecond to Microsecond Time-Resolved Spectroscopy. *J. Phys. Chem. C* **2011**, *115* (10), 4265–4272. <https://doi.org/10.1021/jp112370a>.
- (175) Hamdi, I.; Buntinx, G.; Perrier, A.; Devos, O.; Jaïdane, N.; Delbaere, S.; Tiwari, A. K.; Dubois, J.; Takeshita, M.; Wada, Y.; Aloïse, S. New Insights into the Photoswitching Mechanisms of Normal Dithienylethenes. *Phys. Chem. Chem. Phys.* **2016**, *18* (40), 28091–28100. <https://doi.org/10.1039/C6CP03471C>.
- (176) Jong, J. J. D. de; Lucas, L. N.; Hania, R.; Pugzlys, A.; Kellogg, R. M.; Feringa, B. L.; Duppen, K.; Esch, J. H. van. Photochromic Properties of Perhydro- and Perfluorodithienylcyclopentene Molecular Switches. *Eur. J. Org. Chem.* **2003**, *2003* (10), 1887–1893. <https://doi.org/10.1002/ejoc.200200719>.
- (177) Aloïse, S.; Sliwa, M.; Pawlowska, Z.; Réhault, J.; Dubois, J.; Poizat, O.; Buntinx, G.; Perrier, A.; Maurel, F.; Yamaguchi, S.; Takeshita, M. Bridged Photochromic Diarylethenes Investigated by Ultrafast Absorption Spectroscopy: Evidence for Two Distinct Photocyclization Pathways. *J. Am. Chem. Soc.* **2010**, *132* (21), 7379–7390. <https://doi.org/10.1021/ja910813x>.
- (178) Higashiguchi, K.; Matsuda, K.; Kobatake, S.; Yamada, T.; Kawai, T.; Irie, M. Fatigue Mechanism of Photochromic 1,2-Bis(2,5-Dimethyl-3-Thienyl)Perfluorocyclopentene. *Bull. Chem. Soc. Jpn.* **2000**, *73* (10), 2389–2394. <https://doi.org/10.1246/bcsj.73.2389>.
- (179) Irie, M.; Lifka, T.; Uchida, K.; Kobatake, S.; Shindo, Y. Fatigue Resistant Properties of Photochromic Dithienylethenes: By-Product Formation. *Chem. Commun.* **1999**, No. 8, 747–750. <https://doi.org/10.1039/a809410a>.
- (180) Seiler, A. *Photokinetics of Photochromic Perfluorocyclopentene Difurylethene in Solution*; Universität Konstanz: Germany, 2021.
- (181) Delbaere, S.; Vermeersch, G.; Micheau, J.-C. Quantitative Analysis of the Dynamic Behaviour of Photochromic Systems. *J. Photochem. Photobiol. C Photochem. Rev.* **2011**, *12* (2), 74–105. <https://doi.org/10.1016/j.jphotochemrev.2011.05.004>.
- (182) Kudernac, T.; Kobayashi, T.; Uyama, A.; Uchida, K.; Nakamura, S.; Feringa, B. L. Tuning the Temperature Dependence for Switching in Dithienylethene Photochromic Switches. *J. Phys. Chem. A* **2013**, *117* (34), 8222–8229. <https://doi.org/10.1021/jp404924q>.
- (183) Okuno, K.; Shigeta, Y.; Kishi, R.; Nakano, M. Theoretical Design of Solvatochromism Switching by Photochromic Reactions Using Donor–Acceptor Disubstituted Diarylethene Derivatives with Oxidized Thiophene Rings. *Phys. Chem. Chem. Phys.* **2015**, *17* (9), 6484–6494. <https://doi.org/10.1039/C4CP05946H>.

- (184) Glebov, E. M.; Semionova, V. V.; Lazareva, S. K.; Smolentsev, A. B.; Fedunov, R. G.; Shirinian, V. Z.; Lvov, A. G. Solvent Dependent Photoswitching and Emission of Diarylethenes with a π -Conjugated Push-Pull System. *J. Lumin.* **2022**, *241*, 118472. <https://doi.org/10.1016/j.jlumin.2021.118472>.
- (185) Sherwood, J. R. *Bio-Based Solvents for Organic Synthesis*, University of York, England, 2013.
- (186) Snegir, S. V.; Khodko, A. A.; Sysoiev, D.; Lacaze, E.; Pluchery, O.; Huhn, T. Optical Properties of Gold Nanoparticles Decorated with Furan-Based Diarylethene Photochromic Molecules. *J. Photochem. Photobiol. Chem.* **2017**, *342*, 78–84. <https://doi.org/10.1016/j.jphotochem.2017.04.003>.
- (187) Toyama, T.; Higashiguchi, K.; Nakamura, T.; Yamaguchi, H.; Kusaka, E.; Matsuda, K. Photoswitching of Conductance of Diarylethene–Gold Nanoparticle Network Based on the Alteration of π -Conjugation. *J. Phys. Chem. Lett.* **2016**, *7* (11), 2113–2118. <https://doi.org/10.1021/acs.jpcclett.6b00993>.
- (188) Kronemeijer, A. J.; Akkerman, H. B.; Kudernac, T.; van Wees, B. J.; Feringa, B. L.; Blom, P. W. M.; de Boer, B. Reversible Conductance Switching in Molecular Devices. *Adv. Mater.* **2008**, *20* (8), 1467–1473. <https://doi.org/10.1002/adma.200800053>.
- (189) Arramel; Pijper, T. C.; Kudernac, T.; Katsonis, N.; van der Maas, M.; Feringa, B. L.; van Wees, B. J. Electronic Properties of Individual Diarylethene Molecules Studied Using Scanning Tunneling Spectroscopy. *J. Appl. Phys.* **2012**, *111* (8), 083716. <https://doi.org/10.1063/1.4706568>.
- (190) Liu, Z.; Wang, H. I.; Narita, A.; Chen, Q.; Mics, Z.; Turchinovich, D.; Kläui, M.; Bonn, M.; Müllen, K. Photoswitchable Micro-Supercapacitor Based on a Diarylethene-Graphene Composite Film. *J. Am. Chem. Soc.* **2017**, *139* (28), 9443–9446. <https://doi.org/10.1021/jacs.7b04491>.
- (191) Wang, Q.; Frisch, J.; Herder, M.; Hecht, S.; Koch, N. Electronic Properties of Optically Switchable Photochromic Diarylethene Molecules at the Interface with Organic Semiconductors. *ChemPhysChem* **2017**, *18* (7), 722–727. <https://doi.org/10.1002/cphc.201601442>.
- (192) Hnid, I.; Frath, D.; Lafalet, F.; Sun, X.; Lacroix, J.-C. Highly Efficient Photoswitch in Diarylethene-Based Molecular Junctions. *J. Am. Chem. Soc.* **2020**, *142* (17), 7732–7736. <https://doi.org/10.1021/jacs.0c01213>.
- (193) Seferos, D. S.; Blum, A. S.; Kushmerick, J. G.; Bazan, G. C. Single-Molecule Charge-Transport Measurements That Reveal Technique-Dependent Perturbations. *J. Am. Chem. Soc.* **2006**, *128* (34), 11260–11267. <https://doi.org/10.1021/ja062898j>.
- (194) Chen, H.; Ming, T.; Zhang, S.; Jin, Z.; Yang, B.; Wang, J. Effect of the Dielectric Properties of Substrates on the Scattering Patterns of Gold Nanorods. *ACS Nano* **2011**, *5* (6), 4865–4877. <https://doi.org/10.1021/nn200951c>.
- (195) Pini, V.; Kosaka, P. M.; Ruz, J. J.; Malvar, O.; Encinar, M.; Tamayo, J.; Calleja, M. Spatially Multiplexed Dark-Field Microspectrophotometry for Nanoplasmonics. *Sci. Rep.* **2016**, *6* (1), 22836. <https://doi.org/10.1038/srep22836>.
- (196) Liu, X.; Wu, Z.; Zhang, Q.; Zhao, W.; Zong, C.; Gai, H. Single Gold Nanoparticle-Based Colorimetric Detection of Picomolar Mercury Ion with Dark-Field Microscopy. *Anal. Chem.* **2016**, *88* (4), 2119–2124. <https://doi.org/10.1021/acs.analchem.5b03653>.
- (197) Olmon, R. L.; Slovick, B.; Johnson, T. W.; Shelton, D.; Oh, S.-H.; Boreman, G. D.; Raschke, M. B. Optical Dielectric Function of Gold. *Phys. Rev. B* **2012**, *86* (23), 235147. <https://doi.org/10.1103/PhysRevB.86.235147>.
- (198) Kreibig, U.; Vollmer, M. *Optical Properties of Metal Clusters*; Springer series in materials science; Springer: Berlin ; New York, 1995.

- (199) Hassan, S. Z.; Yu, S. H.; So, C.; Moon, D.; Chung, D. S. End-Functionalization of Diarylethene for Opto-Electronic Switching with High Fatigue Resistance. *Chem. Mater.* **2021**, *33* (1), 403–412. <https://doi.org/10.1021/acs.chemmater.0c04219>.
- (200) Li, C. A Trident Dithienylethene-Perylenemonoimide Dyad with Super Fluorescence Switching Speed and Ratio. *Nat. Commun.* **2014**, *11*.
- (201) Fukaminato, T.; Doi, T.; Tamaoki, N.; Okuno, K.; Ishibashi, Y.; Miyasaka, H.; Irie, M. Single-Molecule Fluorescence Photoswitching of a Diarylethene–Perylenebisimide Dyad: Non-Destructive Fluorescence Readout. *J. Am. Chem. Soc.* **2011**, *133* (13), 4984–4990. <https://doi.org/10.1021/ja110686t>.
- (202) Fihey, A.; Le Guennic, B.; Jacquemin, D. Toward an Enhancement of the Photoactivity of Multiphotochromic Dimers Using Plasmon Resonance: A Theoretical Study. *J. Phys. Chem. Lett.* **2015**, *6* (15), 3067–3073. <https://doi.org/10.1021/acs.jpcclett.5b01333>.
- (203) Yang, Y.; Gu, C.; Li, J. Sub-5 Nm Metal Nanogaps: Physical Properties, Fabrication Methods, and Device Applications. **2019**, *27*.
- (204) Bléteau, P.; Bastide, M.; Gam-Derouich, S.; Martin, P.; Bonnet, R.; Lacroix, J.-C. Plasmon-Induced Grafting in the Gap of Gold Nanoparticle Dimers for Plasmonic Molecular Junctions. *ACS Appl. Nano Mater.* **2020**, *3* (8), 7789–7794. <https://doi.org/10.1021/acsanm.0c01334>.
- (205) Acimovic, S. S.; Kreuzer, M. P.; González, M. U.; Quidant, R. Plasmon Near-Field Coupling in Metal Dimers as a Step toward Single-Molecule Sensing. **2009**, *3* (5), 7.
- (206) Pluchery, O.; Chabal, Y. J.; Opila, R. L. Wet Chemical Cleaning of InP Surfaces Investigated by *in Situ* and *Ex Situ* Infrared Spectroscopy. *J. Appl. Phys.* **2003**, *94* (4), 2707–2715. <https://doi.org/10.1063/1.1596719>.
- (207) Busch, B. W.; Pluchery, O.; Chabal, Y. J.; Muller, D. A.; Opila, R. L.; Raynien Kwo, J.; Garfunkel, E. Materials Characterization of Alternative Gate Dielectrics. *MRS Bull.* **2002**, *27* (3), 206–211. <https://doi.org/10.1557/mrs2002.72>.

Appendix

Chapter 1

A.1.1 Azobenzenes

Similarly to what is observed for diarylethenes, the UV-visible absorption spectrum of an azobenzene (AB) exhibit two main bands. One in the near UV region corresponding to a $\pi \rightarrow \pi^*$ transition commonly observed in aromatic hydrocarbons like stilbene, and one in the visible region corresponding to a $n \rightarrow \pi^*$ involving the free electron pairs of the nitrogen atoms. This second transition prevents from further comparison with other aromatic hydrocarbons like stilbene regarding the photoisomerization mechanism. The cis-trans photoisomerization of azobenzenes occurs upon excitation triggering $S_0 \rightarrow S_1$ and $S_0 \rightarrow S_2$ transitions, while the trans-cis photoisomerization occurs upon excitation triggering $S_0 \rightarrow S_1$ or $S_0 \rightarrow S_2$ transitions. Unlike for diarylethenes, the sum of the quantum yields of both isomerization reactions is not equal to one, meaning that several isomerization channels exist²⁵.

There are three main classes of azobenzenes (or azo-based compounds) differing by the energy of their electronic states which depends on the substituents present on their aromatic rings. These energy differences explain that the transitions do not result in the same absorbance bands on the UV-visible spectrum which in turn explain why each class has a different color. The first and most simple class is the azobenzene type (Ar-N=N-Ar) azobenzenes, very similar to the elementary azobenzene (Ph-N=N-Ph). The $\pi \rightarrow \pi^*$ band on their UV-visible absorption spectrum is very intense, while the $n \rightarrow \pi^*$ is weak, their dominant color is yellow. The second class is the aminoazobenzene type (ortho- or para- X-C₆H₄-N=N-Ar, with X an electron-donor substituent), their two absorbance bands are close from one another (the $\pi \rightarrow \pi^*$ band is slightly redshifted), their main color is orange. The third class is the pseudo-stilbene type (X-C₆H₄-N=N-C₆H₄-Y, with X and Y respectively an electron-donor and an electron-acceptor substituent, these azobenzenes are push-pull systems), the $\pi \rightarrow \pi^*$ band is largely redshifted and appears at a higher wavelength than the $n \rightarrow \pi^*$ band^{25,32}.

The photoisomerization from trans to cis induces a reinforcement of the color intensity, well translated on the UV-visible spectrum. The one of the trans isomer exhibit an intense $\pi \rightarrow \pi^*$ band (with an order of magnitude of 10^4 M.cm⁻¹ for its associated molar absorption coefficient, it is a permitted transition) and a weak $n \rightarrow \pi^*$ band (with an associated molar

absorption coefficient around $400 \text{ M}\cdot\text{cm}^{-1}$, it is a forbidden transition). Conversely, the $n \rightarrow \pi^*$ band is more intense on the spectrum with an associated molar absorption coefficient around $1500 \text{ M}\cdot\text{cm}^{-1}$) of the cis isomer for which this transition is permitted, while the $\pi \rightarrow \pi^*$ band is blueshifted (hypsochromic effect) and its intensity is lower (with an associated molar absorption coefficient around $10^3 \text{ M}\cdot\text{cm}^{-1}$)²⁵. These differences indicate that a photoconversion is possible since the two forms do not respond to the same wavelength. Upon irradiation with a certain wavelength, a photostationary state is reached corresponding to a mix of a certain population of the cis and another of the trans isomer. The response of the molecule to a certain wavelength depends on the substituents born by the aryl groups. It should be noted that the switching mechanism of azobenzenes is not precisely established although it was extensively studied. Bandara et Burdette³² reviewed the studies on the isomerization mechanism of the three classes of azobenzenes and the factors that affect it and its quantum yield. In a few words, the cis to trans isomerization would either occur through a reversion mechanism: the free electronic doublet of each nitrogen atom are able to trigger a $n \rightarrow \pi^*$ ($S_0 \rightarrow S_1$) transition involving the reversal of the one of the N-C bonds (see Figure A.1.1.1), or a rotation mechanism with a $\pi \rightarrow \pi^*$ ($S_0 \rightarrow S_1$) transition leading to a rotation of the N=N bond^{25,32} (see Figure A.1.1.1).

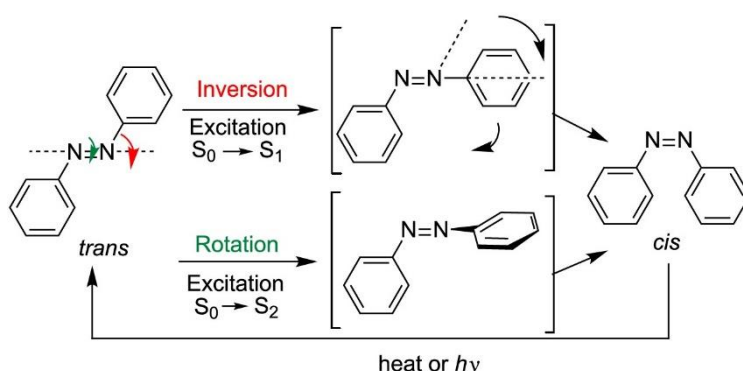


Figure A.1.1.1: Two types of isomerization mechanism hypothesized for azobenzenes. Reprinted from²⁵.

The applications of azobenzenes are plenty and present in various domains. Biology, with the photocontrol of biological processes by introduction of an azobenzene in a molecular system with a biological function; biomedicine, by using ABs for drug delivery; data storage, Stoddart's group developed rotaxane-based bistable memories, smart polymer materials, such as a photo-oriented polymer able to convert luminous energy to mechanical energy; and fundamental chemistry, with photoactive Bronsted bases (bases whose pKa is modified by light irradiation) illustrating the possibility to photocontrol the reactivity (through the conformation)

of a molecule²⁵. Many azobenzene-based molecular devices were fabricated by supramolecular chemistry. A large number of examples are given in the review of Merino et Ribargorda²⁵. A molecular lift (over 7 Å) made of a p-mercaptophenyl terminated (on one side) azobenzenes SAM on an Au(111) layer, the collective response of all AB molecules is quite strong, able to lift a Hg drop deposited on the SAM (work of Ferri et al.). The lift also acted like an electrical photoswitch, a difference of the current density between the Au layer and the Hg drop of one order of magnitude was measured according to the cis or trans configuration of the AB²⁵.

A.1.2 Spiroyrans

The first fully reversible thermochromic i.e., that changes color upon heating, spiroyrans are the di-β-naphtospiroyrans (1926), thermochromism was then observed in the naphto- and indolino- derivatives of the first spiroyrans (dibenzospiroyrans). These derivatives include the benzo-β-naphtospiroyrans, the benzo-β-naphtaisospiroyrans, the di-β-naphtospiroyrans, the indolino-β-naphtospiroyrans, and the indolinobenzospiroyrans. In addition, the derivatives of the isospiroyrans were synthesized, di-β-naphtospiroyrans, di-α-β-naphtospiroyrans, xanthospiroyrans, thioxanthospiroyrans, and acridinospiroyrans. Finally, combined derivatives such as xanthonaphthospiroyrans and benzoxanthospiroyrans were synthesized. All the previously mentioned derivatives are also acidochromic. Following Wizinger observation that the thermochromism of benzopyrans came from the introduction of an auxiliary indolino group to polarize the spiro center, the general characteristic of the thermochromic and acidochromic molecules were determined i.e. the change of color upon heating and the formation of salt in acidic medium. Heating triggers the ring-opening thermal reaction, the pyran parts separated by the spiro center are ionized which opens a radical dissociation pathway. The C-O bond cleaves, and the molecule takes its merocyanine form with its zwitterionic and quinoidal resonance forms to stabilize it. Depending on factors such as the nature of the heterocycle, the substituents on the pyran rings, and the solvent, either one or the other resonance form is the one that better describes the true structure of the molecule. Most of the time, it is the ionic form, furthermore, a balanced charge delocalization means a greater stability of the open form, underlining the importance of selecting the right substituents^{34,36}.

The ring-opening tendency is what defines the possibility to have thermochromism, the different classes of spiroyrans having different propension to ring-opening. It obeys to different rules; the first one is that the spiroyrans molecule must possess at least a naphtospiroyrans as pyran moiety unless its heterocyclic ring grants a large enough

stabilization of the delocalized charge (it is the case for the indolinobenzospiropyran). The second one is that the electron releasing capacity of the heterocyclic ring must be high enough, it can be supported by the stabilization of the phenolate brought by the appropriate substituents on the pyran rings. The third one regards the planarity of the merocyanine form, dictated by steric hinderance of the substituents and the presence of an H on the C'3 (intramolecular stabilization via interaction with the phenol group in the open form). When ring-opening is energetically favorable and the resonance structures of the open form are accessible i.e., sterically unhindered and stabilized (intramolecular interaction): the spirocyanine can adopt many different conformations and isomers. When the merocyanine form is planar, rotations around some of its bonds lead to thermally accessible states at different energy levels. In particular, cisoid and transoid isomers located at different energy levels exist. At a given temperature, a weighted average of all thermally accessible colored isomers is observed. To access all the isomers, one must increase the temperature, in total, there are eight merocyanine conformers and isomers, Z or E configuration at the α , β , and γ bonds. Note that some conformations and rotations suppress photochemical and thermal isomerization. The molecular structure can be blocked in a configuration using molecular organic frameworks (MOFs) or covalent organic frameworks (COFs) or a specific solvent³⁴.

The indolinobenzospiropyran and their derivatives exhibit reversible photochromism. The first photochromic one is the 1,3,3-trimethylindolinobenzospiropyran whose photochromism was discovered in 1952 (12 years after its thermochromism) by Fischer and Hirschberg. They demonstrated the overcoming of thermal barrier separating the closed spiro form and the open merocyanine form by photoexcitation. The switching induced by two photons absorption with visible and NIR light was then demonstrated in 1989. The first observation of photochromism in some of these spirocyanines even where thermochromism is suppressed was rendered possible by the high enough thermal barrier to reversion to the spiro form even where thermochromism is prevented. The thermally activated nature of the ring closure (and subsequent bleaching) required to work at low temperatures to trigger photoswitching to merocyanine isomers. Later, by taking advantage of the stabilization effects provided by integrations of certain substituents, the four transoid species involved in the reversible photoconversion could be directly observed. The photostationary state of spirocyanines corresponds to a mix of the transoid merocyanine (open, more energetically stable) isomers and spiro (closed, less energetically stable) isomers that were not converted³⁴.

The steps of the photoswitching mechanism, illustrated in Figure A.1.2.1, of spiropyrans are the following, first, subsequently to the luminous excitation to the S_1 state, the spiropyran undergoes a $\pi \rightarrow \pi^*$ transition that increases its energy via a spontaneous hybridization change (it loses its double bond character). Secondly, the cleavage of the $C_{\text{spiro}}\text{-O}$ bond in the excited state ${}^1\text{SP}^*$ (S_1) occurs. Then, there is either pericyclic recombination with the concurrent ring opening which yields the ground state CCC-MC that quickly relaxes back to the ring-closed form, or radiationless deactivation of the CCC-1MC* (or species X) to the ground state, yielding either the cisoid (thermally unstable) or transoid (thermally stable) isomer of the open merocyanine form. More specifically, species X, which has a perpendicular orientation undergoes a “free rotor” effect while it travels along the PES $\pi \rightarrow \pi^*$. This effect twists the molecule in a strain-relieving way, placing it in a geometry (XXX) favorable for the radiationless deactivation that occurs once the molecule reaches at the conical intersection. However, the cleavage of the bond in the excited state lowers the energy before any rotation can occur (due to the much faster electronic motion, up to 10^4 , than nuclear motion), with radiationless intersystem crossing to “species X” (with the structure of the CCC, but a perpendicular orientation). Species X therefore either undergoes recombination (electronic motion - reformation of the $C_{\text{spiro}}\text{-O}$ bond) by pericyclic arrangement followed by deexcitation to the ground state of the closed-ring form, or rotation around the $\pi \rightarrow \pi^*$ system after traveling along the PES of the excited state (nuclear motion) to a conical intersection (CI) with the ground state of the open form where radiationless deactivation occurs. Visible light excitation induces the photoreversion of the (non-substituted) indolinobenzomerocyanines, as well as fluorescence. Note that indolinonaphthomerocyanines were the first spiropyrans for which reversible photoswitching was observed. For both the naphtho- and benzospiryran it was demonstrated later, as well as the fact that the photoreversion reaction also occurs via the singlet excited state manifold. Regarding the quantum yields of both reactions, it can be tuned by introducing certain substituents. For example, the ring-opening QY of a disubstituted 6,8-dinitroindolinospiryran, is greater than that of a monosubstituted 6-nitroindolinospiryran, which is greater than that of an unsubstituted indolinospiryran. Nevertheless, it is important to note that an increase of the ring-opening QY means a decrease of the ring-closing QY and vice versa; and that the QY of the ring-closing reaction is usually higher than that of the ring-opening reaction³⁴.

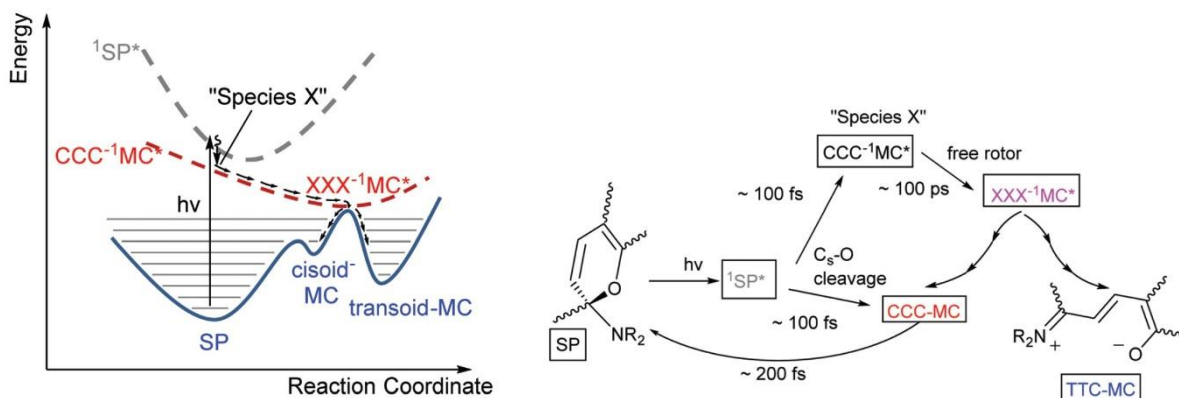


Figure A.1.2.1: Switching mechanism (ring-opening reaction) of unsubstituted spiropyran (singlet state pathway). Adapted from³⁴.

The applications of spiropyran-based polymers for the photocontrol of fluorescence, polymer solubility, volume phase transitions in thermoresponsive polymers, transport through polymeric systems, mechanical properties procurement, and metal ion complexation, but also the applications of spiropyran-functionalized surfaces for the photocontrol of surface wettability, transport through porous media, binding to surfaces, and electrochemical properties were reviewed by Klajn³⁶.

The photoswitching of spiropyran in the solid state is challenging, like other photochromes they undergo quenching. It was demonstrated to be quite restricted in monolayers, thin films, and microstructures and required the use of an additional stimulus (pH or temperature change). Photoswitching of closely packed spiropyran, in thick layers or crystals, is rendered more complicated, particularly the ring-opening which requires considerable geometrical change (elongation and planarization) and charge modification (densely packed non-solvated zwitterionic charges) in a very constrained environment. Switching in the solid state was however made possible by methods that preserved a space large enough around the molecules avoiding their excessive packing. One strategy is to control their packing by inducing columnar (π - π) stacking; another one is to place them in nanocavities (nanocages, MOFs, and COFs) whose size can be adjusted which allows to control the switching kinetics and to retrieve switching rates close to the ones obtained in solution³⁴.

Chapter 2

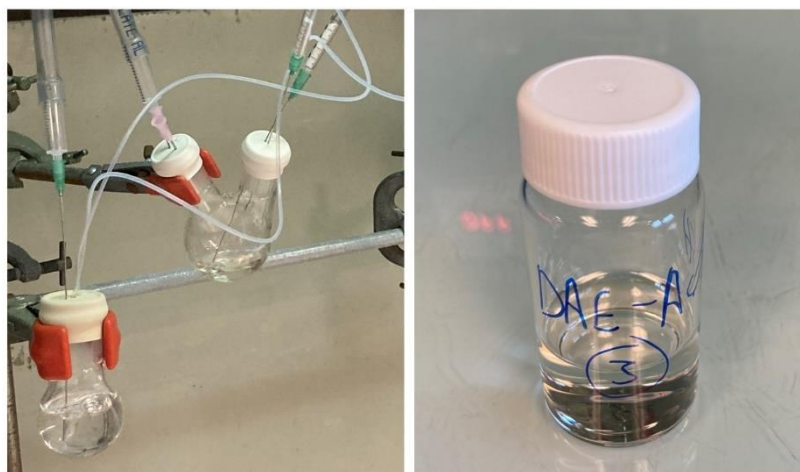


Figure A.2.1: On the left, ammonia (colorless solution in the round-bottom flask) and deprotected C5HT-di-PSH solution (yellowish solution in the two-necks round bottom flask) after deprotection with N_2 /ammonia flow. On the right, Cl-C5HT-PSH solution deprotected by introducing a few drops of ammonia directly in the vial.

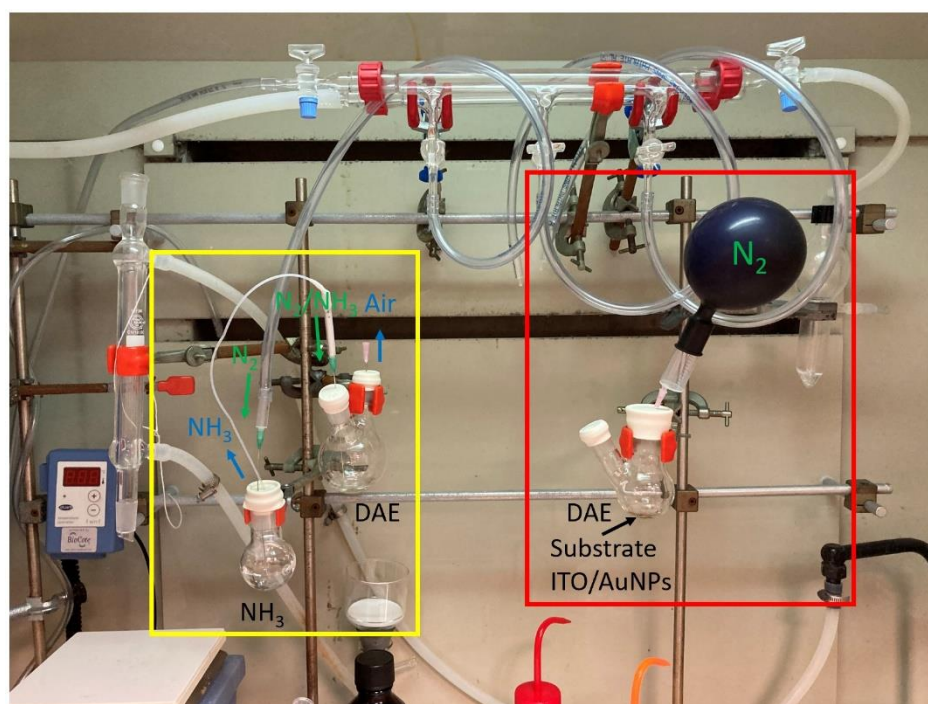


Figure A.2.2: Setup used for the deprotection of diarylethene solutions with an N_2/NH_3 flow (yellow square) and for the grafting of DAE molecules on AuNPs deposited on ITO according to grafting protocol 1 (red square).

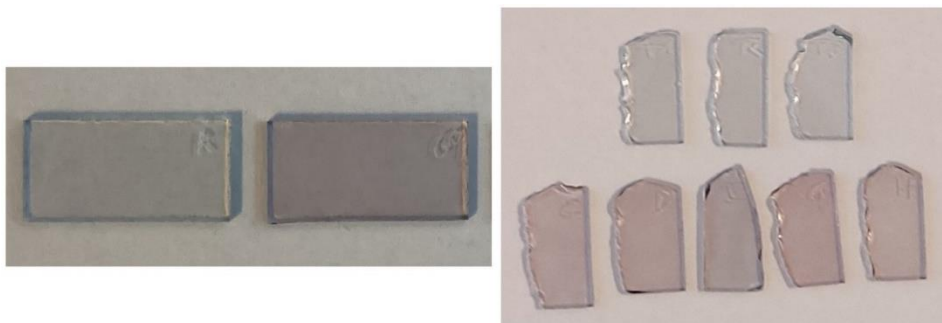


Figure A.2.3: On the first image, a pristine ITO substrate (transparent, used as a reference) and sample ADITO69 (reddish) after AuNPs deposition and DAE grafting following grafting protocol 1. On the second image, the first line of transparent cut ITO substrates (T1, T2 and T3) used as reference; the second line of cut ITO substrates are samples ADITOC, D, I, G and H (reddish) after AuNP deposition and DAE grafting following grafting protocol 2.

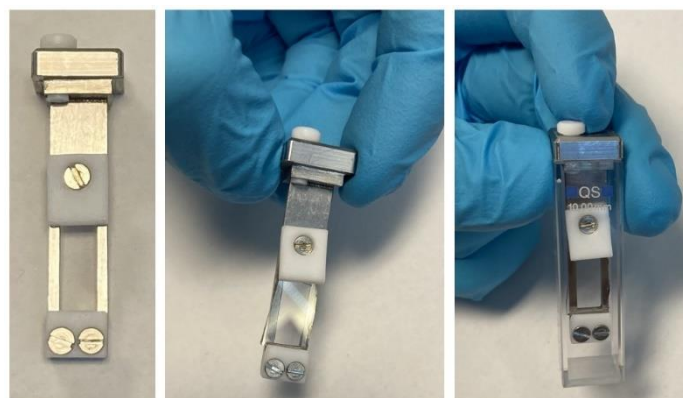


Figure A.2.4: Custom sample-holder (left), custom sample-holder with a cut ITO substrate in it (middle) and custom sample-holder with a cut ITO substrate in it inside the quartz QS cuvette from Hellma (right).

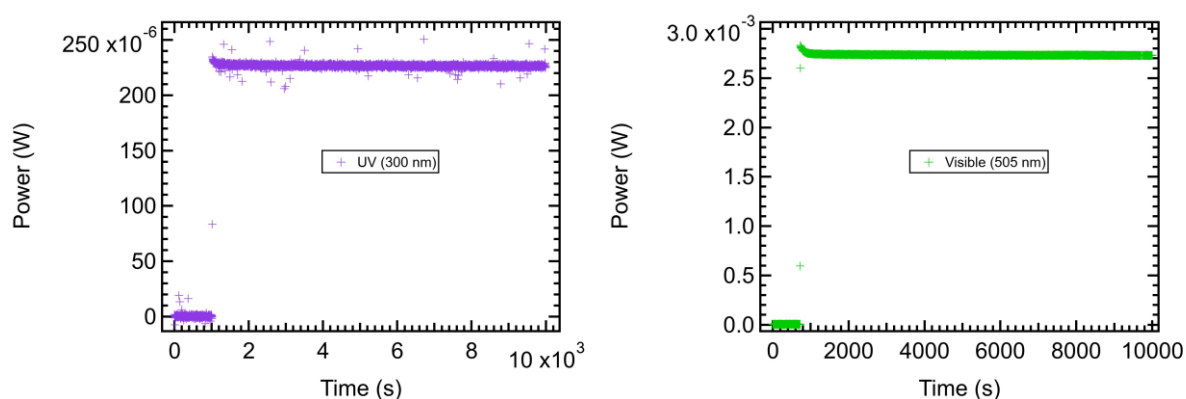


Figure A.2.5: Light flux stability tests, on/off switching of the UV LED (on the left) and visible LED (on the right).

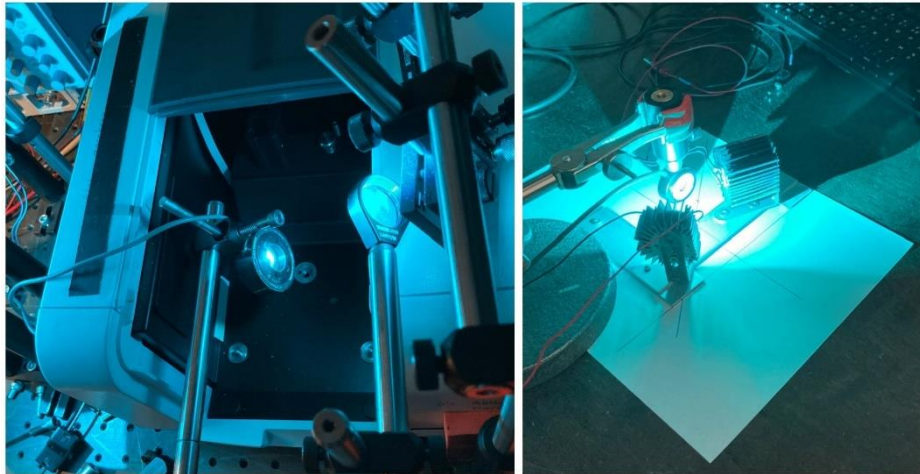


Figure A.2.6: LED power measurements setup for the irradiation LEDs setup in Konstanz university (left) and for the irradiation LEDs setup at INSP (right).

Table A2.1: Fit range for the samples of Table 2.3 and Table 2.4 for which the spectra were recorded with the Jasco V-750.

Sample	Fit range (nm)
ADITO46	515 - 538
ADITO47	513 - 528
ADITO48	502 - 540
ADITO49	509 - 528
ADITO55	516 - 523
ADITO56	512 - 520
ADITO60	509 - 525
ADITO61	510 - 528
ADITO64	528 - 587
ADITO69	516 - 540
ADITОВI	538 - 565

Table A2.2: Results of the fits (with a Gaussian between 511.7 and 573.1 nm, with Igor Pro) of the LSPR peak of the AuNPs from the zone of interest C of sample ADITOR for the two measurement sessions.

AuNP n°	Measure 1		Measure 2		$\Delta\lambda_{\text{LSPR}}$ (nm)	Δ Absorbance at λ_{LSPR}
	λ_{LSPR} (nm)	Absorbance	λ_{LSPR} (nm)	Absorbance		
1	532,72	0,082778	537,31	0,094382	4,59	0,011604
2	533,06	0,043106	539,89	0,054767	6,83	0,011661
5	534,7	0,066589	541,54	0,067125	6,84	0,000536
6	531,57	0,062828	534,43	0,071073	2,86	0,008245
7	535,08	0,077003	537,1	0,084843	2,02	0,00784
8	531,7	0,066581	535,97	0,06849	4,27	0,001909
9	530,3	0,077216	536,92	0,071542	6,62	-0,005674
10	536,69	0,082631	542,92	0,090321	6,23	0,00769
11	532,21	0,08787	543,63	0,065975	11,42	-0,021895
12	531,85	0,098085	538,79	0,076088	6,94	-0,021997
13	535,11	0,080439	540,92	0,058165	5,81	-0,022274
14	533,41	0,097704	533,5	0,101388	0,09	0,003684
15	532,59	0,056304	536,23	0,062623	3,64	0,006319
16	539,35	0,10622	543,58	0,13884	4,23	0,03262
17	533,32	0,078794	535,75	0,1041	2,43	0,025306
18	528,19	0,080238	530,52	0,094867	2,33	0,014629
19	535,59	0,067132	537,24	0,111794	1,65	0,044662
20	530,68	0,085552	532,69	0,110076	2,01	0,024524

Table A2.3: Uncertainty on the fits (with a Gaussian between 511.7 and 573.1 nm, with Igor Pro) of the LSPR peak of the AuNPs from the zone of interest C of sample ADITOR for the two measurement sessions.

AuNP n°	Measure 1		Measure 2		$\Delta u \Delta \lambda_{LSPR}$ (nm)	$\Delta u \Delta \text{Absorbance}$ at λ_{LSPR}
	$\Delta u \lambda_{LSPR}$ (nm)	$\Delta u \text{Absorbance}$	$\Delta u \lambda_{LSPR}$ (nm)	$\Delta u \text{Absorbance}$		
1	0,0818	0,001589	0,076	0,00381	0,1578	0,005399
2	0,176	0,00198	0,0712	0,00496	0,2472	0,00694
5	0,0962	0,00405	0,0675	0,00397	0,1637	0,00802
6	0,0797	0,001427	0,0812	0,00147	0,1609	0,002897
7	0,0796	0,001784	0,0759	0,001382	0,1555	0,003166
8	0,105	0,00269	0,0577	0,001487	0,1627	0,004177
9	0,09	0,001998	0,0721	0,0021	0,1621	0,004098
10	0,071	0,00207	0,072	0,00876	0,143	0,01083
11	0,0886	0,001545	0,15	0,0115	0,2386	0,013045
12	0,0801	0,00233	0,117	0,00256	0,1971	0,00489
13	0,0623	0,00278	0,0733	0,00313	0,1356	0,00591
14	0,0518	0,00218	0,0771	0,001729	0,1289	0,003909
15	0,117	0,00353	0,148	0,00173	0,265	0,00526
16	0,0677	0,00608	0,0848	0,251	0,1525	0,25708
17	0,0648	0,00252	0,056	0,00212	0,1208	0,00464
18	0,0983	0,001602	0,0717	0,001206	0,17	0,002808
19	0,105	0,004	0,0359	0,001898	0,1409	0,005898
20	0,0906	0,00162	0,0612	0,001351	0,1518	0,002971

Chapter 3

FTIR spectroscopy experiment. The FTIR spectroscopy measurements were performed by O. Pluchery. The FTIR spectra were recorded with a Bruker Tensor 27 spectrometer in Transmission geometry with a 70° incidence angle. A reference spectrum was recorded with a cleaned pristine silicon substrate, the exact position of this substrate in the sample holder defines the one that will be used for the recording of the samples' spectra. The FTIR spectra were recorded with 4 cm⁻¹ spectra resolution and a number of accumulation of 500 interferograms^{20,206,207}. Each spectrum was recorded three time successively in order to leave enough time for the nitrogen purge to remove as much water vapor from the sample compartment. Regarding the data treatment, both the rotational and vibrational contributions of the water vapor were removed by signal processing (using Igor Pro) to a contribution of less than 1 x 10⁻⁴ absorbance unit. Consequently, any feature presenting an absorbance superior to

1×10^{-4} is considered as significant i.e., corresponds to the vibration of a molecular species present on the substrate.

The FTIR measurements were performed to confirm the presence of the molecules on the gold nanoparticles substrates after surface saturation was reached. Two samples were prepared using a 18 nm AuNPs solution at 1.22×10^{-9} mol/L⁻¹. The first sample was prepared with the as-synthesized citrate-decorated AuNPs solution and the second sample with AuNPs functionalized with MUDA. For this latter sample, 0.75 mL of MUDA solution was added to 1 mL AuNPs solution so that the final concentration of the solution in MUDA was 2 μ M. The mixture reacted for 15 minutes under stirring. Both AuNPs solutions were centrifugated (to remove the molecules that did not react) for 30 min at 6000 rpm and recompleted with water or a mixture of 50 vol.% ethanol in water after removal of the supernatant respectively for citrate-decorated AuNPs and MUDA-functionalized AuNPs. These solutions were then drop-casted on silicon substrates. Float-zone (FZ) silicon substrates were used, they were chosen for the ultralow amount of inserted oxygen they contain and because they give access to the silicon oxide spectral region ($1000 - 1400$ cm⁻¹) allowing us to monitor the surface chemistry of the AuNPs deposited on silicon oxide. In these conditions the symmetric and asymmetric carbonyl vibrations of the carboxylate can be detected confirming the presence of MUDA on functionalized nanoparticles.

Saturation experiment with dodecanthiol (DDT). A slightly different version of the saturation experiments was conducted with DDT. An 18 nm AuNPs solution at 1.22×10^{-9} M has been used, successive additions of the same 187.5 μ L volume of various DDT solutions at concentrations indicated in Table A.3.1 in a mixture of ethanol/water (proportions also indicated in Table A.3.1). The result of this additional experiment are shown in Figure A.3.1.

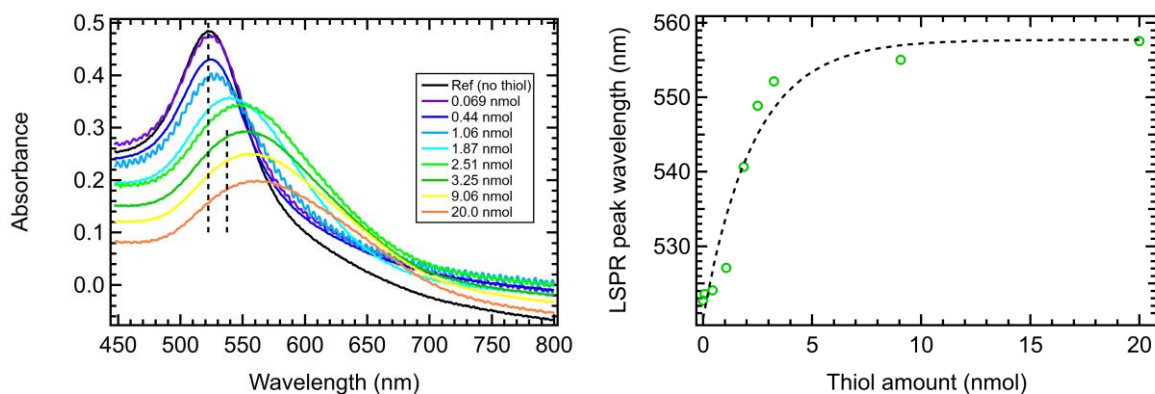


Figure A.3.1: UV-visible spectra of 18 nm spherical gold nanoparticles in solution on which DDT is progressively adsorbed (left). The resulting LSPR wavelength shift is 15.6 nm. The experiment was carried out under stirring, explaining the oscillations present on the spectra due to shocks of the stirring bar on the cuvette. Evolution of the LSPR peak wavelength as a function of the added amount of DDT (right). The dotted line is a guide for the eye.

Table A.3.1: Saturation experiments parameters (concentration of the added aliquot, amount of thiol added to the reacting solution, thiol concentration in the reacting solution, volume of the reacting solution, volume percentage of the solvent, refractive index of the solvent) and measured LSPR peak wavelengths for DDT.

#	[Thiol] (μM) in the added aliquot	n_{thiol} (nmol) added	V_{solution} (μL)	[Thiol] (μM) in the solution	Vol % of EtOH in the solvent	Solvent refractive index	λ_{LSPR} (nm) measured for DDT
0	0	0	1000	0	0	1.333	522.70
1	0.367	0.069	1188	0.058	16	1.344	523.58
2	1.97	0.44	1376	0.32	27	1.352	524.07
3	3.33	1.06	1564	0.68	36	1.357	527.10
4	4.33	1.87	1752	1.07	43	1.359	540.64
5	3.41	2.51	1940	1.3	48	1.361	548.84
6	3.92	3.25	2128	1.53	53	1.362	552.15
7	31	9.06	2316	3.92	57	1.363	555.01
8	58.3	20.0	2504	8	60	1.364	557.54

Chapter 5

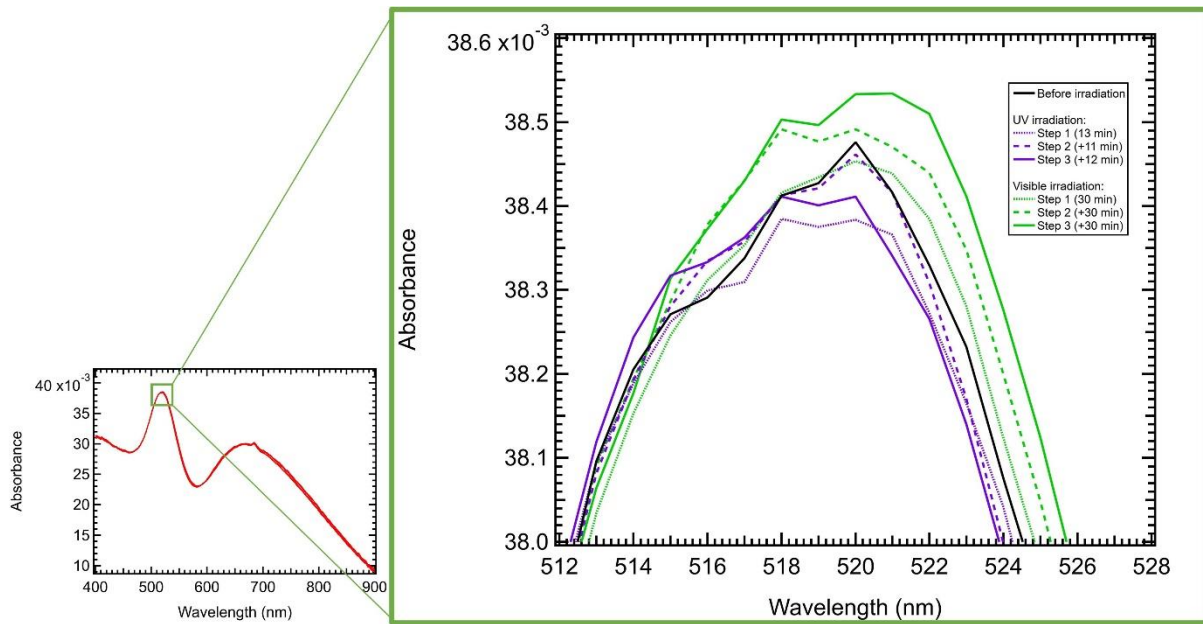


Figure A.5.1: UV-visible spectra corresponding to the control switching measurements on ADITO55 (reference samples with 28 nm AuNPs deposited on ITO).

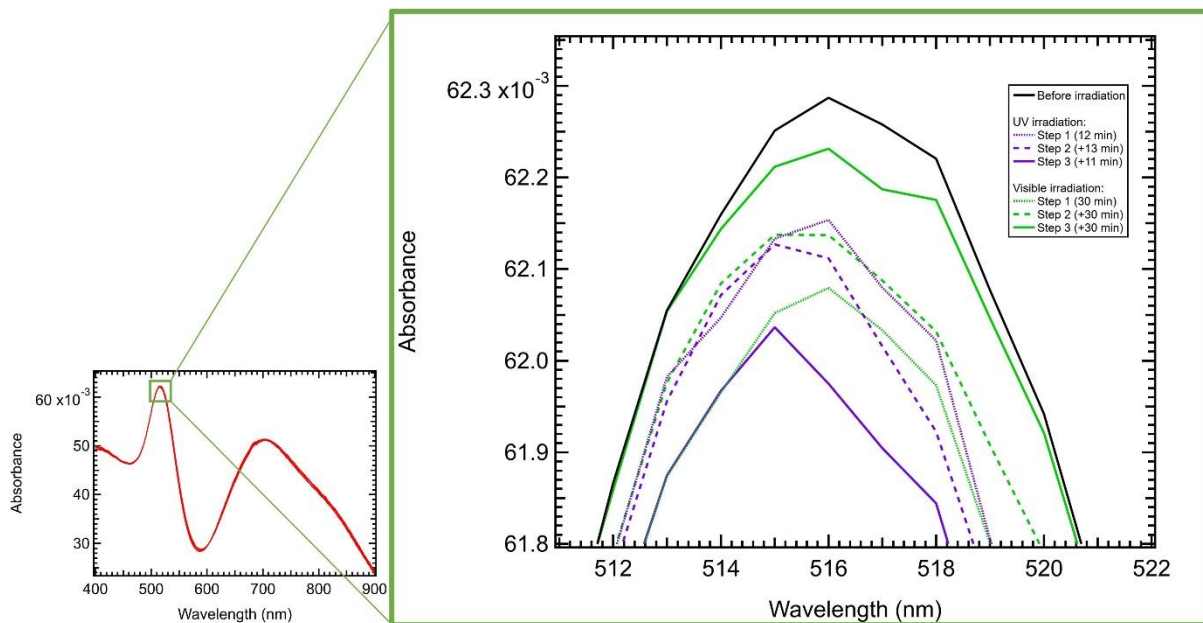


Figure A.5.2: UV-visible spectra corresponding to the control switching measurements on ADITO56 (reference samples with 35 nm AuNPs deposited on ITO).

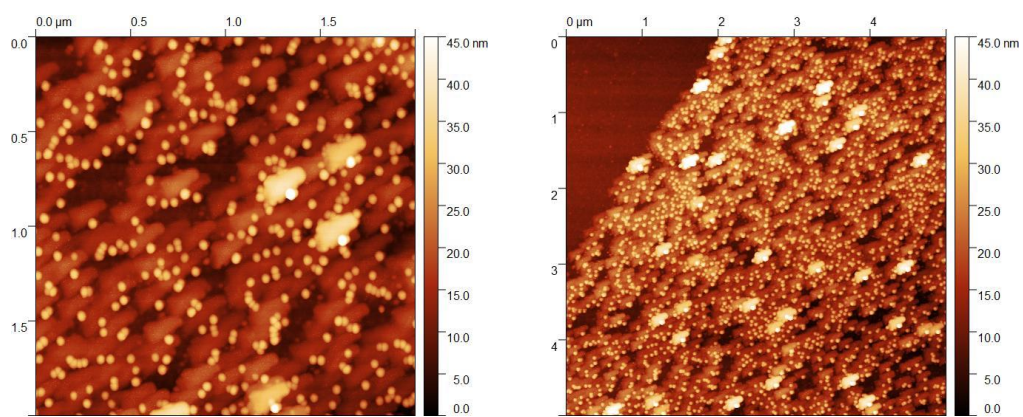


Figure A.5.3: AFM images of sample ADITO46 showing the crystallized molecules on and around the gold nanoparticles but not on the ITO surface (right image).

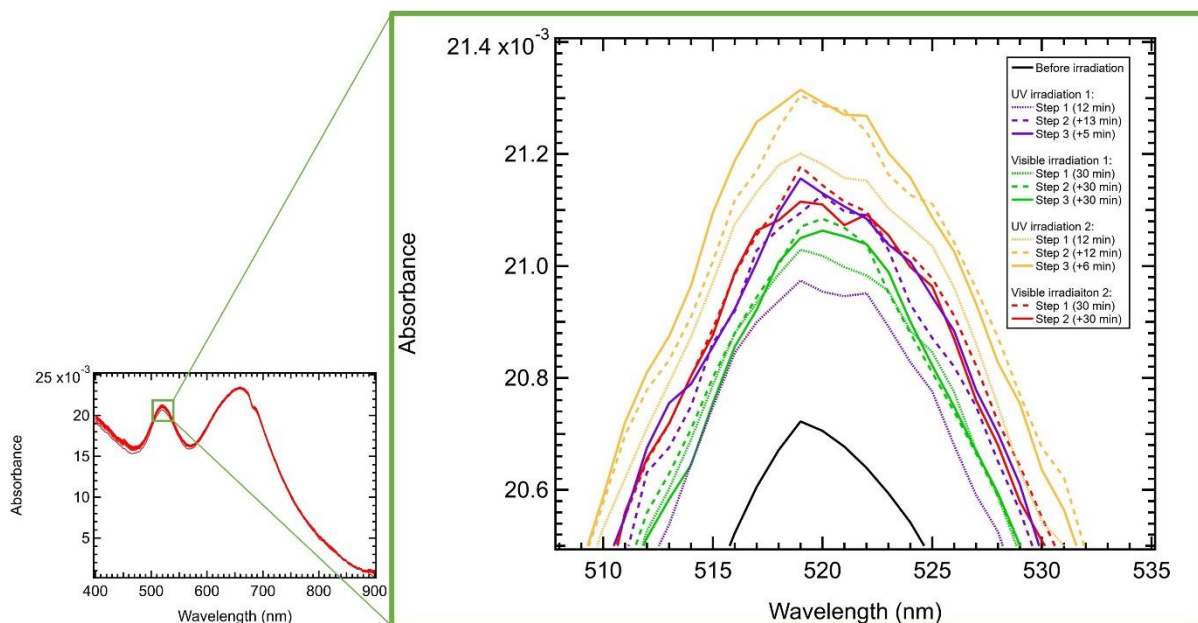


Figure A.5.4: UV-visible spectra corresponding to the switching measurements on ADITO48.

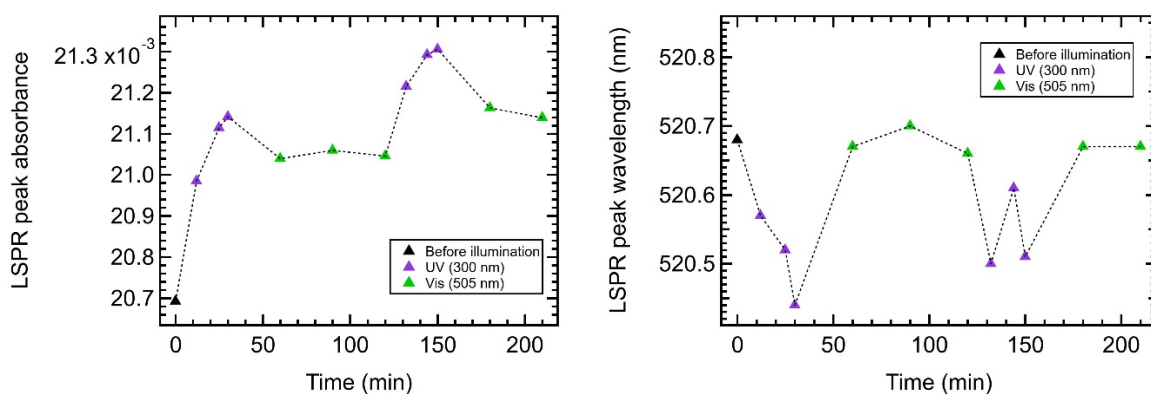


Figure A.5.5: Evolution of the LSPR peak absorbance (left) and wavelength (right) of ADITO48 as a function of time upon irradiation. The dotted line is a guide for the eyes.

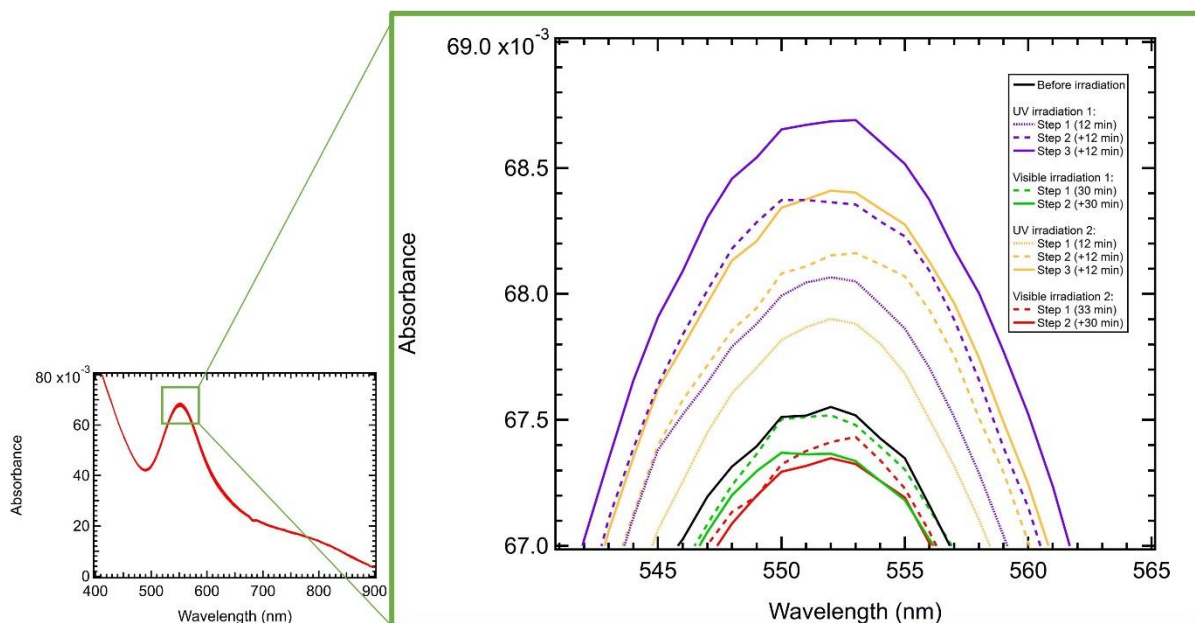


Figure A.5.6: UV-visible spectra corresponding to the switching measurements on ADITTOVI.

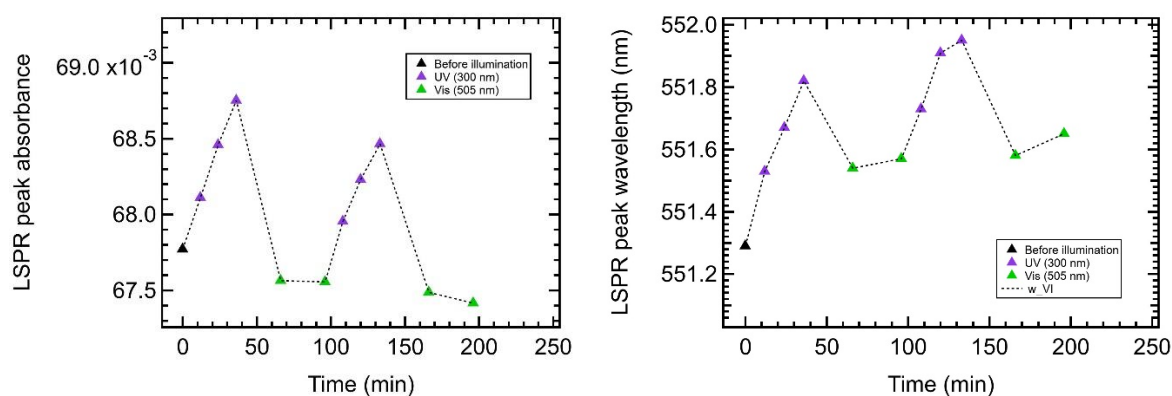


Figure A.5.7: Evolution of the LSPR peak absorbance (left) and wavelength (right) of ADITTOVI as a function of time upon irradiation. The dotted line is a guide for the eyes.

Table A.5.1 : Values of the switching ratios (Vis/UV above, UV/Vis in parenthesis below) calculated for the two cycles the measurements made on ADITOC.

ADITTOVI	Δt_{UV} (min)	Δt_{vis} (min)	SR(UV/Vis)	SR(Vis/UV)
Cycle 1	24	30	0.037	26.7
Cycle 2	37	33	0.052	19.1

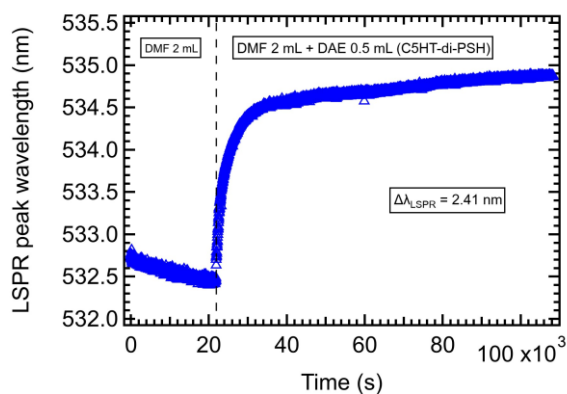


Figure A.5.8: Grafting of C5HT-di-PSH on 25 nm gold nanoparticles deposited on ITO. Deposition carried out in a DAE solution prepared with non-degassed DMF for sample ADITOD.

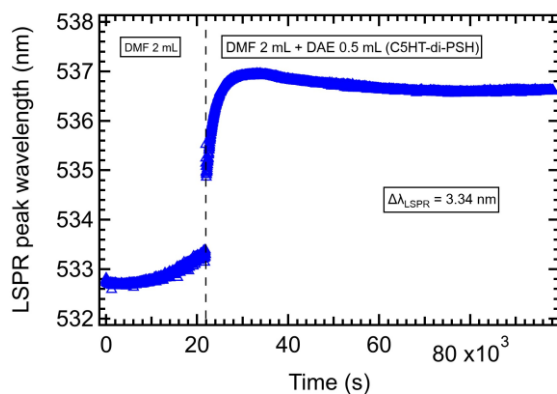


Figure A.5.9: Grafting of C5HT-di-PSH on 25 nm gold nanoparticles deposited on ITO. Deposition carried out in a DAE solution prepared with non-degassed DMF for sample ADITOG.

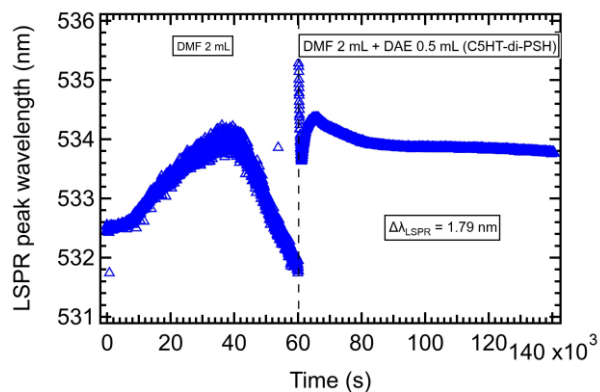


Figure A.5.10: Grafting of C5HT-di-PSH on 25 nm gold nanoparticles deposited on ITO. Deposition carried out in a DAE solution prepared with non-degassed DMF for sample ADITOH.

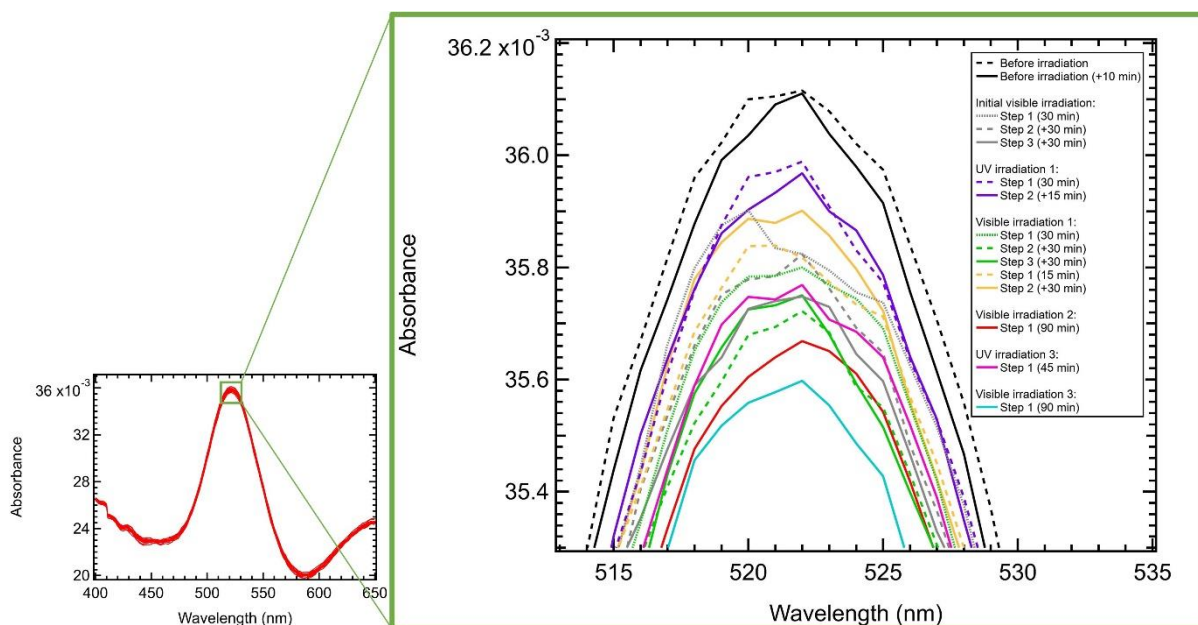


Figure A5.11: UV-visible spectra corresponding to the switching measurements on ADITOI (Day 2).

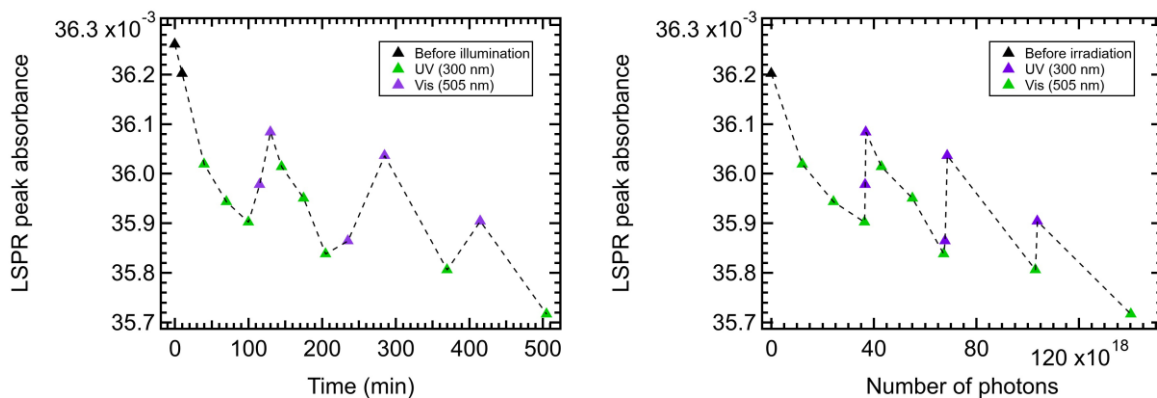


Figure A5.12: Evolution of the LSPR peak absorbance of ADITOI (Day 2) as a function of time (left) or number of photons (right) upon irradiation. The dotted line is a guide for the eyes.

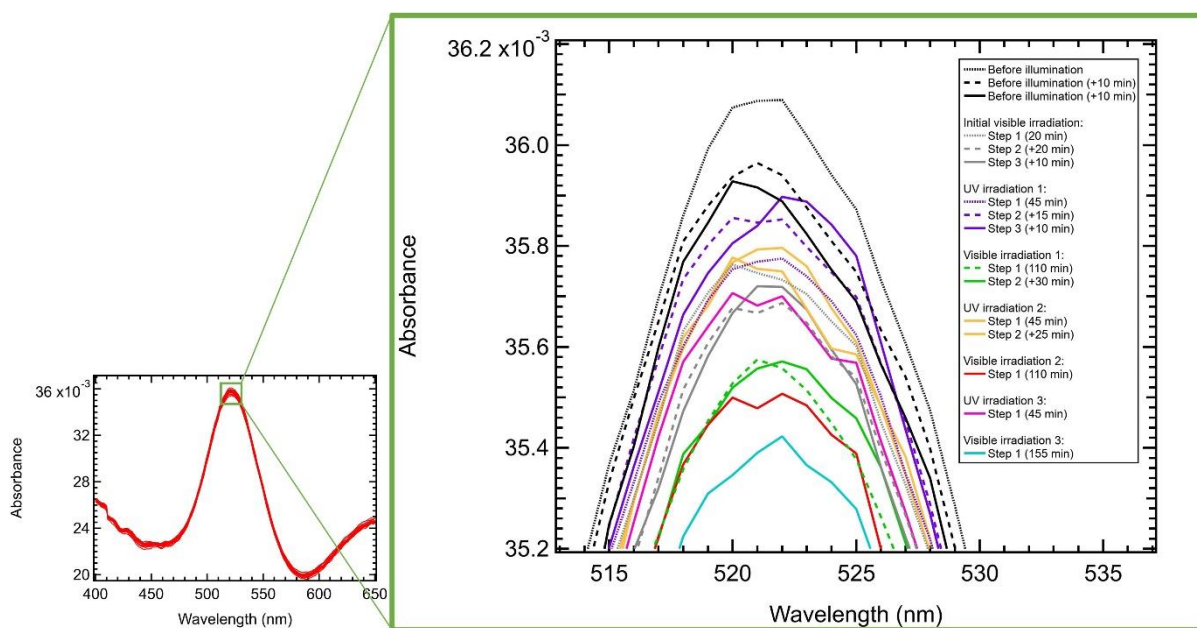


Figure A.5.13: UV-visible spectra corresponding to the switching measurements on ADITOI (Day 3).

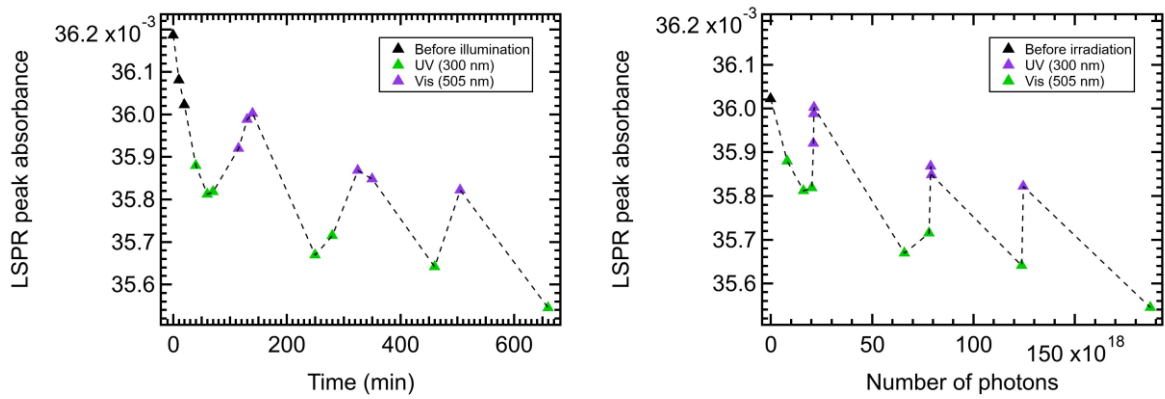


Figure A.5.14: Evolution of the LSPR peak absorbance of ADITOI (Day 3) as a function of time (left) or number of photons (right) upon irradiation. The dotted line is a guide for the eyes.

Calculation of the uncertainty on the values of the switching ratios

Let us first remind the expression of the switching ratio:

$$SR(Vis/UV) = \frac{n_{photons}(Visible)}{n_{photons}(UV)} = \frac{\Delta t_{Vis} \times \Phi_{photons_Vis}}{\Delta t_{UV} \times \Phi_{photons_UV}}$$

The uncertainty on the switching ratio thus depends on the uncertainty on the number of photons and is expressed as:

$$\Delta SR = SR \sqrt{\left(\frac{\Delta n_{photons}(UV)}{n_{photons}(UV)}\right)^2 + \left(\frac{\Delta n_{photons}(Visible)}{n_{photons}(Visible)}\right)^2}$$

The number of photons is calculated using the following expression:

$$n_{photons} = \Phi_{photons} \times \Delta t$$

And the uncertainty on the number of photons is expressed as:

$$\Delta n_{photons} = n_{photons} \sqrt{\left(\frac{\Delta \Phi_{photons}}{\Phi_{photons}}\right)^2 + \left(\frac{\Delta \Delta t}{\Delta t}\right)^2} = n \sqrt{\left(\frac{\Delta P}{P}\right)^2 + \left(\frac{\Delta \Delta t}{\Delta t}\right)^2}$$

ΔP is the uncertainty on the power of the LED and is given by the manufacturer. It corresponds to a 5% uncertainty on the value of the power P for UV photons and to a 3% uncertainty on the value of P for visible photons.

Δt was estimated to be 1 s.

According to the calculations made with this formula (see the examples below), all SR values are given with a 6% uncertainty.

Numerical application for Cycle 1 of ADITO64, using the parameters given in Table 5.1 and Table 5.2:

$$\Delta n_{photons}(UV) = n \sqrt{\left(\frac{\Delta P_{UV}}{P_{UV}}\right)^2 + \left(\frac{\Delta \Delta t_{UV}}{\Delta t_{UV}}\right)^2} = 7.73 \times 10^{17} \sqrt{(0.05)^2 + \left(\frac{1}{2040}\right)^2} = 3.87 \times 10^{16}$$

$$\Delta n_{photons}(Visible) = n \sqrt{\left(\frac{\Delta P_{Vis}}{P_{Vis}}\right)^2 + \left(\frac{\Delta \Delta t_{Vis}}{\Delta t_{Vis}}\right)^2} = 2.43 \times 10^{19} \sqrt{(0.03)^2 + \left(\frac{1}{3000}\right)^2} = 7.29 \times 10^{17}$$

$$\Delta SR = 31.4 \sqrt{\left(\frac{3.87 \times 10^{16}}{7.73 \times 10^{17}}\right)^2 + \left(\frac{7.29 \times 10^{17}}{2.43 \times 10^{19}}\right)^2} = 1.83$$

Numerical application for Cycle 1 of ADITOI, using the parameters given in Table 5.3 and Table 5.4:

$$\Delta n_{photons}(UV) = n \sqrt{\left(\frac{\Delta P_{UV}}{P_{UV}}\right)^2 + \left(\frac{\Delta \Delta t_{UV}}{\Delta t_{UV}}\right)^2} = 5.98 \times 10^{17} \sqrt{(0.05)^2 + \left(\frac{1}{2040}\right)^2} = 2.99 \times 10^{16}$$

$$\Delta n_{photons}(Visible) = n \sqrt{\left(\frac{\Delta P_{Vis}}{P_{Vis}}\right)^2 + \left(\frac{\Delta \Delta t_{Vis}}{\Delta t_{Vis}}\right)^2} = 8.49 \times 10^{18} \sqrt{(0.03)^2 + \left(\frac{1}{1260}\right)^2} = 2.55 \times 10^{17}$$

$$\Delta SR = 16.1 \sqrt{\left(\frac{2.99 \times 10^{16}}{5.98 \times 10^{17}}\right)^2 + \left(\frac{2.55 \times 10^{17}}{8.49 \times 10^{18}}\right)^2} = 0.94$$

Chapter 6

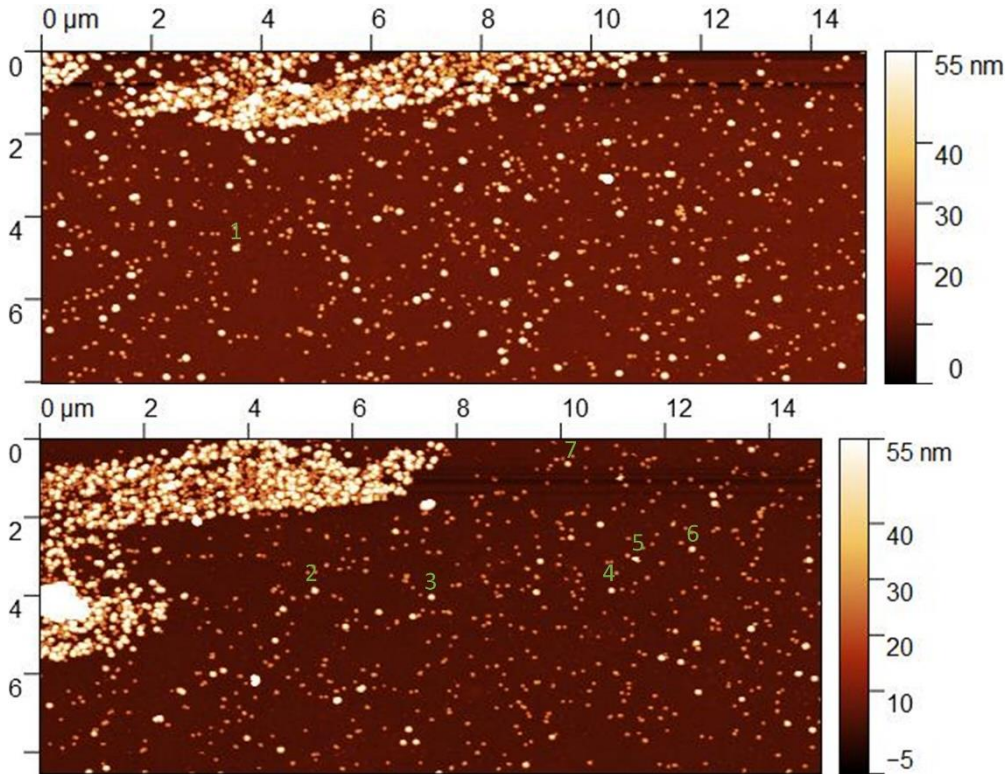


Figure A.6.1: AFM images of AuNPs 1 to 7 from the zone of interest of ADITO80.

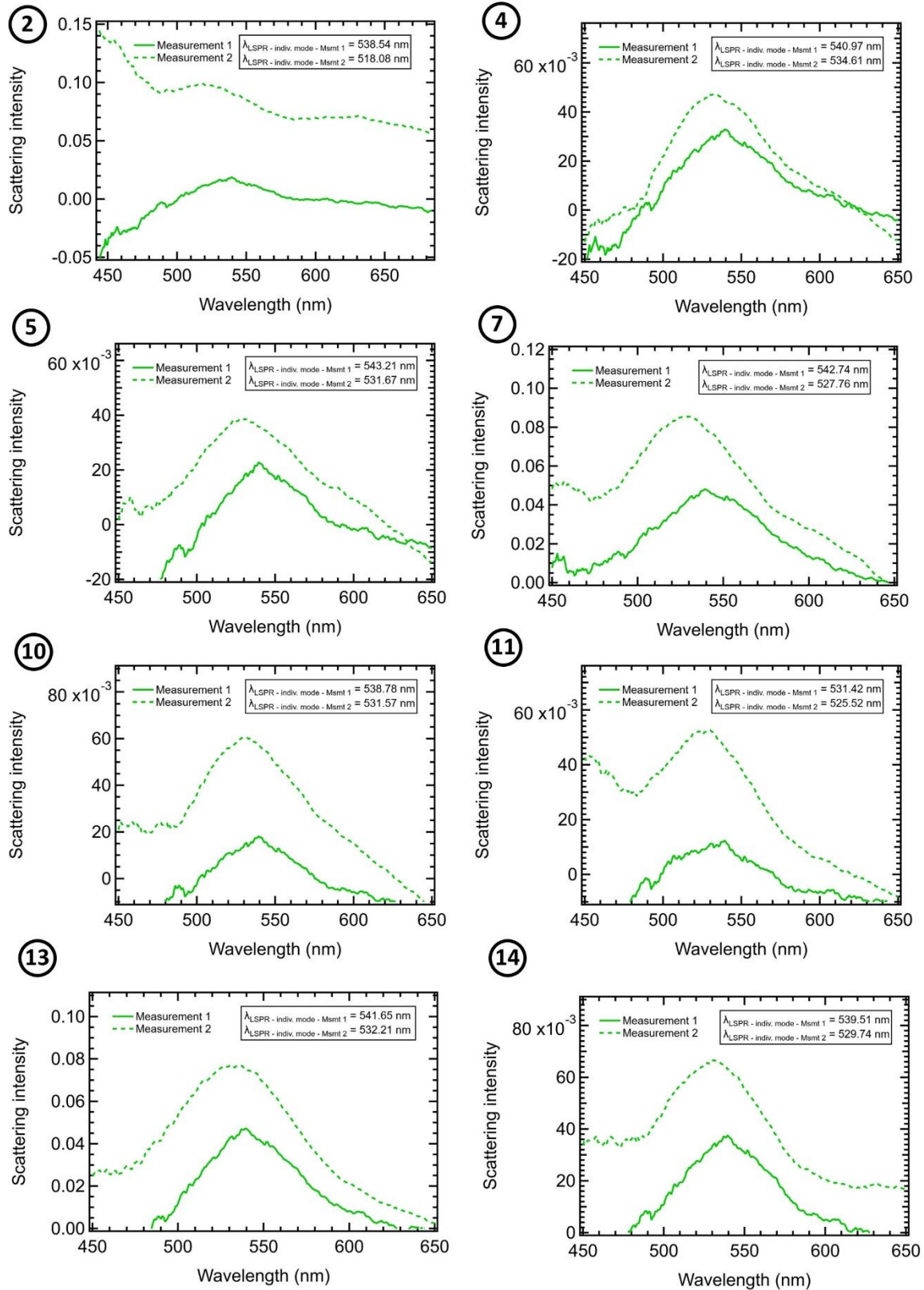
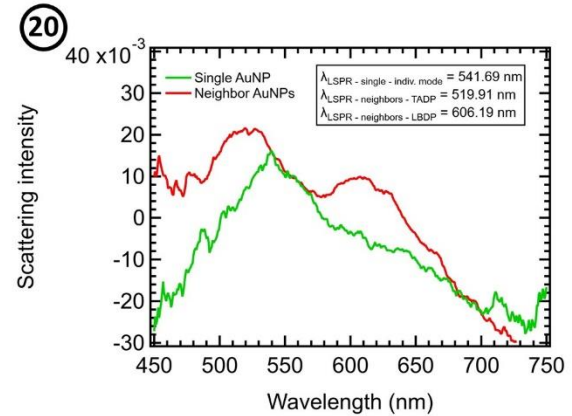
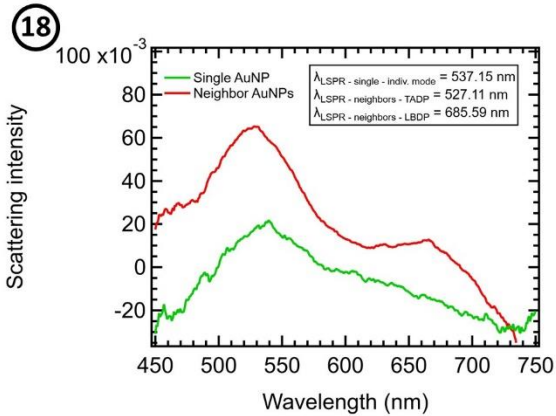
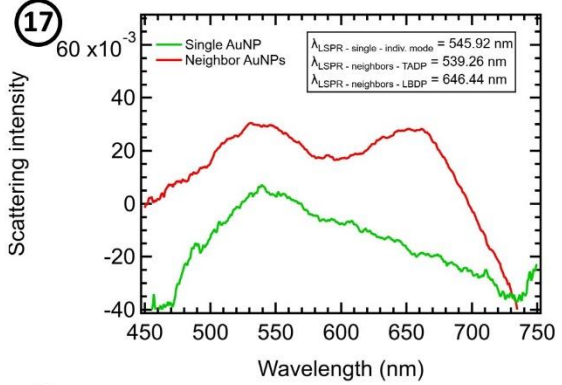
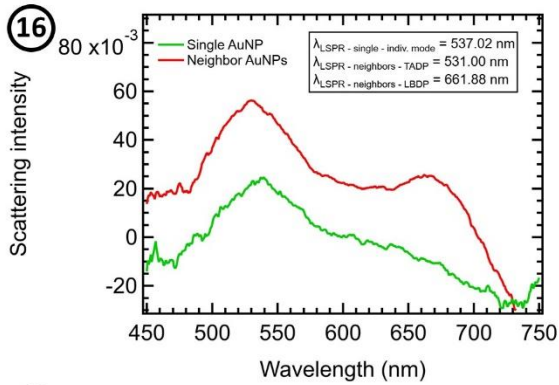
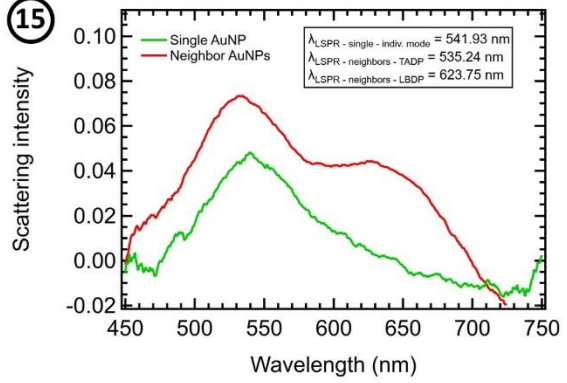
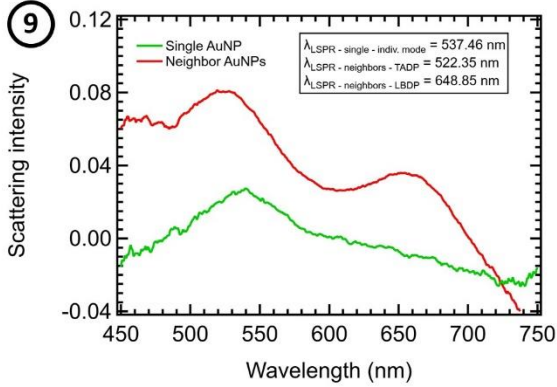
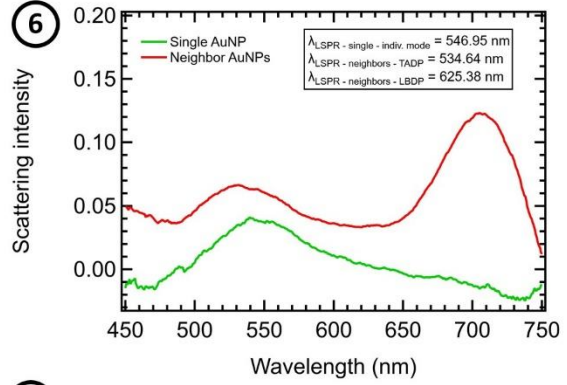
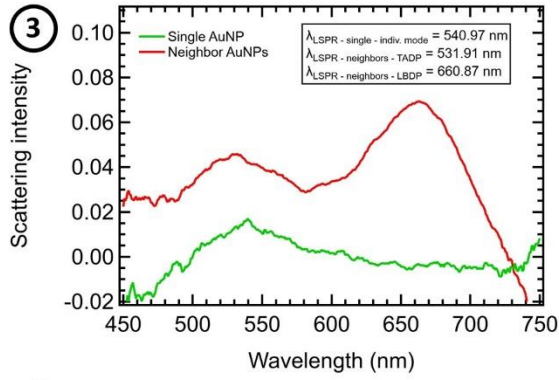


Figure A.6.2: UV-visible spectrum of the AuNPs that do not possess a 28 nm neighbor before (Measure 1) and after (Measure 2) the drop casting of 28 nm satellite AuNPs took place.



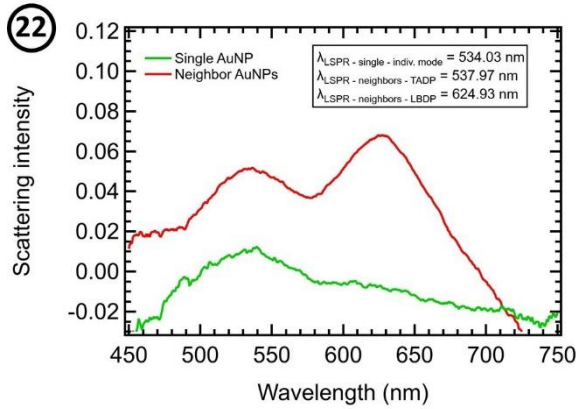


Figure A.6.3: UV-visible spectra of the AuNPs possessing a 28 nm neighbor before and after the drop casting of 28 nm satellite AuNPs took place.

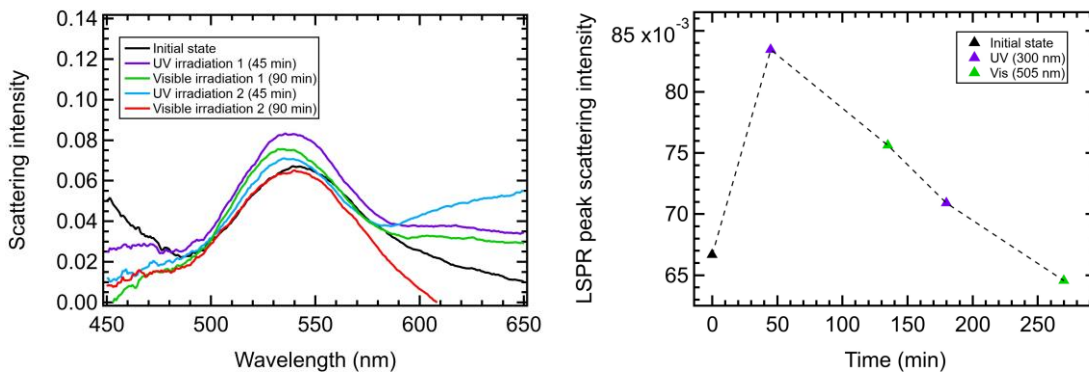


Figure A.6.4: UV-visible spectra corresponding to the switching measurements on AuNP 13 (left). Evolution of the scattering intensity at λ_{LSPR} upon irradiation as a function of time.

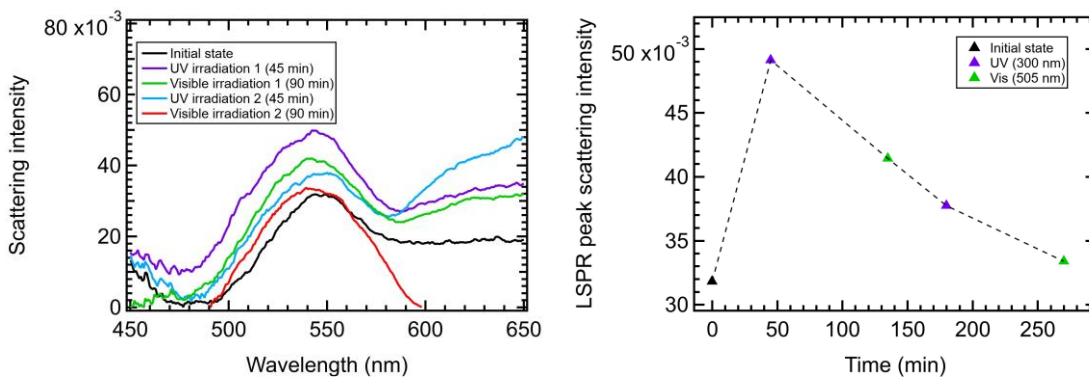


Figure A.6.5: UV-visible spectra corresponding to the switching measurements on AuNP 20 (left). Evolution of the scattering intensity at λ_{LSPR} upon irradiation as a function of time.

List of Figures

- Figure 1.1: Example of a typical and widely studied diarylethene: 1,2-bis(2,5-dimethyl-3-thienyl)perfluorocyclopentene. Adapted from²⁶. 12
- Figure 1.2: Example of the absorption spectrum of a typical diarylethene (1,2-bis(2,5-dimethyl-3-thienyl)perfluorocyclopentene). Adapted from²⁶. 13
- Figure 1.3: Structure and photoisomerization of an azobenzene. The distance between the carbon atoms in position 4 goes from 9 Å to 5.5 Å upon isomerization from the flat E form with no dipolar moment to the Z form with an angular geometry and a 3.0 D dipolar moment. Adapted from²⁵. 14
- Figure 1.4: Typical photochromic indolinobenzospiran in its spiro (SP) form on the left and its merocyanine (MC) form on the right. 15
- Figure 1.5: (a) Synthesis of a [2]catenane obtained by a double cyclization following Grubbs ring-closing methodology of an entwined compound with a copper(I) center formed from a 1,10-phenanthroline derivative. (b) A degenerate donor-acceptor [2]rotaxane or "molecular shuttle". The CBPQT⁴⁺ ring moves back and forth (1000 times a second in acetone at room temperature) along the axle in between its two terminal hydroquinone recognition sites. (Top) The first switchable donor-acceptor [2]rotaxane whose switching is triggered by drop of acid that protonates the benzidine recognition unit where the presence of the CBPQT⁴⁺ ring is favored. Upon the protonation, the presence of the ring becomes more favored on the biphenol unit to which it migrates. Back-switching is triggered by an addition of base (Bottom). (c) Chemical structure and steps occurring during the rotation of a first-generation biaryl-based 4-step unidirectional molecular rotary motor (Top left). Schematic representation of the four steps composing its 360° rotation (Top right). Molecular models and structure and STM image of a four-wheel molecular nano-car based on rotary motors (Middle). Chemical structure of the third-generation symmetric molecular motor used for the nano-car (Bottom). Adapted from^{38,40,42,43}. 17
- Figure 1.6: Chemical structure of the two isomers hexatriene (HT) and cyclohexadiene (CHD). Adapted from⁴⁶. 18
- Figure 1.7: On the left, scheme of the known switching mechanism of diarylethene. The energies for the S₀(1A) (orange, bottom) and S₁(2A) (green, top) electronic states are represented in the space of two nuclear coordinates: (1) reaction coordinate: the internuclear C-C distance connecting CHD and HT isomers and (2) branching space coordinate: a linear combination of the gradient difference vector (GDV) and the derivative coupling vector (DCV) at the conical intersection (ConInt₁). On the right, two-dimensional simplification of the PESs describing the reaction paths for the ring-closing and ring-opening reactions of the diarylethene. The letters "c" and "o" in parenthesis respectively stand for "closed" form and "open" form. Adapted from^{26,45}. 20
- Figure 1.8: On the left, scheme of the fatigue mechanism leading to the formation of the by-product of diarylethenes. The energies for the S₀(1A) (orange, bottom) and S₁(2A) (green, top) electronic states are represented in the space of two nuclear coordinates: (1) reaction coordinate: the internuclear C-C distance connecting CHD and HT isomers and (2) initial fatigue coordinate: the internuclear C-CH₂ distance. In the middle, scheme of the fatigue mechanism after the vertical excitation of the system in the FC region. On the right, structure of the by-product. Adapted from⁴⁵. 29
- Figure 1.9: (a) Structure of the diarylethene and of perfluoronaphthalene used to make the cocrystal implemented as a molecular crystal cantilever (top). Bending (photomechanical work) of the 0.17 mg molecular crystal cantilever (made of the cocrystal represented above) lifting a 46.77 mg lead ball. The direction of the UV light irradiation is indicated by the blue

arrow (bottom). (b) Structures of the diarylethene molecules used to make the rod-shaped cocrystal implement as an actuator (top). Bending (photomechanical deformation) of the actuator triggering the rotation of the gears of a wheel (bottom). Adapted from ^{26,28}	31
Figure 1.10: (a) Scheme of the working principle of a S-R latch made of two cross-coupled NOR gates circuit, with Q the complement of Q . (b) Structure of both isomers of a diarylethene compound usable as a S-R latch and how to switch between them. (c) Truth table of the schematized S-R latch, with Q the current memorized (Q_{current}) state and the following state (Q_{next}), which is the actual response triggered by the input. (d) Scheme of the logic function of a S-R latch, the number between parenthesis corresponds to the entry of the truth table. Adapted from ⁶¹	34
Figure 1.11: Structure of the all-closed isomer FGc-DTEc of their multifunctional photochromic logic molecular system (left) Network formed by all the isomers and the stimuli allowing to switch between them (bottom). The diarylethene unit is represented in red while the fulgimide units are represented in blue. Adapted from ²⁷	35
Figure 1.12: Scheme of a gold nanoparticles-diarylethene network. The gold nanoparticles are bridged by the dithiolated diarylethenes: a photocontrolled network of interdigitated gold nanoparticles used as electrodes is obtained, it commands the conductance between the two large gold electrodes. Adapted from ^{26,63}	36
Figure 1.13: (a) Scheme of a SAM containing a dodecanthiol matrix with individual diarylethene integrations scanned by STM in constant current mode (top). Chemical structure of the closed isomer of the asymmetric diarylethene corresponding to its conductive “on” state (left) and of its open isomer corresponding to its insulating “off” state (bottom). (b) Sequence of cropped STM images (of a 100 nm ² zone) showing the photoinduced switching between the more conductive “on” state of the DAE appearing as bright protrusion with a higher apparent height and the insulating “off” state of the diarylethene for which the protrusion disappears after 13 minutes of visible light irradiation (top). Evolution of the apparent height as a function of the irradiation time (bottom). (c) I-V characteristics and dI/dV curves recorded simultaneously at 77K using the lock in technique (the bias voltage V is applied to the tip and the sample is grounded). Top left: I-V curves of As-DE (average of 160 traces obtained at four different locations). Top right: dI/dV curves of As-DE. Bottom left: I-V curves of DT (average of 1500 traces obtained at five different points and averaged to give the resulting curve. Bottom right: dI/dV curves of DT. Adapted from ^{26,64}	37
Figure 1.14: Schematic illustration of the localized surface plasmon resonance (LSPR) in metallic nanospheres. The induced (by the incident electric field) polarization p is indicated by the white arrows. In response to the incident electric field, the electrons from the metal collectively oscillate, hence the description of the NPs as oscillating dipoles. Adapted from ⁶⁵	38
Figure 1.15: Scheme of the two decay channels of a photoexcited plasmonic gold nanoparticle. Subsequently to its excitation by the incident electric field, the LSPR decays both radiatively by re-emitting photons (top) and non-radiatively by generating hot carrier which triggers lattice heating via electron-phonon coupling (bottom). T_{electron} , T_{lattice} , and T_{room} are the temperature of the electron system, the lattice, and the environment, respectively. Reprinted from ⁷²	39
Figure 1.16: Schematics of a metallic nanosphere with the coordinates required to express the external electric field using the electrostatic model (left). Plasmonic nanoparticle described as an oscillating dipole (the electrons of its LSPR oscillate as a whole) because the wavelength of the excitation wave is much larger than its radius ($\lambda \gg R$) (right). Adapted from ⁷⁰	40
Figure 1.17: Calculated spectra of 28 nm AuNPs showing respectively their absorption, extinction, and scattering efficiencies. $Q = \sigma/\pi R^2$. Calculated with ⁷⁴	42

Figure 1.18: (a) Illustration of the electromagnetic coupling between a 10 nm silver NP and an Al_2O_3 substrate in which charge images are induced, in function of the distance between them. (b) Induced local field for an applied field normal (left) and parallel (right) to the interface. (c) Extinction efficiency of the AgNP according to the distance from the substrate d for an external field normal (left) and parallel (right) to the substrate. The influence of the distance on the extinction efficiency is much stronger when the field is normal than when the field is parallel. Adapted from⁷⁶..... 43

Figure 1.19: (a) Oscillating dipole (at the origin) and its radiated electric field at point M located at a distance r from the center of the dipole. Logarithmic plot of the amplitude of the electric field as a function of the distance from the center, along the x axis showing the two radiation zones of the dipole: the near field with a decay in $1/kr^3$ and the far field with a decay in $1/kr$. Reprinted from⁷⁷..... 45

Figure 1.20: Electromagnetic field radiated by a gold nanoparticle illuminated at its plasmon resonance $\lambda_{\text{LSPR}} = 520$ nm in water corresponding to a near-field enhancement of a factor 20 in the vicinity of the AuNP. Reprinted from⁷⁷..... 46

Figure 1.21: Illustration of the concept of plasmonic nanoantenna through the example of a $400 \times 100 \times 50$ nm³ silver nanorod. Mapping of the calculated near-field for three plasmonic modes ($n = 1$, $\lambda_{\text{LSPR}} = 1375$ nm; $n = 2$, $\lambda_{\text{LSPR}} = 770$ nm; $n = 3$, $\lambda_{\text{LSPR}} = 630$ nm), blue and red correspond to an enhancement factor of respectively 0.1 and 100. The nanorod is on a glass substrate and illuminated from the top by a plane wave tilted 20° with respect to the vertical direction and polarized along its long axis. Reprinted from⁷⁰..... 48

Figure 1.22: (a) Scheme illustrating the SERS detection of the reduction of 4-NTP to 4-ATP by hot-electrons generated at the tip of the Ag antenna, in the presence of 0.1M HCl, and under illumination at $\lambda = 633$ nm and 1mW (left). Time-dependent Raman spectra showing the conversion of 4-NTP (blue peak) to 4-ATP (green peaks) (right). (b) Illustration representing the mechanism of H_2 dissociation by plasmon-induced hot electrons generated at the surface of the AuNPs. (c) O_2 dissociation by plasmon-induced hot electrons. Top left: density of states of O_2 adsorbed on an Ag (100) surface calculated by DFT, the dashed line materializing the Fermi level of Ag, the blue curve the bonding orbitals of O_2 , and the red line the antibonding orbitals of O_2 . Top right: PES of O_2 and O_2 on Ag(100). An energy transfer occurs from the hot electrons to the O_2 (activating the molecules) vibrational mode after they get transferred back to Ag. Bottom left: scheme of O_2 dissociation triggered by vibrationally excited states. Bottom right: aerobic oxidation of p-ATP mediated by hot-electrons acting on the antibonding orbital of the O_2 molecule, producing the long-lived O_2 that oxidizes p-ATP. Adapted from^{83,86,88}..... 50

Figure 1.23: (a) Diarylethene molecules in their “on” state (red) and open, “off” state (blue). Schemes of 2D networks: of gold nanoparticles protected by octanethiols (left side of the arrow) and connected by diarylethene molecules in their “on” state (right side of the arrow). Scheme of the setup used to measure light-induced (Hg lamp) conductance switching or optical switching (low-intensity white light source). Absorption spectra of the 2D AuNPs network before (solid, black line) and after (red, dash-dotted line) insertion of the diarylethene molecules to bridge the AuNPs, which made the LSPR peak shift, and the conductance increase of a factor of 18. (b) Conductance and molecular switching. They kept the sample in the dark until $t = 0$. They made the experiment in an argon flow cell at room temperature. The sample undergoes an alternance of illumination with either visible (green) or UV (pink) light and period in the dark, after which an optical spectrum is recorded and the conductance at that time t is indicated by a red dot. The evolution of G versus the time is plotted in the upper graph, while that of λ_{LSPR} versus the time is plotted in the lower graph. Visible light illumination makes G and λ_{LSPR} increase, while UV light illumination makes them decrease. Inset: First three optical spectra: black, solid line, spectrum at $t = 0$; blue, dash-dotted line,

after first visible illumination, λ_{LSPR} decreased; red, dashed line, after first UV illumination, λ_{LSPR} increased, closer to its initial value. The optical spectra demonstrate the molecular switching, DAEs in their “off” state having a lower permittivity than DAEs in their “on” state. Conductance switching cycles. The conductance G is plotted versus illumination time t for a sample with all its DAE bridges in the ON state. In the dark, before the beginning of the measurements (at $t < 0$) the sample conductance is constant. At $t = 0$, visible light illumination starts, G immediately decreases, upon UV irradiation (at $t = 245$ s), G increases again. Eight switching cycles consisting in 245 s of visible light irradiation followed by 125 s of UV light irradiation were performed. For $2095 < t < 2650$ s the sample was left in the dark. The experiment was done in an argon flow cell at room temperature. To determine G , they recorded I-V curves, with $-10 < V < 10$ V, so that for each molecular junction the bias was at most ~ 10 mV (linear regime). Note that in real time, this experiment lasted over 5 h. Adapted from³³ 52

Figure 1.24: Scheme of the structure of their Au-poly(DE) systems. Reprinted from¹⁰¹ 53

Figure 1.25: Scheme underlining the difference between a plasmonic dimer and a chemical dimer. 55

Figure 1.26: Typical plasmonic modes hybridization diagram for a dimer of spherical nanoparticles. Adapted from¹¹¹ 56

Figure 1.27 : Plasmon coupling in dimers of spherical nanoparticles separated with small gaps. (a) Constructive dipolar coupling in spherical AgNPs with light polarized along the dimer axis. (b) Destructive interference between the dipoles of spherical AgNPs with light polarized perpendicularly to the dimer axis. (c) Electric field intensity of 10 nm spherical AgNPs separated by a 5 nm gap interfering constructively. The scale bar is 10 nm. (d) Electric field intensity of 10 nm spherical AgNPs separated by a 5 nm gap interfering destructively. The scale bar is 10 nm. (e) Extinction efficiency of a dimer of 10 nm spherical AgNPs with gaps of 50 (darkest trace), 40, 30, 20, 10, 5, 4, 3, 2, and 1 (lightest trace) nm, and with light polarized along the dimer axis. (f) Same as (e) but for light polarized perpendicularly to the dimer axis. Reprinted from⁶⁸ 59

Figure 1.28: (a) Experimental representative dark field scattering spectra of individual hybrid dimers (50 nm AuNS - 50 nm AuNP) of each class. The three classes were defined according to the position of the LBDP mode on the scattering spectra. The point-contact class, in blue, comprising the dimers for which the LBDP is located at 707.7 ± 3.1 nm; the edge-contact class, in green, comprising the dimers for which the LBDP is located at 726.9 ± 5.6 nm; the face-contact class, in red, comprising the dimers for which the LBDP is located 771.5 ± 13.2 nm. (b) Simulated spectra by the FDTD method of ideal and hybrid dimers and their corresponding plasmon hybridization diagram. The results for the ideal dimers are in black, those for the hybrid dimers are respectively in blue (point contact), green (edge contact), and red (face contact). (c) Scheme of the three hybrid dimers configurations: point contact (blue), edge contact (green), face contact (red). Adapted from¹⁰⁴ 60

Figure 1.29: (a) Simulated plasmon shift vs the center-to-center distance in an Au disc dimer for different disc diameters and their least-squares fits to single-exponential decay function $y = y_0 + a \cdot e^{-x/l}$. The decay lengths l extracted from the fit are respectively 13.7, 15.5, and 17.7 nm for nanodisc of respective diameter $D = 54, 68,$ and 86 nm. b) Simulated fractional plasmon shift vs the ratio of interparticle gap to nanodisc diameter for discs with various diameters which all follow the same trend and were all fitted by a single-exponential decays (solid curves) of equation $y = a \cdot e^{-x/\tau}$ with $a = 0.14 \pm 0.01$ and $\tau = 0.23 \pm 0.03$. (c) Experimental fractional plasmon shift measured for an 88 nm diameter disc in function of the ratio of gap to diameter and its exponential fit (solid curve) with $a = 0.10 \pm 0.01$ and $\tau = 0.18 \pm 0.02$. Adapted from⁶⁷ 62

Figure 2.1: Structure of the opened and closed forms of the molecules C5HT-di-PSAc (above) and Cl-C5HT-PSAc (below).	65
Figure 2.2: Solution of C5HT-di-PSAc at 1.25×10^{-5} M in DMF before any irradiation so with most of the molecules are in the open state (colorless solution on the left) and after UV irradiation with most of the molecules in the closed state (purple solution on the right).	65
Figure 2.3: Synthesis of bis(chlorothienyl)cyclopentene (parent DAE). i) glutaryl dichloride, AlCl ₃ , CS ₂ , 98%; ii) Zn, TiCl ₃ (THF) ₃ , THF, 50%. Adapted from ¹¹⁴	67
Figure 2.4: Synthesis of C5HT-di-PSAc. a) <i>n</i> BuLi, THF, 298 K; b) B(OBu) ₃ , THF, 298 K; c) ArBr, [Pd(PPh ₃) ₄], 2M aqueous Na ₂ CO ₃ , ethylene glycol, THF, reflux. Adapted from ¹¹⁵	68
Figure 2.5: UV-visible spectrum, TEM image and photo of the red solution obtained for 28 nm AuNPs (YPOP49B) and 50 nm AuNPs (YPOP57E).	72
Figure 2.6: Scheme of the main components of a single-beam UV-visible spectrophotometer similar to the Jasco V-750.	82
Figure 2.7: Noise and stability over time test (test n°1), UV-visible spectra recorded every hour without putting anything inside the spectrophotometer.	84
Figure 2.8: Signal to noise ratio test (test n°2) 3 spectra of an ITO substrate with 28 nm gold nanoparticles deposited on it recorded in a row.	84
Figure 2.9: Influence of recording the baseline with different pristine ITO substrate test (test n°3). First spectra recorded during test n°2 with the baseline recorded with T1, T2, and T3 respectively.	85
Figure 2.10: Stability in time of the wavelength and absorbance values of the plasmon peak test (test n°4). LSPR peak wavelength and absorbance values of 9 UV-visible spectra of an ITO substrate with 28 nm gold nanoparticles deposited on it recorded every 15 minutes.	86
Figure 2.11: Influence of the repositioning of the sample holder test (test n°5). Spectra recorded before and after lifting and putting back the sample holder (with the ITO/AuNPs substrate in it) in the cuvette.	87
Figure 2.12: Emission spectra of the LEDs.	91
Figure 2.13: Setup for a sample directly put inside the sample holder for substrates from Jasco ("substrate version"). The sample holder, UV LED and visible LED are respectively indicated by a red arrow, a purple arrow, and a green arrow.	92
Figure 2.14: Setup for a sample inside the quartz cuvette ("cuvette version"). The cuvette, UV LED and visible LED are respectively indicated by a red arrow, a purple arrow, and a green arrow.	92
Figure 2.15: Setup used in Konstanz university for the irradiation (LEDs, on the left) and recording of the spectra (Cary 60 spectrophotometer, on the right). The following additional elements were also used: 1 - UV LED (300 nm); 2 - Visible LED (505 nm); 3, 4, 6 - Lenses; 5 - Quartz cuvette; 7 - Mirrors; 8 - Stirrer; yellow arrows – Shutters.	94
Figure 2.16: Power measurements for both LEDs.	95
Figure 2.17: Scheme of the elements of a microscope in dark-field configuration and of the path that light takes in such configuration.	96
Figure 2.18: Dark field microscopy images with 10x magnification and 100x magnification of single 51 nm AuNPs (the green dots) on ITO (zone B of sample ADITO81). Luminosity 75 %, gain 6.2 x, exposure time 700 ms.	97
Figure 2.19: DF image (magnification 100x, 75 % luminosity, 6.2 x gain, and 700 ms exposure time) of a zone of interest with a set of 20 AuNPs (zone C from sample ADITOR) and spectrum of AuNP 14 from this set.	100
Figure 2.20: Scheme illustrating the main elements of an AFM. Reprinted from ¹³³	101
Figure 2.21: AFM images obtained in Taping mode of samples ADITOI (left) and ADITOC (right), they are both made of an ITO substrate covered with a layer of 28 nm gold nanoparticles functionalized with C5HT-di-PSH.	103

Figure 3.1: Chemical structure and abbreviation of the thiol molecules used for this study: 11-mercaptoundecanoic acid (MUDA) and 16-mercaptohexadecanoic acid (MHDA).....	105
Figure 3.2: UV-visible spectra of 22 nm spherical gold nanoparticles in solution on which MUDA is progressively adsorbed. The resulting LSPR wavelength shift is 2.7 nm. Zoom on the LSPR peak maximum (in the green frame).....	106
Figure 3.3: FTIR (Fourier-Transform Infra-Red) adsorption spectra of the two AuNPs solutions (citrate decorated - spectrum (a) and MUDA-functionalized - spectrum (b)) drop-casted on silicon substrates, recorded in Transmission with 70° incidence.....	107
Figure 3.4: UV-visible spectra of 22 nm spherical gold nanoparticles in solution on which MHDA is progressively adsorbed. The resulting LSPR wavelength shift is 3.9 nm. Zoom on the LSPR peak maximum (in the green frame).....	108
Figure 3.5: Evolution of the LSPR peak wavelength as a function of the added amount of thiol, MUDA (red square) and MHDA (blue dots). The dotted curves are guides for the eye.	110
Figure 3.6: Evolution of the extinction cross section of 22 nm AuNP in a medium whose refractive index is increased from 1 to 1.8 (left). Calculations are done with the Mie theory. Plot of the extinction maximum (solid red line, left axis) as a function of the optical index of the surrounding solvent. Value of the max extinction cross section (blue open circles, right axis). Within the range of 1.3 - 1.6, the evolution is approximately linear with a slope of $m = 69 \text{ nm.RIU}^{-1}$. Bichromatics calculator was used ¹⁵⁷	113
Figure 3.7: a) Spherical nanoparticle of diameter D in a medium of index $n_0 + \Delta n'$ b) the same nanoparticle bearing a molecular layer of thickness d , in a medium of index n_{solvent} c) the same nanoparticle with a partial molecular coverage $\theta < 1$. The refractive index of the incomplete molecular layer n_{MG} is calculated with the Maxwell-Garnett formula.....	114
Figure 3.8: a) Spherical nanoparticle of radius R , bearing a molecular layer of thickness d , in a medium of index n_0 ; The near field radiated by the particle extends over a length l_d . b) 2D representation of the near-field enhancement by a gold nanoparticle in water upon excitation at its plasmon resonance ($\lambda = 520 \text{ nm}$). The intensity of electric field is enhanced of a factor of 20 in the vicinity of the nanoparticle surface and decay as $1/r^3$. Reprinted from ¹⁶⁴	116
Figure 3.9: Decay of the radiated electric near field along the axis xx' and zz' for a gold nanoparticle in water.	117
Figure 3.10: UV-visible spectra recorded during the kinetics measurements.....	120
Figure 3.11: Evolution of the LSPR peak wavelength upon functionalization of the AuNPs surface with MUDA plotted versus the time (to elucidate the functionalization kinetics). The solution was not stirred during the acquisition of the spectra. 50 μL of MUDA at 35 μM were added to 2 mL of AuNPs at $0.66 \times 10^{-9} \text{ mol/L}$, leading to a final MUDA concentration of 0.86 μM in the reacting solution (in the cuvette). The dotted line corresponds to a fit of the data with a single exponential.....	121
Figure 4.1: Semi-developed formula of the two diarylethenes molecules.	124
Figure 4.2: Subunits of diarylethene molecule C5HT-di-PSAc.....	125
Figure 4.3: Simplified Jablonski diagram summarizing the transitions occurring during the cyclization reaction (left) and cycloreversion (right). Note that 'o' stands for opened and 'c' for closed, referring to the opened or closed isomer of the molecule.	126
Figure 4.4: Photocyclization and photocycloreversion reaction and the spectra corresponding to the opened and closed form of each molecule. The isosbestic point are circled in dotted line. The spectral transitions corresponding to each band are indicated. The molecules are solubilized in DMF at a concentration of $1.25 \times 10^{-5} \text{ M}$ in a 1 cm cuvette.....	130
Figure 4.5: Evolution of the spectra under UV and visible irradiation for C5HT-di-PSAc (on the left) and Cl-C5HT-PSAc (on the right). The isosbestic points are circled in dotted line.	133

Figure 4.6: Evolution of the absorbance under UV irradiation monitored at various wavelength for C5HT-di-PSAc (on the left) and Cl-C5HT-PSAc (on the right).....	134
Figure 4.7: Evolution of the normalized absorbance under UV irradiation monitored at various wavelengths for C5HT-di-PSAc (on the left) and Cl-C5HT-PSAc (on the right). ...	135
Figure 4.8: Spectra allowing to demonstrate the presence of a small hypsochromic shift for prolonged UV irradiation of Cl-C5HT-PSAc.	137
Figure 4.9: Isosbestic points for a UV irradiation of 30 000 s (C5HT-di-PSAc, on the left) and of 60 000 s (Cl-C5HT-PSAc, on the right).	137
Figure 4.10: Evolution of the absorbance at the isosbestic point throughout the UV illumination, for C5HT-di-PSAc (left) and Cl-C5HT-PSAc (right).	138
Figure 4.11: Hypothetic by-product of Cl-C5HT-PSAc.	139
Figure 4.12: Reversibility measurements for C5HT-di-PSAc (on the left) and Cl-C5HT-PSAc (on the right). The molecules are illuminated with UV light for 3000 s and then with visible light until they all switch back to their opened form.....	143
Figure 4.13: Reversibility measurements according to the number of photons for C5HT-di-PSAc (on the left) and Cl-C5HT-PSAc (on the right).	144
Figure 4.14: Evolution of the absorbance over 40 switching cycles for C5HT-di-PSAc (on the left) and Cl-C5HT-PSAc (on the right). In the case of C5HT-di-PSAc, each cycle consists in 3 consecutive UV light irradiations of 30 s followed by 6 consecutive visible light irradiations of 135s. In the case of Cl-C5HT-PSAc, each cycle consists in 3 consecutive UV light irradiations of 90 s followed by 6 consecutive visible light irradiations of 165s. The insert is a zoom on the three first cycles for C5HT-di-PSAc.	146
Figure 4.15: Absorbance amplitude of each of the 40 cycles for C5HT-di-PSAc (top) and Cl-C5HT-PSAc (bottom).	147
Figure 4.16: Evolution of the absorbance of C5HT-di-PSAc under UV irradiation monitored at $\lambda_{\max} = 546$ nm (band in the visible range corresponding to the maximum absorbance of the closed-ring molecules) (left) and then visible light irradiation monitored at $\lambda_{\text{exc}}(\text{Vis}) = 505$ nm (right).....	151
Figure 4.17: Evolution of the absorbance of Cl-C5HT-PSAc under UV irradiation monitored at $\lambda_{\max} = 492$ nm (band in the visible range corresponding to the maximum absorbance of the closed-ring molecules) (left) and then visible light irradiation monitored at $\lambda_{\text{exc}}(\text{Vis}) = 505$ nm (right).....	151
Figure 4.18: Temporal derivative of the absorbance evolution of the C5HT-di-PSAc closed-ring molecules (dA_{closed}/dt) versus the absorbance of the closed-ring molecules (A_{closed}) (left) opposite of the temporal derivative of the absorbance of the open form ($-dA_{\text{open}}/dt$) versus $10 - A_{\text{open}}$ (right).	152
Figure 4.19: Temporal derivative of the absorbance evolution of the Cl-C5HT-PSAc closed-ring molecules (dA_{closed}/dt) versus the absorbance of the closed-ring molecules (A_{closed}) (left) opposite of the temporal derivative of the absorbance of the open form ($-dA_{\text{open}}/dt$) versus $10 - A_{\text{open}}$ (right).	153
Figure 5.1: Normalized UV-visible spectrum of 28 nm AuNPs in water, 28 nm AuNPs deposited on ITO and C5HT-di-PSAc (left) in DMF or Cl-C5HT-PSAc (right).	159
Figure 5.2: UV-visible spectra recorded after the deposition of the AuNPs, after the desilanization and after the adsorption of the Cl-C5HT-PSH molecules.....	160
Figure 5.3: Scheme of the type of sample obtained with grafting protocol 1: ITO/AuNPs(28 nm)/Cl-C5HT-PSH. The green sticks are silanes (APTES). Note that this sketch is not on scale since the size of the DAE molecules is 1.39 nm, that of the APTES molecules is 0.5 nm and that of the AuNPs in 28 nm.	161
Figure 5.4: UV-visible spectra corresponding to the switching measurements on ADITO69 (28 nm AuNPs).....	162

Figure 5.5: Evolution of the LSPR peak absorbance (left) and wavelength (right) of ADITO69 as a function of time upon irradiation. The dotted line is a guide for the eyes.	163
Figure 5.6: UV-visible spectra corresponding to the switching measurements on ADITO49 (28 nm AuNPs).....	165
Figure 5.7: Evolution of the LSPR peak absorbance (left) and wavelength (right) of ADITO49 as a function of time upon irradiation. The dotted line is a guide for the eyes.	165
Figure 5.8: UV-visible spectra corresponding to the switching measurements on ADITO46 (28 nm AuNPs).....	166
Figure 5.9: Evolution of the LSPR peak absorbance (left) and wavelength (right) of ADITO46 as a function of time upon irradiation. The dotted line is a guide for the eyes.	167
Figure 5.10: UV-visible spectra corresponding to the switching measurements on ADITO47 (35 nm AuNPs).....	168
Figure 5.11: Evolution of the LSPR peak absorbance (left) and wavelength (right) of ADITO47 as a function of time upon irradiation. The dotted line is a guide for the eyes.....	168
Figure 5.12: Scheme of the type of sample obtained with grafting protocol 1 without the desilanization step: ITO/AuNPs(28 nm)/Cl-C5HT-PSH. The green sticks are silanes (APTES). Note that this sketch is not on scale since the size of the DAE molecules is 1.39 nm, that of the APTES molecules is 0.5 nm and that of the AuNPs in 28 nm.....	169
Figure 5.13: UV-visible spectra corresponding to the switching measurements on ADITO60.	170
Figure 5.14: UV-visible spectra corresponding to the switching measurements on ADITO61.	170
Figure 5.15: Evolution of the LSPR peak absorbance of ADITO60 (left) and ADITO61 (right) as a function of time upon irradiation. The dotted line is a guide for the eyes.	171
Figure 5.16: UV-visible spectra corresponding to the switching measurements on ADITO64.	172
Figure 5.17: Evolution of the LSPR peak absorbance (left) and wavelength (right) of ADITO64 as a function of time upon irradiation. The dotted line is a guide for the eyes.....	172
Figure 5.18: Example of the determination of Δt_{UV} and Δt_{vis} for the calculations of the switching ratios with the data from the cycling measurements made on ADITO64. The time value corresponding to the absorbance value at the crossing of the black and the red dotted line is the one used to delimit Δt_{UV} . The black dotted line is a guide for the eyes.	174
Figure 5.19: UV-visible spectrum of sample ADITOC (ITO/AuNPs(28 nm)) in air ($\lambda_{LSPR} = 511.7$ nm) and in DMF ($\lambda_{LSPR} = 532.4$ nm) and associated calculated spectra of 28 nm AuNPs in air ($\lambda_{LSPR} = 499.3$ nm) and in an effective medium ITO/DMF ($\lambda_{LSPR} = 518.4$ nm).....	176
Figure 5.20: Control experiments conducted with sample ADITOB in degassed solvent (control experiment 1, on the left) and sample ADITO8 in non-degassed solvent (control experiment 2, on the right).	177
Figure 5.21: Two UV-visible spectra from each phase of the experiment (control) made with ADITOB. On the left, spectrum 10/800 (in black) and spectrum 800/800 ($t = 21893$ s) of the stabilization phase. On the right, spectrum 10/2808 (in black) and spectrum 2800/2808 ($t = 86480$ s) of the adsorption phase (in red).....	178
Figure 5.22: Two UV-visible spectra from each phase of the experiment (control) made with ADITO8. On the left, spectrum 10/611 (in black) and spectrum 600/611 ($t = 16503$ s) of the stabilization phase. On the right, spectrum 10/2800 (in black) and spectrum 2800/2800 ($t = 84964$ s) of the adsorption phase (in red).....	178
Figure 5.23: Evolution of λ_{LSPR} during three different stabilization phases, two with degassed solvent (one from the control experiment made with sample ADITOB in green, one from the experiment made with sample ADITOC, in red) and one with non-degassed solvent (from the control experiment made with sample ADITO8).....	179

Figure 5.24: Control experiments made with degassed (in green) and non-degassed (in blue) solvent.	180
Figure 5.25: Tentative of grafting of the protected molecules C5HT-di-PSAc (on the left, sample ADITOI) and Cl-C5HT-PSAc (on the right, sample ADITO5) on 25 nm gold nanoparticles deposited on ITO.....	181
Figure 5.26: Two UV-visible spectra from each phase of the experiment made with ADITOI. On the left, spectrum 10/572 (in black) and spectrum 570/572 (t = 23009 s) of the stabilization phase. On the right, spectrum 10/2182 (in black) and spectrum 2180/2182 (t = 93807 s) of the mixing phase (in red).	182
Figure 5.27: Two UV-visible spectra from each phase of the experiment made with ADITO5. On the left, spectrum 10/757 (in black) and spectrum 750/757 (t = 19894 s) of the stabilization phase. On the right, spectrum 10/2904 (in black) and spectrum 2900/2904 (t = 86680 s) of the mixing phase (in red).	182
Figure 5.28: Grafting of C5HT-di-PSH on 25 nm gold nanoparticles deposited on ITO. Deposition carried out in a DAE solution prepared with non-degassed DMF for sample ADITOI (on the left) and in a DAE solution prepared with degassed DMF for sample ADITOC (on the right).....	183
Figure 5.29: Two UV-visible spectra from each phase of the experiment made with ADITOI. On the left, spectrum 10/633 (in black) and spectrum 620/633 (t = 17119 s) of the stabilization phase. On the right, spectrum 10/2528 (in black) and spectrum 2500/2528 (t = 76552 s) of the adsorption phase (in red).....	184
Figure 5.30: Two UV-visible spectra from each phase of the experiment made with ADITOC. On the left, spectrum 10/571 (in black) and spectrum 570/571 (t = 15377 s) of the stabilization phase. On the right, spectrum 10/2805 (in black) and spectrum 2800/2805 (t = 86447 s) of the adsorption phase (in red).....	185
Figure 5.31: Scheme of the type of sample obtained with grafting protocol 2: ITO/AuNPs(28 nm)/C5HT-PSH. The green sticks are silanes (APTES). Note that this sketch is not on scale since the size of the DAE molecules is 1.79 nm, that of the APTES molecules is 0.5 nm and that of the AuNPs in 28 nm.	185
Figure 5.32: UV-visible spectra corresponding to the switching measurements on ADITOI (Day 1).....	187
Figure 5.33: Evolution of the LSPR peak absorbance of ADITOI (Day 1) as a function of time (left) or number of photons (right) upon irradiation. The dotted line is a guide for the eyes.	187
Figure 5.34: Example of the determination of Δt_{UV} and Δt_{vis} for the calculations of the switching ratios with the data from the cycling measurements made on ADITOI (Day 1). The time value corresponding to the absorbance value at the crossing of the black and the red dotted line is the one used to delimit Δt_{vis} . The black dotted line is a guide for the eyes.....	188
Figure 5.35: Evolution of the LSPR peak absorbance of ADITOI over 3 consecutive days of measurements as a function of time upon irradiation. The time scale between each measurement day (in the 2 dotted lines zone) was voluntarily shortened, it does not actually correspond to how much time passed in between the series of measurement.	188
Figure 5.36: UV-visible spectra corresponding to the switching measurements on ADITOC.	189
Figure 5.37: Evolution of the LSPR peak absorbance of ADITOC as a function of time (left) or number of photons (right) upon irradiation. The dotted line is a guide for the eyes.	190
Figure 5.38: Evolution of the LSPR peak absorbance of ADITOI as a function of time.	193
Figure 5.39: Calculation of the molar absorptivity for 25 nm AuNPs within the electrostatic approximation. The molar absorptivity is proportional to this curve, and we obtain $\epsilon_{AuNP} = 2.7 \times 10^9 \text{ M}^{-1} \cdot \text{cm}^{-1}$ at 520 nm (left). Calculated effective molar absorptivity ϵ_{mix} of a mixture of AuNP and DAE in the case there is no interaction between the two species (right).	196

Figure 5.40: Scheme of the phenomena occurring in the areas around a spherical gold nanoparticle.	198
Figure 6.1: Dark field microscopy image of the zone of interest (zone A of ADITO80). The 22 AuNPs indicated in orange are part of a selection of single 51 nm AuNPs. Magnification 100x, exposure time 700 ms, gain 6.2. Red inset: doughnut shaped AuNP. Blue inset: bright dot AuNP.....	201
Figure 6.2: AFM image of the zone of interest. The 22 AuNPs indicated in green are those from the selection of single 51 nm AuNPs. The AuNP 19 that went missing is indicated in red.....	203
Figure 6.3: Zoomed images of AuNPs 1, 6, 17, and 21.	203
Figure 6.4: Scattering spectra of each of the 22 AuNPs from the selection of single 51 nm AuNPs (on the left). Example of a single 51 nm AuNP (AuNP 1) spectrum (on the right)..	205
Figure 6.5: UV-visible spectrum of AuNP 1 and the AuNP batch it came from YPOP57E (AuNPs in aqueous solution).....	205
Figure 6.6: Dark field microscopy image of the zone of interest after the drop casting of 28 nm satellite AuNPs took place. The 22 AuNPs indicated in orange are those from the selection of single 51 nm AuNPs which might now possess a neighbor 28 nm AuNP. The AuNP 19 that went missing is indicated in red. Magnification 100x, exposure time 700 ms, gain 6.2.....	207
Figure 6.7: Scheme and dark field microscopy images of the Hg ²⁺ sensor. Reprinted from ¹⁹⁶	208
Figure 6.8: AFM image of AuNPs 1 to 8 (indicated in green) after the drop casting of 28 nm satellite AuNPs took place.	209
Figure 6.9: Zoomed images of AuNPs 1 to 8.....	209
Figure 6.10: AFM image of AuNPs 9 to 22 (indicated in green) after the drop casting of 28 nm satellite AuNPs took place.	210
Figure 6.11: Zoomed images of AuNPs 9 to 21.....	211
Figure 6.12: Asymmetric plasmonic dimer made of a 51 nm AuNP and a 28 nm AuNP separated by a gap distance d_{gap} . The dimer axis forms an angle α with the surface. The green sticks are silanes (APTES).	212
Figure 6.13: Scattering spectrum of AuNP 8 before (Measurement 1) and after (Measurement 2) the drop casting of 28 nm satellite AuNPs took place.	213
Figure 6.14: UV-visible spectrum of AuNP 1 (on the left) and AuNP 21 (on the right) before (single AuNP) and after (neighbor AuNPs) the drop casting of 28 nm satellite AuNPs took place.	215
Figure 6.15: (a) Scattering spectra of a single Au nanoparticle monomer and a single dimer on ITO and scheme of the dark field spectroscopy setup used to record the spectra. (b) Simulated scattering spectra of a single Au nanoparticle monomer and a single dimer on ITO. Reprinted from ¹⁰⁵	216
Figure 6.16: (a) Extinction spectra of 60 nm AuNPs dimers modified with C5 (5-carboxy-1-pentanethiol), C7 (7-carboxy-1-heptanethiol), C10 (10-carboxy-1-decanethiol) and C15 (15-carboxy-1-pentadecanethiol). (b) Simulated spectra of 60 nm AuNPs dimers with interparticle gaps of 1.0 nm, 1.4 nm, 2.0 nm and 3.0 nm. Adapted from ¹⁰⁶	217
Figure 6.17: Plasmon hybridization diagram for an asymmetric plasmonic dimer of spherical gold nanoparticles. The arrows inside the AuNPs indicate the direction of the induced dipole moment corresponding to the charge separation occurring upon LSPR excitation.	218
Figure 6.18: Simulated spectra of a symmetric (left) and an asymmetric dimer (right) in vacuum in function of their gap distance d_g . The symmetric dimer is made of two AuNPs of 60.2 nm whereas the asymmetric dimer is made of an AuNP of 60.2 nm and an AuNP of 29.1 nm.....	221

Figure 6.19: Simulated spectra of a symmetric (left) and an asymmetric dimer (right) deposited on ITO in function of their gap distance d_g . The symmetric dimer is made of two AuNPs of 60.2 nm whereas the asymmetric dimer is made of an AuNP of 60.2 nm and an AuNP of 29.1 nm. In both cases, the dimer axis is parallel to the substrate (no angle α). The following parameters were used, $e_s = 80$ nm (thickness of the substrate's ITO layer) $\epsilon_s = 3.6159$ (dielectric permittivity of the substrate's ITO layer), the layer of glass below that of ITO is considered infinite and with a dielectric permittivity of $\epsilon_{glass} = 2.3207$, the AuNPs are considered separated by a distance $d_s = 0.9729$ nm from the substrate (solid curves) corresponding to the size of an APTES molecule.....	222
Figure 6.20: Simulated spectra of asymmetric dimers deposited on ITO with various gap distances d_g (left) or various angles α between the dimer axis and the substrate, for a fixed gap distance of 0.5 nm (right). The asymmetric dimer is made of an AuNP of 60.2 nm and an AuNP of 29.1 nm.	223
Figure 6.21: Dark field microscopy image of the zone of interest (zone B of ADITO82). The 22 AuNPs indicated in orange and blue are part of a selection of single 51 nm AuNPs. The AuNPs indicated in blue are those used for the switching measurements. Magnification 100x, exposure time 700 ms, gain 6.2.....	225
Figure 6.22: Scheme of the type of sample obtained with grafting protocol 1: ITO/AuNPs(28 nm)/C5HT-di-PSH. The green sticks are silanes (APTES). Note that this sketch is not on scale since the size of the DAE molecules is 1.79 nm, that of the APTES molecules is 0.5 nm and that of the AuNPs is 51 nm.	226
Figure 6.23: Spectrum of a single AuNP (AuNP 6) before and after DAE grafting.	226
Figure 6.24: LSPR peak wavelength value before (AuNP) and after the DAE grafting (DAE functionalized AuNP) given for each AuNP.....	227
Figure 6.25: LED irradiation setup combined to the setup made of the UV-visible spectrophotometer coupled to the optical microscope. The UV light coming from the LED (trajectory indicated by the purple arrow) is focused on the sample by a lens of $f = 25$ mm yielding an illumination zone of 0.27 cm ²	229
Figure 6.26: UV-visible spectra corresponding to the switching measurements on AuNP 19 (left). Evolution of the scattering intensity at λ_{LSPR} upon irradiation as a function of time...	231
Figure 6.27: UV-visible spectra corresponding to the switching measurements on AuNP 14 (left). Evolution of the scattering intensity at λ_{LSPR} upon irradiation as a function of time...	232

List of Tables

Table 1.1: Values of the ring-closing and ring-opening quantum yields of a few common diarylethenes. Adapted from ²⁶	21
Table 2.1: Batches of AuNPs synthesized and used for the studies, sizes calculated using TEM images and the method of Haiss et al. ¹²²	72
Table 2.2: Samples ITO/AuNPs prepared following the different AuNPs deposition protocols.....	75
Table 2.3: Samples ITO/AuNPs/Cl-C5HT-PSH prepared following DAE grafting protocol 1.....	76
Table 2.4: Samples ITO/AuNPs/C5HT-di-PSH prepared following DAE grafting protocol 1.....	77
Table 2.5: Samples ITO/AuNPs/DAE prepared following DAE grafting protocol 2.....	79
Table 2.6: Parameters used for all the UV-visible measurements (tests and experiments) performed with the Jasco V-750 spectrophotometer.....	83
Table 2.7: Main characteristics of the LEDs.....	91
Table 2.8: LEDs parameters for the switching measurements presented in Chapter 5 given for both versions of the setup.....	93
Table 2.9: LEDs parameters for the switching measurements presented in Chapter 4.....	95
Table 2.10: Parameters used for the recording of all the UV-visible spectra of individual gold nanoparticles with the QE Pro spectrophotometer.....	99
Table 2.11: Parameters used to measure in Tapping mode.....	103
Table 3.1: Saturation experiments parameters (concentration of the added aliquot, amount of thiol added to the reacting solution, and concentration of the reacting solution) and measured LSPR peak wavelengths for MUDA and MHDA.....	109
Table 3.2: Values of the LSPR peak wavelength (λ_{LSPR}) and of the extinction cross section at λ_{LSPR} as a function of the index of the surrounding solvent.....	114
Table 3.3: Calculated and measured values of the LSPR wavelength shift induced by the grafting of each molecule. The effective length of the molecules is given assuming a tilt angle from the normal to the surface $\alpha = 30^\circ$	119
Table 4.1: Characteristics of each absorption band present on the UV-visible spectra of the two molecules.....	131
Table 4.2: Absorbance value, and molar absorption coefficient at $\lambda_{\text{exc}}(\text{UV} - 300 \text{ nm})$, $\lambda_{\text{exc}}(\text{Vis} - 505 \text{ nm})$ and λ_{iso}	132
Table 4.3: UV LED ($\lambda_{\text{exc}}(\text{UV}) = 300 \text{ nm}$) parameters for the ring-closing reaction monitoring.....	133
Table 4.4: LEDs ($\lambda_{\text{exc}}(\text{UV}) = 300 \text{ nm}$ and $\lambda_{\text{exc}}(\text{Vis}) = 505 \text{ nm}$) parameters for the reversibility measurements.....	142
Table 4.5: LEDs ($\lambda_{\text{exc}}(\text{UV}) = 300 \text{ nm}$ and $\lambda_{\text{exc}}(\text{Vis}) = 505 \text{ nm}$) parameters for the cycles measurements.....	145
Table 4.6: Quantum yield and conversion values ($\lambda_{\text{exc}}(\text{UV}) = 300 \text{ nm}$ and $\lambda_{\text{exc}}(\text{Vis}) = 505 \text{ nm}$).....	154
Table 4.7: Switching ratio values calculated for both molecules ($\lambda_{\text{exc}}(\text{UV}) = 300 \text{ nm}$ and $\lambda_{\text{exc}}(\text{Vis}) = 505 \text{ nm}$).....	155
Table 5.1: LEDs parameters used for the switching measurements made on the samples prepared with grafting protocol 1.....	161
Table 5.2: Values of the switching ratios calculated for the two cycles the measurements made on ADITO64.....	174

Table 5.3: LEDs parameters used for the switching measurements made on the samples prepared with grafting protocol 2.....	186
Table 5.4: Values of the switching ratios (Vis/UV above, UV/Vis in parenthesis below) calculated for each cycle of each measurement day of ADITOI.	189
Table 5.5: Values of the switching ratios (Vis/UV above, UV/Vis in parenthesis below) calculated for the two cycles the measurements made on ADITOC.....	190
Table 5.6: Values of SR(Vis/UV) obtained for C5HT-di-PSH grafted on 28 nm AuNPs deposited on ITO.	194
Table 6.1: LSPR peak wavelength and height (measured on the AFM images) of each AuNP of the selection.	204
Table 6.2: Values of the LSPR peak wavelength of the AuNPs from the selection that do not possess a 28 nm AuNP neighbor before ($\lambda_{\text{LSPR single - individual mode Msmt 1}}$) and after ($\lambda_{\text{LSPR single - individual mode Msmt 2}}$) the drop casting of the 28 nm satellite AuNPs took place; difference between the LSPR peak wavelength values of the peak corresponding to the individual oscillation mode ($\Delta\lambda_{\text{LSPR single - individual mode}}$).	214
Table 6.3: Values of the LSPR peak(s) wavelength(s) of the AuNPs from the selection that possess a 28 nm AuNP neighbor before ($\lambda_{\text{LSPR single - individual mode}}$) and after ($\lambda_{\text{LSPR neighbors - individual mode}}$ and $\lambda_{\text{LSPR neighbors - collective mode}}$) the drop casting of the 28 nm satellite AuNPs took place; difference between the LSPR peak wavelength values of the peak corresponding to the individual ($\Delta\lambda_{\text{LSPR neighbors - individual mode}}$) and of that corresponding to the collective ($\Delta\lambda_{\text{LSPR neighbors - collective mode}}$) oscillation mode.	216
Table 6.4: Values of the gap distances calculated with the plasmon ruler equation.....	219
Table 6.5: Values of the measured LSPR peak wavelength before the functionalization ($\lambda_{\text{LSPR initial}}$) and after it ($\lambda_{\text{LSPR DAE functionalized AuNP}}$); values of the difference between these LSPR peak wavelengths ($\Delta\lambda_{\text{LSPR}}$).	228
Table 6.6: LEDs parameters for the switching measurements.	230

Diarylethenes used as molecular switches for the connection of gold nanoparticles

Abstract:

Diarylethene molecules used as molecular switches are envisioned as components of molecular electronic devices. These photochromic molecules exhibit high thermal stability, resistance to fatigue, and switching efficiency. Nevertheless, the switching of most diarylethenes (DAEs) is asymmetric: their photocycloreversion reaction possessing a much lower quantum yield than that of their photocyclization reaction. A strategy to solve that asymmetric switching issue was tested, it consisted in connecting the diarylethene molecules to gold nanoparticles (AuNPs). Indeed, gold nanoparticles exhibit both a localized surface plasmon resonance (LSPR), very useful for the monitoring of the adsorption of the DAEs at the surface of the AuNPs, and a plasmonic nanoantenna effect. This nanoantenna effect, generating a large enhancement of the electromagnetic field in the close vicinity of the nanoparticle, was expected to increase the efficiency of the photocycloreversion reaction (its quantum yield), leading to a more symmetric switching.

The switching of the dithienylethene (DTE) molecules was first characterized for the molecules alone in solution. Then, the functionalization of 28 nm gold nanoparticles deposited on ITO by the DTE molecules was monitored in situ by UV-visible spectroscopy. Switching measurement on the samples ITO/AuNPs/DTE were performed by UV-visible spectroscopy combined with an irradiation setup. It resulted that for the diarylethene molecules chosen for this study connected to 28 nm AuNPs, although the switching capacity was preserved upon grafting on the AuNPs, the quenching was largely dominant. As a consequence, a slowing of the photo-induced reactions was caused and not an acceleration.

Gold nanoparticles were also studied at the single nanoparticle scale by AFM and dark field microscopy coupled to UV-visible spectroscopy. On the one hand, the functionalization of individual 51 nm gold nanoparticles was monitored by dark field microscopy coupled to UV-visible spectroscopy. Switching measurements were then conducted on the diarylethenes molecules beard by single AuNPs, revealing that this switching was comparable to the one previously measured on a more global scale. On the other hand, asymmetric plasmonic dimers made of a 51 nm AuNP and a 28 nm AuNP were prepared and characterized.

Keywords: gold nanoparticles, diarylethenes, molecular switches, plasmonic nanoantenna.

Diaryléthènes utilisés comme interrupteurs moléculaires pour la connexion de nanoparticules d'or

Résumé :

Les molécules de diaryléthène utilisées comme interrupteurs moléculaires sont envisagées comme composants de dispositifs électroniques moléculaires. Ces molécules photochromiques présentent une stabilité thermique, une résistance à la fatigue et une efficacité de commutation élevées. Néanmoins, la commutation de la plupart des diaryléthènes (DAEs) est asymétrique : leur réaction de photocycloréversion possède un rendement quantique bien inférieur à celui de leur réaction de photocyclisation. Une stratégie pour résoudre ce problème de commutation asymétrique a été testée, elle consistait à connecter les molécules de diaryléthène à des nanoparticules d'or (AuNPs). En effet, les nanoparticules d'or présentent à la fois une résonance plasmonique de surface localisée (LSPR), très utile pour le suivi de l'adsorption des DAEs à la surface des AuNPs, et un effet de nanoantenne plasmonique. Cet effet de nanoantenne, générant une importante amplification du champ électromagnétique au voisinage immédiat de la nanoparticule, devait augmenter l'efficacité de la réaction de photocycloréversion (son rendement quantique), conduisant à une commutation plus symétrique.

La commutation des molécules de dithiényléthène (DTE) a d'abord été caractérisée pour les molécules seules en solution. Ensuite, la fonctionnalisation de nanoparticules d'or de 28 nm déposées sur ITO par les molécules de DTE a été suivie in situ par spectroscopie UV-visible. Les mesures de commutation sur les échantillons ITO/AuNPs/DTE ont été réalisées par spectroscopie UV-visible combinée à un dispositif d'irradiation. Il en est résulté que pour les molécules de diaryléthène choisies pour cette étude connectées à des AuNPs de 28 nm, bien que la capacité de commutation ait été préservée lors du greffage sur les AuNPs, le piégeage (« quenching ») était largement dominant. Par conséquent, un ralentissement des réactions photo-induites a été provoqué et non une accélération.

Les nanoparticules d'or ont également été étudiées à l'échelle de la nanoparticule unique par AFM et microscopie en champ sombre couplée à la spectroscopie UV-visible. D'une part, la fonctionnalisation de nanoparticules d'or individuelles de 51 nm a été suivie par microscopie en champ sombre couplée à la spectroscopie UV-visible. Des mesures de commutation ont ensuite été effectuées sur les molécules de diaryléthènes portées par les AuNPs uniques, révélant que cette commutation était comparable à celle précédemment mesurée à une échelle plus globale. D'autre part, des dimères plasmoniques asymétriques constitués d'un AuNP de 51 nm et d'un AuNP de 28 nm ont été préparés et caractérisés.

Mots clés : nanoparticules d'or, diaryléthènes, interrupteurs moléculaires, nanoantenne plasmonique.